Hydrogen and Carbon Monoxide Electrochemical Oxidation Reaction Kinetics on Solid Oxide Fuel Cell Anodes

by

Weifang Yao

A thesis
presented to the University of Waterloo
in fulfillment of the
thesis requirement for the degree of
Doctor of Philosophy
in
Chemical Engineering

Waterloo, Ontario, Canada, 2013

AUTHOR'S DECLARATION

I hereby declare that I am the sole author of this thesis. This is a true copy of the thesis, including any required final revisions, as accepted by my examiners.

I understand that my thesis may be made electronically available to the public.

Abstract

Solid oxide fuel cells (SOFCs) are promising power generation devices due to its high efficiency and low pollutant emissions. SOFCs operate with a wide range of fuels from hydrogen (H_2) to hydrocarbons, and are mainly intended for stationary power generation. Compared to combustion systems, SOFCs have significantly lower environmental impacts. However, the full scale commercialization of SOFCs is impeded by high cost and problems associated with long-term performance and durability. The cell performance can be affected by various internal losses, involving cathode, anode and electrolyte. Anodic losses make a significant contribution to the overall losses, practically in anode-supported cells. Therefore, it is desirable to reduce the anodic losses in order to enhance the overall cell performance. Knowledge of the actual elementary reaction steps and kinetics of electrochemical reactions taking place on the anode is critical for further improvement of the anode performance. Since H_2 and carbon monoxide (CO) are the primary reforming products when hydrocarbons are used as SOFC fuels, investigation of electrochemical reactions involving H_2 and CO should provide a better understanding of SOFC electrochemical behavior with hydrocarbon feeds. However, still exist uncertainties concerning both H_2 and CO electrochemical reactions.

The overall objective of this research is to investigate the mechanistic details of H_2 and CO electrochemical reactions on SOFC anodes. To achieve this objective, Ni/YSZ pattern anodes were used in the experimental study and as model anodes for the simulation work due to their simplified 2-D structure.

The Ni/YSZ pattern anodes were fabricated using a bi-layer resist lift-off method. Imaging resist nLOF2035 and sacrificial resist PGMI SF11 were found to be effective in the bi-layer photolithographic process. Suitable undercut size was found critical for successful pattern fabrication. A simple method, involving taking microscopic photographs of photoresist pattern was developed, to check if the undercut size is large enough for the lift-off; semi-circle wrinkles observable in photographs indicate whether the undercut is big enough for successful pattern anode fabrication. The final product prepared by this method showed straight and clear Ni patterns.

A systematic study was performed to determine the stable conditions for Ni/YSZ pattern anode performance. The microstructure and electrochemical behavior changes of the pattern anode were evaluated as a function of Ni thickness, temperature and H_2O content in H_2 environment. Ni/YSZ pattern anodes with 0.5 µm thick Ni were tested in dry H_2 at 550°C without significantly changing the TPB line. Ni/YSZ pattern anodes with Ni thickness of 0.8 µm were tested at 550°C under dry and humidified H_2 (3-70% H_2O) conditions without TPB line change. For 0.8 µm thick patterns, the TPB length showed pronounced changes in the presence of H_2 with 3-70% H_2O at 700°C. Significant increase in TPB length due to hole formation was observed at 800°C with 3% and 10% H_2O. Ni/YSZ pattern anodes with 1.0 µm thick Ni were stable in H_2 with 3% H_2O in the range 500-800°C, with only slight changes in the TPB line. Changes of TPB line and Ni microstructure were observed in the presence of 3-70% H_2O above 700°C. Stabilization of the pattern anode performance depends on temperature. To accelerate stabilization of the cell, pre-treatment of the cell in H_2 with 3% H_2O for ~22 hrs at 750°C or 800°C could be performed.

In addition, comprehensive data sets for H_2 and CO electrochemical oxidation reactions on Ni/YSZ pattern anodes were obtained under stable test conditions. For the H_2/H_2O system, the polarization resistance (R_p) increases as temperature, overpotential, H_2 partial pressure, TPB length decreases. R_p is also dependent on H_2O content. When the H_2O content is between 3% and 30-40%, R_p decreased with increasing H_2O content. However, R_p is less affected with further increases in H_2O content. For the CO/CO_2 system, polarization resistance depends on partial pressure of CO and CO_2, temperature and overpotential. Moreover, the polarization resistance decreases when the partial pressure of CO_2 and temperature increase. The partial pressure of CO has a positive effect on the polarization resistance. The polarization resistance decreases to a minimum when the overpotential is 0.1 V. For both H_2 and CO electrochemical oxidations, charge transfer reactions contribute to the rate limiting steps.

A 1-D dynamic SOFC half-cell model considering multiple elementary reaction kinetics was developed. The model describes elementary chemical reactions, electrochemical reactions and surface diffusion on Ni/YSZ pattern anodes. A new charge transfer reactions mechanism proposed by Shishkin and Ziegler (2010) based on Density Functional Theory (DFT) was investigated through kinetic modeling and pattern anode experimental validation. This new mechanism considers hydrogen oxidation at the interface of Ni and YSZ. It involves a hydrogen atom reacting with the oxygen ions bound to both Ni and YSZ to produce hydroxyl (charge transfer reaction 1), which then reacts with the other hydrogen atom to form water (charge transfer reaction 2). The predictive capability of this reaction mechanism to represent our experimental results was evaluated. The simulated Tafel plots were compared with our experimental data for a wide range of H_2 and H_2O partial pressures and at different temperatures. Good agreements between simulations and experimental results were obtained. Charge transfer reaction 1 was found to be rate-determining under cathodic polarization. Under anodic polarization, a change in rate-limiting process from charge transfer reaction 1 to charge transfer reaction 2 was found when increasing the H_2O partial pressure. Surface diffusion was not found to affect the H_2 electrochemical performance.

Acknowledgements

I would like to express my sincere gratitude and appreciation to my supervisor, Professor

Eric Croiset, who gave me the opportunity to work in his lab, and provided me with a great guidance, invaluable comments and encouragement.

I would also like to thank all my committee members, Professor Mark Pritzker, Professor Ting Tsui, Professor John Wen, Professor Kunal Karan for their valuable time in reading this thesis and their comments.

Financial support through funding from NSERC Solid Oxide Fuel Cell Canada Strategic Research Network from Natural Science and Engineering Research Council (NSERC) and other sponsors listed at www.sofccanada.ca are greatly appreciated. Professor Viola Birss, Professor Kunal Karan, Professor Tom Ziegler, Dr. Scott Paulson and Dr. Maxim Shishkin form University of Calgary are appreciated for their helpful discussions about this work. I thank Dr. Scott Paulson for his help depositing platinum on the YSZ single crystal.

I would like to thank the Ms. Liz Bevan, Ms. Judy Caron, Ms. Rose Guderian and Ms. Ingrid Sherrer in the Department of Chemical Engineering for their great help in administration work. Mr. Dennis Herman and Mr. Bert Habicher are greatly appreciated for their technical support.

All my colleagues and friends in the chemical reaction engineering group, Mazni Ismail, Asmida Ideris, Dr. Aiyu Yan, Dr. Ashraf Amin, Dr. Monrudee Phongaksorn, Dr. Noorlisa Harum and many more; thanks for all your help and support.

Ni/YSZ pattern anode fabrication, which is one of the important parts of my Ph.D theis was carried out in the Center for Integrated RF Engineering (CIRFE) at the University of Waterloo. I would like to express my special thanks to Professor Raafat Mansour for allowing us to use the clean room facilities. Mr. Bill Jolley, Dr. Salam Gabran, Dr. Sara Attar and other members from CIRFE are also greatly appreciated for their technical support and valuable advices.

Last but not least, I gratefully acknowledge my husband Babak Rajabi for his great support and patience during my study. I also would like to thank my parents for their encouragement through this process.

Table of Contents

List of Figures

List of Tables

Nomenclature

Roman symbols

A_i , B_i, C_i, D_i	Species involved chemical reactions
a,b	Reaction orders
c	Constants
C	Capacitance
c_i	Area-specific concentration of surface species i (mol/cm^2)
D_i	Diffusion coefficient of surface species i (cm^2/s)
D_i^0	Pre-exponential constants (cm^2/s)
d_{elyt}	Electrolyte thickness (cm)
E_r	Reversible cell potential (V)
E^0	Ideal standard cell potential (V)
$E(t)$	Sinusoidal voltage as a function of time (V)
E_{st}	Bias voltage (V)
$E_{CT,f}$	Activation energy for forward charge transfer reaction (J/mol)
E_i^{act}	Activation energy for surface diffusion (J/mol)
F	Faraday constant (96487 C/mol)
ΔG	Gibbs free energy change of a reaction (J/mol)
h	Molar enthalpy (kJ/mol)
i	Current (A)
$i(t)$	Sinusoidal current as a function of time (A)
j	Current density (A/cm^2)
j^0	Exchange current density (A/cm^2)
j_L	Limiting exchange current density (A/cm^2)
j_F	Faradic current density (A/cm^2)

$j_{F,T}$	Total faradic current density (A/cm^2)
j'	Imagining number
J_i	Molar flux of surface species *i* (mol/cm s)
k	Reaction rate constant (mol, cm, s)
k'	Reverse reaction rate constant (mol, cm, s)
k^0	Pre-exponential coefficient (mol, cm, s)
K_{eq}	Equilibrium constants
n	Electron number transferred during a electrochemical reaction
N	Molar (mol)
N_k	Area-specific density (mol/cm^2)
p	Pressure (Pa)
Q	Constant phase element
r	Reaction rate (mol/cm^2 s)
R	Gas constant (8.314 J/K mol)
R_p	Polarization resistance (Ω cm^2)
Rs	Ohmic resistance (Ω)
s_i	Molar entropy (J/mol K)
T	Temperature (K)
V	Voltage (V)
v_i'	Stoichiometric factor of species *i* in forward reaction
v_i''	Stoichiometric factor of species *i* in reverse reaction
X1,X2	Variables for impedance calculation
z	Distance along the surface perpendicular to the TPB line (cm)
Z	Impedance (Ω)
Z_0	Impedance amplitude (Ω)
Z'	Real part of impedance (Ω)

Z''	Imagining part of impedance (Ω)
$\|Z\|$	Absolute impedance (Ω)

Greek symbols

a	Transfer coefficient
η	Overpotential (V)
η_{act}	Activation overpotential (V)
η_{ohmic}	Ohmic overpotential (V)
η_{conc}	Activation overpotential (V)
ω	Angular frequency (radians/s)
φ	Phase angle
Θ	Surface coverage
τ	Period (s)

Subscripts

an	Anode
act	Activation
ca	Cathode
CO	Carbon monoxide
CO_2	Carbon dioxide
conc	Concentration
CT	Charge Transfer Reaction
CTRs	Charge Transfer Reactions
dl	Electrical double layer
F	Faraday

$f_{,m}$	Forward reaction
H_2	Hydrogen
i	Surface species
k	Ni or YSZ surface
m	Adsorption, desorption and surface reactions
O_2	Oxygen
r,m	Reverse reaction
st	Stationary
v	Amplitude of the excitation voltage or current

Abbreviation

AFC	Alkaline Fuel Cell
AFM	Atomic Force Microscopy
APU	Auxiliary Power Units
BSE	Back-Scattered Electrons
CEM	Controlled Evaporation and Mixing
CPE	Constant Phase Element
CHP	Combined Heat and Power
DFT	Density Functional Theory
DI	Deionized
EDX	Energy-Dispersive X-ray Spectroscopy
elde	Electrode
elyt	Electrolyte
EIS	Electrochemical Impedance Spectroscopy
GDC	Gadolinium-Doped Ceria
ICB	Ionized Cluster Beam

IPA	Isopropyl Alcohol
IT-SOFC	Intermediate Temperature Solid Oxide Fuel Cell
GPL	liquefied Petroleum Gas
LSM	Lanthanum Strontium Manganite
LSR	Line Specific Resistance
MCFC	Molten Carbonate Fuel Cell
Ni	Nickel
OCV	Open Circuit Voltage
OD	Outer Diameters
PAFC	Phosphoric Acid Fuel Cell
PEMFC	Polymer Electrolyte Membrane Fuel Cell
PGMI	Polydimethyl Glutarimide
PLD	Pulsed Laser Deposition
PVD	Physical Vapor Deposition
Pt	Platinum
ref	Reference
SDC	Samaria-Doped Ceria
SE	Secondary Electrons
SEM	Scanning Electron Microscope
SOFC	Solid Oxide Fuel Cell
TPB	Triple Phase Boundary
UV	Ultraviolet
YSZ	Yttria-Stabilised-Zirconia
Y-TZP	Yttria-Tetragonal Zirconia

Chapter 1

Introduction

1.1 Motivation

The energy crisis and its related environmental issues has become one of the hottest topics in the new century. Conventional energy sources are non-renewable and will be exhausted in the future. Besides, consumption of conventional fossil fuels has created serious environmental problems, which are not easily reversible. Global warming and climate change demand an urgent need for clean energy that creates a carbon-constrained environment and makes sustainable energy development possible.

As clean energy generators, fuel cells have attracted significant attention. Fuel cells directly convert the chemical energy contained in the fuel into electricity. Electricity can be continuously produced as long as fuels are supplied (O'Hayre et al., 2006).

Solid oxide fuel cells (SOFCs) operate at high temperature (600-1000°C), and can be used for applications ranging from small mobile technology (e.g. small portable chargers) to large stationary plants (Minh, 2004; O'Hayre et al., 2006; Singhal & Kendall, 2004).

SOFCs operate with a wide range of fuels: hydrogen (H_2) and hydrocarbons such as natural gas, coal-derived synthesis gas, liquefied petroleum gas (GPL) and alcohols, etc. Compared to conventional electricity generation, the electrical efficiency of SOFCs is much higher. Therefore, carbon dioxide (CO_2) emissions are greatly reduced when using SOFCs. In addition, CO_2 emitted from the SOFC operation is already separated from the air and the energy penalty for CO_2 capture from the SOFC is significantly less than that from conventional coal or natural gas power plants (Suwanwarangkul, 2005).

Although benefits of SOFC are clear, the full commercialization of SOFC has still not occurred. Problems such as high cost, poor long term performance and poor tolerance for hydrocarbon fuels still exist. Therefore, it is urgent to overcome these obstacles.

The long term cell performance loss could be attributed to losses from different components of the fuel cell, such as cathode, electrolyte and anode. Fuel oxidation occurs at the anode, which makes them susceptible to degradation and redox instability. When hydrocarbon fuels are used, carbon deposition and sulfur poisoning can also significantly degrade the anode performance (Bieberle et al., 2001). Therefore, anodic losses can represent a significant part of the overall internal loss, particularly in anode-supported cells. Reduction of these losses would improve the anode performance and further enhance the overall cell performance.

Knowledge of the elementary reaction steps and kinetics of electrochemical reactions occurring at the anode is a key to further improve the anodic performance. The overall objective of this research is to improve our understanding of the mechanistic details of the electrochemical reactions involving H_2 and carbon monoxide (CO) on SOFC anodes. Knowledge of the mechanisms of H_2 and CO oxidation should provide insight into the fundamental behavior of SOFCs and which should help optimize their design. Work remains to be done regarding the development, refinement and validation of H_2 and CO reaction mechanisms and the corresponding kinetic models. In addition, the direct utilization of hydrocarbon fuels is one of the trends in SOFC applications. However, the state-of-art anode material consisting of porous Ni/Yttria-Stabilized Zirconia (YSZ) is prone to carbon deposition. The hydrocarbon fuel can be converted to H_2 and CO through steam reforming or partial oxidation within the porous Ni/YSZ anode with humidified fuel. The study of H_2 and CO electrochemical reactions will enable a better understanding of the performance of SOFCs with hydrocarbon feed, as H_2 and CO are the primary products from hydrocarbon reforming.

Although significant studies have been conducted to elucidate the electrochemical oxidation of H_2, no consistent conclusions have been reached. Far fewer investigations have been conducted regarding the CO electrochemical oxidation, In addition, due to the complicated interpenetrating network microstructure of conventional Ni/YSZ cermet SOFCs, it is very difficult to isolate the reaction kinetic parameters, such as the triple phase boundary (TPB) length from transport phenomena (Bieberle et al., 2001). Therefore, mechanistic details of H_2 and CO oxidation are still not fully understood.

In this study, Ni/YSZ pattern anodes were employed to avoid the effects of the complicated 3-D structure on the electrochemical reactions that take place in Ni/YSZ cermet anodes. Moreover, the influence of gas transport in porous media is eliminated in pattern anodes.

In order to achieve our goal, both experimental and simulation work were carried out. The experimental study includes Ni/YSZ pattern anode fabrication and electrochemical characterization in H_2-H_2O and CO-CO_2 atmospheres. The Ni/YSZ pattern anodes were fabricated using a bi-layer resist lift-off method. The dependence of pattern anode performance on a wide range of gas compositions, TPB lengths, temperature and overpotential were evaluated. The overall goal of the modeling study was to validate and refine previously proposed H_2 reaction mechanisms, particularly a recently proposed mechanism based only on DFT calculations (Shishkin & Ziegler, 2010). A 1-D dynamic SOFC half-cell model considering multiple elementary reaction kinetics was developed. Different types of charge transfer reactions are considered in the model. One of the charge transfer reactions is oxygen spillover from the YSZ surface to Ni surface, which was employed by Bieberle & Gauckler (2002). Another charge transfer reaction is hydrogen spillover from the Ni surface to oxygen ions or hydroxyl ions on YSZ surface, which was used by Vogler et al. (2009). Shishkin and Ziegler (2010) concluded from their theoretical analysis that H_2 oxidation occurs at the interface between Ni and YSZ, where oxygen atoms are bound to both Ni and ZrO_2 (or Y_2O_3).

1.2 Introduction to Fuel Cells

Fuel cells are electrochemical conversion devices that produce electricity directly from oxidaition of fuels. The main difference between a battery and a fuel cell is that the fuel cell can generate electricity continuously as long as fuel is supplied (O'Hayre et al., 2006). A typical fuel cell is composed of an electrolyte phase in contact with an anode and a cathode. The anode is the electrode where oxidation occurs, while the cathode is the electrode where reduction takes place (de Boer, 1998; O'Hayre et al., 2006). In this system, hydrogen is typically used as fuel and oxygen as the oxidant. The global reaction for hydrogen oxidation is described as follows (O'Hayre et al., 2006):

$$\mathrm{H_2} + \frac{1}{2}\mathrm{O_2} \rightleftarrows \mathrm{H_2O} \qquad 1.1$$

Fuel cells can be classified into different types according to the electrolyte being used: (1) phosphoric acid fuel cell (PAFC), (2) polymer electrolyte membrane fuel cell (PEMFC), (3) alkaline fuel cell (AFC), (4) molten carbonate fuel cell (MCFC) and (5) solid oxide fuel cell (SOFC). The main features of these fuel cells are given in Table 1-1.

Fuel cells have applications in three main areas: portable, stationary and transport. Portable fuel cells are used in applications designed to be moved, including auxiliary power units (APU). The typical power range of this type of fuel cells is from 5 W to 20 kW. Portable fuel cells are usually used for military purposes, such as portable soldier-borne power and skid-mounted generators. Other portable fuel cell devices include torches, battery chargers, mp3 players and cameras. PEMFC is the main type of fuel cell used for this function. Stationary fuel cells are units which are designed to produce electricity at a fixed location. MCFC, PAFC, PEMFC and SOFC which can be used for this purpose can produce 0.5 kW to 400 kW power. Stationary fuel cells can be used for large stationary combined heat and power (CHP) and small stationary micro-CHP application. Transport fuel cells (1 kW-100 kW) are mainly used in electronic vehicles. So far, only PEMFC is being considered for this application (Fuel cell today, 2012).

Table 1-1 Overview of major fuel cell types (O'Hayre et al., 2006; Vogler, 2009)

	PEMFC	PAFC	AFC	MCFC	SOFC
Electrolyte	Polymer membrane	Liquid phosphoric acid	Liquid Potassium hydroxide	Molten carbonate	Ceramic
Charge carrier	H^+	H^+	OH^-	CO_3^{2-}	O^{2-}
Operating temperature	80˚C	200˚C	60-220˚C	650˚C	600-1000˚C
Cell components	Carbon based	Carbon based	Carbon based	Stainless based	Ceramic based
Fuels	H_2, methanol	H_2	H_2	H_2, hydrocarbons	H_2, hydrocarbons
Cogeneration Heat	None	Low quality	None	high	high
Efficiency (%)	<40	40-45	>60	50-60	50-60

1.2.1 Working Principle of Solid Oxide Fuel Cells (SOFCs)

A SOFC is distinguished from other fuel cells by using a dense ceramic electrolyte. It is a high temperature electrochemical device which converts chemical energy to electrical energy. Like other fuel cells, a SOFC is composed of an anode, a cathode and an electrolyte. When air is fed to the cathode side, oxygen undergoes a reduction reaction and is converted into oxide ions, which then cross the electrolyte to the anode. Meanwhile, the fuel, which is fed to the anode, undergoes an oxidation reaction and consequently releases electrons. The electrons flow from the anode to the cathode through an external circuit producing electricity. The principle of SOFC operation is illustrated in Figure 1-1.

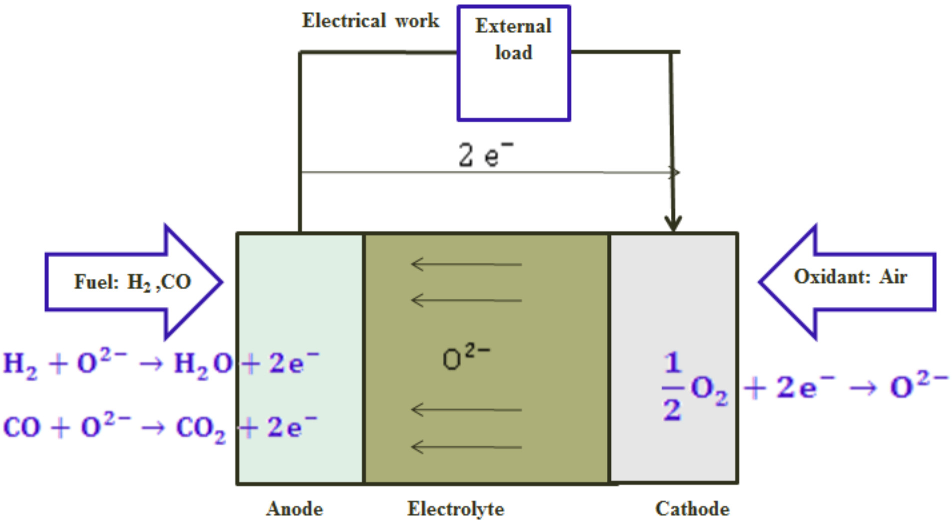

Figure 1-1 Principle of solid oxide fuel cell operation

1.2.2 Benefits of SOFCs

Compared to conventional power generation methods (e.g. conventional diesel generators), SOFCs have higher electrical efficiency because operate at high temperature and convert the chemical energy of fuel directly into electrical energy (Minh & Takahashi, 1995). When SOFCs are used in combination with gas-turbines, a total efficiency (electrical and useful heat) of 85% can be expected, which is higher than the efficiency of other fuel cells (Vogler, 2009).

In addition to the high efficiency, SOFCs are environmentally friendly. They can also operate using a wide range of fuels, such as hydrogen, carbon monoxide, or hydrocarbons. However, unlike combustion of fossil fuels, no nitrogen oxide pollutants are produced in SOFCs. Furthermore, SOFC is an excellent CO_2 capture technology which can reduce greenhouse gas (Suwanwarangkul, 2005). The direct use of hydrocarbon fuels can lower equipment cost and further increase the energy efficiency. Moreover, SOFC technology enables cleaner environment and so should reduce health care costs.

SOFCs are mainly used in stationary power plants. Based on demands, SOFCs can be fabricated into different sizes. Moreover, the operation of SOFCs is continuous as long as the fuel is available. This reduces the loss and costs of power transportation, which is especially useful in remote communities (http://www.sofccanada.com/).

SOFC technology can also be an efficient way for waste management. Wastes store significant amounts of energy which can be used to produce biogas using anaerobic digesters. Biogas can be employed as fuels for SOFC operation either through internal reforming or external processing into hydrogen (Fuel cell today, 2012).

When SOFC technology is combined with other renewable energy technologies (e.g. wind and solar power), renewable energy systems could be established. Wind and solar power are affected by nature and are highly variable and unpredictable. It is desirable to store the excess power whenever possible and then use the stored power when sufficient electricity is not available. One possible way to store the energy is in the form of hydrogen. Electricity is fed into an electrolyser cell, which operates in the reverse to a fuel cell. The electrolyser uses electricity to decompose water into hydrogen and oxygen. The hydrogen is then fed to the SOFC to generate electricity when needed (Fuel cell today, 2012).

1.2.3 SOFC Materials

Research on SOFCs has done for more than a century. However, due to problems such as material cost and durability SOFC commercialization has been limited (Kendall, 2005). Therefore, development of suitable materials for the major components of SOFCs has become an important aspect in SOFCs research. Basically, an SOFC consists of three major components: electrolyte, cathode, and anode.

Electrolyte

The electrolyte plays a very important role in SOFC design (Kendall, 2005; Vogler, 2009). The electrolyte should be a dense solid, crystalline oxide with high ionic conductivity and low electronic conductivity at the cell operating temperature (O'Hayre et al., 2006; Singhal & Kendall, 2004). The high ionic conductivity helps oxygen ions migrate through the electrolyte to the anode side while the low electronic conductivity prevents the electrons passing through the electrolyte to the cathode side, which would cause a short circuit (Vogler, 2009). In addition, the electrolyte should be as thin as possible to minimize the ohmic losses and should also be stable in both fuel oxidizing and oxidant reducing environments. In addition, no chemical interactions or inter-diffusion between the electrolyte and the other cell components should occur. Meanwhile, the electrolyte thermal expansion must match that of its adjoining components.

Yttria-stabilized-zirconia (YSZ, $Y_{2x}Zr_{1-2x}O_{2-x}$, where x is the concentration of the dopant in mol-% Y_2O_3 in ZrO_2) is the most common electrolyte material. ZrO_2 is doped with Y_2O_3 that enables a direct substitution of a trivalent cation (Y^{3+}) for the host lattice cation Zr^{4+}. Y_2O_3 introduces high concentrations of oxygen vacancies into the ziroconia crystal structure at the rate of one vacancy per mole of the dopant. Also, it stabilizes the zirconia crystal structure in the cubic phase, which is the most conductive state of the zirconia. Usually, zirconia is doped with 8% yttria (Minh & Takahashi, 1995; O'Hayre et al., 2006).

Over the past few years, samaria-doped ceria (SDC, $(CeO_2)_{1-x}(SmO_{1.5})_x$) and gadolinium-doped ceria **(**GDC**)** have been extensively used as electrolytes for SOFCs operating at lower temperatures. Compared to YSZ, SDC and GDC show high ionic conductivity over the temperature range of 300-800°C (Minh & Takahashi, 1995; Chen et al., 2009).

Cathode

The cathode material used in SOFC needs to be highly stable in the reducing environment at high temperatures. In addition, it should have good electrical conductivity, high catalytic activity for oxygen reduction as well as thermal and chemical compatibility with other cell components. Typical cathode materials for SOFCs are $La_{1-x}Sr_xMnO_{3-d}$, (lanthanum strontium manganite or LSM) with x between 0.15 and 0.25 (de Boer, 1998; Singhal & Kendall, 2004; Snyder & Haile, 2004; Vogler, 2009). Since LSM is mainly an electronic conductor, oxygen is assumed to be reduced at the interface between the cathode and the electrolyte (de Boer, 1998).

Anode

The anode in a SOFC provides reaction sites for fuel oxidation. Anode materials are required to have adequate electronic conductivity ability as well as high catalytic activity for fuel oxidation (Singhal & Kendall, 2004). Ni/YSZ cermet is currently the state-of-art anode material used in SOFCs due to its lower cost, high stability under SOFC operating conditions, a similar thermal expansion coefficient as YSZ electrolyte and low charge transfer resistance at the Ni/YSZ boundary (Zhu & Deevi, 2003). Ni/YSZ cermet is prepared from a mixture of NiO and YSZ with a weight ratio of ~ 50:50. NiO can be reduced to Ni particles dispersed in the YSZ, which increases the porosity of the final anode (Snyder & Haile, 2004). Nickel exhibits high catalytic activity for the electrochemical reactions and high electronic conductivity to transfer electrons from the reaction sites to the current collector. It is also active for methane reforming (Atkinson et al., 2004). YSZ acts as an ionic conducting phase which can also enlarge the active area for electrode reaction. The thermal expansion coefficient of YSZ matches that of other SOFC components. Besides, nickel and YSZ are immiscible in each other and chemically stable over a wide temperature range (Bieberle, 2000; Zhu & Deevi, 2003). Although Ni/YSZ cermet anodes have a number of benefits, they also have some problems. One of the problems is that Ni is easily oxidized in the presence of air (e.g. during start-up and shut-down), which leads to a decrease in anode performance after several redox cycles (Kendall, 2005). Another problem related is carbon deposition. When hydrocarbon fuels are used, the carbon from the fuels tends to enter the crystal lattice of Ni and eventually precipitates as carbon fibers on its surface. This deactivates the catalyst, and significantly degrades the anode performance (Atkinson et al., 2004; Kendall, 2005). Sulfur poisoning is another serious issue regarding Ni-related anode whenever sulfur-containing fuels are used. The sulfur in the fuel is usually in the form of H_2S and can dramatically decrease the anode performance (Kendall, 2005).

Ceria-based anodes, which are both ionic and electronic conductors, have attracted more and more attention due to their catalytic activity for steam reforming and the oxidation of hydrocarbons (Atkinson et al., 2004). Perovskite-type materials (e.g $(LaSr)(CoFe)O_3$) and titanates have also been investigated as candidate materials for SOFC anodes (Bieberle, 2000). The main purpose of these studies is to improve the performance of the anodes. As more studies consider hydrocarbons as potential fuels, the importance of choosing suitable anode materials to prevent carbon deposition becomes significant (Bieberle, 2000).

1.2.4 Thermodynamics of SOFC Reactions

Thermodynamics studies transfer of energy from one form to another. In fuel cells, the chemical energy of the fuel is converted directly into electrical energy, which is exhibited in terms of cell potential and electrical current output. At constant temperature and pressure, the maximum electrical work ($W_{elec,\ max}$) done by a process is given by the negative of the Gibbs energy difference (ΔG) for the process (Equation 1.2). Thus, the maximum possible potential (or reversible potential) is the potential produced by the fuel cell at thermodynamic equilibrium (O'Hayre et al., 2006).

$$\Delta G = -W_{elec,max} = -nFE_r \qquad 1.2$$

where E_r is the maximum possible potential (V), n is the electron number transferred during the electrochemical reaction and F is the Faraday constant (96,487 C/mol).

The Nernst equation describes the relation between the reversible cell potential change and the concentration of reactants and products. For a general electrochemical reaction, the Nernst equation is written as (O'Hayre et al., 2006):

$$E_r = E^0 - \frac{RT}{nF} ln \frac{\Pi\, \alpha_{product}^{v_i}}{\Pi\, \alpha_{reactant}^{v_i}} \qquad 1.3$$

This equation provides a relationship between the standard potential (E^0) for the cell reaction and the equilibrium potential (E_r) at other partial pressures of reactants and products. In this equation, R is the gas constant (8.314 J/K mol), T is temperature (K), $\alpha_{reactant}$ and $\alpha_{product}$ are the activity of reactant and product species, and v_i is the stoichiometric coefficient of species *i*.

In an SOFC, a common way to describe E_r is in terms of the oxygen partial pressures at the active anode and cathode sites. The reduction and oxidation reactions of oxygen at cathode and anode are expressed in Equations 1.4 and 1.5. The corresponding E_r is given in Equation 1.6 (Suwanwarangkul, 2005).

$$\text{Cathode: } \mathrm{O_2(ca) + 4e^- \rightleftarrows 2O^{2-}(el)} \tag{1.4}$$

$$\text{Anode: } \mathrm{2O^{2-}(el) \rightleftarrows O_2(an) + 4e^-} \tag{1.5}$$

$$E_r = E_{ca} - E_{an} = \frac{RT}{4F} ln(\frac{P_{O_2,ca}}{P_{O_2,an}}) \tag{1.6}$$

where (*ca*), (*el*) and (*an*) represent cathode, electrolyte and anode, respectively. E_{ca} and E_{an} are cathode and anode potentials. $P_{O_2,ca}$ and $P_{O_2,an}$ denote the partial pressure of oxygen at cathode and anode sites. If the cathode is directly exposed to the air, the $P_{O_2,ca}$ is 0.21 atm. $P_{O_2,an}$ is determined based on the thermodynamic equilibrium of the fuel gases. For reactions involving H_2 and CO (see reactions 1.7 and 1.8), $P_{O_2,an}$ are given as in Equations 1.9 and 1.10.

$$\mathrm{H_{2,an} + \frac{1}{2}O_{2,an} \rightleftarrows H_2O_{an}} \tag{1.7}$$

$$\mathrm{CO_{\,an} + \frac{1}{2}O_{2,an} \rightleftarrows CO_{2,an}} \tag{1.8}$$

$$(P_{O_2,an})_{H_2} = (\frac{P_{H_2O}}{K_{eq,H_2}P_{H_2}})^2 \tag{1.9}$$

$$(P_{O_2,an})_{CO} = (\frac{P_{CO_2}}{K_{eq,CO}P_{CO}})^2 \tag{1.10}$$

here, P_{H_2}, P_{H_2O}, P_{CO}, and P_{CO_2} are partial pressures of H_2, H_2O, CO and CO_2, respectively. K_{eq,H_2} and $K_{eq,CO}$ are equilibrium constants for H_2 and CO oxidation, and they are described as a function of temperature and Gibbs free energy changes (△G: kJ/mol).

$$K_{eq,H_2} = exp(-\frac{\Delta G_{H_2}}{RT}) \tag{1.11}$$

$$K_{eq,CO} = exp(-\frac{\Delta G_{CO}}{RT}) \tag{1.12}$$

By combining Equations 1.6, 1.9, 1.11, E_r for H_2 oxidation can be written as a function of Gibbs free energy changes and partial pressure of H_2 and H_2O (see Equation 1.13). By combining equations 1.6, 1.10 and 1.12, E_r for CO oxidation can be written as a function of Gibbs free energy changes and partial pressure of CO and CO_2 (see equation 1.14) (Suwanwarangkul, 2005).

$$(E_r)_{H_2} = -\frac{\Delta G_{H_2}}{2F} + \frac{RT}{2F} ln(\frac{P_{H_2} P_{O_{2,ca}}^{0.5}}{P_{H_2O}}) \quad 1.13$$

$$(E_r)_{CO} = -\frac{\Delta G_{CO}}{2F} + \frac{RT}{2F} ln(\frac{P_{CO} P_{O_{2,ca}}^{0.5}}{P_{CO_2}}) \quad 1.14$$

1.2.5 Electrochemical Kinetics of SOFC Anodes

Electrochemical reactions, as heterogeneous reactions in SOFCs, take place at the interface between the electrode and the electrolyte. The reaction involves charge transfer between the electrode and the gas species. Electrochemical kinetics is concerned with electrochemical reaction pathways and rates. It also determines the energy loss associated with activation of electrochemical reactions. The cell performance is directly related to the electrochemical process of the electrode (Li, 2005).

Faraday's law is used to relate the current produced by the electrochemical reaction with the reaction rate (O'Hayre et al., 2006).

$$i = nF\frac{dN}{dt} \quad 1.15$$

where i is the current (A), $\frac{dN}{dt}$ is the reaction rate of the electrochemical reaction (mol/s).

Polarization, or overpotential, is the voltage loss during operation compared to the reversible voltage. Polarization can not be eliminated but can be minimized by choosing suitable electrode materials. Three types of polarization occur in fuel cells: activation polarization, ohmic polarization and concentration polarization.

Activation Polarization

Activation polarization is caused by the energy barrier that must be overcome for an electrochemical reaction. This energy barrier is called activation energy, which determines the electrochemical reaction rate and the current density associated with the reaction. The Bulter-Volmer equation is used to describe the relationship between the current density (j) and the activation overpotential (η_{act}) (O'Hayre et al., 2006).

$$j = j^0 \left(exp\left(\frac{\alpha n F \eta_{act}}{RT}\right) - exp\left(\frac{-(1-\alpha) n F \eta_{act}}{RT}\right)\right) \quad 1.16$$

where j^0 is the exchange current density (A/cm^2), α is the transfer coefficient with value between 0 and 1.

The Tafel equation described in Equation 1.17, is a limiting case of the Butler-Volmer equation when the reverse reaction of the reaction can be ignored (Li, 2005; O'Hayre et al., 2006; EG&G Technical Services, 2004). The exchange current density and transfer coefficient can be obtained through Tafel plots (see Figure 1-2).

$$\eta_{act} = \frac{RT}{\alpha n F} ln\left(\frac{j}{j^0}\right) \quad (\eta_{act} > 0.05 \text{ V}) \quad 1.17$$

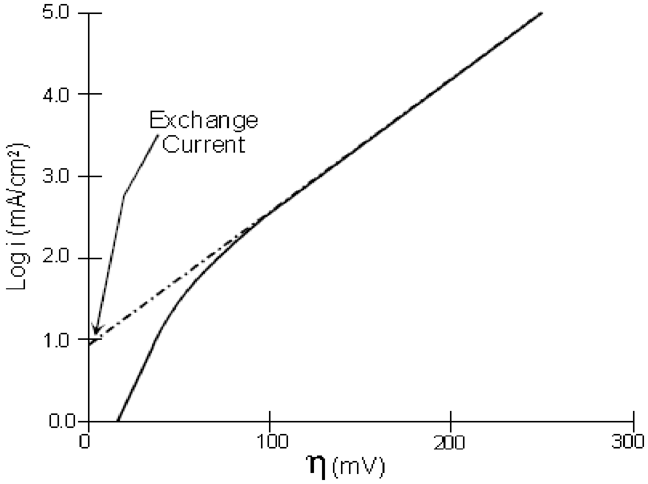

Figure 1-2 Tafel plot (EG&G Technical Services, 2004)

Ohmic Polarization

Ohmic loss is due to the electrical resistance in the cell, which includes electrical resistance in the two electrodes and the electrolyte (O'Hayre et al., 2006). The ohmic overpotential (η_{ohmic}) is defined as:

$$\eta_{ohmic} = iR_{ohmic} \quad 1.18$$

where R_{ohmic} is the total resistance of the cell (expressed in Ω).

Usually, ionic charge transport is slower than electronic charge transport, so its contribution to the ohmic loss tends to dominate. In most SOFCs, the electrolyte ohmic loss is the main contributor to the total ohmic loss, especially in thick electrolyte-supported cells (O'Hayre et al., 2006).

Concentration Polarization

Concentration polarization is caused by resistance to mass transport within the fuel cell. Poor mass transport can lead to significant cell performance loss. Because the concentration of reactant and product within the active reaction area affects the cell performance, reactant depletion and product accumulation within the active area could significantly affect the cell performance (O'Hayre et al., 2006). The total concentration loss (η_{conc}) can be expressed as:

$$\eta_{conc} = c \, ln \, (j_L/(j_L - j)) \qquad 1.19$$

$$c = (RT/nF)\,(1 + 1/\alpha)$$

$$j_L = nFD^{eff}\, c_R/\delta$$

where j_L is the limiting current density (A/cm^2), which is the highest current density a fuel cell can reach (Minh & Takahashi, 1995; O'Hayre et al., 2006). c_R is the flow channel reactant concentration (mol/cm^3), D^{eff} is the effective reactant diffusivity (cm^2/s), and δ is the diffusion layer thickness.

The actual cell voltage of a fuel cell is the difference between the ideal cell voltage (or reversible cell voltage) and all polarization losses (EG&G Technical Services, 2004).

$$E_{actual} = E_r - \eta_{act} - \eta_{ohmic} - \eta_{conc} \qquad 1.20$$

Figure 1-3 represents a polarization curve (i.e. voltage vs. current density) and highlights the region where the various polarizations dominate.

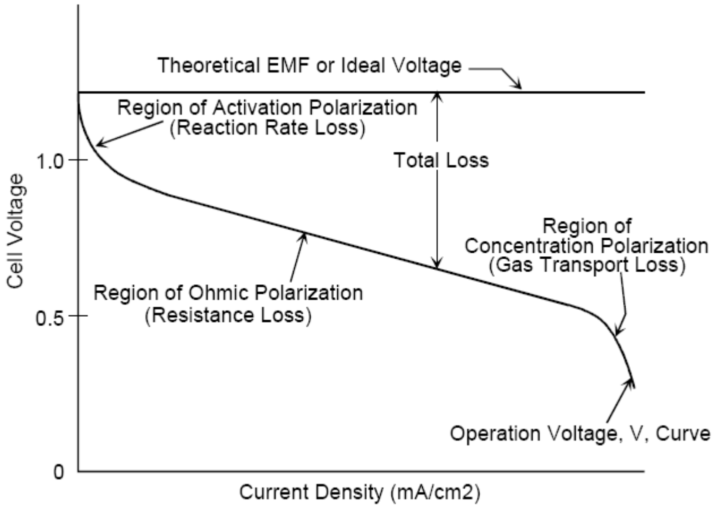

Figure 1-3 Actual and ideal fuel cell voltage/current characterization (EG&G Technical Services, 2004)

1.2.6 Electrochemical Characterization of SOFCs

The most widely used techniques for fuel cell characterization are current-voltage (I-V) and electrochemical impedance spectroscopy (EIS) measurements.

I-V Measurements

I-V measurements give an overall evaluation of fuel cell performance and fuel cell power density. Two types of I-V curves are presented generally. One is the current-voltage relationship. In this curve, the actual cell voltage is plotted against the current density. The other form is called the Tafel plot: the current density on logarithmic scale is plotted against the overpotential imposed on the cell. Both the exchange current density and transfer coefficient can be obtained from Tafel plot measurement (O'Hayre et al., 2006; Vogler, 2009).

EIS Measurements

EIS measures a system's ability to impede the flow of electrical current, with regards to time- or frequency-dependent phenomena. In addition, EIS measurements are able to distinguish between activation, ohmic and concentration polarization. During potentiostatic EIS measurement, a small sinusoidal voltage perturbation *E(t)* is imposed to the system, and the corresponding current change *i(t,)* is determined, ie.,

$$E(t) = E_v \, cos(\omega t) \qquad 1.21$$

$$i(t) = i_v \, cos(\omega t - \varphi) \qquad 1.22$$

In the above formula, ω is the angular frequency (radians/s), φ is the phase shift angle between the input voltage and output current, while E_v *and* i_v are the amplitudes of the excitation voltage and current respectively.

The impedance is defined as the ratio between the imposed voltage and the corresponding current *i*.

$$Z = \frac{E(t)}{i(t)} = Z_0 \, (cos \, \varphi - j' \, sin \, \varphi) \qquad 1.23$$

where Z_0 is the impedance magnitude, and j' represents the imaginary number ($j' = \sqrt{-1}$).

The impedance can also be expressed as a real component (Z') and an imaginary component (Z'') (Bieberle, 2000; O'Hayre et al., 2006).

$$Z = Z' + j'Z" \qquad 1.24$$

$$Z' = Z_0 \, cos \, \varphi \;\; , \;\; Z^{"} = Z_0 \, sin \, \varphi \quad |Z| = \sqrt{(Z')^2 + (Z")^2}$$

where |Z| is the absolute impedance.

Impedance spectra can be plotted in two ways. One is the Nyquist plot, where the negative of the imaginary component of the impedance ($Z^{"}$) is plotted versus the real component of the impedance (Z'). The other type is the Bode plot, which plots the absolute impedance |*Z*|, and the phase shift φ versus the angular frequency ω (Bieberle & Gauckler, 1999).

From impedance plots, the polarization resistance, electrolyte resistance and relaxation frequency can be obtained (Bieberle & Gauckler, 1999). Polarization resistance can be calculated from the difference between the low frequency intercept and the high frequency intercept on the real-axis of Nyquist plot. Electrolyte resistance can be obtained from the high frequency, real-axis intercept of the Nyquist plot (Bieberle & Gauckler, 1999; O'Hayre et al., 2006). The relaxation frequency is the frequency at the maximum of the imaginary component in the Nyquist plot. It is also a characteristic feature of an electrochemical process (Bieberle & Gauckler, 1999).

Equivalent circuit models are commonly used to fit the impedance data. Circuit elements are used to model processes that occur inside a fuel cell. These circuit elements include a resistor, capacitor and inductor (O'Hayre et al., 2006). In the equivalent circuit model, a simple resistor represents the ohmic conductive process in a fuel cell. For a pure resistor in a Nyquist plot, the imaginary part and phase shift angle are zero, and so appears as a point on the real axis. The impedance is independent of the frequency (O'Hayre et al., 2006).

The electrical double layer capacitance (C_{dl}) can be modeled as a capacitor. A capacitor is purely negative imaginary component in the impedance plots. The impedance of a capacitor is described in Equation 1.25 (O'Hayre et al., 2006).

$$Z = \frac{V(t)}{i(t)} = \frac{1}{jwC_{dl}} \qquad 1.25$$

Current (i_{dl}) due to the electrical double-layer is defined by Equation 1.26 (Bieberle & Gauckler, 1999; Orazem & Tribollet, 2008; O'Hayre et al., 2006).

$$i_{dl} = C_{dl}\frac{dV(t)}{dt} \qquad 1.26$$

At steady-state, i_{dl} is zero, and the capacitor represents an open circuit (Orazem & Tribollet, 2008).

For a sinusoidal voltage perturbation $V = V_0\ exp(jwt)$, the electrical double-layer current is given by Equation 1.27 (Orazem & Tribollet, 2008).

$$i_{dl} = C_{dl}(jw)V_0\ exp(jwt) \qquad 1.27$$

In an equivalent circuit model, constant phase element (CPE) is introduced due to non-uniformity of material properties on a microscopic level due to the impurities or surface defects and non-uniform charge mobility at the interface (Bieberle & Gauckler, 1999; Barsoukov & Macdonald, 2005).

The definition for the impedance of a CPE is given in Equation 1.28.

$$Z_{CPE} = \frac{1}{Q(jw)^n} \qquad 1.28$$

where Q denotes the constant phase element and n is an empirical exponent, which is between 0 and 1. The value of n signifies the deviation from the ideal situation (Bieberle & Gauckler, 1999).

In a SOFC, the interface between the electrode and the electrolyte is not a uniform surface (Evgenij Barsoukov, J. Ross Macdonald, 2005). Therefore, compared to a capacitor, a constant phase element may provide a much better fitting of the impedance data due to the empirical exponent (n) (Bieberle & Gauckler, 1999).

1.3 Thesis Outline

This thesis is composed of eight chapters. In chapter 1, introduction to fuel cells and the motivation of this thesis are described.

Chapter 2 is the literature review on the studies conducted to elucidate the electrochemical reaction mechanisms of H_2 and CO on SOFC anodes.

Chapter 3 describes the electrochemical measurement set-up for button cells, the characterization techniques for the Ni/YSZ pattern anode used in this study, and the fabrication of Ni/YSZ pattern anodes. In this chapter, the operating principle of photolithography and metal deposition methods are introduced in detail. Related works found in the literature are also reviewed. Moreover, the methods for parameter optimization and the fabrication of Ni/YSZ pattern anode are finalized.

Chapter 4 presents a stability study of Ni/YSZ pattern anode in an H_2-H_2O environment. Microstructure and electrochemical performance changes with Ni thickness, temperature and H_2O content was investigated.

Chapter 5 discusses the electrochemical oxidation of H_2 using Ni/YSZ pattern anodes. The dependence of pattern anode performance on temperature, overpotential, partial pressure of H_2 and H_2O, and TPB length was studied. Results were also compared with those obtained in the literature.

Chapter 6 discusses the electrochemical oxidation of CO using Ni/YSZ pattern anodes. Electrochemical tests were performed in different gas compositions, temperature, and overpotential conditions.

Chapter 7 introduces a 1-D dynamic model describing the electrochemical behavior of H_2 on a SOFC pattern anode. Two different reaction mechanisms were implemented into the model and compared to the experimental data from chapter 5.

Chapter 8 presents the conclusions of the thesis and the recommendations for future work.

Chapter 2

Literature Review

As mentioned in the previous chapter, long-term durability caused by carbon deposition, and sulfur poisoning on SOFC anodes are currently limiting factors that impedes SOFC large scale commercialization (Bieberle et al., 2001). In order to achieve high performance, internal losses in all the SOFC components should be as low as possible. The anodic loss represents a significant part of the total fuel cell losses. Thus, it is desirable to decrease the SOFC anodic loss to improve the overall cell performance (Bieberle, 2000; Bieberle et al., 2001). At the core of the process, electrochemical reactions occurring on the anode play an important role in determining the overall performance of the cell and in choosing strategies to improve the performance. Yet, they are not well understood (Bieberle et al., 2001; Utz et al., 2010; Vogler et al., 2009; Yurkiv et al., 2011; Yao & Croiset, 2013a) . A good understanding of the electrochemical reaction mechanisms of H_2 and CO is necessary to better understand many phenomena occurring simultaneously and then to optimize SOFC design.

Ni/YSZ cermet is currently the state-of-the-art material for SOFC. However, carbon deposition is one of the problems related to Ni/YSZ cermet anodes when hydrocarbons are used as fuels. Carbon deposition originates from cracking, Boudouard, and CO hydrogenation reactions (Phongaksorn, 2010), i.e.,

$$\mathrm{CH_4} \rightarrow \mathrm{C} + \mathrm{H_2}\ \text{(methane cracking)} \qquad 2.1$$

$$2\mathrm{CO} \rightleftarrows \mathrm{C} + \mathrm{CO_2}\ \text{(Boudouard)}$$

$$\mathrm{CO} + \mathrm{H_2} \rightleftarrows \mathrm{C} + \mathrm{H_2O}\ \text{(CO hydrogenation)}$$

The development of new porous anode materials (e.g. ceria-based materials) for the direct utilization of hydrocarbon fuels has attracted extensive interests recently. It would be desirable to be able to reform internally those hydrocarbons. If not possible, these hydrocarbons fuels will have to be reformed externally prior to entering the SOFC. In both cases, the main products (from internal or external reforming by steam reforming and/or partial oxidation) reaching the SOFC active sites are H_2 and CO. Good understandings of the fundamental electrochemical reactions of H_2 and CO will provide guidelines to solve the surface carbon deposition problem (Habibzadeh, 2007).

A number of studies have been carried out to understand the electrochemical reaction mechanism of H_2, although no consensus has been reached. Several studies were performed on CO oxidation reaction mechanisms (Mizusaki et al., 1992; Holtappels et al., 1999; Weber et al., 2002; Lauvstad et al., 2002; Sukeshini et al., 2006; Ehn et al., 2010; Utz et al., 2011; Yurkiv et al., 2011). Both hydrogen and carbon monoxide oxidation mechanistic details remain unclear.

Most studies on electrode reactions of SOFCs agree that the electrochemical reactions occur through the TPB line, where the gas, electrode and electrolyte phases meet (Mizusaki et al., 1994). Anode kinetic studies were therefore investigated on specialized anode assemblies such as Ni pattern electrodes, Ni point electrodes and Ni grid electrodes. The goal of those specialized assemblies was to replace the complicated three dimensional structures by two dimensional structures, where the TPB length is well defined (Bieberle & Gauckler, 2001).

2.1 Literature Review on H_2 Electrochemical Reaction Kinetics

No controversy exists concerning the overall oxidation of H_2 on SOFC anodes (Goodwin et al., 2009; Vogler, 2009):

$$\mathrm{H_2(g) + O_O^X \rightarrow H_2O(g) + V_{\ddot{O}} + 2e^-(Ni)} \qquad 2.2$$

where $\mathrm{O_O^X}$ and $\mathrm{V_{\ddot{O}}}$ are an oxygen ion and oxygen vacancy in the YSZ electrolyte, respectively. However, different authors have proposed different reaction mechanism for this reaction; thus the elementary reaction steps are still not completely understood (Goodwin et al., 2009; Vogler, 2009).

The differences between the various proposed reaction mechanisms involve the charge transfer reactions, surface reactions and the site of water formation. Despite these differences, all proposed mechanisms have some common features, such as:

- They all involve dissociative adsorption/desorption reactions of H_2.
- H atoms adsorbs only on Ni surface.

2.1.1 H_2 Electrochemical Reaction Kinetic Studies on Ni/YSZ Pattern Anodes

Due to their simplified geometry and well defined TPB length, Ni/YSZ pattern anodes have been used by several groups for H_2 kinetic studies. In the following, the main results obtained from these research groups are presented.

Mizusaki's group (Yokohama National University, Japan)

Mizusaki et al. (1994a) studied the H_2 reaction mechanism by using Ni/YSZ pattern anodes. Ionized cluster beam (ICB), photolithography and chemical etching techniques were applied to make Ni patterns on a single crystal YSZ surface with different TPB lengths. Electrochemical measurements such as EIS and steady-state polarization were carried out at H_2 partial pressures ranging from 1×10^2 Pa to 1×10^4 Pa and H_2O partial pressures from 3×10^2 Pa to 2×10^3 Pa at 700°C. The experimental results showed that the electrode interface conductivity which is inversely related to the polarization resistance, increased as pH_2 and pH_2O were raised. However, the dependence of electrode interface conductivity on pH_2 was very small. In addition, the Nyquist plot showed one semi-circle.

The following mechanism (see Table 2-1) was proposed by Mizusaki et al. (1994), which is one of the earliest ones reported. It assumed that all surface reactions take place on the Ni surface, and that oxygen spills over from the YSZ to the Ni surface.

Table 2-1 H_2 reaction mechanism proposed by Mizusaki's group (Mizusaki et al., 1994)

Adsorption/desorption of H_2 on Ni surface:	$\mathrm{H_2(g) + 2(Ni) \rightleftarrows 2H(Ni)}$
Adsorption/desorption of H_2O on Ni surface:	$\mathrm{H_2O(g) + (Ni) \rightleftarrows H_2O(Ni)}$ $\mathrm{H_2O(Ni) + (Ni) \rightleftarrows OH(Ni) + H(Ni)}$ $\mathrm{OH(Ni) + (Ni) \rightleftarrows O(Ni) + H(Ni)}$
Spillover of oxygen from YSZ to Ni surface:	$\mathrm{O^{2-}(YSZ) + (Ni) \rightleftarrows O(Ni) + 2e^-}$

In another study, Mizusaki et al. (1994b) found that the electrode interface conductivity increases linearly with TPB length. They mentioned that the rate-determining step is either the adsorption/desorption of reactant gas (H_2 or H_2O) on the Ni surface or the surface diffusion of the adsorbed species on the Ni surface close to the TPB line. A modified Butler-

Volmer type equation was developed by Mizusaki et al. (1994b) to explain their experimental results.

$$j = kP_{H_2}\, exp\left(\frac{2FE}{RT}\right) - k'P_{H_2O}^{\frac{1}{2}} exp(-\frac{FE}{RT}) \qquad 2.3$$

In this equation, *k, k'* are reaction rate constants, P_{H_2}, P_{H_2O} are the partial pressures of H_2 and H_2O, *j* is the current density, *E* is the electrode potential.

de Boer's study (University of Twente, the Netherlands)

In order to elucidate the H_2 oxidation mechanism, Ni/YSZ pattern anodes were also employed in de Boer's study (de Boer, 1998). Impedance was performed as a function of pH_2 (4.95×10^3 Pa - 9.98×10^4 Pa) and pH_2O (6.03×10^2 Pa - 3.08×10^4 Pa) at 850°C. Impedance measurements as a function of overpotential (50-500 mV) and temperatures (600°C-850°C) were also carried out. Several observations were made from the experimental data. The electrode conductivity was found to increase with increasing the perimeter length of Ni pattern. Based on this observation, de Boer claimed that charge transfer is the rate-limiting process, which occurs at or near the TPB line. Besides, three semi-circles were observed in the impedance spectra. Comparison was made between the total resistance found by de Boer (9.7 kΩ.cm^2 at 700°C with $pH_2 = 9.98\times10^4$ Pa, $pH_2O = 2.3\times10^3$ Pa and a nickel perimeter length of 2.9 m/cm^2) with that of Mizusaki et al. (1994a) (4 kΩ.cm^2 at 700°C with $pH_2 = 1.65\times10^3$ Pa, $pH_2O = 1.0\times10^4$ Pa and a nickel perimeter length of 3.3 m/cm^2). A fair agreement was obtained when the experimental differences in both studies were considered. The following elementary reaction steps were postulated (Table 2-2).

Table 2-2 H_2 reaction kinetics proposed by de Boer (1998)

Adsorption/desorption of H_2 on Ni surface:	$\mathrm{H_2 + 2(Ni) \rightleftarrows 2H(Ni)}$
Spillover of hydrogen to OH: Spillover of hydrogen to O:	$\mathrm{H(Ni) + OH^-(YSZ) \rightleftarrows H_2O(YSZ) + e^-(Ni) + (Ni)}$ $\mathrm{H(Ni)\ + O_O^X \rightleftarrows OH_O^{\cdot} + e^- + (Ni)}$
Reactions on YSZ surface:	$\mathrm{OH_O^{\cdot} + (YSZ) \rightleftarrows OH^-(YSZ) + V_O^{\cdot\cdot}}$
Adsorption/desorption of H_2O on YSZ surface:	$\mathrm{H_2O(YSZ) \rightleftarrows H_2O + (YSZ)}$

Gauckler's group (Swiss Federal Institute of Technology Zurich, Switzerland)

Bieberle et al. (2001) investigated the effect of overpotential (0 mV<η<300 mV), gas composition (10^4 Pa < pH_2 < 8.8×10^4 Pa, 40 Pa < pH_2O < 2×10^3 Pa), temperature (673 K < T < 973 K) and pattern geometry on the electrochemical performance of SOFC pattern anodes. Impedance spectroscopy experiments performed under the above conditions revealed that one electrode process was found to be the dominant process. It was found that the electrode response is affected by overpotential, temperature, water partial pressure and TPB length and that the polarization resistance decreases as each of these parameters is increased. Based on what they observed, Bieberle et al. claimed that the rate-limiting process is either adsorption/desorption of hydrogen or removal of oxygen ions from YSZ. In addition, both processes could be linked to the charge transfer process.

In Bieberle's modeling study (Bieberle & Gauckler, 2002), an electrochemical kinetic model with Ni/YSZ pattern anodes in H_2/H_2O system was developed. The model included rate equations for different surface species participating in six elementary reaction steps on the Ni surface. Current density was expressed as a function of charge transfer reaction rate. However, surface diffusion was not included in the model. Simulations were performed under different overpotential, TPB lengths, pH_2 and pH_2O conditions. Simulation and experimental results were compared to verify the model. Table 2-3 presents the elementary reaction steps used in the model.

Table 2-3 H_2 reaction kinetics in Bieberle and Gaukler's model (Bieberle & Gauckler, 2002)

Adsorption/desorption of H_2:	$H_2 + 2(Ni) \rightleftarrows 2H(Ni)$
Adsorption/desorption of H_2O:	$H_2O + (Ni) \rightleftarrows H_2O(Ni)$
Reactions on Ni surface:	$H(Ni) + O(Ni) \rightleftarrows OH(Ni) + (Ni)$ $H_2O(Ni) + O(Ni) \rightleftarrows 2OH(Ni)$ $OH(Ni) + H(Ni) \rightleftarrows H_2O(Ni) + (Ni)$
Oxygen spillover:	$O_O^X + (Ni) \rightleftarrows O(Ni) + V_{\ddot{O}} + 2e^-(Ni)$

This reaction mechanism is essentially the same reaction as the one proposed by Mazusaki (Mizusaki et al., 1994), with the addition of one more reaction for the formation of water from hydroxyl. They assumed that all the reactions occur on the Ni surface. An active YSZ surface was not considered to simplify the model.

E. Ivers-Tiffée's group (University of Karlsruhe, Germany)

In the work performed by Utz et al. (2010), the performance of pattern anodes was evaluated as a function of pH_2, pH_2O, temperature, and overpotential (8×10^2 Pa < pH_2 < 9×10^4 Pa, 2×10^1 Pa < pH_2O < 6×10^4 Pa, 450°C < T < 800°C, $0 < \eta < 300$ mV). Electrochemical impedance tests revealed three semi-circles, which were attributed to gas diffusion, charge transfer on the pattern anode and charge transfer reaction caused by reactions on the counter electrode. The charge transfer coefficient, activation energy and reaction orders for H_2 and H_2O were calculated. Hydrogen spillover was proposed as the rate-limiting step. In another study, Utz et al. (2011a) investigated the effects of gas composition, Ni layer thickness and temperature on the stability of Ni pattern anodes. They concluded that the temperature range for the characterization of Ni pattern anodes with thin Ni layers (50 nm-200 nm) should be between 300-400°C when the water content was up to 80%. They also suggested that Ni pattern anodes with thickness of 800 nm or above should be used when the test temperature was between 700-900°C with water content more than 20%. When the Ni pattern anode with Ni thickness of 800 nm was tested at 800°C, it was found that the pattern anode experienced an activation process during the first 20-25 hrs due to morphology changes in the Ni thin film, and then degradation that depended on water content in the fuel stream.

Bessler's group (University of Heidelberg, Germany)

Bessler's group has done extensive modeling work regarding H_2 oxidation reaction mechanisms. Both Ni/YSZ pattern anodes and cermet anodes were considered in their research. In one of their studies (Vogler et al., 2009), the reaction mechanism on Ni/YSZ pattern anode was studied and different possible charge transfer reactions were considered.

The model used in their study describes a half-cell of a SOFC with a patterned Ni anode on a YSZ single crystal. In this model, no assumption was made concerning the rate-limiting steps and no attempt was made to derive a modified Butler-Volmer type equation. However, they assumed the charge transfer reaction to be a surface spillover reaction occurring at the TPB.

The reaction mechanism considered in the Bessler's study is shown in Table 2-4. Surface diffusion was modeled in one dimension perpendicular to the TPB.

Table 2-4 H_2 reaction mechanism in Bessler and co-workers' study (Vogler et al., 2009)

Adsorption/desorption of H_2 on Ni surface:	$\mathrm{H_2 + 2(Ni) \rightleftarrows 2H(Ni)}$
Adsorption/desorption of H_2O on Ni surface:	$\mathrm{H_2O + (Ni) \rightleftarrows H_2O(Ni)}$
Reactions on Ni surface:	$\mathrm{H(Ni) + O(Ni) \rightleftarrows OH(Ni) + (Ni)}$ $\mathrm{H_2O(Ni) + O(Ni) \rightleftarrows 2OH(Ni)}$ $\mathrm{OH(Ni) + H(Ni) \rightleftarrows H_2O(Ni) + (Ni)}$
Hydrogen spillover:	$\mathrm{H(Ni) + O^{2-}(YSZ) \rightleftarrows OH^{-}(YSZ) + (Ni) + e^{-}(Ni)}$ $\mathrm{H(Ni) + OH^{-}(YSZ) \rightleftarrows H_2O(YSZ) + (Ni) + e^{-}(Ni)}$
Oxygen spillover:	$\mathrm{O^{2-}(YSZ) \rightleftarrows O^{-}(YSZ) + e^{-}(Ni)}$ $\mathrm{O^{2-}(YSZ) + (Ni) \rightleftarrows O^{-}(Ni) + (YSZ) + e^{-}(Ni)}$ $\mathrm{O^{-}(Ni) \rightleftarrows O(Ni) + e^{-}(Ni)}$ $\mathrm{O^{2-}(YSZ) + (Ni) \rightleftarrows O(Ni) + (YSZ) + 2e^{-}(Ni)}$
Hydroxyl spillover:	$\mathrm{OH^{-}(YSZ) + (Ni) \rightleftarrows OH(Ni) + (YSZ) + e^{-}(Ni)}$
Reactions on YSZ surface:	$\mathrm{H_2O + (YSZ) \rightleftarrows H_2O(YSZ)}$ $\mathrm{2OH^{-}(YSZ) \rightleftarrows O^{2-}(YSZ) + H_2O(YSZ)}$ $\mathrm{O_O^X(YSZ) + (YSZ) \rightleftarrows V_{\ddot{O}}(YSZ) + O^{2-}(YSZ)}$

The mechanism used in their model summarized almost all the possible published elementary reaction steps and charge transfer reactions. In this mechanism, water could be produced at both the Ni and YSZ surface. The following are the main conclusions from their study:

(1) Only the mechanism involving the two hydrogen spillover pathways showed good agreement with the complete experimental data.

(2) Hydrogen spills over to oxide ions, water dissociation on YSZ, water desorption from YSZ and surface diffusion of hydroxyl ions adsorbed on YSZ may be the dominating processes for the mechanism.

(3) Small increase in the kinetics of charge transfer reaction was observed when the partial pressure of H_2 increased; however, a more important positive effect was found when the partial pressure of H_2O increased.

(4) Surface diffusion plays a key role on the electrochemical behaviour at the TPB.

<u>Goodwin's group (California Institute of Technology, USA)</u>

Goodwin et al. (2009) developed a one-dimensional model that coupled elementary chemistry, electrochemistry and surface diffusion within a Ni/YSZ pattern anode configuration. Furthermore, modeling results were compared with experimental results (Mizusaki et al., 1994a). A hydrogen spillover process was proposed to explain the experimental results.

The Ni surface reactions in this model are the same as in Bieberle's (2002) model. Also, chemistry and thermodynamic properties on YSZ were investigated in Goodwin et al.'s study. In their model, YSZ surface was assumed to contain an equal number of oxygen and zirconium (or yttrium) atoms to maintain charge neutrality. Two types of surface sites identified were occupied Zr sites and empty (x) sites. The surface oxygen atom was located at the center of four zirconium atoms and was slightly above than the zirconium plane. An open (x) site is defined as "the position that surface oxygen would occupy if it were present".

This surface structure was originally studied by Nishimura et al. (Nishimura et al., 2001), who claimed that vacancy formation at the top O layer is easier than in the bulk. The following dynamic equilibrium between surface and bulk vacancies was proposed. (Goodwin et al., 2009).

$$\mathrm{O_O^{2-}} + (x) \rightleftarrows \mathrm{O^{2-}}(x) + \mathrm{V_O^{\cdot\cdot}} \qquad 2.4$$

The following pathway for water chemisorption was also proposed (see reactions 2.5 and 2.6).

$$\mathrm{H_2O(g)} + (\mathrm{Zr}) + \mathrm{O^{2-}}(x) \rightleftarrows \mathrm{OH^-(Zr)} + \mathrm{OH^-}(x) \qquad 2.5$$

$$\mathrm{OH^-}(x) + (\mathrm{Zr}) \rightleftarrows \mathrm{OH^-(Zr)} + (x) \qquad 2.6$$

Water chemisorption occurs by bonding gas phase H_2O to a Zr site and the subsequent transfer of a proton to the nearby surface oxygen. Since $\mathrm{OH^-}(x)$ is not stable, it immidiately reacts with a Zr site until equlibrium is reached. The thermodynamic data of $\mathrm{OH^{-}(Zr)}$ was obtained by fitting the experimental data of Raz et al. (2001). Hydrogen chemisorption on YSZ surface was eliminated from the reaction mechanism because of low surface coverage.

The following oxygen spillover and hydrogen spillover pathways were considered to interpret experimental results of Mazusaki et al. (1994b).

Oxygen spillover pathway:

$$\mathrm{O^{2-}}(x) \rightleftarrows \mathrm{O^{-}}(x) + \mathrm{e^{-}} \tag{2.7}$$

$$\mathrm{O^{-}}(x) + (\mathrm{Ni}) \rightleftarrows \mathrm{O(Ni)} + (x) + \mathrm{e^{-}} \tag{2.8}$$

Hydrogen spillover pathway:

$$\mathrm{H(Ni)} + \mathrm{O^{2-}}(x) \rightleftarrows \mathrm{OH^{-}}(x) + (\mathrm{Ni}) + \mathrm{e^{-}} \tag{2.9}$$

$$\mathrm{H(Ni)} + \mathrm{OH^{-}}(x) \rightleftarrows \mathrm{H_2O(Ni)} + (x) + \mathrm{e^{-}} \tag{2.10}$$

The characteristic of this pathway is water formation on the Ni surface from the charge transfer reaction. Moreover, single channel and dual channel hydrogen spillover pathways were investigated. The difference between single channel and dual channel hydrogen spillover is that two different sets of pre-exponential and symmetry factors for the second charge transfer reaction (2.10) were chosen. These pre-exponential and symmetry factors were adjusted to fit the experimental data of Mazusaki et al.'s (1994b). The results showed that the single-channel hydrogen spillover pathway provides a reasonable representation of the data, especially for the anodic branches by adjusting symmetry factors. The dual-channel hydrogen spillover could also enable a good fitting of the anodic branches but it has a little effect on the cathodic branches. They also found that the surface diffusion process is not a rate-limiting process, which is different from the result obtained by Vogler et al. (2009).

2.1.2 Other Studies on H_2 Electrochemical Reaction Kinetics (Not on Pattern Anodes)

In addition to the studies on H_2 electrochemical reaction mechanism using pattern anodes, some investigations were performed employing cermet anodes, porous and point anodes.

Mogensen's group (Risø National Laboratory, Denmark)

Primdahl and Mogensen (1997) studied the oxidation of H_2 on Ni/YSZ cermet anodes by impedance spectroscopy. The effect of temperature, overpotential, partial pressures of H_2 and H_2O were investigated. The temperature ranged between 850°C and 1000°C. Three semi-circles were identified in the impedance spectra. They also found that the polarization resistance at high frequencies (1 kHz-50 kHz) is independent of gas composition and overpotential, but dependent on the anode structure. At medium (10 Hz-1 kHz) and low frequencies (0.1Hz-1Hz), the polarization resistances depend on the partial pressures of H_2 and H_2O and overpotential. Based on the experimental results, they claimed that the high frequency process is associated with transfer of H^+ across the Ni/YSZ interface and oxygen ions through YSZ in the cermet anode. The low frequency process was proposed to involve adsorption of water on the YSZ surface. However, no direct evidence on the identity of the medium frequency process was obtained.

In another study, Mogensen and Skaarup (1996) pointed out that it is unlikely that the dissociative adsorption and surface diffusion of H on Ni surface are the rate-limiting processes due to the high surface coverage of H on Ni surface and the high H mobility. They suggested that the rate-determining process should occur along the TPB line or the region close to YSZ surface.

Jiang's group (Ceramic Fuel Cells Limited, Australia)

Jiang and Badwal (1997) investigated H_2 oxidation in SOFCs with porous Ni electrode and yttria-tetragonal zirconia (Y-TZP) electrolyte. Galvanostatic current interruption and electrochemical impedance spectroscopy were performed at 1000°C to investigate the H_2 oxidation mechanism. Different H_2/H_2O compositions (dry H_2, 99.14% H_2 with 0.86% H_2O, 98% H_2 with 2% H_2O) were used in the measurements. They found that the kinetics and mechanism of H_2 oxidation reaction on a porous Ni electrode are strongly related to the H_2O content in the gas feed. The impedance behavior is characterized by two overlapping arcs in the studied frequency domain. The water content in the fuel reduces the size of both high frequency and low frequency, but the major effect is on the low frequency arc. They also found that the increase in electronic and ionic conductivities of the electrolyte surface by doping with an oxide reduces the high frequency arc. In order to elucidate these phenomena, they proposed reaction mechanism in the Table 2-5 to describe oxidation of humidified H_2 fuels.

Table 2-5 H_2 oxidation mechanism proposed by Jiang and Badwal (1999)

Adsorption/desorption of H_2 on Ni surface:	$\mathrm{H_2(g) + 2(Ni) \rightleftarrows 2H(Ni)}$
H_2O dissociation on Ni surface:	$\mathrm{H_2O(g) + (Ni) \rightleftarrows O(Ni) + H_2(g)}$
Reactions on Ni surface:	$\mathrm{H(Ni) + O(Ni) \rightarrow OH(Ni) + (Ni)}$
Surface diffusion:	$\mathrm{H(Ni) \rightarrow H(Ni)_{TPB}, OH(Ni) \rightarrow OH(Ni)_{TPB}}$
Hydrogen spillover:	$\mathrm{H(Ni)_{TPB} + (Y - TZP) \rightarrow H(Y - TZP)_{TPB} + (Ni)}$ $\mathrm{OH(Ni)_{TPB} + (Y - TZP) \rightarrow H(Y - TZP)_{TPB} + O(Ni)}$
Charge transfer reactions:	$\mathrm{O^{2-}(Y - TZP) + H(Y - TZP)_{TPB}}$ $\mathrm{\rightarrow H_2O(g) + V_{\ddot{O}} + 2e^{-}(Y - TZP)_{TPB}}$ $\mathrm{2e^{-}(Y - TZP)_{TPB} \rightarrow 2e^{-}(Ni)}$

In dry H_2 fuels, they claimed that the dissociative adsorption rate of H_2 on Ni surface is very low at the SOFC operating temperature, which leads to low surface coverage of H. Thus, the actual concentration of H available for charge transfer reaction is low and limits H_2 oxidation, which contributes to the low frequency feature in the impedance spectra. This conclusion gives counter to that of Mogensen and Skaarup(1996) discussed previously. In humidified H_2 fuels, H_2O is proposed to adsorb on Ni surface and dissociate to O and H_2 gas, which differs from what other groups proposed. The adsorbed O atom reacts with H atom to form OH, which diffuses to Y-TZP surface through a fast spillover pathway. Thus, the dissociative adsorption of H_2 speeds up. The high frequency arc was suggested to be related to charge transfer.

Holtappels's group (Risø National Laboratory, Denmark)

Holtappels et al. (1999a) investigated the reaction of H_2/H_2O mixtures on Ni/YSZ cermet anodes as functions of temperature, overpotential, and reactant partial pressure. Current-voltage measurements were carried out of three different gas compositions (48% H_2 with 12% H_2O, 48% H_2 with 5% H_2O, 19% H_2 with 5% H_2O) at temperatures between 725°C and 950°C.

From current-voltage measurements, they found that H_2 oxidation reaction at 950°C depends on the partial pressure of H_2 only at low overpotential. The reaction order of H_2 (0.5) is almost constant with overpotential at 725°C, while it decreases from 0.6 at -900 mV (the actual cell potential) to 0.1 at -800 mV at 950°C. They also gave a possible explanation for the independence of the reaction rate on the H_2 partial pressure with increasing overpotential in the high temperature range, which might be due to high surface coverage of H atoms on Ni surface caused by the high adsorption rate of the H_2 on Ni surface.

Finally, Holtappels et al. (1999a) claimed that in the low temperature region (725-845°C), the overall reaction is controlled by charge transfer, whereas both charge transfer and possible adsorption are rate-limiting reactions in the high temperature region (above 845°C).

In another study, Holtappels et al. (1999b) investigated the impedance behavior of the Ni/YSZ cermet anodes at the same temperatures and reactant partial pressures as they considered for the current-voltage measurements. They found from EIS measurements of the H_2/H_2O reaction on Ni/YSZ cermet anodes at OCV that three processes are important: charging of the electrical double layer, proton diffusion in YSZ and charge transfer process. They also found that the real part of the impedance was controlled by the charge transfer reaction at temperatures below 845°C, while both charge-transfer and adsorption of H_2 or H_2O determined the total reaction rate at temperatures above 890°C. The impedance study further confirmed the conclusion they made on the basis of the current-voltage tests. Table 2-6 lists the reaction mechanism proposed by this group. In this reaction mechanism, the formation of interstitial hydrogen ($\mathrm{H_i}$) was assumed. H is transferred from the Ni surface to the YSZ surface via the interstitial H. It undergoes a series of reactions to form $\mathrm{OH_O^-}$ (YSZ), which is then transferred back to the Ni surface.

Table 2-6 H_2 reaction kinetics suggested by Holtappels et al. (Holtappels et al., 1999a; Holtappels, 1999b)

Adsorption/desorption of H_2 on Ni surface:	$\mathrm{H_2 + 2(Ni) \rightleftarrows 2H(Ni)}$
One possible way is on Ni surface: The other way is formation of interstitial protons:	$\mathrm{H(Ni) + OH^-(Ni) \rightleftarrows H_2O + e^-(Ni) + (Ni)}$ $\mathrm{H(Ni) \rightleftarrows H_i\,(YSZ) + e^-(Ni) + (Ni)}$
Hydroxyl between Ni and YSZ:	$\mathrm{OH_O^-\,(YSZ) \rightleftarrows OH^-(Ni)}$
Reaction on YSZ surface:	$\mathrm{H_i\,(YSZ) + O_O^X \rightleftarrows OH_O^-(YSZ) + V_O^{\cdot\cdot}}$

Kee's group (Colorado School of Mines Golden, USA)

The model presented by Zhu et al. (2005) described a planar porous anode-supported SOFC. The following hydrogen oxidation reaction mechanism (Table 2-7) was proposed.

Table 2-7 H_2 oxidation mechanism investigated by Zhu and co-workers (Zhu et al., 2005)

Adsorption/desorption of H_2 on Ni surface:	$\mathrm{H_2 + 2(Ni) \rightleftarrows 2H(Ni)}$
Hydrogen spillover to O: Hydrogen spillover to OH:	$\mathrm{H(Ni) + O^{2-}(YSZ) \rightleftarrows OH^-(YSZ) + (Ni) + e^-(Ni)}$ $\mathrm{H(Ni) + OH^-(YSZ) \rightleftarrows H_2O(YSZ) + (Ni) + e^-(Ni)}$
Adsorption/desorption of H_2O on YSZ surface: Surface diffusion of oxygen ion between bulk and surface YSZ:	$\mathrm{H_2O(YSZ) \rightleftarrows H_2O + (YSZ)}$ $\mathrm{O_O^X + (YSZ) \rightleftarrows O^{2-}(YSZ) + V_O^{\cdot\cdot}}$

In this reaction mechanism, H_2 and H_2O are assumed to adsorb on the Ni and YSZ surfaces, respectively. Charge transfer reactions involve hydrogen spillover from the Ni surface to YSZ surface and water is produced on the YSZ surface, which is very similar to the mechanism proposed by de Boer (1998).

Gewies and Bessler's study (University of Heidelberg, Germany)

In addition to the investigations of H_2 oxidation mechanism using Ni/YSZ pattern anodes, Bessler's group (Gewies & Bessler, 2008) also employed a symmetric half-cell Ni/YSZ cermet electrode. Hydrogen spillover from the Ni surface to the hydroxyl on the YSZ surface was assumed to be the only charge transfer pathway. Other surface reactions were assumed to be the same as those used in the pattern anode study (Vogler, 2009). Electrical double layer effects were also incorporated in their model.

The impedance spectra of the symmetrical cell model show three features at low (~6 Hz), intermediate (200 Hz-400 Hz), high (500 Hz-20 kHz) frequencies. The model was simplified by neglecting electrical double layer effects or transport processes in order to compare with the impedance data. The results show that transport in gas channel causes the low frequency response, while gas diffusion in the porous cermet and current collector contributes to the immediate frequency response, whereas the high frequency response is affected by complex electrochemical processes (charge transfer reaction and electrical double layer). The result obtained in this study was based on assumption that hydrogen spillover is the active charge transfer reaction. Other charge transfer mechanisms, such as oxygen spillover and interstitial hydrogen transport could not be excluded.

Ziegler's group (University of Calgary, Canada)

Shishkin and Ziegler (2008) studied the possibility of H_2 and CH_4 oxidation on different YSZ surface using Density Functional Theory (DFT) calculations. They found that the oxygen-enriched YSZ surface is energetically favorable for the direct oxidation of H_2 and CH_4. Moreover, the reaction rate could be raised increasing the oxygen input rate. It was suggested that the coking problem could be prevented by choosing a cermet anode with a chemically inactive metal. In another study, Shishkin and Ziegler (2009) elucidated the interaction between fuel and Ni and YSZ in a Ni/YSZ cermet model with Ni cluster covering part of the YSZ surface. They assumed that the region close to the YSZ surface is oxygen-enriched, while the bulk YSZ is deficient in oxygen. However, the DFT study showed that the oxygen-enriched YSZ surface of the cermet is not as active as the pure oxygen enriched YSZ surface for the adsorption and oxidation of fuels. They determined that the dissociative adsorption of

H_2 on the Ni surface of the cermet is similar to that of the infinite Ni surface, which is exothermic with reaction energy of 23 kcal/mol and energy barrier less than 1 kcal/mol. Based on the DFT results, they concluded that H_2 adsorbs on the Ni surface of the Ni/YSZ cermet, while the direct oxidation of H_2 on the YSZ surface is not possible. In a recent study, Shishkin and Ziegler (2010) found that both oxygen and hydrogen spillovers have high energy barriers (46 and 52 kcal/mol), which makes both pathways unlikely. However, the direct water formation at the interface between Ni and ZrO_2 (or Y_2O_3) is more feasible with an energy barrier of 27 kcal/mol. Finally, they claimed that H_2 oxidation occurs at the interface between Ni and YSZ, where oxygen atoms are bound to both Ni and ZrO_2 (or Y_2O_3).

2.2 Literature Review on CO Oxidation Reaction Mechanism

CO can be used as fuel for SOFCs by direct electrochemical oxidation or by the water-gas-shift reaction with subsequent H_2 oxidation (Habibzadeh, 2007). The overall water-gas-shift reaction is described as:

$$\mathrm{CO} + \mathrm{H_2O} \rightleftarrows \mathrm{CO_2} + \mathrm{H_2} \qquad 2.11$$

Several studies on CO electrochemical oxidation on SOFC anodes have been reported, but without general agreements regarding the detailed reaction mechanism (Lauvstad et al., 2002; Utz et al., 2011b; Yurkiv et al., 2011; Shi et al., 2012).

Early in 1971, T. H. Etsell and S. N. Flengas (Etsell & Flengas, 1971) studied the overpotential behavior in oxide electrolyte fuel cells with Pt porous anodes. Different reaction mechanisms were proposed to elucidate the overpotential behavior of the cell operating with CO/CO_2 mixtures. Based on the experimental observations, they concluded that either gaseous or adsorbed CO or gaseous CO_2 could participate in the electrochemical reactions.

In order to investigate the electrode reaction kinetics in CO/CO_2 atmosphere, Mizusaki et al. (1992) fabricated porous Pt electrodes with stabilized zirconia electrolytes and investigated those electrodes using EIS and Tafel measurements. The impedance was represented by a circuit containing resist and Warburg impedance in parallel. The Warburg impedance was attributed to diffusion of the reactants. Polarization resistance was observed to increase with decreasing the ratio of pCO/pCO_2. Except for the region close to equilibrium, the anodic current varied with $pCO^{1/2}$, while the cathodic current was independent of pCO. In their study, the dependence of polarization resistance and current density on pCO_2 was not evaluated experimentally.

Based on the experimental results, they proposed that the chemical reaction across TPB is the rate-limiting process (reaction 2.12).

$$\mathrm{CO_{ad}(Pt) + O_{ad}(el) \rightarrow CO_{2,ad}(Pt)} \qquad 2.12$$

The expression they used for the reaction rate of the above reaction is:

$$r = kp_{CO}^{1/2}a_O^{1/2} - k'p_{CO_2}^{1/2} \qquad 2.13$$

where *k, k'* are the forward and reverse reaction rates respectively, p_{CO} , p_{CO_2} are the partial pressure of CO and CO_2, while a_O is the activity of surface adsorbed oxygen.

Holtappels et al. (1999c) investigated the reaction of CO/CO_2 mixtures on Ni/YSZ cermet anodes. Their results showed that the overall reaction rate for CO oxidation is much slower than the reaction rate of H_2 oxidation. They also found that the CO electrochemical reaction rate is periodically changing. A possible explanation was the reconstruction of the Ni surface, which resulted in different carbon coverage. But in their study, no elementary reaction steps were proposed.

Based on the reaction mechanism proposed by other investigators (Etsell & Flengas, 1971; Mizusaki et al., 1992), Lauvstad et al. (2002a) considered different reaction mechanisms for modeling steady-state and impedance response using Pt and Ni metal point electrodes in CO/CO_2 gases. The overall CO/CO_2 reaction is shown in reaction 2.14.

$$\mathrm{CO_2(g) + V_O^{\cdot\cdot} + 2e^- \rightleftarrows CO(g) + O_O^X} \qquad 2.14$$

They assumed that the overall electrochemical reaction is composed of elementary steps (see Table 2-8). In the first reaction mechanism, only one adsorbed species, O_{ad}, was included. Two adsorbed species, O_{ad} and CO_{ad}, were assumed to participate in the second reaction mechanism. Oxygen was assumed to be adsorbed on the electrolyte surface, while CO was assumed to be adsorbed on the electrode surface. The third reaction mechanism is the limiting case of reaction mechanism II obtained by assuming the lifetime of atomic oxygen on the electrolyte surface to be quite short. In all these mechanisms, surface diffusion of adsorbed species was neglected. In a fourth model they included the effect of CO diffusion, but no clear conclusion was obtained.

It was found that only the second reaction mechanism with two adsorbed species show fourth-quadrant impedance behavior, as reported in another experimental results study (Lauvstad et al., 2002b).

In their experimental study (Lauvstad, et al., 2002b), both Pt and Ni point anodes were used. The following conclusions were reached from the experimental measurements.

1. Decreasing pCO while keeping pCO_2 constant at 0.667 atm resulted in polarization resistance going through a maximum for the Pt electrode.
2. With Ni as electrode material, polarization resistance decreased sharply when pCO was reduced from 0.333 to 0.067 atm, but remained almost constant upon further reduction to 0.0067 atm.
3. With Ni as electrode material, decreasing pCO_2 while keeping pCO constant resulted in an increase in polarization resistance.
4. At constant ratio of pCO /pCO_2, a decrease in temperature resulted in an increase in polarization resistance for Pt (827-950°C). For Ni electrodes, polarization resistance first decreased with an increase in temperature from 775°C to 825°C, and then increased with further increasing temperature from 825 to 924°C. A minimum value in the polarization resistance was observed in the temperature range studied.
5. Applying anodic overpotential decreased the total polarization resistance, whereas applying cathodic overpotential increased the polarization resistance.
6. The different performance of Pt and Ni electrodes in both impedance and in steady-state measurements confirmed that metal used for the electrode was of great importance to the electrochemical reaction.
7. The electrode reactions involving CO-CO_2 were slower than those involving H_2-H_2O for both Ni and Pt point anodes.
8. No diffusion limitations were reported on the basis of impedance spectra.

Table 2-8 CO reaction mechanism proposed by Lauvstad et al. (2002a)

Reaction mechanism I	$CO_2(g) + S \rightleftarrows CO(g) + O_{ad}$ $O_{ad} + V_O^{\cdot\cdot} + 2e^- \rightleftarrows S + O_O^X$	S denotes the available adsorption site on electrode or electrolyte surface.
Reaction mechanism II	$CO_2(g) + S_{el} + S_{ed} \rightleftarrows O_{ad,el} + CO_{ad,ed}$ $CO_{ad,ed} \rightleftarrows CO(g) + S_{ed}$ $O_{ad,el} + V_O^{\cdot\cdot} + 2e^- \rightleftarrows S_{el} + O_O^X$	S_{el}, S_{ed} are empty electrolyte and electrode surface available for adsorption.
Reaction mechanism III	$CO_2(g) + V_O^{\cdot\cdot} + 2e^- + S \rightleftarrows CO_{ad} + O_O^X$ $CO_{ad} \rightleftarrows CO(g) + S$	S is the vacant site of electrode or electrolyte

Weber et al. (2002) investigated the oxidation of H_2, CO and methane on Ni/YSZ cermet anodes under different steam/carbon ratio conditions in the fuel stream. DC techniques and impedance spectroscopy were applied for cell characterization. They found that the cell performance decreased at high CO concentrations (>90%) in CO/H_2 mixtures. As for CH_4/H_2O mixtures, the cell performance was enhanced by decreasing the steam/carbon ratio. They also claimed that it is possible to oxidize dry CO or dry methane as long as the oxygen supply is sufficient. The cell performance loss was not significant under dry methane operating conditions. However, carbon deposition occurred on the gas supply and current collector which affected the long term stability of the cell.

Sukeshini et al. (2006) studied the electrochemical reaction of H_2, CO, CO/H_2 mixtures on Ni/YSZ pattern anodes. Electrochemical impedance tests for H_2, CO and CO/H_2 mixtures were carried out in dry and wet environments. Their results showed that within the temperature range studied (750-850°C), the reaction rate of H_2 oxidation was significantly faster than that of CO oxidation. Addition of H_2O did not cause a decrease in polarization at OCV condition for H_2. For CO oxidation, H_2O appeared to inhibit equilibration of the electrochemical process. The adsorption of H_2O on either the YSZ or Ni surface near the TPB may inhibit reactions between CO and O^{2-} at low overpotential. They also claimed that the adsorption/desorption equilibration on the anode surface had a very important role on the oxidation of H_2 and CO at high temperatures. The experimental results also showed that the behavior of CO/H_2 mixtures down to 25% H_2 exhibited similar behavior as that of pure H_2.

Costa-Nunes et al. (2005) compared the performance of Cu/CeO_2/YSZ and Ni/YSZ cermet SOFC anodes while operating under H_2, CO, and syngas feed conditions. Similar cell performance was observed in H_2, CO atmospheres on Cu/CeO_2/YSZ anodes. However, the performance of SOFCs with Ni/YSZ anodes operating with CO gas was poor compared to the same cell with H_2 fuel at 973K. Increasing the catalytic activity of Cu/CeO_2/YSZ by adding Co could increase the cell performance using CO fuel, so that it was even higher than that under H_2 gas. Based on this, they suggested that the H spillover from Ni surface to YSZ was the main reason for the high activity of H_2 oxidation. However, this spillover pathway does not exist in CO oxidation mechanism. The charge transfer process for CO and H_2 is completely different.

Habibzadeh (2007) studied CO oxidation in SOFCs using Ni pattern anodes with YSZ as the electrolyte. EIS and voltammetry measurements were carried out to investigate the electrochemical behavior of CO oxidation. The effect of overpotential, temperature, humidity, and electrode geometry on CO oxidation was explored. It was found that the polarization resistance for CO oxidation did not vary linearly with the logarithm of the overpotential, which means that processes other than charge transfer reaction played a major role in CO oxidation. Unlike H_2 electrochemical oxidation, charge transfer resistance of CO oxidation does not increase exactly with the TPB length. However, the polarization resistance decreases with increasing Ni surface area. Moreover, a small amount of water (3%) in the fuel could promote the charge transfer process. It was suggested that CO is consumed through both water-gas-shift reaction and oxidation. The detailed reaction mechanism is given in Table 2-9. The dissociative adsorption of CO and CO_2 on the Ni surface was taken from the study of Janardhanan and Deutschmann (2006).

The rate-limiting process was confined to a region very close to TPB. A combination of overpotential and temperature plays a role in the rate-determining process. At high overpotential (~300 mV) and temperature (750°C-775°C), the charge-transfer reaction was assumed to be rate-limiting. At low overpotential (~100 mV) and temperature (700°C-

725°C), adsorption or surface diffusion combined with charge transfer are the rate-limiting processes.

Table 2-9 CO oxidation mechanism presented by Habibzadeh (2007)

Adsorption and desorption reactions on Ni surface:	$H_2 + 2(Ni) \rightleftarrows 2H(Ni)$
	$H_2O + (Ni) \rightleftarrows H_2O(Ni)$
	$CO + (Ni) \rightleftarrows CO(Ni)$
	$CO_2 + (Ni) \rightleftarrows CO_2(Ni)$
	$O_2 + 2(Ni) \rightleftarrows 2O(Ni)$
Adsorption, desorption and surface reactions on YSZ surface:	$H_2O + (YSZ) \rightleftarrows H_2O(YSZ)$
	$H_2O(YSZ) + O^{2-}_{YSZ} \rightleftarrows 2OH^{-}_{YSZ}$
Ni surface reactions:	$H(Ni) + O(Ni) \rightleftarrows OH(Ni) + (Ni)$
	$H_2O(Ni) + O(Ni) \rightleftarrows 2OH(Ni)$
	$OH(Ni) + H(Ni) \rightleftarrows H_2O(Ni) + (Ni)$
	$CO(Ni) + (Ni) \rightleftarrows C(Ni) + O(Ni)$
	$CO(Ni) + O(Ni) \rightleftarrows CO_2(Ni) + (Ni)$
Charge transfer reactions at Ni/YSZ TPB:	$H(Ni) + O^{2-}(YSZ) \rightleftarrows OH^{-}(YSZ) + (Ni) + e^{-}(Ni)$
	$H(Ni) + OH^{-}(YSZ) \rightleftarrows H_2O(YSZ) + (Ni) + e^{-}(Ni)$
	$CO(Ni) + O^{2-}(YSZ) \rightleftarrows CO_2(Ni) + (YSZ) + 2e^{-}(Ni)$

Ehn et al. (2010) investigated the electrochemical behavior of Ni pattern anodes in both H_2/H_2O and CO/CO_2 atmospheres. The effect of H_2O on the polarization resistance was evaluated at both low and high temperature with the H_2O content between 0.6% and 2.6%. Although the data were corrected for degradation, the evaluation of H_2O effects was not conducted under stable conditions. The effect of heat treatment on Ni pattern anode performance was also evaluated at different temperatures. An initial increase in polarization resistance was observed each time the temperature was increased. The pattern anodes with different Ni thicknesses showed different degradation behavior at high temperature (700°C), but similar degradation behavior at low temperature (400°C). In order to avoid major structural changes, electrochemical tests of Ni pattern anodes below 500°C were suggested. For thin Ni pattern anodes (0.5 µm), the polarization resistance was about 17 times higher in

$CO-CO_2$ than in H_2-H_2O. For thicker anodes (1μm), the difference of polarization resistance was very small in these two gas environments. Also, the dependence of polarization resistance on pCO was different when using pattern anodes with different Ni thicknesses. Polarization resistance showed decreased as the partial pressure of CO was raised when using thin Ni pattern anodes, whereas it increased with increasing pCO on thicker Ni pattern anodes. In addition, cells with different TPB lengths demonstrated different performance in CO/CO_2 environments. The performance of the cell seemed very unstable.

Utz et al. (2011b) used EIS to evaluate the dependence of polarization resistance on pCO, pCO_2 and temperature using Ni/YSZ pattern anodes. Polarization resistance in a $CO-CO_2$ atmosphere was only slightly higher than that in H_2-H_2O, indicating that H_2 and CO oxidation proceed at a similar rate. An inverse dependence was found for the polarization resistance on pCO_2 with the reaction order varying from 0.61 to 0.79. When $pCO < 2\times10^4$ Pa, polarization resistance decreased with increasing pCO. When $pCO > 2\times10^4$ Pa, the opposite trend was found. The activation energies in the temperature range of 700-800°C varied between 0.85 and 1.42 eV with different gas compositions. Changes in the reaction mechanism with different gas compositions were proposed.

Yurkiv et al. (2012) investigated the CO oxidation by implementing elementary reaction steps into a kinetic model and validating the kinetic model with the experimental data reported by Utz et al. (2011b). In the model, CO/CO_2 adsorption/desorption as well as CO oxidation occur on both Ni and YSZ surfaces.

It was proposed that the charge transfer reactions proceed through two consecutive single-electron charge transfer reactions. The first reaction is a single electron oxidation step of O^{2-}_{YSZ} with the formation of O^{-}_{YSZ}. The second one is either spillover of O^{-}_{YSZ} to the Ni surface or the transfer of an electron to the Ni surface, leaving O species on the YSZ. The detailed reaction mechanism is given in Table 2-10. The simulation results revealed that the CO and CO_2 compositions have strong effects on the electrode kinetics. Comparisons were made between the simulation and experimental results from Utz et al. (2011b). Two different charge transfer reaction mechanisms were proposed. When the partial pressure of CO is high, charge transfer reaction proceeds via a two-step oxygen spillover reaction mechanism and CO is oxidized on the Ni surface. When the partial pressure of CO is low, most oxygen ions are reduced on the YSZ surface, and CO is oxidized on the YSZ surface. No oxygen ions spillover occurs.

Table 2-10 Elementary reaction steps for CO oxidation on Ni/YSZ pattern anodes (Yurkiv et al., 2012)

Adsorption and desorption reactions on Ni surface:	$\mathrm{CO} + (\mathrm{Ni}) \rightleftarrows \mathrm{CO(Ni)}$
	$\mathrm{CO_2(Ni)} \rightleftarrows \mathrm{CO_2} + (\mathrm{Ni})$
	$\mathrm{CO} + \mathrm{O(Ni)} \rightleftarrows \mathrm{CO_2} + (\mathrm{Ni})$
	$\mathrm{CO(Ni)} + \mathrm{O(Ni)} \rightleftarrows \mathrm{CO_2(Ni)} + (\mathrm{Ni})$
Adsorption, desorption and surface reactions on YSZ surface:	$\mathrm{CO} + (\mathrm{YSZ}) \rightleftarrows \mathrm{CO(YSZ)}$
	$\mathrm{CO} + \mathrm{O(YSZ)} \rightleftarrows \mathrm{CO_2} + (\mathrm{YSZ})$
	$\mathrm{O^{2-}_{YSZ}} + \mathrm{V_{\ddot{O},YSZ}} \rightleftarrows \mathrm{O^{X}_{O,YSZ}} + \mathrm{YSZ}$
Charge transfer reactions at Ni/YSZ TPB:	$\mathrm{O^{2-}_{YSZ}} \rightleftarrows \mathrm{O^{-}_{YSZ}} + \mathrm{e^{-}(Ni)}$
	$\mathrm{O^{-}_{YSZ}} + (\mathrm{Ni}) \rightleftarrows \mathrm{O(Ni)} + \mathrm{YSZ} + \mathrm{e^{-}(Ni)}$
	$\mathrm{O^{-}_{YSZ}} = \mathrm{O(YSZ)} + \mathrm{e^{-}(Ni)}$

Shi et al. (2011) developed a model describing elementary steps for CO oxidation on Ni/YSZ pattern anodes, and surface diffusion. In their study, adsorption and desorption of CO and CO_2 were considered on the Ni surface. On YSZ surfaces, only bulk-surface exchange of oxygen was included in the model. The CO oxidation mechanism used in this study, which is summarized in Table 2-11, was the same as the CO oxidation mechanism used in Habibzadeh's study (2007).

The simulation results were compared with their experimental results based on an anode-supported button cell with Ni/YSZ cermet anode. They found that the simulated polarization curve reasonably well predicted the experimental behavior of CO oxidation. They considered carbon deposition in their model, and they found that lowering the temperature and operating voltage helped reduce carbon deposition on the Ni surface.

Table 2-11 CO oxidation mechanism used in Shi et al.'s works (Shi et al., 2011)

Adsorption/desorption reactions and surface reactions on Ni:	$\mathrm{CO} + (\mathrm{Ni}) \rightleftarrows \mathrm{CO(Ni)}$
	$\mathrm{CO_2} + (\mathrm{Ni}) \rightleftarrows \mathrm{CO_2(Ni)}$
	$\mathrm{O_2} + 2(\mathrm{Ni}) \rightleftarrows 2\mathrm{O(Ni)}$
	$\mathrm{CO(Ni)} + (\mathrm{Ni}) \rightleftarrows \mathrm{C(Ni)} + \mathrm{O(Ni)}$
	$\mathrm{CO(Ni)} + \mathrm{O(Ni)} \rightleftarrows \mathrm{CO_2(Ni)} + (\mathrm{Ni})$
Bulk surface exchange of oxygen on YSZ:	$\mathrm{O^{2-}_{YSZ}} + \mathrm{V_{\ddot{O},YSZ}} \rightleftarrows \mathrm{O^{X}_{O,YSZ}} + \mathrm{YSZ}$
Charge transfer reactions at Ni/YSZ TPB:	$\mathrm{CO(Ni)} + \mathrm{O^{2-}_{YSZ}} \rightleftarrows \mathrm{CO_2(Ni)} + (\mathrm{YSZ}) + 2\mathrm{e^-}$

In another study, Shi et al. (2012) developed a similar model as the one described above, but used it to predict the experimental data reported by Habibzadeh (2007). Polarization curves and impedance spectra were simulated and compared with the experimental data. The simulation results showed qualitative agreement with the changes in the experimental impedance upon variation of polarization voltage and temperature. However, they observed obvious deviations between the simulated and experimental impedance and suggested further studies on detailed charge transfer reactions and mass transport processes. They also claimed that surface diffusion may be one of the rate-determining steps under low temperature and higher polarization voltage conditions.

All the above studies regarding CO electrochemical reaction mechanisms were investigated at temperatures of 700°C or above. Offer and Brandon (Offer & Brandon, 2009) investigated the oxidation of dry CO in intermediate temperature solid oxide fuel cells (IT-SOFCs). The cell used in their study was composed of gadolinium doped ceria (GDC) as the electrolyte, nickel oxide cermet (50:50 NiO/GDC) as the anode, and strontium cobalt doped lanthanum ferrite (50:50 $\mathrm{La_{0.6}Sr_{0.4}Co_{0.2}Fe_{0.8}O_3}$/GDC) as the cathode. The cell was operated at temperatures of 500°C, 550°C and 600°C, and at current densities of 0, 50 mA/cm^2 and 100 mA/cm^2. Dry CO was used as the fuel in order to investigate carbon formation from a single reaction (Boudouard reaction). Their results showed that both temperature and current density affected carbon deposition of the cell in a dry CO atmosphere. By operating the cell at a current density of 100 mA/cm^2 at 500°C, carbon deposition could be minimized and the electrochemical performance of anode with an exchange current density of 51 mA/cm^2 could be maintained before and after operating the cell with dry CO for an hour.

2.3 Summary of the Literature Review on the Electrochemical Oxidation of H_2 and CO

As discussed earlier, all the proposed H_2 electrochemical reaction mechanisms involve adsorption/desorption of H_2 on Ni surface only. In most studies, the polarization resistance of the cell decreases with increases in the water partial pressure, temperature and overpotential, while being almost constant with changes in the H_2 partial pressure. Only de Boer's (1998) experimental data did not follow this trend of the H_2 dependence. Moreover, the qualitative value of polarization resistance is quite different from the different research groups. In the modeling studies, different surface reactions, charge transfer reactions were also involved in the proposed mechanisms. YSZ surface was given less attention due to the lack of YSZ surface chemistry knowledge.

No consensus has been reached about the rate-limiting step(s) for H_2 oxidation (Bieberle, 2000; Goodwin et al., 2009; Vogler, 2009; Utz et al., 2010; Yao & Croiset, 2013a). By using Ni/YSZ pattern anodes, both experimental and modeling studies showed one semi-circle in the EIS arc except for three semi-circles in de Boer and Utz et al.'s measurements (Bessler, 2005; Bieberle & Gauckler, 2002; de Boer, 1998; Mizusaki et al., 1994a; Utz et al., 2010). However, three semi-circles were observed in the EIS arc using Ni/YSZ cermet (Gewies et al., 2007; Gewies & Bessler, 2008; Holtappels et al., 1999b; Primdahl & Mogensen, 1997). In Mizusaki and de Boer's study (de Boer, 1998; Mizusaki et al., 1994b), a rate-limiting step was assumed, and the corresponding Bulter-Volmer equation was derived. For Bieberle and Bessler's study, no rate-limiting reactions were chosen and the Bulter-Volmer equation was not used. The current density was calculated based on the reaction rate of charge transfer reactions. Bieberle et al. (2000) claimed that the rate-limiting process was either adsorption/desorption of hydrogen or removal of oxygen ions from YSZ. In addition, both processes could be combined with charge transfer process. Vogler et al. (2009) concluded that hydrogen spillover with water formation on YSZ surface was the mechanism which correctly predicted the observed relationship between polarization resistance and H_2 and H_2O partial pressures. They also proposed that hydrogen spillover to oxide ions, water dissociation on YSZ, water desorption from YSZ, and surface diffusion of hydroxyl ions adsorbed on YSZ might be the possible dominating processes. Goodwin et al. (2009) stated that hydroxyl spills over to Ni surface with water formation on Ni surface can provide a good fit to the experimentally observed Tafel plot. However, Shishkin and Ziegler (2010) proposed that the H_2 oxidation occurs on the oxygen atoms at the interface between Ni and ZrO_2 (or Y_2O_3).

As for CO electrochemical oxidation, some research groups showed that CO oxidation was much slower than H_2 oxidation (Habibzadeh, 2007; Lauvstad et al., 2002b; Holtappels et al., 1999c; Sukeshini et al., 2006), while others reported that the reaction rate in CO-CO_2 environments was just slightly lower than that in H_2-H_2O environments (Ehn et al., 2010; Utz et al., 2011b). Different trends for the dependence of polarization resistance on partial pressure of CO and CO_2 were reported (Yao & Croiset, 2013b). Mizusaki et al. (1992) studied the effect of pCO on current density using porous Pt-stabilized zirconia. They observed that the anodic current was dependent on the pCO, whereas the cathodic current was independent on the pCO. The reaction order for the current dependence on pCO was 0.5. This means that polarization resistance decreases when increasing pCO. Lauvstad et al. (2002b) emphasized the different performances of Ni and Pt point anodes both in impedance and steady-state measurements. The dependence of polarization resistance on the partial pressures of CO and CO_2 were different when using Ni and Pt electrodes.

Utz et al. (2011b) reported negative dependence of polarization resistance on pCO_2 with the reaction order varying from 0.61 to 0.79. Regarding the polarization resistance dependence on pCO, a change was found at low and high partial pressure of CO. At high pCO ($> 2\times10^4$ Pa), polarization resistance increases with increasing pCO, whereas it decreases with increasing pCO at lower pCO. Boulenouar et al. (Boulenouar, et al., 2001; Utz et al., 2011b) reported the value to be 0.5 for pCO variation. Ehn et al. (2010) observed different trends of polarization resistance dependence on pCO when using thin (0.5 μm) and thick (1μm) Ni pattern anode. For thin Ni pattern anode, polarization resistance decreased as the pCO increasing. Opposite trend was observed when the thicker Ni pattern anode was used. The reaction order was not reported in their study.

Among all these studies, only Utz et al. (2011b) and Ehn et al. (2010) reported the activation energy for the CO oxidation. Utz et al. studied the temperature range of 700-800°C for CO oxidation and suggested that the activation energy varies between 0.85 and 1.42 eV. Ehn et al. did not give detailed information about the relationship between polarization resistance and temperature. They just mentioned that the activation energy for CO oxidation is the same as that for H_2 oxidation, which was 1 eV.

Regarding the CO electrochemical reaction mechanism, No consensus has been reached for the detailed elementary reactions of CO oxidation and where these steps occur.

Mizusaki et al. (1999) proposed that the rate-dominating process is the chemical reaction across the TPB line between CO and oxygen ions. Lauvstad et al. (2002a) proposed that the possible rate-limiting reaction might be due to the CO adsorption or CO_2 desorption reaction. Habibzadeh (2007) claimed that the rate-determining process depends on the overpotential and temperature. Under high overpotential and temperature, charge-transfer is the rate-limiting. Under low overpotential and temperature, adsorption or surface diffusion combined with charge transfer are the rate-limiting processes. The most recent modeling studies by Bessler’s group (Yurkiv et al., 2012) described adsorption/desorption of CO and CO_2 on both Ni and YSZ surfaces, surface chemical reactions, and possible charge transfer reaction at the TPB. They claimed excellent agreement between their modeling results with experimental results reported by Utz et al. (2011b). Besides, two different charge transfer reaction mechanisms were proposed at higher and lower pCO / pCO_2 ratios.

Chapter 3

Experimental Methods

This chapter describes the button cell electrochemical measurement set-up, techniques for characterization of Ni/YSZ pattern anodes, and fabrication of SOFC button cells with Ni/YSZ pattern anodes. Characterization techniques of the Ni/YSZ pattern anodes include scanning electron microscopy (SEM), optical microscopy, and Ni thickness measurement profilometer.

3.1 Experimental Set-up

All the electrochemical measurements in this study were conducted in a button cell test station. The experimental set-up includes five main parts: 1) button cell, 2) test rig, 3) gas conditioning and controlling system, 4) furnace, and 5) electrochemical test equipment. Figure 3-1 shows a schematic of the electrochemical test set-up for Ni/YSZ pattern anode characterization, which can be used for impedance and polarization measurements. It can also be used to evaluate the cell performance as a function of gas composition, polarization and temperature.

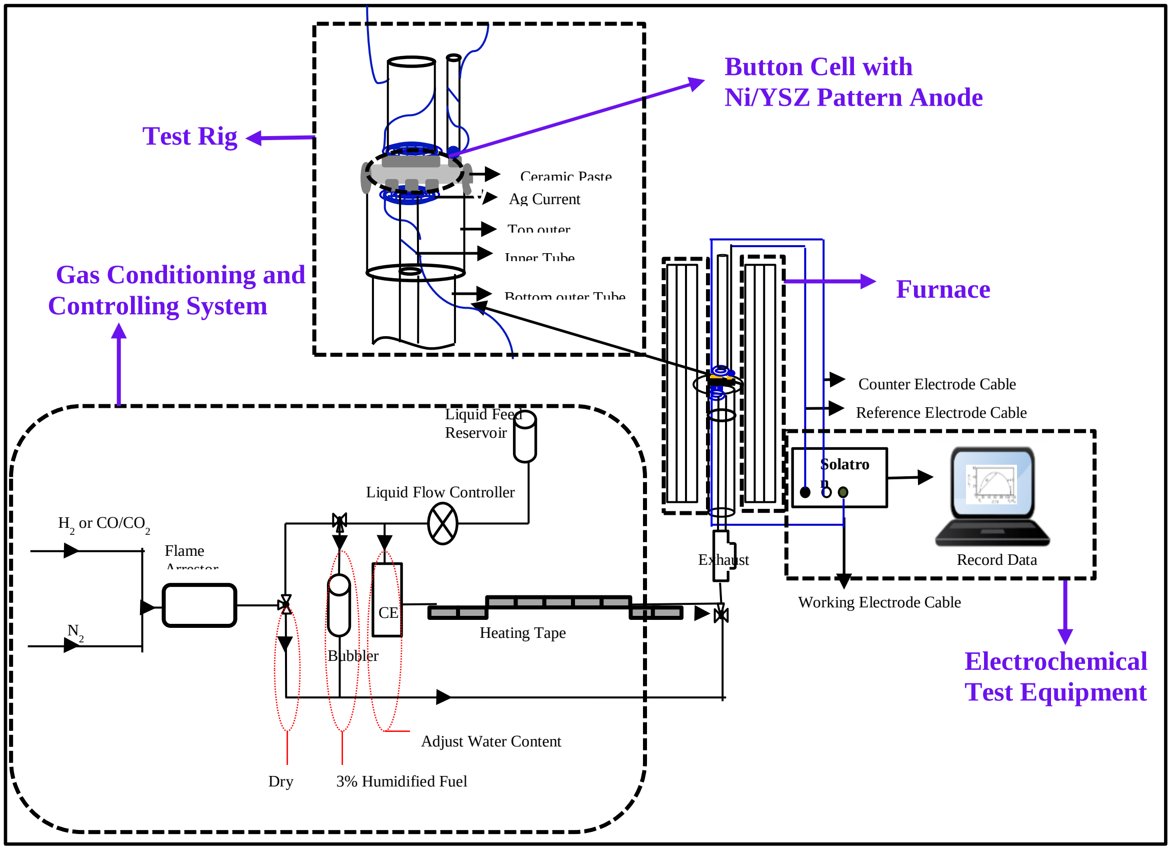

Figure 3-1 Schematic of the electrochemical test set up for Ni/YSZ pattern anode characterization.

3.1.1 Electrochemical Button Cell

The button cells used in this study were electrolyte-supported cells. The electrolyte is a YSZ single crystal with thickness of 0.5 mm. Ni pattern anode is on one side of the cell, whereas platinum (Pt) cathode is on other side of the YSZ and is symmetric to the Ni anode, but not patterned. The Pt reference electrode is placed on the same side as the cathode electrode. The reference electrode is used in order to study just the pattern anode performance. The pattern anode is the working electrode, whereas the cathode acts as the counter electrode.

The detailed geometry information and fabrication of Ni/YSZ pattern anode is presented in section 3.3.

3.1.2 Test Rig

The alignment of the cell in this study is presented in Figure 3-2. In this system, the cell sits on co-axial alumina tubes with anode side facing down. The outer tube is connected by two alumina tubes with different outer diameters (OD) and lengths. The length and OD of the top outer tube are 2.0 cm and 15 mm respectively, whereas the bottom outer tube is 40 cm long with an OD of 13 mm. The size of the outer tube is slightly bigger than that of the cell (12.7 ×12.7 mm), and is used to support the cell (see the test rig in Figure 3-1). Meanwhile, the inner alumina tube (OD: 3 mm) works as a fuel pathway to supply fuels to the anode. The fuel flows towards the anode side through the inner alumina tube and leaves through the annulus space between the outer and inner alumina tubes to the exhaust outlet. Besides supplying fuels, the inner alumina tube also ensures tight contact between the current collector and the Ni/YSZ pattern anode. The other end of the inner alumina tube is connected to a metal steel tee using a ceramic seal. A three way valve, which is used to switch between high H_2O content fuel (>3%), 3% humidified fuel and dry fuel, is connected to the bottom of the metal steel tee.

Ceramic paste is used to seal the cell, while silver wire and silver mesh were used as current collectors. One end of the silver wire is made into round cycles and then covered with a layer of silver mesh. The cathode (facing up) contacts a silver current collector. The alumina tube on the top of the cathode side acts as a light weight to ensure good contact between the current collector and the cathode.

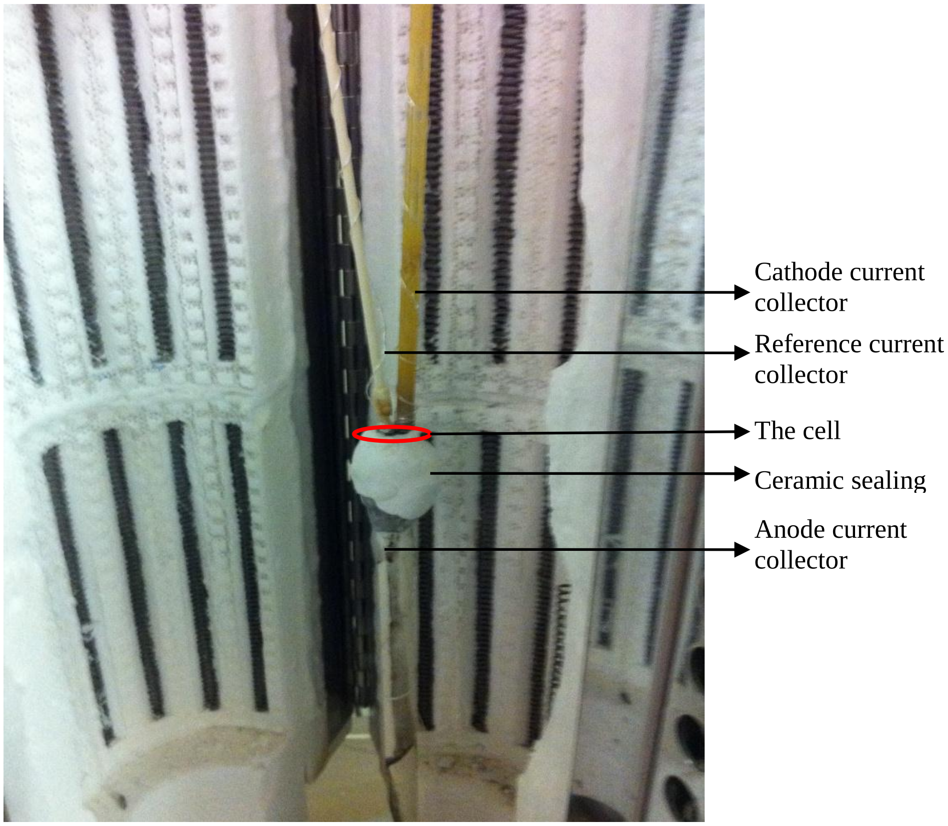

Figure 3-2 Photograph of the SOFC with Ni/YSZ pattern anode set up. The anode side faces down and is sealed with ceramic paste, while the cathode and reference electrode face up. Silver wire and silver mesh are used for current collectors.

3.1.3 Gas Conditioning and Controlling System

Fuel gases used in this study are H_2, N_2, CO and CO_2. The composition of these gases can be adjusted by varying the flow rate of each gas species using individual mass flow controllers (Omega, Co, Ltd). Labview-field point program is used in this test system to communicate between the PC and mass controller. The mass controller accepts commands from the labview program. The labview control panel also monitors the actual gas output.

In this setup, fuels with any desired water content can be achieved through a water bubbler system (3% H_2O) or a Controlled Evaporation and Mixing system (CEM, Bronkhorst). The CEM system includes a liquid flow controller and a temperature controlled mixing and evaporation device. The flow controller is used to control the liquid flow rate in order to achieve the desired water content. The water is combined with the gaseous fuel in the CEM, and then evaporated.

Equation 3.1 is used to determine the liquid flow rate (m_w) of H_2O in g/h to a achieve a desired water content.

$$m_w = \frac{18*60}{22400} * \left(\frac{\%H_2O}{1-\%H_2O}\right) * \sum v_i \qquad 3.1$$

In this expression, $\%H_2O$ is the mole percentage of H_2O in gas stream, and v_i is the volumetric flow rate of gaseous species i (ml/min).

3.1.4 Furnace

A vertical tube furnace (Carbolite, VST 12/400) which can reach a maximum of 1200°C was used to control the temperature for the cell. The alumina tube which holds the pattern anode cell was placed inside the furnace. A heat-up program was used to completely seal the cell and heat the cell to the desired temperature. Due to the requirement of the ceramic seal, the temperature was raised to 98°C and hold for 2 hours before increasing the temperature to 260°C and holding for another 2 hours. The temperature was then increased at a rate of 1°C/min during the whole process. A N_2 environment was maintained in the furnace throughout this process.

3.1.5 Electrochemical Test Equipment

The cell performance in this study was measured by Tafel plots and electrochemical impedance spectroscopy (EIS). Tafel plots were measured using a Solartron Electrochemical Interface 1287 in the potentiostatic mode. EIS of the working electrode was recorded using a Solartron Frequency Response Analyzer 1260 coupled with a Solartron 1287. During the measurement, Solartron 1260 generates the input signal to the Solartron 1287. The impedance was calculated as the ratio between the imposed voltage and the corresponding current response. The frequency range used in the measurements was from 0.1 Hz to 10^5 Hz. The DC voltage was set at OCV, and an excitation voltage of 10 mV was used to ensure that the measurement was performed in the linear regime. A standard 3-electrode configuration was used to characterize the electrochemical behavior of Ni/YSZ pattern anodes (see Figure

3-3). Zplot and Corrware softwares were used to monitor and control the experiment, whereas Zview and Corrview were used to analyze the data. The impedance data were analyzed using Nyquist and Bode plots.

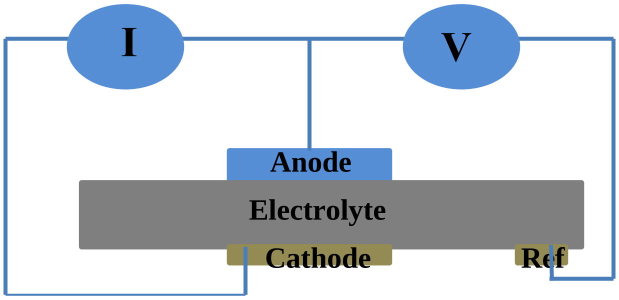

Figure 3-3 Electrochemical measurement configuration

3.2 Characterization Techniques for Ni/YSZ Pattern Anodes

Scanning electron microscopy (SEM) was used to obtain information concerning the sample surface morphology and composition. SEM generates images through a focused beam of electrons scanning the surface of a sample and detecting secondary electrons (SE) and back-scattered electrons (BSE) that are generated. Secondary electron signal is caused by the interactions of electron beam with the atom at or near the sample surface, whereas the back-scattered electron signal is generated by the interaction of the electron beam with the nucleus of an atom in the sample. With back-scattered detector, elements with higher atomic number are brighter than the elements with lower atomic number. A LEO 1530 SEM and energy-dispersive X-ray spectroscopy (EDX) were used in this study to characterize the Ni/YSZ pattern anode microstructure and composition. An accelerating voltage of 10 kV was chosen for the secondary mode. Due to the low conductivity of the Ni/YSZ pattern anode, a thin gold film was deposited on the sample surface before loading the sample for SEM to reduce electronic charging effects.

Optical microscopy employs visible light to observe a magnified image of the sample. The visible light is transmitted through or reflected from the sample. The magnified image can be detected directly by eyes. In this study, an optical microscope equipped with a high-resolution digital camera was used to generate images from the samples. The image can be shown in a computer screen.

The thickness of the Ni pattern was measured by a Sloan (Veeco) Dektak-I Profilometer System, which is a contact profilometer system equipped with PC interface. This profilometer measures step heights on a surface by a very low force stylus scanning the surface. An instaCal data capture interface card and TracerDAQ data capture interface software were used to capture the sample surface profile.

3.3 Ni/YSZ Pattern Anode Fabrication

This section describes the advantage of pattern anodes in studying electrochemical reactions occurring on SOFC anodes. Various methods for metal micro-fabrication are also given. Photolithography and metal deposition techniques are introduced in detail. The choice of fabrication methods and optimization of Ni/YSZ pattern anode fabrication conditions are presented. It was concluded that Ni/YSZ pattern anodes could be fabricated using bi-layer resist lift-off method combining by DC magnetron sputtering for Ni deposition.

3.3.1 Introduction

Ni/YSZ currently represents the state-of-art anode material for SOFCs, and Ni/YSZ pattern anodes have been widely used in fuel electrochemical reaction mechanism studies (Bieberle & Gauckler, 2000; Bieberle et al., 2001; de Boer, 1998; Ehn et al., 2010; Mizusaki et al., 1994; Sukeshini et al., 2006; Utz et al., 2010; Utz et al., 2011a;Vogler et al., 2009).

Ni/YSZ pattern anodes are ideally suited to study H_2 and CO electrochemical oxidation mechanisms because they have the advantage of forming a well-defined 2-D structure without the complicated 3-D structure effects on the electrochemical reactions that take place in cermet anodes. Moreover, the influence of gas transport in porous media is eliminated for the pattern anodes, and the TPB length of pattern anodes can be calculated accurately in principle (Bieberle et al., 2001; Utz et al., 2010).

Ni/YSZ pattern anodes with a well-defined structure require that the translation of the pattern from the mask to the substrate is accurate. Besides, the corner and edge of the pattern should be precise and clear, so that the TPB length can be accurately determined. Furthermore, precise control of the photolithographic process becomes the critical step in the fabrication of pattern anodes.

Two traditional methods exist to fabricate Ni/YSZ pattern anodes: 1) chemical etching and 2) lift-off. Both methods include photolithography and Ni thin film deposition.

Chemical etching is commonly used to make micro-patterns on a substrate. In this process, a metal thin film is first deposited on the substrate surface then the photoresist is applied and patterned. After immersing the patterned substrate in the etchant, the portions of metal film region not covered by the photoresist are etched away leaving behind the portions covered by photoresist (Adams et al., 2010). Details of this process are shown in Figure 3-4(a).

Lift-off is an alternative approach to make micro-patterns. The photoresist is spun on a clean substrate and patterned followed by metal thin film deposition. The metal film with photoresist underneath is washed away by a remover, whereas the metal film directly deposited on the metal film to produce the desired thin film pattern (Adams et al., 2010). Figure 3-4(b) describes the lift-off process.

Photolithography

Photolithography is a process which transfers patterns defined on a mask to a substrate. The patterns on the mask are first transferred to a photoresist, which undergoes chemical structure changes under exposure to a radiation source. Two types of photoresist (positive and negative photoresists) can be used for this process (Koep, 2006; Cherry, 2007).

Exposure of a positive photoresist to ultraviolet light (UV) shone through a mask with the desired patterns changes the chemical structure of the exposed photoresist region. The exposed patterns become soluble in the developer solution and can be easily stripped to leave behind the unexposed region. Unlike the positive photoresist, the exposed region of the negative photoresist through the mask becomes polymerized and insoluble in the developer solution, thus remaining on the substrate. Meanwhile, the unexposed region is removed by the developer solution (Adams, 2010).

Metal Deposition

Physical vapor deposition (PVD) is a physical process transferring atoms or molecules from source material to the substrate surface and is extensively used for thin film deposition. PVD has the advantage of depositing high quality thin films. Electron-beam evaporation (namely

E-beam evaporation) and DC magnetron sputtering are two typical PVD processes (Beckel et al., 2007; Geng, 2005; Mattox, 2010). These two methods have been commonly used to fabricate patterned electrodes in previous studies (Bieberle & Gauckler, 2000; Bieberle et al., 2001; de Boer, 1998; Ehn et al., 2010; Koep, 2006; Sukeshini et al., 2006; Utz et al., 2010; Utz et al., 2011).

In the E-beam evaporation process, the source material is heated to the boiling and evaporating point by a focused electron beam. The evaporated molecules move freely in the chamber due to the high vacuum (~10^{-6} mbar), and precipitate on all solid surfaces. In addition, high chamber vacuum minimizes existence of background gas, and increases the mean free path of metal particles. Hence, the metal film has less chance to be contaminated and sidewalls are not likely to be coated with the metal film (Cherry, 2007).

During DC magnetron sputtering, a target with the source material and an arrangement of permanent magnets are employed. The magnets generate a magnetic field to capture and focus electrons. The collision between electrons and inert sputtering gas atoms (argon) creates argon ions. By applying a negative voltage to the target, argon ions are accelerated toward the target and eject atoms from the target material (Geng, 2005; Mattox, 2010; Cherry, 2007).

Compared to evaporation process, DC sputtering has the advantage of depositing uniform thickness film on the substrate. Besides, the metal film grain size and stress between the film and substrate can be well controlled. Furthermore, the sputtering process allows for better adhesion between the deposited film and the substrate (Koep, 2006; Cherry, 2007).

Related work

Although several groups fabricated Ni/YSZ pattern anodes for kinetic studies, none of them clearly mentioned fabrication details. Besides, the fabrication technique is extremely sensitive and requires very fine tuning of several fabrication parameters. Also, some parameters are difficult to control but must be taken into account, such as the prebake temperature of the resist on a hotplate and consistent shaking during the development process.

Chemical etching has been used in several studies to fabricate Ni/YSZ pattern anodes (Bieberle & Gauckler, 2000; Bieberle et al., 2001; de Boer, 1998; Ehn et al., 2010; Mizusaki et al., 1994; Sukeshini et al., 2006). Although chemical etching is easy to perform, it is hard to control so that over-etching is prone to occur. It is extremely difficult to produce anodes with smooth patterns by this method, which further reduces the accuracy of TPB length calculation (see Figure 3-5(a)). Lift-off can also be used for pattern anodes fabrication, and the pattern edge obtained with this method is straight. However, the evaporation technique used in this process limits the thickness of Ni film deposited on the substrate (See Figure 3-5(b)). Furthermore, adhesion between Ni and YSZ is weak.

Stormer’s group at Karlsruhe University demonstrated a method for pattern anode fabrication with better defined TPB length (Utz et al., 2010). This method involves using a bi-layer resist system (sacrificial and imaging resists) for photolithography. The sacrificial resist is not photoactive, but can create an undercut, which is critical for effective lift-off after Ni deposition by DC sputtering. The undercut ensures that a discontinuity exists between the side-wall films and horizontal films after sputtering, so that the resist structure and unwanted Ni films can be removed cleanly by lift-off (Koep, 2006; Utz et al., 2010). The process of photolithography with bi-layer resist system is shown in Figure 3-4(c).

Kim et al. (2010) applied a very different method than that described above to fabricate nanopore-patterned Pt array (circular openings array) cathodes for investigation of geometric effects at TPBs. The patterned Pt array cathodes were prepared in the following way. Firstly, a mask suspension with a desired size of monosized spherical silica particles was prepared. The monosized spherical silica particles were then transferred onto YSZ surface with a Langmuir–Blodgett trough technique to form a close-packed monolayer of spherical particles on YSZ surface. Pt with thickness of 60 nm was then deposited on the YSZ surface through the interspacing between the particles. Last, the silica particles were stripped off the YSZ substrate using ultrasonication. The patterned Pt cathode fabricated in this way was reported to yield a stable performance and an almost unchanged microstructure after electrochemical testing for 12 hrs at 450°C and 500°C.

In the current study, a similar method as the one used by Utz et al. (2010) was employed, but different resists were chosen. It turned out that the bi-layer resist system is very effective for Ni/YSZ pattern anode fabrication when proper imaging and sacrificial resists are used.

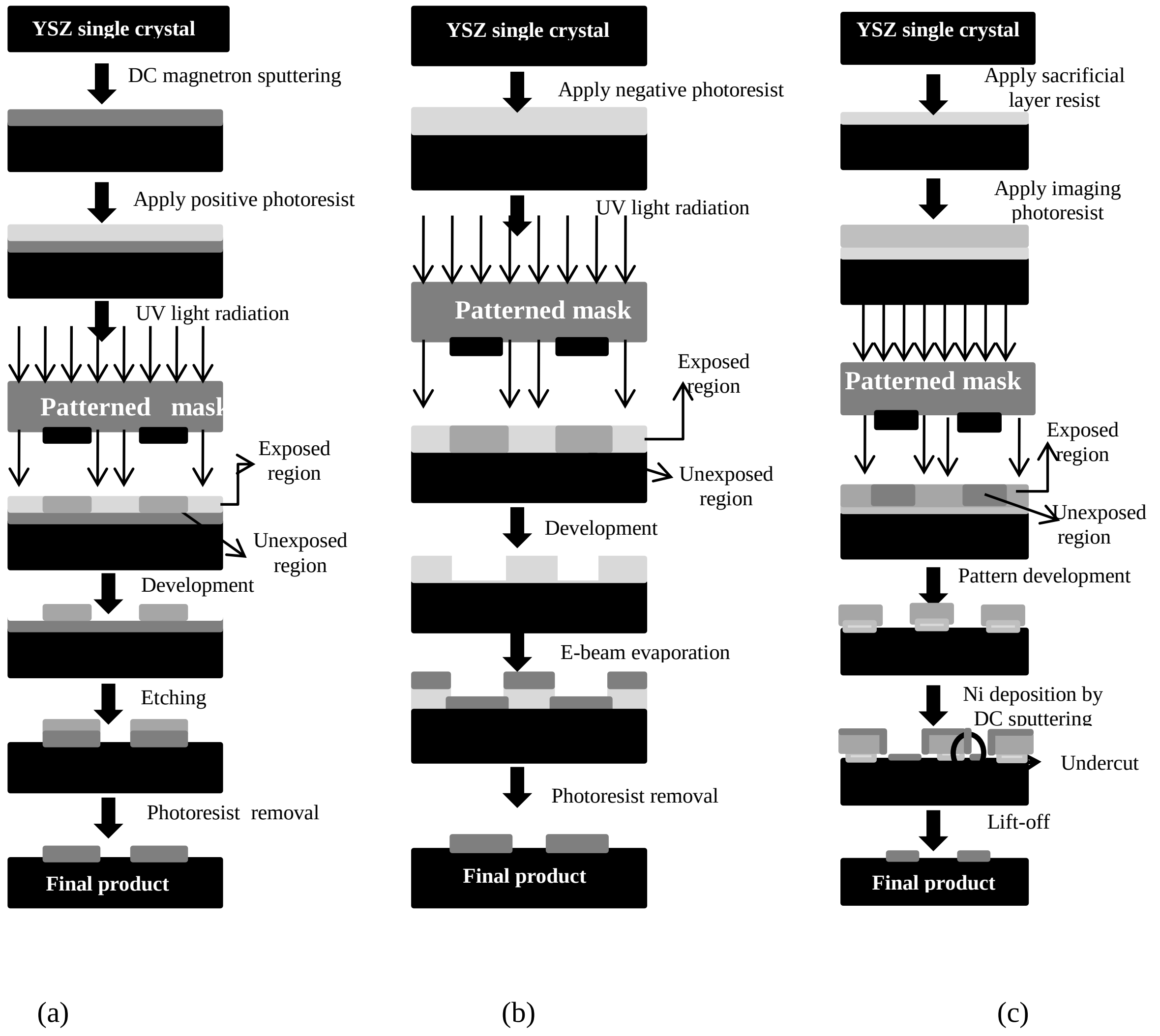

Figure 3-4 Thin film fabrication processes: (a) chemical etching, (b) lift-off, (c) bi-layer lift-off.

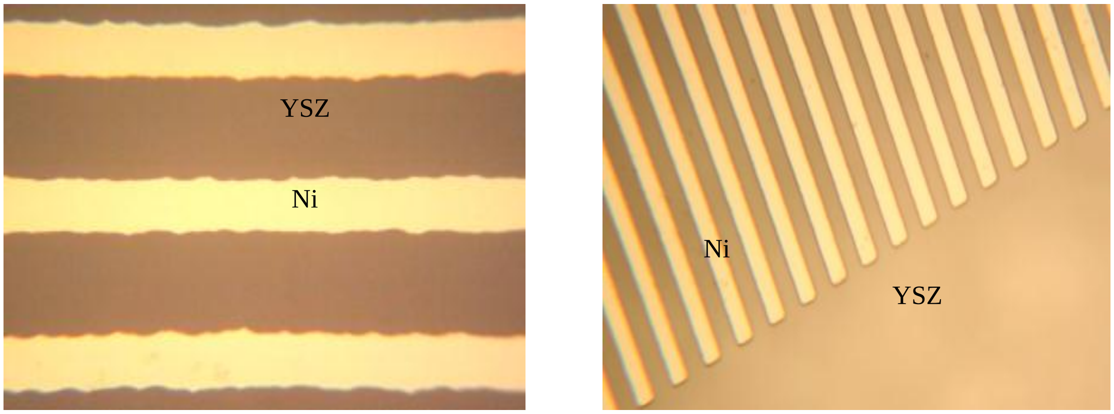

Figure 3-5 (a) Ni patterns fabricated by chemical etching; 1 µm thick Ni deposited by DC sputtering, (b) Ni patterns fabricated by lift-off; 0.1 µm thick Ni prepared by e-beam evaporation.

3.3.2 Experimental

The electrolyte used in this study is an 8 mol% Y_2O_3-stabilized ZrO_2 single crystal disc with (100) orientation (MTI corporation). It is a 0.5" × 0.5" square disc with both sides polished to the same roughness (< 5 Å by AFM). An YSZ single crystal was chosen to ensure successful photolithographic process. Positive masks fabricated by a commercial company (Fineline Imaging Laser Imaged Phototooling) were used in this study. These masks are patterned chromium on soda lime glasses. The design of the Ni/YSZ pattern anode is given in Figure 3-6.

The photolithographic process, and in particular the choice of resist, plays an important role for successful micro-pattern fabrication. In this study, various fabrication conditions were optimized, such as selection of photoresists, exposure time, spin speeds for both sacrificial and imaging resists, soft-bake temperature and development time. A polydimethyl glutarimide (PGMI) S11 (MicroChem) resist was used as the sacrificial layer. Negative photoresist nLOF2035 (AZ Electronic Materials) or ma-N-1420 (Micro Resist Technology) was used as the imaging layer.

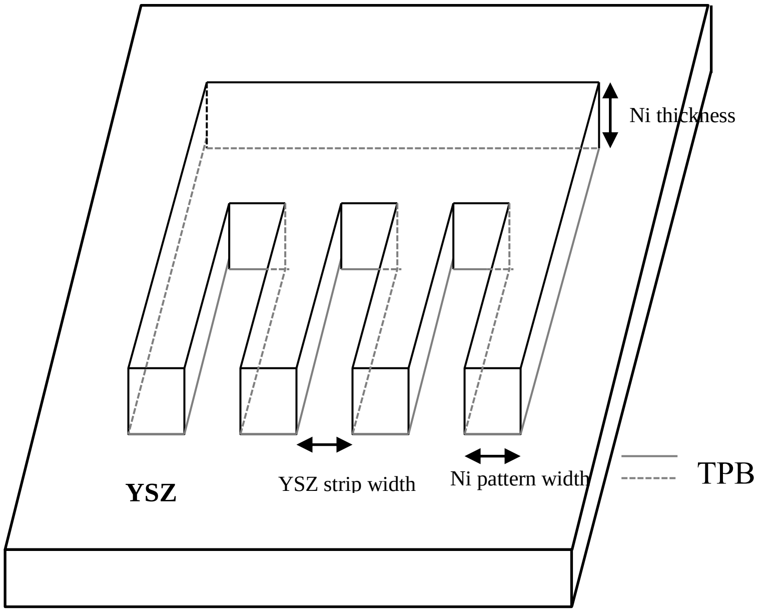

Figure 3-6 Schematic geometry of the SOFC with Ni/YSZ pattern anode

Before performing photolithography, YSZ substrates were cleaned by acetone, isopropyl alcohol (IPA), deionized (DI) water and RCA solution (H_2O: NH_3OH: H_2O_2=5:1:1) in this order. Then, the YSZ substrates were dried up on a hotplate for 10 minutes at 160°C. Sacrificial resist PGMI S11 was spun on the clean YSZ surface at 4500 rpm for 45s. Then the substrate was placed on a vacuum hotplate to soft-bake at 160°C for 5 minutes. After, the substrate was cooled down to room temperature, and the imaging photoresist nLOF2035 was applied by spin-coating at 3000 rpm for 30s and soft-baked at 110°C for one minute. Once cooled down, the substrate was placed in a mask aligner (Oriel Corp). Meanwhile, the mask was loaded on the mask holder. Both positions of the mask and the YSZ substrate were adjusted to make perfect contact and enabled transfer of the patterns on the mask to the YSZ.

An Ultraviolet Illumination System (Oriel Corp.) was used to expose the photoresist to UV radiation for 14 s. A post-exposure bake was conducted at 110°C for 1 minute prior to exposure to the developer. The photoresist pattern development was performed in an AZ300 MIF (metal ion-free) developer solution (AZ Electronic Materials) at room temperature. The development time was optimized in order to create a suitable undercut to facilitate the lift-off process. The substrate with photoresist patterns was deposited with nickel by DC magnetron sputtering. The size of Ni target in this study was 6" dia. × 0.125with a purity of 99.99%. The operating conditions listed in Table 3-1 were chosen to deposit the Ni film.

Table 3-1 DC magnetron sputtering parameters for Ni film deposition

Parameters	Value (unit)
Sputtering gas flow rate	50 sccm
Basis pressure in the chamber	6.7×10^{-6} mbar
Pressure during sputtering	5.1×10^{-3} mbar
Power provided at the target	400 W
Sputtering rate	1 μm h^{-1}

The last step was the lift-off step, which was processed in an AZ-Kwik Strip Remover (AZ Electronic Materials). In this process, the Ni patterns with photoresist underneath were washed away, while the Ni patterns without photoresist underneath remained. Thus, the Ni patterns obtained were the same as that in the mask.

Platinum (Pt) cathodes and Pt reference electrodes with thickness of 100 nm were deposited by DC magnetron sputtering. The Pt cathode (not patterned) was placed symmetrically to the pattern anode on the opposite side of the YSZ single crystal. Configurations of the Ni/YSZ pattern anode, Pt cathode and Pt reference electrode are shown in Figure 3-7.

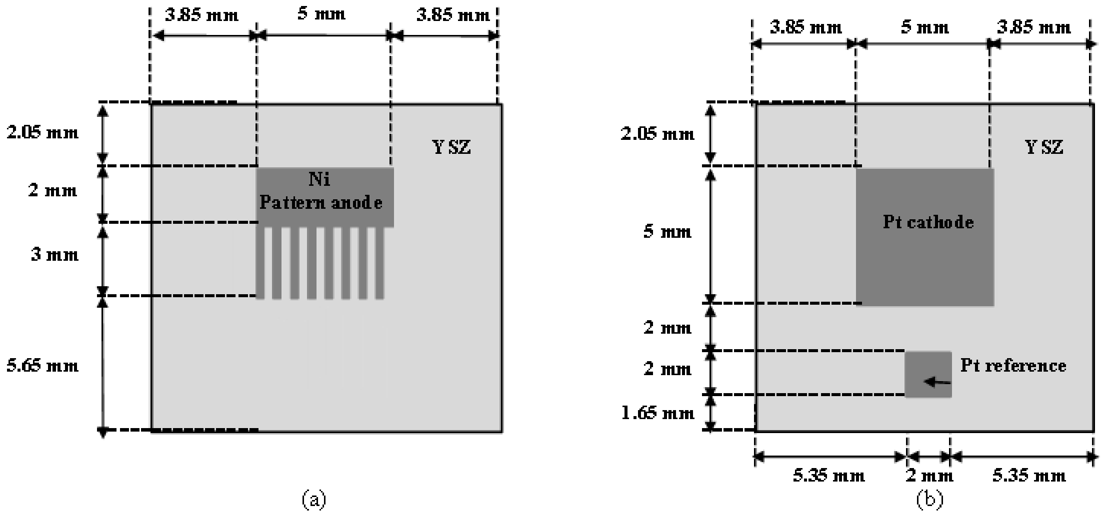

Figure 3-7 Schematic top view design of Ni/YSZ pattern anode, Pt cathode and Pt reference electrode. Ni and YSZ strips have the same width.

3.3.3 Results and Discussion

The spin and soft-bake conditions for PGMI SF11 were the same when any of the two imaging photoresists were used as the top layer. For both ma-N-1420 and nLOF2035, the spin speed and soft-bake conditions used were those recommended by the manufacture, although some optimization of the recommended conditions was also performed. The exposure time and development time were also optimized. It was found that the development time was the most critical parameter for successful fabrication of Ni patterns. If the soft-bake temperature is fixed, the development time directly affects the size of undercut, which should not be too small or too big. If the undercut is too small, the side wall of Ni film will connect with the horizontal film after sputtering and make the lift-off impossible. If the undercut is too big, the resist pattern structure will be destroyed. Although it is very important to choose a suitable size of undercut, the undercut size is very hard to measure. Besides, the undercut size changes from batch to batch. A significant number of experiments revealed that development time of 1 to 2 minutes recommended by the manufacture is not enough for a suitable undercut formation. Instead, a development time of about 8 minutes was best. In one experiment, the development time was extended to 9 minutes, at which point the resist started to peel off, indicating that the undercut was too large. In the following experiments, the development time was controlled between 8 minutes and 8.5 minutes. It turned out that clear patterns were produced after lift-off using this method. Light microscope photographs of the nLOF2035 resist structure with different development times are shown in Figure 3-8(a) and Figure 3-8(b).

Figure 3-8(a) presents the resist patterns after developing for 8 minutes. The development time of 1.5 minutes for the resist patterns shown in Figure 3-8(b) follows the manufacture's recommendations. Figure 3-8(a) shows semi-circle wrinkles on the resist side, which is caused by the overdevelopment of the resist. The semi-circle wrinkles also indicate that large undercuts are formed. If the development time is not long enough, these semi-circle wrinkles will not appear, as shown in Figure 3-8(b). Thus the appearance of the wrinkles is a simple, fast and effective way to identify if the undercut size is adequate.

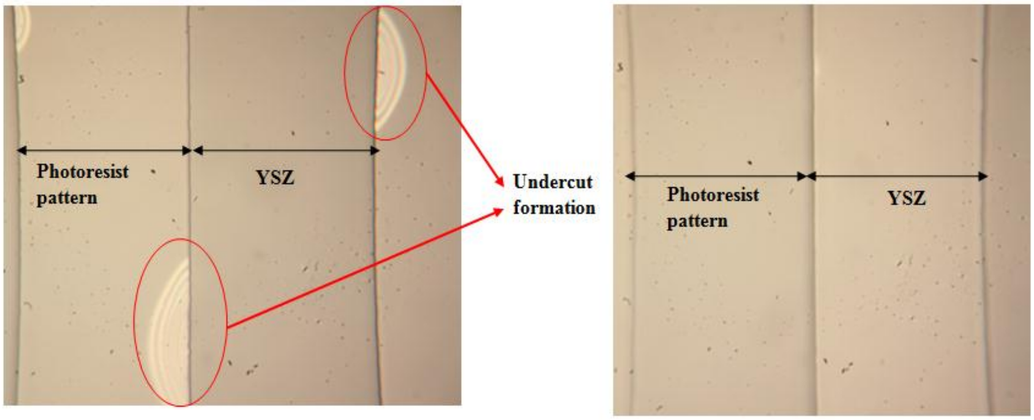

Figure 3-8 Patterns of photoresist after developing (a) long development time with large undercut formation, (b) short development time without sign of big undercut formation.

After making the resist patterns, Ni was deposited by DC magnetron sputtering. Figure 3-9 shows a top view of the pattern after Ni deposition and reveals a clean and smooth Ni film layer.

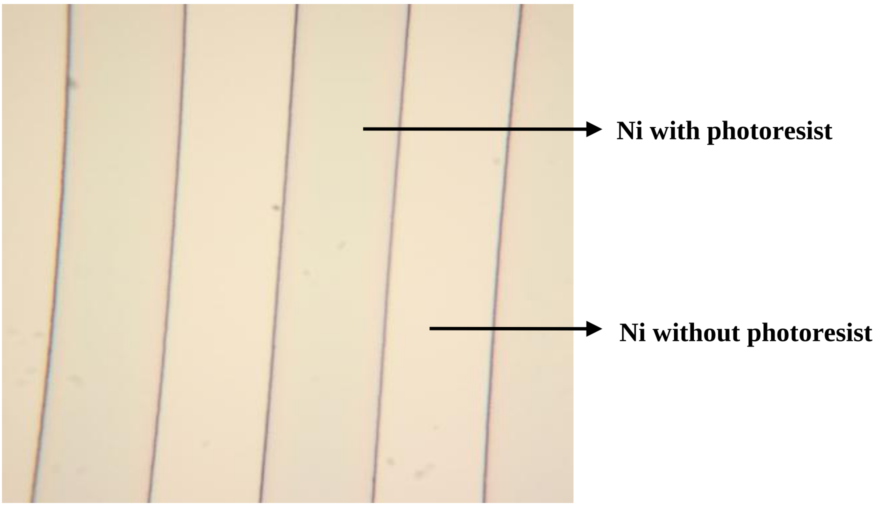

Figure 3-9 Patterns after Ni deposition by DC sputtering

The final product after removing the resists is presented in Figure 3-10.

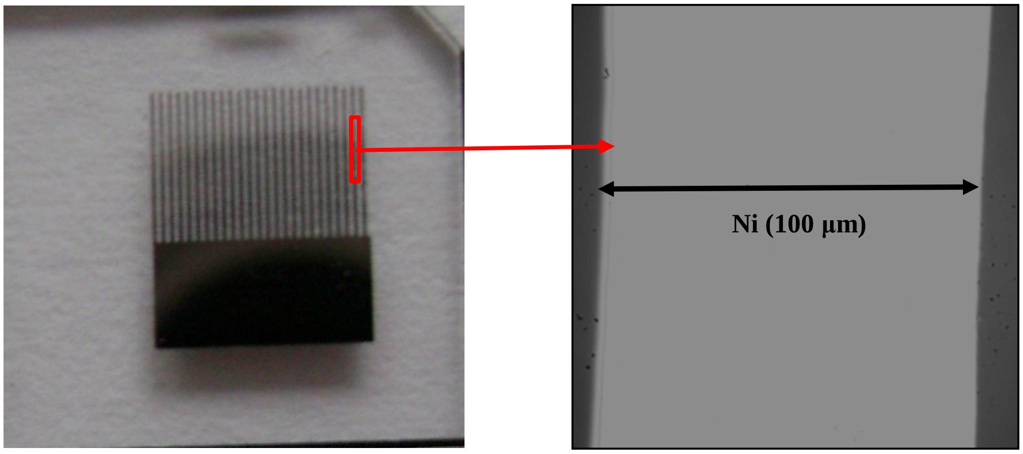

Figure 3-10 A Ni/YSZ pattern anode fabricated using bi-layer resist lift-off; Ni was deposited by DC sputtering with thickness of 1.0 µm

Three different types of Ni pattern anodes were prepared with Ni widths of 100 µm, 50 µm and 20 µm (see Figure 3-11). On the one hand, the Ni pattern edges for these three Ni/YSZ pattern anodes are smooth and precise. On the other hand, the pattern widths are not exactly the same as those of the mask. The Ni strip width and the YSZ strip width in the mask are the same, whereas the Ni strip width is wider than the YSZ strip width in the final product due to the overdevelopment of the resist. The difference between the Ni and YSZ strip width increases as the pattern width decreases from 100 μm to 20 μm. Thus, the actual Ni area is bigger and the TPB length per Ni area is shorter compared to the theoretical value. However, the real TPB length can still be easily and accurately determined.

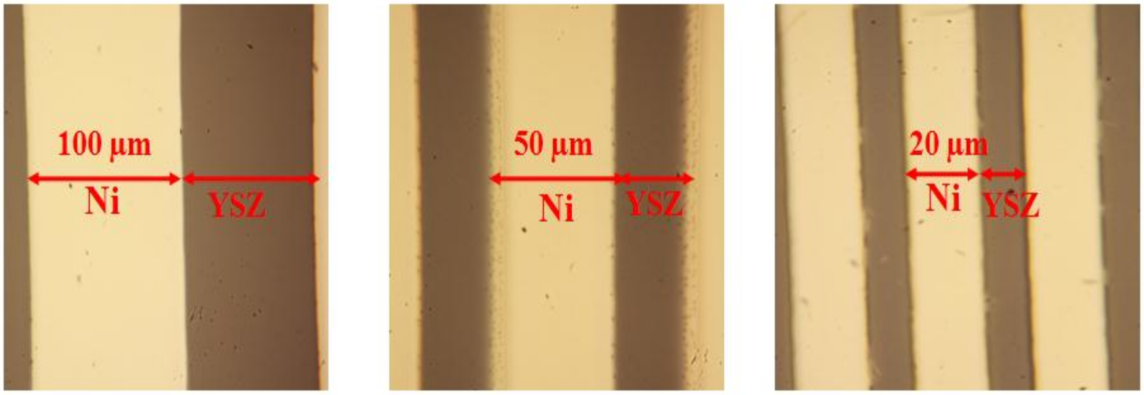

Figure 3-11 Ni patterns with different Ni strip width (a) 100 μm, (b) 50 μm, (c) 20 μm

Figure 3-12 shows an example of a Ni pattern thickness profile. The thickness of the Ni film for the Ni pattern shown in Figure 3-12 is 0.8 μm based on the Dektak measurement.

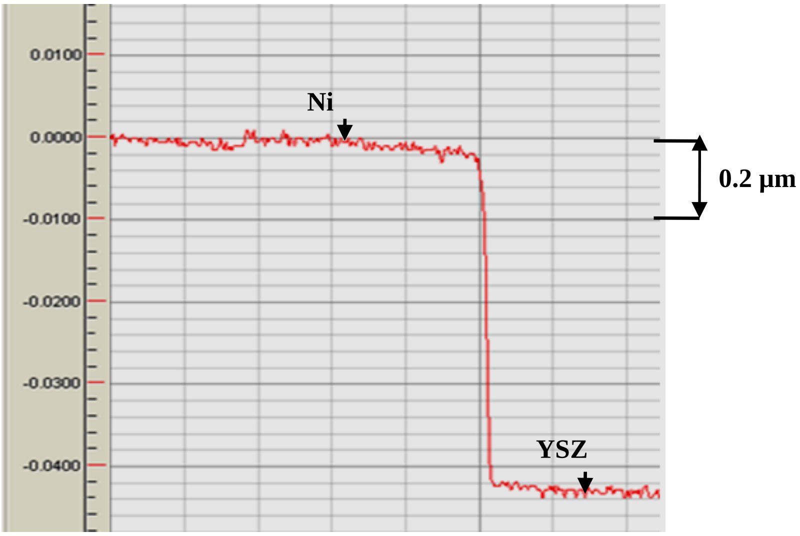

Figure 3-12 Ni pattern thickness profile

The photolithographic conditions for photoresist ma-N-1420 were also optimized in a similar manner as that was done for nLOF2035. However, Ni patterns could not be successfully made. In the lift-off step, , the unwanted Ni could not be nicely removed using the recommended organic solvent mixture remover PG was used. Although the large feature (2×2 mm) could be obtained, small Ni patterns peeled off from the YSZ. Thus, it was very hard to control the Ni pattern quality using ma-N-1420. Figure 3-13 represent the final Ni pattern anode product prepared using ma-N-1420 photoresist and PMGI SF11 resist. Therefore, nLOF2035 was chosen as the imaging resist in Ni pattern anodes fabrication.

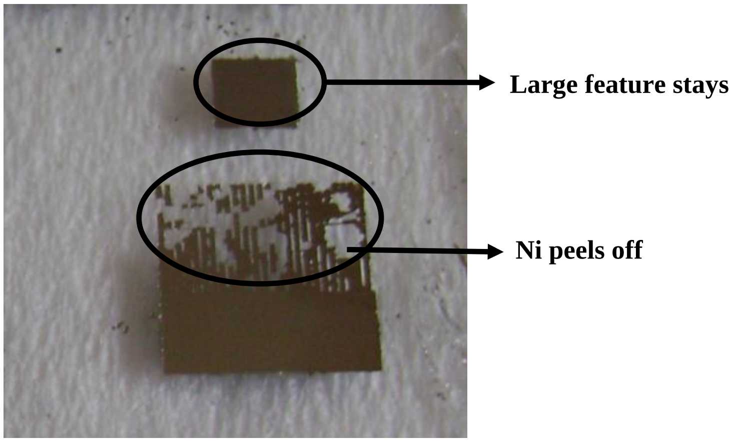

Figure 3-13 Ni/YSZ pattern anode prepared using imaging resist ma-N-1420 and sacrificial resist PGMI SF11

3.3.4 Conclusions

Photolithography process with a bi-layer resist system is an effective method to fabricate well-defined Ni/YSZ pattern anode fabrication. However, imaging and sacrificial resists must be carefully selected. In addition, various fabrication conditions must be optimized. In this study, imaging resist nLOF2035 and sacrificial resist PGMI SF11 were found to be effective in the bi-layer photolithographic process. A suitable size of the undercut was also observed to be a key factor for the successful fabrication of pattern anodes because undercut size directly affects the ease of removing unwanted Ni material. A simple method, involving taking microscopic photographs of the photoresist pattern was proposed to check if the undercut size is large enough for the lift-off; semi-circle wrinkles in the photograph indicates that the undercut is large enough for successful pattern anode fabrication. The final product prepared in this way showed precise and smooth Ni patterns.

Chapter 4

Ni/YSZ Pattern Anodes Microstructure and Electrochemical Behavior Changes in H_2-H_2O Environments

This chapter describes an experimental study of the stability of Ni/YSZ pattern anodes in H_2-H_2O environments. The electrochemical performance and microstructure changes of Ni/YSZ pattern anodes were evaluated as a function of temperature, pH_2, pH_2O, Ni pattern width and thickness.

4.1 Introduction

SOFC anode performance is affected by its microstructure. Different fabrication methods yield various anode microstructures (Bieberle, 2000). Several studies have been conducted to investigate the electrochemical behavior of H_2 by using Ni/YSZ pattern anodes (Mizusaki et al., 1994a; de Boer, 1998; Bieberle et al., 2001; Sukeshini et al., 2006; Ehn et al., 2010; Utz et al., 2010; Utz et al., 2011a). Most of these studies have shown that the polarization resistance (R_p) of the anode decreases when the hydrogen and water partial pressures, temperature and overpotential are increased. However, no consensus exists regarding the activation energy, charge transfer coefficient, hydrogen reaction order and water reaction order. Moreover, the qualitative value of polarization resistance is shown to be quite different from one research group to another.

Differences in some of the results may be attributed to the impurities, inaccurate estimation of the active TPB length and even the time over which data were collected (Ehn et al., 2010; Utz et al., 2010; Yao & Croiset, 2013a). Therefore, it is extremely important to better understand the microstructure changes and their effects on the electrochemical behavior of Ni/YSZ pattern anodes before evaluating detailed electrochemical processes. However, stability studies of pattern anodes were only conducted by Utz et al. (2011a) and Ehn et al. (2010) in previous studies. Utz et al. (2011a) focused on the effects of temperature, H_2O content and Ni thickness on Ni pattern anode stabilization. Ehn et al. (2010) mainly evaluated the effect of temperature (<700°C) on the stabilization of the pattern anodes. Moreover, the influence of H_2O on the pattern anode performance was evaluated in a very small range except in the study performed by Utz et al. (2010).

4.2 Experimental

Experiments on the effects of Ni thickness, temperature and H_2O concentration on Ni/YSZ pattern anode structure were performed by installing the pattern anode cell in the electrochemical test system described in Chapter 3. The EIS were performed using a Solartron Frequency Response Analyzer 1260 and a Solartron Electrochemical Interface 1287. The frequency range used in those measurements was from 0.1 Hz to 10^5 Hz. An excitation voltage of 10 mV was used to ensure that the measurement was performed in the linear regime. A standard three-electrode configuration was applied to characterize the electrochemical behavior of Ni/YSZ pattern anode. The Polarization resistance is obtained from the difference of the low frequency intercept and the high frequency intercept on the real-axial of the Nyquist plot. The microstructure of the Ni/YSZ pattern anode before and after the electrochemical tests was characterized by SEM.

4.3 Results and Discussion

4.3.1 Ni/YSZ Pattern Anode Microstructure Changes in H_2-H_2O Atmosphere

Pattern anodes with Ni thicknesses of 0.5µm, 0.8 µm and 1.0 µm were employed to evaluate their effect of Ni thickness on pattern microstructure after the electrochemical tests. Ni pattern microstructure changes with temperature and H_2O concentration were also investigated.

In Figure 4-1, SEM images of a group of Ni/YSZ pattern anodes with Ni thickness of 0.5 µm are presented. SEM micrographs of Ni patterns just after fabrication are shown in Figure 4-1(a). These images show that smooth and precise TPB are obtained after pattern anode fabrication. Besides, the Ni grain size is very small and distributed evenly. Figure 4-1(b) shows anodes after heat treatment at 550°C for 20 hrs in a N_2 environment. In this case, the TPB still remains straight. However, the Ni grain size increased compared to that of the metal before the heat treatment. In Figure 4-1(c), the Ni/YSZ pattern anode sample was exposed to N_2 and H_2 mixtures at 550°C for 20 hrs. The pattern on the top image of Figure 4-1(c) is very similar to that on the top image of Figure 4-1(b), indicating that the presence of dry H_2 has only a small effect on the TPB line. However, comparison of the bottom images of Figure 4-1(b) and 4-1(c) shows that the Ni particles began to aggregate after exposure of the patterned anode to dry H_2. The Ni/YSZ pattern anode shown in Figure 4-1(d) was treated in N_2 and humidified H_2 with 3% water at 700°C for 12 hrs. After the test, part of the Ni patterns delaminated from the YSZ and holes were also formed on the remaining Ni patterns, which showed a network structure. The high magnification SEM images revealed the aggregation of Ni particles.

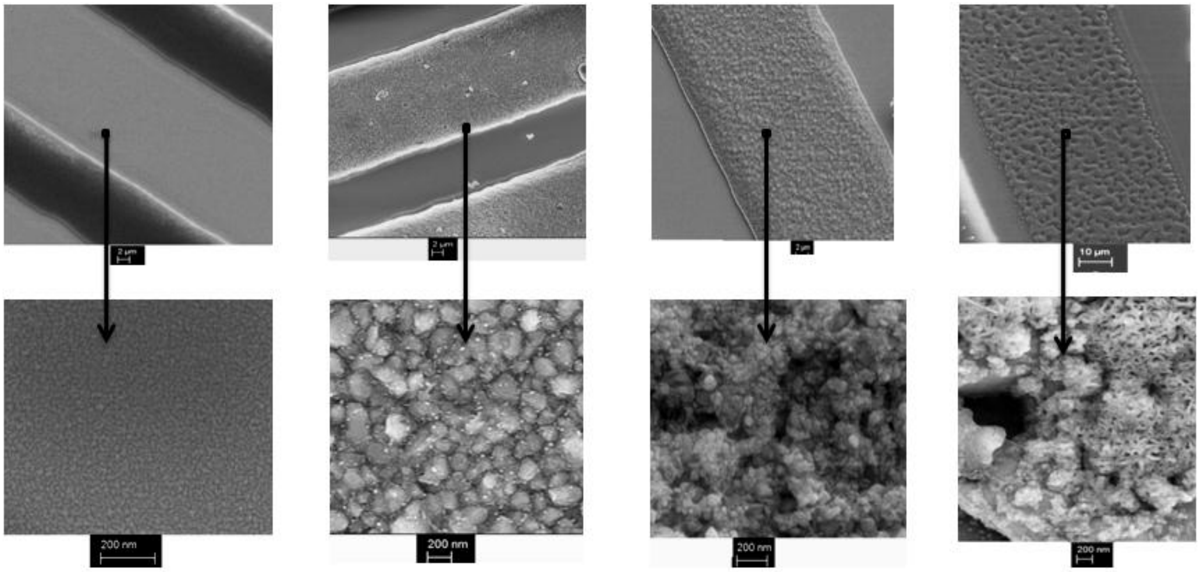

(a) (b) (c) (d)

Figure 4-1 Effects of temperature, H_2, and H_2O on 0.5 µm thick Ni patterns after (a) fabrication, (b) heat treatment in N_2 at 550°C for 20 hrs, (c) heat treatment in a N_2 and dry H_2 (20%) mixture for 20 hrs at 550°C, (d) heat treatment in a mixture of N_2 and humidified H_2 (20%) and 3% H_2O at 700°C for 12 hrs.

Another series of Ni/YSZ pattern anode samples with Ni thickness of 0.8 µm was evaluated in a similar way are shown in Figure 4-2. Figure 4-2(a) shows that heat treatment at 550°C in N_2 for 20 hrs on the sample did not affect the TPB line. When the sample was exposed to N_2/H_2 gas mixtures with H_2O content in the range 3-70% at 550°C for 20 hrs, the TPB line also did not change significantly, as seen in Figure 4-2(b). However, the Ni particles became much larger. In this process, the water content was first set at 3% and then increased to 10%, 30%, 50% and 70%. Each water condition was hold for one hour. After exposing the anode to 70% for one hour, the water content was decreased to 3% until the end of the experiment. In Figure 4-2(c), the cell was tested under the same conditions as the cell in Figure 4-2(b) except that the temperature was increased to 700°C. After the electrochemical test, none of the Ni patterns peeled off, but holes had formed in the Ni patterns and a network structure appeared. Therefore, the TPB length experienced important changes. In Figure 4-2(d), Ni/YSZ pattern anode sample with the same thickness (0.8 μm) was tested with humidified H_2 (3% H_2O) at 700°C, the TPB line did not show significant changes. Results from Figures 4-2(b) to 4-2(d) highlight the effect of high amount of water on the Ni pattern microstructure at higher temperatures (e.g. 700°C).

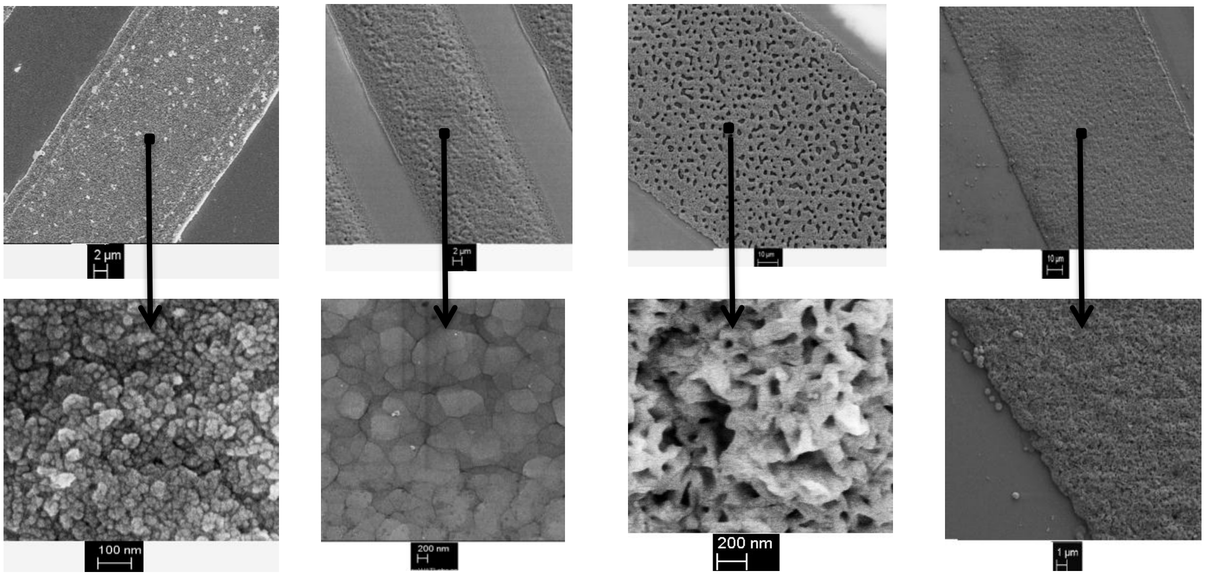

(a) (b) (c) (d)

Figure 4-2 Effects of temperature, H_2, and H_2O on 0.8 μm thick Ni patterns after exposure to (a) N_2 at 550°C for 20 h, (b) N_2 and H_2 mixture (20%) with 3-70% H_2O for at 550°C for 20 hrs, (c) Ni patterns after exposure to N_2 and H_2 (20%) with 3-70% H_2O at 700°C for 24 hrs, (d) the mixture of N_2 and H_2 (50%) with 3% H_2O at 700°C for 24 hrs.

In another experiment, the SOFC with 0.8 μm thick Ni pattern anode was exposed to H_2 fuel with 3% H_2O in the temperature range of 500-800°C. In this process, the temperature was increased in a linear manner with steps of 50°C. The EIS test lasted for half an hour at each temperature and then was performed at 800°C until the end of the test. After the EIS tests, most parts of the Ni pattern maintained a dense structure, but some holes appeared. Besides, the Ni pattern edges were not straight any more. The SEM image in Figure 4-3(a) describes the Ni pattern changes. More holes in the Ni pattern were observed when the H_2O content was increased to 10%, which is shown in Figure 4-3(b).

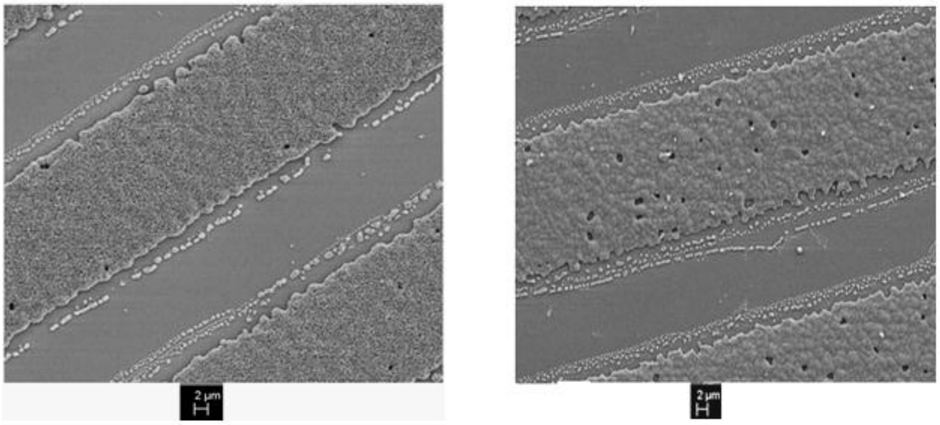

(a) (b)

Figure 4-3 SEM images of 0.8 μm thick Ni patterns after electrochemical tests in different conditions (a) gas composition: N_2, H_2 (50%), H_2O (3%); T: 500-800°C; test time: 46 hrs, (b) gas composition: N_2, H_2 (50%), H_2O (3-10%); T: 500-800°C; test time: 46 hrs.

Ni/YSZ pattern anodes with 1.0 μm thick Ni were also tested in H_2 environments with different H_2O contents. Figure 4-4 shows the Ni pattern after being tested in H_2 with 3% H_2O in the temperature range of 500-800°C. No holes were formed under this condition, but the Ni pattern edge was slightly modified leading to an increase in TPB length. This would not be as much of a problem since it is possible to calculate the new TPB length using imaging technique.

However, the presence of higher amount of H_2O (3-70%) at 700°C altered the Ni pattern microstructure as seen in Figure 4-5. Holes formed in the Ni pattern, and Ni was found to be in the oxidized state (confirmed by EDX). For such a microstructure, it is hard to accurately calculate the actual TPB length by imaging techniques.

Utz et al. (2011a) mentioned that when water contacts with a Ni surface, gaseous Ni species, especially $Ni(OH)_2$, can form readily. They also indicated that the amount of $Ni(OH)_2$

increases when increasing temperature and water concentration, which can lead to the disappearance of some Ni grain boundaries. This is also the reason for hole formation at elevated temperature when a high amount of water exists in the fuel (>20%).

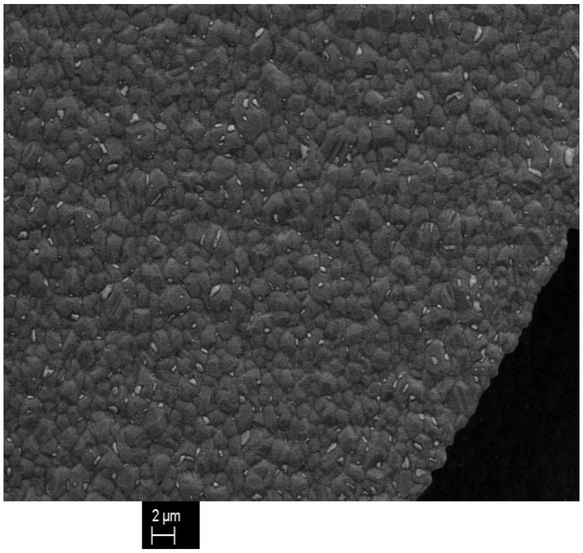

Figure 4-4 SEM images of the Ni pattern with 1.0 µm thickness after being tested in H_2 (50%) with 3% H_2O in the temperature range of 500-800°C

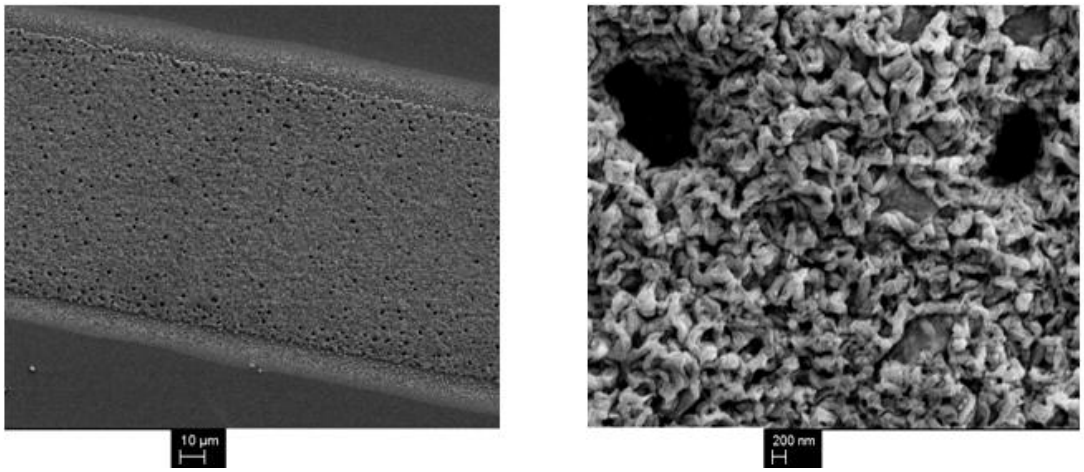

(a) (b)

Figure 4-5 Schematic view of microstructural changes in the Ni pattern after electrochemical test in H_2 (20%) with H_2O content in the range of 3-70% (a) low magnification, (b) high magnification.

In previous studies, Sukeshini et al. (2006) employed Ni/YSZ pattern anodes to investigate the electrochemical oxidation of H_2, CO and H_2/CO mixtures. The Ni thickness in their study was 0.1-0.15 µm, and all the patterns turned into island structure after electrochemical tests at 735-850°C in both dry H_2 and wet H_2 (4% H_2O) environments. Utz et al. (2011a) evaluated the microstructure changes of Ni/YSZ pattern anode under different conditions regarding temperatures and H_2 and H_2O partial pressures conditions. Partly interconnected islands formed on the thin Ni layers (0.15 µm and 0.2 µm), whereas holes formed on the thicker Ni layers (0.4 µm) after experiments in which the temperature varied from 550 to 800°C in a dry H_2 environment. They also claimed that patterns with 0.8 µm thick Ni maintained dense structure during the tests even in the presence of high amounts of water (>20%) at high temperature (800°C). Ehn et al. (2010) observed island formation in thin Ni layers (0.25 µm) exposed to H_2 with 3% H_2O after at temperatures from 350 to 500°C. Hole formation was observed in thicker Ni layers (0.25-0.5 µm) in humidified H_2 (3% H_2O) at temperatures from 400 to 700°C. They also mentioned that Ni patterns with thickness of 1.0 µm kept their original shape with their edge slightly modified when heated to 700°C in humidified H_2 (3% H_2O).

In our study, 0.5 µm thick Ni patterns showed stable structure in dry H_2 environments at 550°C or below. When the temperature was increased to 700°C, holes appeared on the Ni pattern. Ni pattern with Ni thickness of 0.8 µm remained as a dense structure when the cell was tested in both dry H_2 and humidified H_2 (3-70% H_2O) at 550°C. At both 700°C and 800°C, holes formed when the H_2O content was between 3% and 70%. Holes formation occurred in 1.0 µm thick Ni at 700°C for H_2O contents of 10% and above. Our observations regarding the stability of the patterned anode in the presence of water was thus different from those of Utz et al. (2011a) who suggested that the Ni microstructure remained stable during electrochemical tests at high H_2O content (>20%) in the temperature range of 700°C to 900°C when the Ni thickness was 0.8 µm or above.

4.3.2 Electrochemical Behavior of Ni/YSZ Pattern Anode in H_2-H_2O Atmosphere

The electrochemical behavior of the Ni/YSZ pattern anode with 1.0 µm thick Ni was characterized by EIS in H_2 environments with H_2O content from 3% to 70% in the temperature range of 550-800°C. Figure 4-6(a) gives EIS Nyquist plots of experimental and equivalent circuit fitting results for a fuel composed of 50% H_2 and 3% H_2O at 700°C. Figure 5.6(b) presents the equivalent circuit model used for the fitting. In this equilibrium circuit model, *Rs(R1CPE1)(R2CPE2)*, *Rs* represents pure ohmic resistance, *R1* and *R2* are resistances related to activation polarization, and *CPE1* and *CPE2* are constant phase elements. Two main semi-circles appear in the impedance Nyquist plot. The polarization resistance for the first and second semi-circles (*R1* and *R2*) are 112.5 $\Omega\cdot cm^2$and 21.3 $\Omega\cdot cm^2$, respectively.

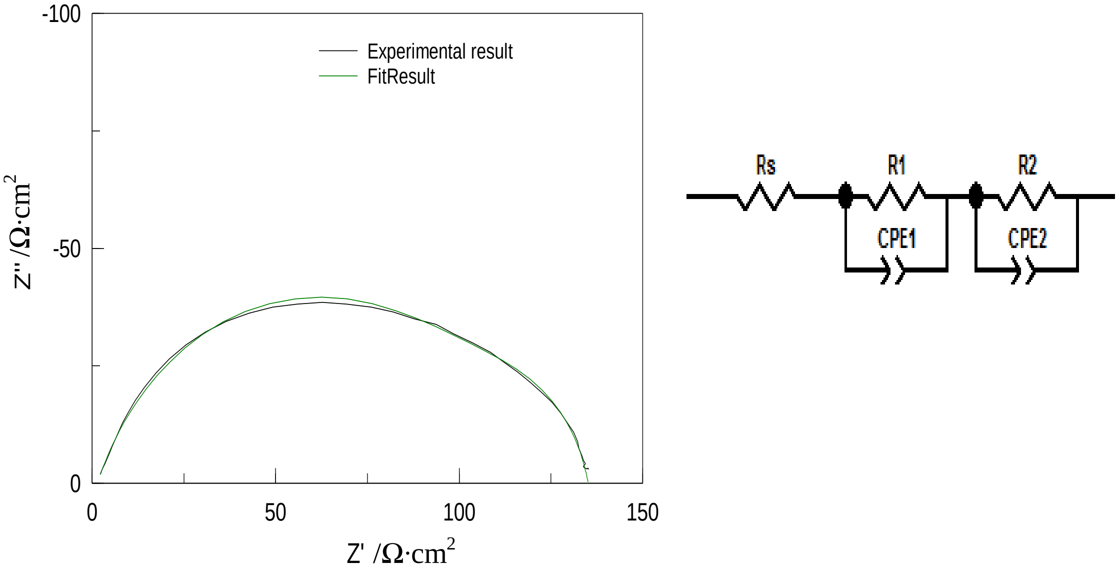

(a) (b)

Figure 4-6 (a) Experimental and fitted impedance plots when the test was performed in 50% H_2 with 3% H_2O at 700°C, (b) equilibrium circuit fitting model.

In previous studies, one main semi-circle was mentioned for impedance spectra in H_2 environments by Mizusaki et al. (1994a) and Bieberle et al. (2001). In de Boer's study (1998) three semi-circles were obtained through equivalent circuit fitting for H_2 electrochemical tests. In H_2 environment, Ehn et al. (2010) observed two main semi-circles in the impedance spectra whereas Sukeshini et al. (2006) observed one conductive circle and one resistive circle. In Utz et al.'s study (2010) electrochemical impedance test revealed three semi-circles, which were attributed to gas diffusion, charge transfer process in the pattern anode and a process caused by the counter electrode. Our pattern fabrication method is similar to that in the work of Utz et al. The fact they observed three semi-circles, whereas we observed two could be attributed to the two-electrode system they used vs. the three-electrode configuration in our study.

The effects of temperature and H_2O content on polarization resistance are investigated in Section 4.3.2.1 and 4.3.2.2, while section 4.3.2.3 is concerned with the stabilization of polarization resistance under constant conditions.

4.3.2.1 Effect of temperature on polarization resistance

In the following experiment, polarization resistance changes with time at different temperatures with 3% H_2O and 10% H_2O were monitored to yield the data shown in Figure 4-7(a) and Figure 4-7(b). Table 4-1 gives the initial polarization resistances as well as the degradation rates after each change in temperature. The cell was first tested in H_2 with 3% H_2O at 700°C for 7 hrs, when the polarization resistance increased at a rate of 5.3 $\Omega\cdot cm^2\cdot h^{-1}$ during this period. The temperature was then increased to 750°C for 2 hrs, during which the polarization resistance degradation rate reached 6.4 $\Omega\cdot cm^2\cdot h^{-1}$. When the temperature was lowered to 700°C again, the polarization resistance degradation rate (2.8 $\Omega\cdot cm^2\cdot h^{-1}$) was lower than that of the first seven hours. This means that the Ni pattern microstructure stabilizes faster at 750°C compared to 700°C.

The temperature was increased from 700°C to 800°C, after which the polarization resistance degradation rate was 5.0 $\Omega\cdot cm^2\cdot h^{-1}$ over a two hour period. The experiment continued by decreasing the temperature to 750°C, which yielded a polarization resistance degradation rate of 2.3 $\Omega\cdot cm^2\cdot h^{-1}$. The degradation rate of polarization resistance (2.3 $\Omega\cdot cm^2\cdot h^{-1}$) at 750°C is lower than the 6.4 $\Omega\cdot cm^2\cdot h^{-1}$ tested at 750°C before increasing the temperature to 800°C, which can be related to faster Ni microstructure stabilization at higher temperature.

When the temperature was lowered to 550°C, and then increased to 700°C, the polarization resistance was very similar to the value before the temperature was lowered. This indicates that when the temperature is below 700°C, temperature does not have any effect on the Ni pattern microstructure.

When the H_2O content was increased to 10%, the degradation rate of polarization resistance was 17.3 $\Omega\cdot cm^2\cdot h^{-1}$ at 700°C, which was higher than that with 3% H_2O (6.9 $\Omega\cdot cm^2\cdot h^{-1}$).

When the cell was heated to 750°C with 10% H_2O, a degradation rate of 11.9 $\Omega\cdot cm^2\cdot h^{-1}$ was obtained. The temperature was then lowered to 700°C, and the degradation rate became 6.2 $\Omega\cdot cm^2\cdot h^{-1}$. The polarization resistance degradation rate at 800°C was 3.9 $\Omega\cdot cm^2\cdot h^{-1}$, which later became 5.5 $\Omega\cdot cm^2\cdot h^{-1}$ when the temperature was lowered to 750°C. The polarization degradation rate at 750°C of 5.5 $\Omega\cdot cm^2\cdot h^{-1}$ is much lower than that obtained at the same temperature, but four hours before (11.9 $\Omega\cdot cm^2\cdot h^{-1}$). Again, this may due to the increase of TPB length. After that the temperature was changed back to 700°C, and the degradation rate became 20.6 $\Omega\cdot cm^2\cdot h^{-1}$. The increased degradation rate after a 40 hour test was due to delamination of Ni layer, which was observed after the electrochemical test. When the temperature was lowered to 650°C, the polarization resistance reached 615.7 $\Omega\cdot cm^2$, and the degradation rate became 64.4 $\Omega\cdot cm^2\cdot h^{-1}$. These values are much higher than the values in Figure 4-7(a) when the H_2O content is 3% at the same temperature. The polarization resistance increased to 2500 $\Omega\cdot cm^2$ with further reduction in the temperature to 600°C, and the corresponding degradation rate was 87.3 $\Omega\cdot cm^2\cdot h^{-1}$.

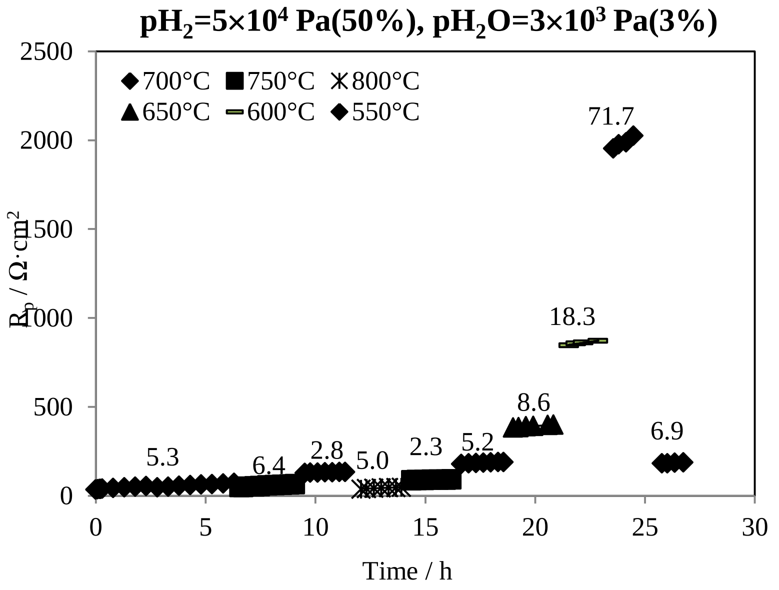

(a)

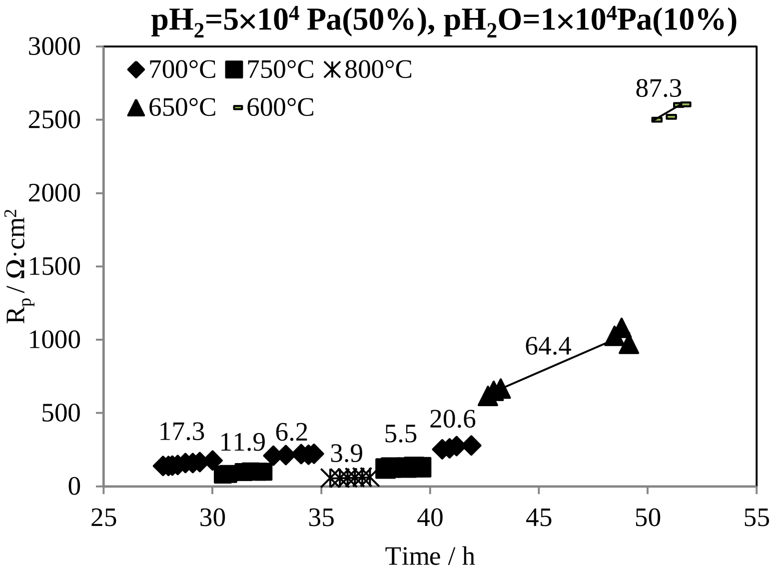

(b)

Figure 4-7 Polarization resistance changes of a 1.0 µm thick Ni/YSZ pattern anode with time at different temperatures in 50% H_2 containing (a) 3% H_2O, (b) 10% H_2O.

Table 4-1 Initial polarization resistances and degradation rates after each variation in temperature

	3% H_2O		10% H_2O	
Temperature (°C)	Initial R_p (Ω·cm^2)	Degradation rate (Ω·cm^2·h^{-1})	Initial R_p (Ω·cm^2)	Degradation rate (Ω·cm^2·h^{-1})
700	32.5	5.3	137.6	17.3
750	49.8	6.4	78.8	11.9
700	128.0	2.8	207.3	6.2
800	37.0	5.0	55.1	3.9
750	87.3	2.3	120.6	5.5
700	179.0	5.2	251.7	20.6
650	383.0	8.6	615.7	64.4
600	820.6	18.3	2500.0	87.3
550	1952.8	71.7	-	-
700	181.9	6.9	-	-

In previous studies, de Boer (1998), Mizusaki et al. (1994a) and Ehn et al. (2010) observed an initial increase in polarization resistance with time when the Ni/YSZ pattern anodes were tested in a H_2 environment. In our study, we observed the same trend. However, Utz et al. (2010) claimed that the polarization resistance decreased with time in the first 25 hrs followed by an increase in polarization resistance depending on gas compositions.

4.3.2.2 Effect of H_2O content on polarization resistance

In order to further evaluate the effects of H_2O on electrochemical performance of the Ni/YSZ pattern anode, another experiment was carried out to characterize the polarization resistance changes with time with H_2O content ranging from 3% to 70%. Results are shown in Figure 4-8 and Table 4-2. Similar to the experiment related to Figure 4-7, the cell was first tested in H_2 environment with 3% H_2O at 700°C for 2 hrs. The degradation rate was measured at 37.3 $\Omega \cdot cm^2 \cdot h^{-1}$ under these conditions. The H_2O content was increased to 10% and kept for 1 h followed by decreasing H_2O content back to 3%. The polarization resistance degradation rates were 45.7 $\Omega \cdot cm^2 \cdot h^{-1}$ at 10% H_2O and 13.9 $\Omega \cdot cm^2 \cdot h^{-1}$ at 3% H_2O. Subsequently, the H_2O content was elevated to 30% from 3%, and then decreased back to 3%. The polarization resistance rate changed from 40.9 $\Omega \cdot cm^2 \cdot h^{-1}$ at 30% H_2O to 21.9 $\Omega \cdot cm^2 \cdot h^{-1}$ at 3% H_2O. This value was still lower than the initial degradation rate (37.3 $\Omega \cdot cm^2 \cdot h^{-1}$). The cell was then exposed to 50% H_2O for 1 h with a degradation rate of 41 $\Omega \cdot cm^2 \cdot h^{-1}$. Then the H_2O concentration was decreased back to 3%, and the polarization resistance degradation rate became 83 $\Omega \cdot cm^2 \cdot h^{-1}$, which is much higher than the 37.3 $\Omega \cdot cm^2 \cdot h^{-1}$ observed previously. Thus, cell exposure to 50% H_2O at 700°C severely degraded the polarization resistance. The cell was then exposed to 70% H_2O for 1 h and then back to 3% H_2O, at which point the polarization resistance started to stabilize at ~500 $\Omega \cdot cm^2$. The polarization resistance degradation rate was 32.4 $\Omega \cdot cm^2 \cdot h^{-1}$ when the H_2O content was 70%. Another experiment at 700˚C with the H_2O content kept constant at 3% for 50 hrs showed that the polarization resistance increased linearly without reaching a plateau. This demonstrated that the presence of the higher amount of water helped in stabilizing the polarization resistance.

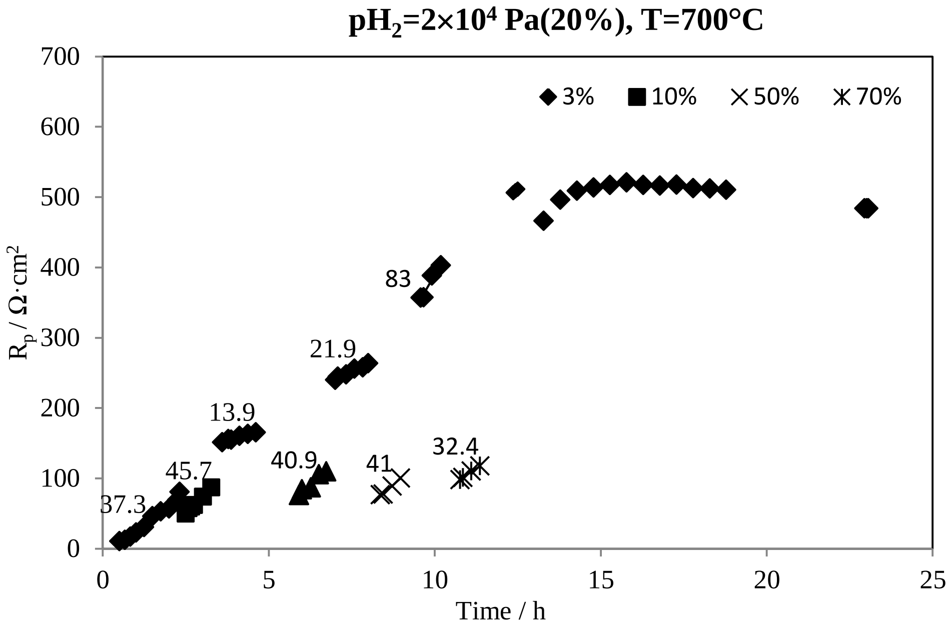

Figure 4-8 Polarization resistance changes with time in H_2 (20%) with H_2O content from 3% to 70% at 700°C.

Table 4-2 Initial polarization resistances and degradation rates after each variation in water content

H_2O content (%)	Initial R_p ($\Omega\cdot cm^2$)	Degradation rate ($\Omega\cdot cm^2\cdot h^{-1}$)
3	10.6	37.3
10	49.5	45.7
3	151.0	13.9
30	76.2	40.9
3	240.0	21.9
50	76.7	41.0
3	375.1	83.0
70	98.0	32.4
3	506.2	-

4.3.2.3 Stabilization of Ni /YSZ pattern anode performance

In this section, conditions for stabilization of Ni/YSZ pattern anodes are explored. Effects of temperature, partial pressure of H_2, Ni pattern width and thickness on the stabilization of Ni/YSZ pattern anodes were evaluated.

A sample with Ni pattern width of 100 μm and thickness of 1.0 μm was tested in H_2 (50%) with 3% H_2O (balance N_2) at 750°C. Variation of the polarization resistance with time is presented in Figure 4-9. Polarization resistance increases with time and then stabilizes at ~140 $\Omega\cdot cm^2$ after 22 hrs.

SEM image of the Ni pattern after electrochemical test in H_2/3% H_2O environments is given in Figure 4-10. The Ni pattern maintained a dense structure and the TPB line was slightly modified. The new TPB length can be calculated by imaging techniques.

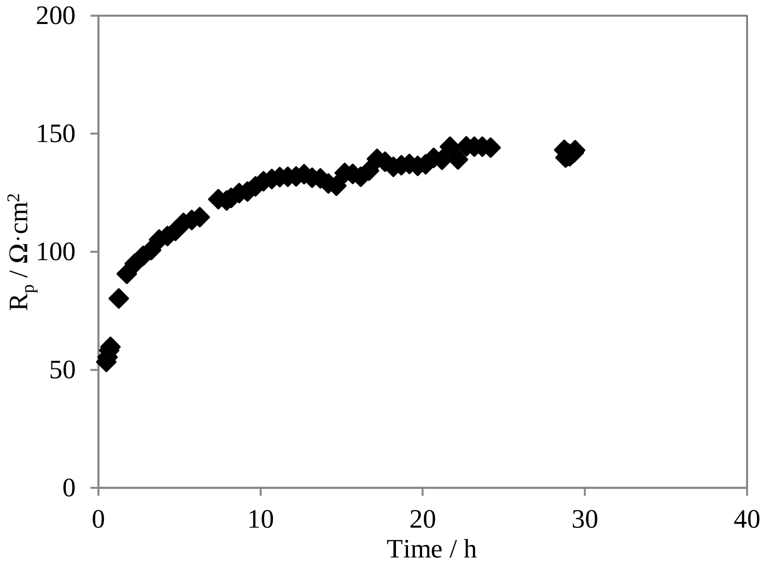

Figure 4-9 R_p changes with time in the following conditions: $pH_2=5\times10^4$ Pa (50%), $pH_2O=3\times10^4$ Pa (3%), T=750°C.

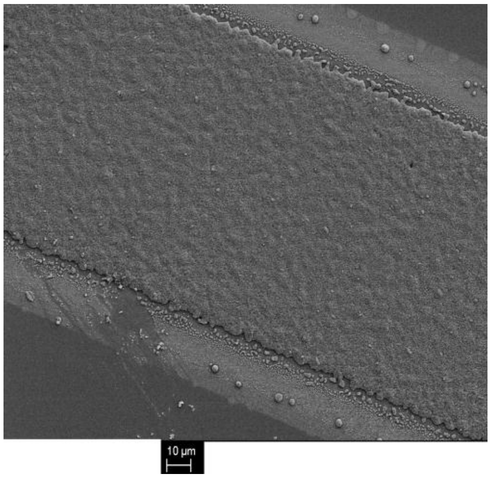

Figure 4-10 SEM image of the Ni pattern after electrochemical tests, it corresponds to the Ni/YSZ pattern anode sample used in Figure 4-9.

The cell used in Figure 4-11 had the same Ni pattern width and thickness as that in Figure 4-9. The difference is that it was pre-treated with 50% H_2 and 3% H_2O (balance with N_2) at 800°C. It took about 21 hrs before the polarization resistance stabilized, similar to that shown Figure 4-9, but the polarization stabilized at a lower value (~78 $\Omega\cdot cm^2$) because of exposure to the higher temperature.

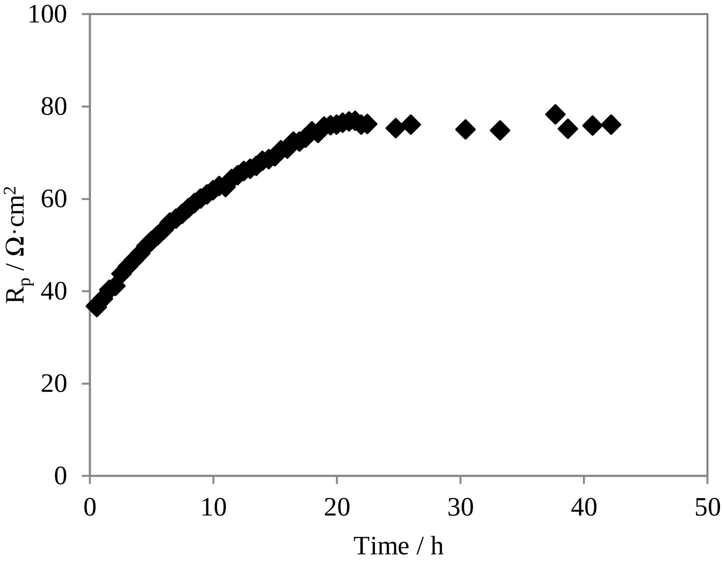

Figure 4-11 R_p changes with time in the following conditions: $pH_2=5\times10^4$ Pa (50%), $pH_2O=3\times10^4$ Pa (3%), T=800°C.

Ni/YSZ pattern anodes with Ni pattern width of 50 µm and 20 µm were also pre-treated under the same conditions as the sample shown in Figure 4-9. The Ni thickness of these two samples was 1.0 µm. The stabilization time of these two samples was between 20 hrs and 25 hrs. Another cell with Ni pattern width of 100 µm and Ni thickness of 0.8 µm was pre-treated in 50% H_2 with 3% H_2O at 700°C for about 17 hrs until the polarization resistance becomes stable.

The stabilization of Ni/YSZ pattern anode performance depends on the pre-treatment conditions of the sample, such as temperature. For the pattern anodes with 1.0 µm thickness, pre-treatment of the sample at 700°C did not lead to stabilization of the cell performance, at least not within the first 50 hours. Pre-treatment of the 1.0 µm thick sample at 750°C or 800°C resulted in the stabilization of the polarization resistance after testing the cell with 50% H_2 / 3% H_2O for about 20-25 hrs.

Heat treatment results in morphological changes of the Ni patterns due to growth and aggregation of Ni grains caused by thermal stress. The temperature affects grain growth and aggregation, and therefore it affects the time to stabilize anode performance. However, when the pre-treatment temperature is as high as 750°C, the Ni grain growth rate is sufficiently fast that further increase in the temperature only leads to a small further increase in the grain growth rate. Therefore, stabilization time for pattern anodes is similar at 750°C and 800°C.

The stabilization time of pattern anode performance is very similar between samples with different Ni pattern widths. Since those cells have the same Ni surface area (0.175 cm^2), this indicates that the Ni surface area, rather than the TPB length, affects the time needed to stabilize the cell. The partial pressure of H_2 did not affect the stabilization time. However, thinner Ni thickness required shorter stabilization time.

4.4 Conclusions

A comprehensive set of experiments was conducted with H_2/H_2O mixtures to evaluate the effects of Ni thickness (0.5-1µm), temperature (500-800°C), and H_2O concentrations (3%-70%) on Ni/YSZ pattern anode microstructure and electrochemical performance changes.

Ni/YSZ pattern anodes with Ni thickness of 0.5 µm led to significant changes in the TPB length above 550°C and are, therefore, not suitable for electrochemical tests. Only experiments with dry H_2 at 550°C led to stable patterns.

Ni/YSZ pattern anodes with Ni thickness of 0.8 µm do not experience significant changes in TPB line for all dry H_2 and humidified H_2 (3-70% H_2O) tests at 550°C. At 700°C, the TPB line does not change for tests carried out with dry and humidified (3%) H_2. More holes formed when the water content was increased to 10% or above. At 800°C, the TPB line experienced coarsening and some holes appeared in the Ni pattern when the cell was exposed to 3% H_2O.

Ni/YSZ pattern anodes with Ni thickness of 1.0 µm maintained its dense structure when the cell was tested in H_2 with 3% H_2O in the temperature range of 500-800°C, although the TPB line was slightly modified. Nonetheless, the new TPB length can be determined through imaging techniques. For Ni patterns with 1.0 µm thickness, the TPB length still experienced significant change when the test was conducted in H_2 with 3-70% H_2O at 700°C. The TPB length can be estimated through imaging techniques or modeling (treated as a free fit parameter).

Effects of temperature and H_2O content on Ni pattern anode performance were conducted. Moreover, stabilization of Ni pattern anode performance was studied under constant conditions. The time for pattern anode to reach stable performance is correlated to the temperature: the Ni pattern microstructure stabilized faster when the temperature was increased to 750°C or 800°C (where it took ~22 hrs) compared to 700°C (where it took more than 50 hrs). Similar stabilization times were observed when the cells were made with different Ni pattern width (20 µm and 50 µm), but with the same Ni thickness. The stabilization time was also not affected by pH_2. For a thinner Ni layer (0.8 µm), the pre-treatment time was shorter (~17 hrs at 700°C).

Chapter 5

Electrochemical Performance of Ni/YSZ Pattern Anodes in H_2-H_2O Environments

In this chapter, the electrochemical behavior of Ni/YSZ pattern anodes in H_2-H_2O environments is studied systematically. Anode performance upon variation of temperature, overpotential, partial pressure of H_2 and H_2O and triple phase boundary (L_{TPB}) was examined under stable conditions. In addition, the reaction orders for H_2 and H_2O and activation energy of the anode electrode process were calculated.

5.1 Introduction

Good understanding of the reaction mechanism for H_2 oxidation helps optimize SOFC anode design and improve its performance. Controversies still exist regarding this mechanism despite extensive studies performed. In previous studies, several groups experimentally investigated H_2 electrochemical reaction mechanisms using Ni/YSZ pattern anodes. However, due to differences in the fabrication methods of the pattern anodes and electrochemical test conditions, various results were reported.

The objective of the present study is to obtain a comprehensive and consistent data set for H_2 oxidation under stable test conditions. The data set obtained in this study can be used for modeling studies and contribute new insights into H_2 kinetics. Impacts of the temperature, overpotential, triple phase boundary length, and a wide range of gas compositions on anode performance are evaluated under the stable test conditions.

5.2 Experimental

The electrochemical test conditions for the Ni/YSZ pattern anodes are summarized in Table 5-1.

Table 5-1 Electrochemical tests conditions for Ni/YSZ pattern anodes in H_2-H_2O atmosphere

Parameters	Value (unit)
Temperature	500 ºC-800 ºC
Total gas flow rate	100 ml/min
Partial pressure of H_2	5×10^3 Pa - 9.7×10^4 Pa
Partial pressure of H_2O	3×10^3 Pa - 7×10^4 Pa
Overpotential	0-0.2 V
Frequency	0.1 Hz -1×10^5 Hz
Excitation voltage	10 mV

In order to determine the dependence of the polarization resistance on different parameters, a series of experiments were carefully designed and performed by changing one parameter at a time, while keeping others constant. Effects of temperature, overpotential, pH_2 and pH_2O, and TPB length were evaluated. EIS and Tafel plots under different conditions were measured. Note that in the Tafel plots, the x-axis is the potential vs. reference potential. The potential applied on the anode electrode is the difference between OCV and overpotential.

Before evaluating the effects of these parameters, pretreatment of Ni/YSZ pattern anode under constant conditions was carried out to stabilize the pattern anode performance.

Activation energy of the electrode process, reaction orders for H_2 and H_2O were calculated by making use of the expression for the exchange current density proposed by in Utz et al. (2010). Equation 5.1 describes the dependence of the exchange current density (j_0) on pH_2, pH_2O and temperature at constant overpotential. Since R_p is inversely proportional to j_0, at constant temperature, R_p can be written as in Equation 5.2 for constant pH_2O or as in Equation 5.3 for constant pH_2. When the gas composition is fixed, R_p can be expressed as a function of temperature, as given in Equation 5.4. Here, c, c_1, c_2, and c_3 are constants. Note that c is proportional to the TPB length, whereas c_1, c_2 and c_3 are proportional to the inverse of the TPB length. The parameters a and b are reaction orders. E_{act} is the activation energy (kJ/mol), whereas R and T are the ideal gas constant (J/mol·K) and temperature (K), respectively. In the work performed by Utz et al. (2010), line specific resistance (*LSR*) was used instead of the area specific polarization resistance, and defined as the product of the polarization resistance (Ω), TPB length per electrode area (m/cm^2), and the electrode area (cm^2). In order to make a fair comparison with the results reported by Utz el al. (2010), *LSR* was also used in this study to calculate H_2 and H_2O reaction orders (a and b). They were obtained by plotting LSR versus the gas partial pressure in logarithmic scale at OCV. *Rp* was obtained through the equilibrium circuit fitting of EIS data.

$$j_0 = c(pH_2)^a(pH_2O)^b\,exp\left(-\frac{E_{act}}{RT}\right) \tag{5.1}$$

R_p is proportional to the inverse of j_0, therefore:

$$R_p = c_1(pH_2)^{-a} \quad \text{(constant pH}_2\text{O and T)} \tag{5.2}$$

$$R_p = c_2(pH_2O)^{-b} \quad \text{(constant pH}_2\text{ and T)} \tag{5.3}$$

$$R_p = c_3\,exp\left(\frac{E_{act}}{RT}\right) \quad \text{(constant pH}_2\text{ and pH}_2\text{O)} \tag{5.4}$$

The activation energy (E_{act}) was calculated by plotting ln(R_p) versus the *1/T*. The slope of the plot is E_{act}/R.

5.3 Results and Discussion

5.3.1 Effect of Temperature

At OCV, the effect of temperature on the polarization resistance was evaluated over the temperature range of 500-800°C when the fuel contains 50% H_2 and 3% H_2O. The temperature was increased in a linear manner in 50°C increments, and the measurement lasted half an hour at each temperature. The results are presented in Figure 5-1. As expected, the polarization resistance decreases as the temperature increases. A difference of activation energy was observed in the temperature range of 500-650°C and 650-800°C. The activation energy is 0.73±0.05 eV when the temperature varies between 500°C and 650°C. In the temperature range of 650-800°C, the value of activation energy is higher and equals 1.17±0.01 eV. The change of activation energy may indicate changes in the dominating process(es) depending on the temperature.

de Boer (1998) reported that the activation energy was as high as 1.61 eV in the temperature range of 600-850°C. An activation energy of 0.88 eV was reported by Bieberle et al. (2001) when the cell was tested between 400-700°C. Utz et al. (Utz et al., 2010) also claimed two different activation energies in the temperature range of 450-650°C (1.37 eV) and 700-800°C (1.01 eV). They also mentioned that the activation energy obtained by Mizusaki et al. (1994a) was 0.75 eV. In our study, the activation energy is higher in the high temperature range than that in the lower temperature range, which is different from that observed by Utz et al. (2010).

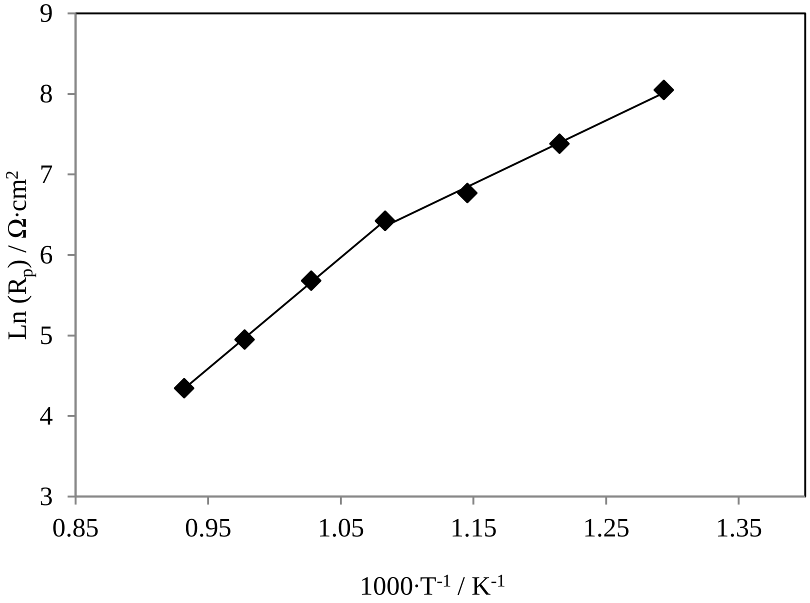

Figure 5-1 Dependence of R_p on temperature at constant pH_2 and pH_2O conditions: $pH_2=5\times10^4$ Pa (50%), $pH_2O=3\times10^3$ Pa (3%).

5.3.2 Effect of Overpotential

EIS was conducted for a mixture of 20% H_2 /3% H_2O in the overpotential range of 0 to 0.3 V at 700°C. Nyquist plots under different overpotential conditions are presented in Figure 5-2. According to the equivalent circuit fitting, two semi-circles are in the Nyquist plot, although they are not clearly separated. However, when the overpotential of 0.3 V was supplied, two semi-circles were clearly separated. Bieberle et al. (2001) also observed two clearly separated semi-circles at the overpotential of 0.4 V. They explained that this behavior might be due to the increased amount of H_2O produced, which caused diffusion problem. In our study (Yao and Croiset, 2013c), the impedance shape changes were interpreted by the changes in charge transfer reactions. This is explained in detail in Chapter 7.

Dependence of the polarization resistance and relaxation frequency on overpotential is shown in Figures 5-3(a) and 5-3(b). The natural logarithm of the polarization resistance decreases linearly with increasing overpotential within the overpotential range studied. The strong response of the R_p to the overpotential suggests that the electrode process may be determined by charge transfer reactions. The relaxation frequency increases exponentially from 12.6 Hz to 631 Hz when increasing the overpotential from 0 to 0.3 V. The corresponding relaxation time decreases from 0.08 s to 0.0016 s. This showed that the electrode process is accelerated by ~ 50 times when increasing the overpotential from 0 to 0.3 V. This value is higher than the value (25 times) mentioned by Bieberle et al. (Bieberle et al., 2001), but still of the same order of magnitude.

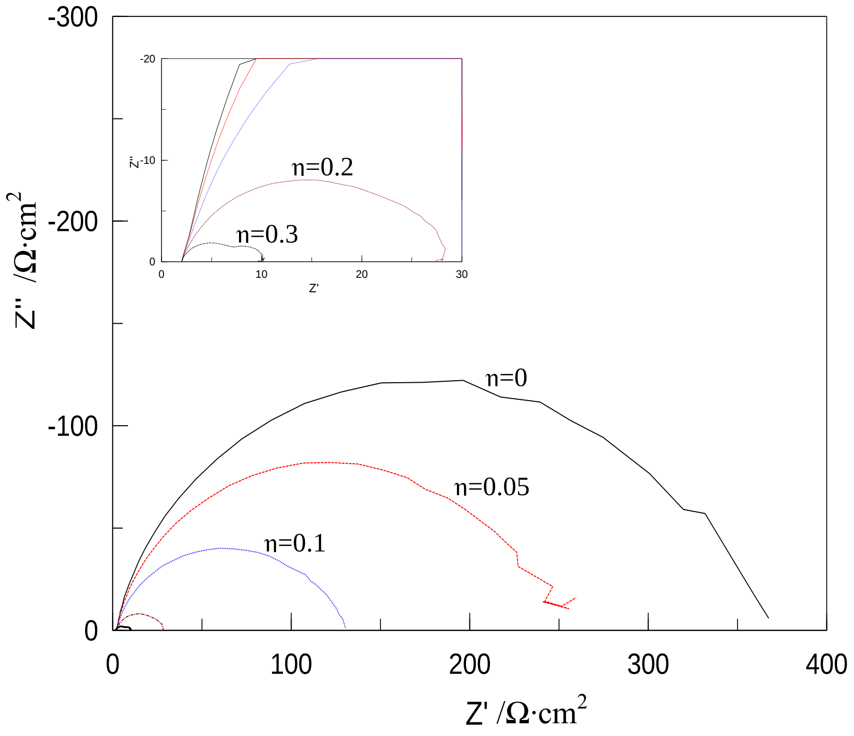

Figure 5-2 Dependence of R_p on overpotential in Nyquist plots, $pH_2=2\times10^4$ Pa (20%), $pH_2O=3\times10^3$ Pa (3%), T=700 °C, Ni pattern width: 100 µm.

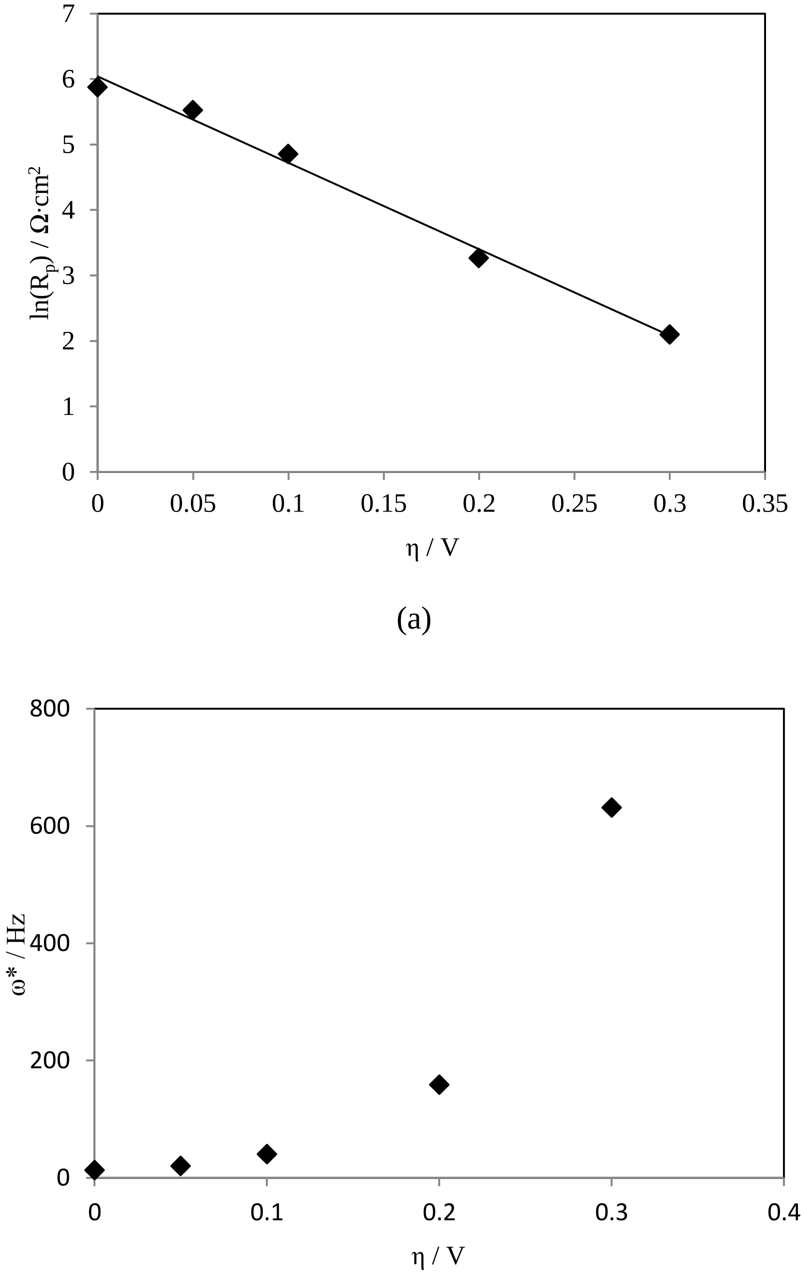

(a)

(b)

Figure 5-3 (a) R_p as a function of overpotential, (b) relaxation frequency as a function of overpotential, $pH_2=2\times10^3$ Pa (20%), $pH_2O=3\times10^3$ Pa (3%), T=700 °C.

5.3.3 Effect of Partial Pressure of H_2

The dependence of the polarization resistance on pH_2 was characterized at two different temperatures at OCV. Figure 5-4 and 5-5 represent plots of polarization resistance and current density versus pH_2 at low (550°C) and high (700°C) temperatures. The cells used at both temperatures have the same Ni thickness (1.0 μm). At both temperatures, pH_2 ranged from 5×10^3 Pa to 9.0×10^4 Pa.

Polarization resistance changes with pH_2 at 550ºC and 700ºC are presented in Figure 5-4(a) and 5-5(a), and the corresponding Tafel plots are given in Figure 5-4(b) and 5-5(b), respectively. With increasing pH_2, the polarization resistance decreases. At 550ºC, the H_2 reaction order shown in Figure 5-4(a) is 0.13. However, it changes from 0.096 to 0.13 over different tests. At 700ºC, the reaction order shown in Figure 5-5(a) is 0.093. But in other tests, it ranges from 0.092 to 0.145. The difference of the H_2 reaction order is very small at different temperatures.

In previous studies, Utz et al. (Utz et al., 2010; Utz, 2011) reported the H_2 reaction order to be 0.07 at 800°C. But they also mentioned that the reaction order differs from -0.15 to 0.14 between different samples. They extracted the H_2 reaction orders from other studies using the same calculation method. The reaction order reported by Mizusaki et al. (1994a) was 0.09-0.15 at 700°C. A value of 0.11 was obtained by Bieberle et al. (2001) at 700°C, and -0.26 at 850°C by de Boer (1998). Compared to the H_2 reaction orders reported in the literature, the value (0.092-0.145) obtained in our study is very similar to the value claimed by Mizusaki et al. Also, it is close to the values reported by Bieberle et al. at 700°C and by Utz et al. at 800°C. No negative value for H_2 reaction order was found in our study.

The Tafel plots in both Figures 5-4(b) and 5-5(b) show that current density increases when increasing pH_2 under anodic polarization, which is consistent with the results observed in Figure 5-4(a) and 5-5(a). However, the current density is not significantly affected by pH_2 under cathodic polarization. This reveals that the overall reverse reaction of H_2 oxidation is less affected by pH_2. Under anodic polarization, the current density first increases with decreasing electrode potential, and then remains almost constant with further decreasing electrode potential. At 550°C, the limiting current density which is the highest current density the cell can reach does not change with changing pH_2. According to the definition of

j_L in Equation 1.19, j_L is proportional to H_2 if the electrode process is H_2 diffusion controlled. Therefore, the constant current density in the lower anodic potential range is not caused by H_2 diffusion. However, it may be caused by diffusion of removing produced H_2O. At 700°C, j_L increases linearly with increasing pH_2 (see Figure 5.5(c)), which indicates the electrode process is H_2 diffusion controlled.

Mizusaki et al. (1994b) also claimed that the current density was proportional to pH_2 under anodic polarization, while independent of pH_2 under cathodic polarization. The electrode potential used in their study varied from -1.3 V to -0.9 V with pH_2 ranging from 1×10^3 to 1×10^4 Pa at constant pH_2O (8.5×10^2 Pa).

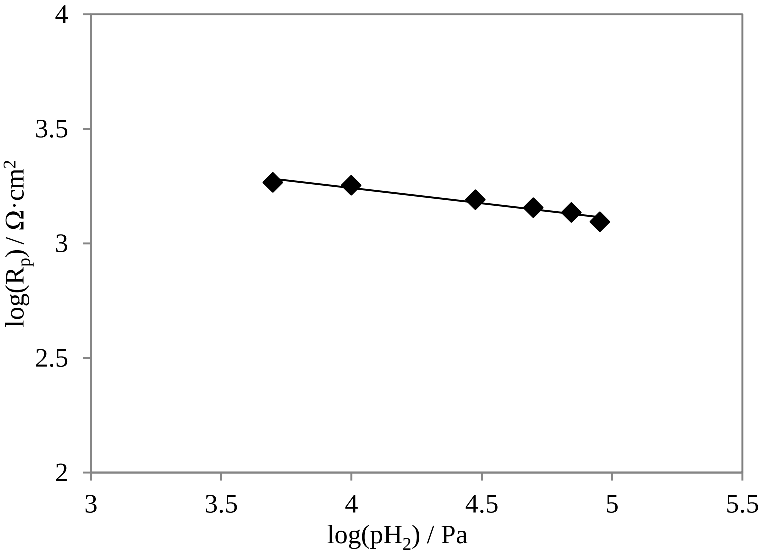

(a)

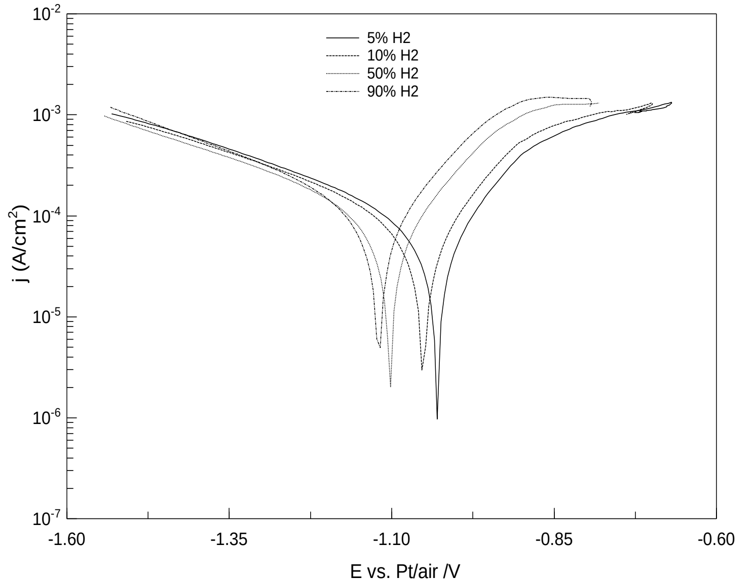

(b)

Figure 5-4 (a) Dependence of R_p on pH_2 at 550°C, (b) the corresponding Tafel plots, $pH_2O=3\times10^3$ Pa (3%).

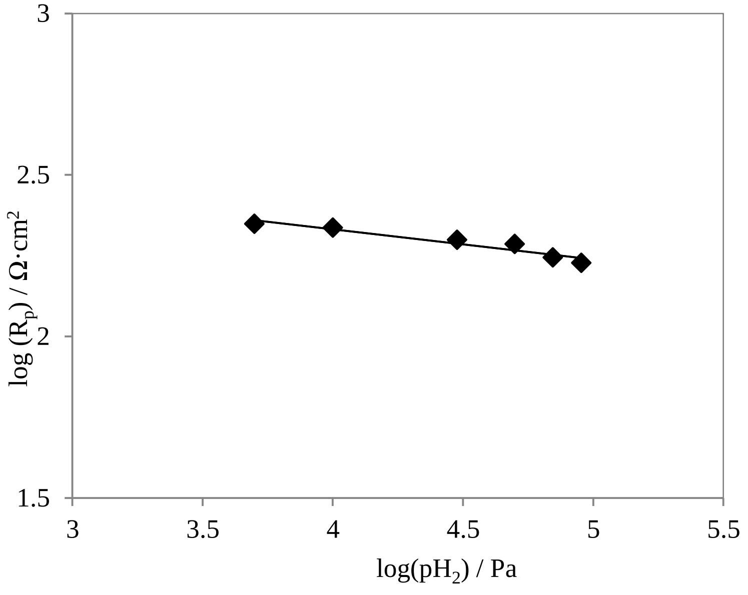

(a)

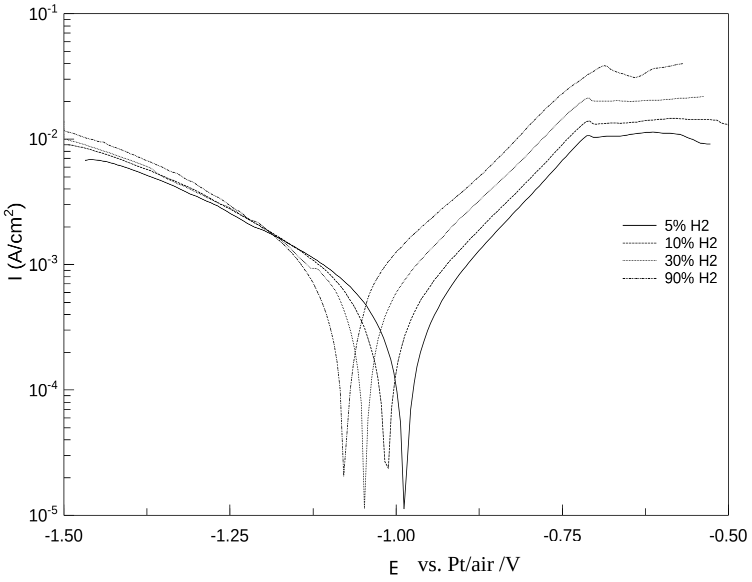

(b)

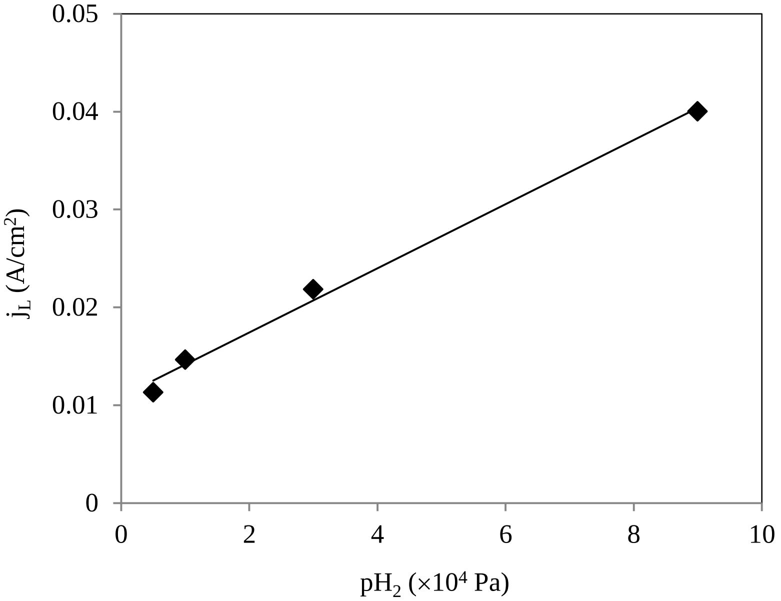

(c)

Figure 5-5 (a) R_p changes with pH_2 at 700°C, (b) the corresponding Tafel plots, $pH_2O=3\times10^3$ Pa (3%), (c) the effect of pH_2 on the limiting current density

Figure 5-6 shows the variation of the relaxation frequency with pH_2. At 700°C, the relaxation frequency increased from 389.1 Hz to 501.2 Hz when the pH_2 was increased from 5×10^3 to 9×10^4 Pa. At 550°C, the relaxation frequency (63.1 Hz) showed very little change when the pH_2 was increased from 5×10^3 Pa to 9×10^4 Pa. The very small effect of pH_2 on the electrode process indicates that it is not strongly affected by pH_2.

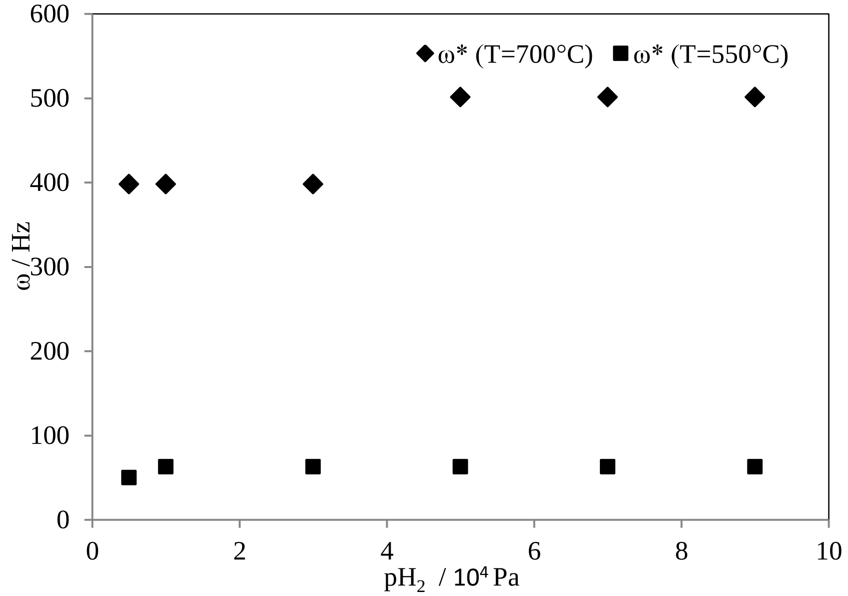

Figure 5-6 Relaxation frequency as a function of pH_2 at 550°C and 700°C, $pH_2O = 3\times10^3$ Pa (3%).

5.3.4 Effects of Partial Pressure of H_2O

As reported previously (Yao and Croiset, 2012a), high amount of H_2O (>10%) at elevated temperatures (e.g. 700°C) has dramatic effects on the Ni pattern structure. However, the pattern anode maintains dense structure and straight TPB line when the test is performed at lower temperature (e.g. 550°C). Therefore, the effect of pH_2O on the polarization resistance was investigated in the range of 5×10^3 Pa to 7×10^4 Pa at 550°C. The pH_2 was kept constant at 2×10^4 Pa. EIS and Tafel data were measured. Figure 5-7(a) shows the dependence of the polarization resistance on pH_2O. The corresponding Tafel plots are given in Figure 5-7(b). As shown in Figure 5-7(a), the polarization resistance decreases with increasing H_2O content between 0 and 30-40%, above which polarization resistance shows small dependence on

pH_2O. As shown in Figure 5-7(b), under cathodic conditions, the current density increases when H_2O content is increased from 0 to 30-40%, above which the current density shows small dependence on pH_2O. The trend of cathodic current density changes with pH_2O is consistent with the polarization resistance changes with pH_2O. Under anodic conditions, the current density is almost independent of pH_2O. Mizusaki et al. (1994b) also observed a positive dependence of cathodic current density on pH_2O and an independent behavior of anodic current density on pH_2O. However, the range of H_2O composition studied by Mizusaki et al. was considerably shorter, 0.4-1.7% at constant pH_2 (3%). The reaction order of H_2O is 0.3 in this study. In the work performed by Utz et al. (2010), they determined an H_2O reaction order of 0.68 at 800°C. The H_2O reaction order from Mizusaki et al. (1994a), de Boer (1998), and Bieberle et al. (2001) were calculated using Equation 3 by Utz et al. (2010), and they were found to be 0.32-0.88 at 700°C, 0.37 at 850°C, and 0.67 at 700°C.

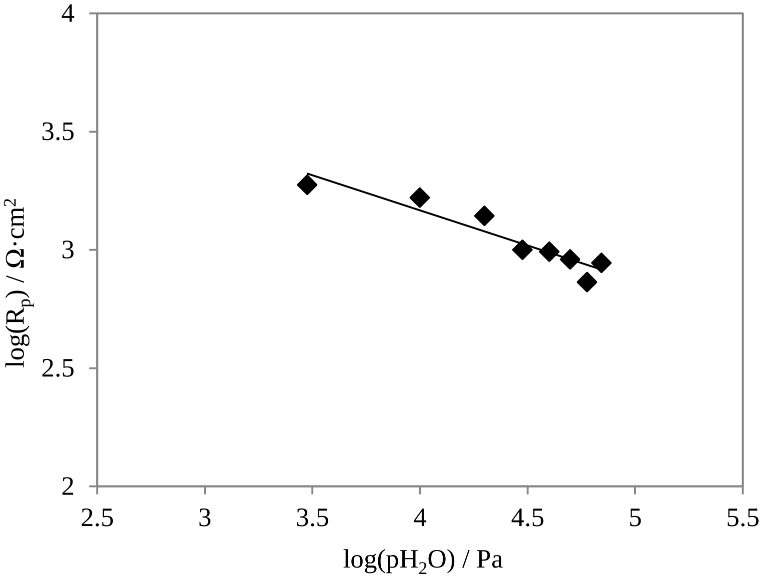

(a)

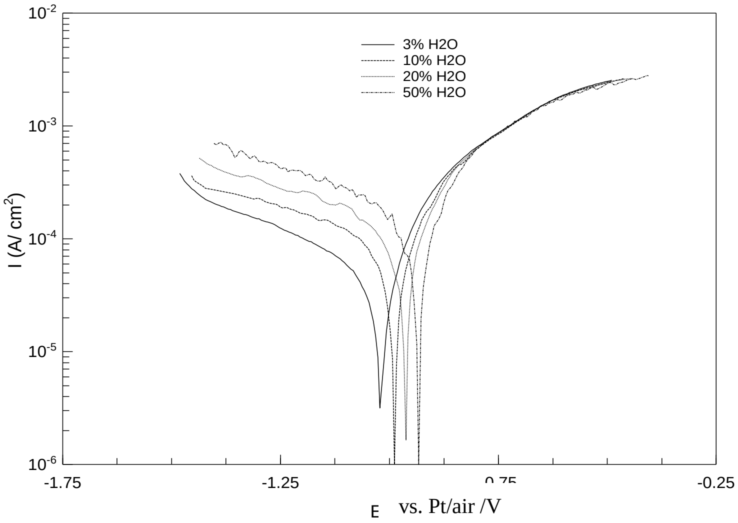

(b)

Figure 5-7 (a) R_p changes with pH_2O at $pH_2=2\times10^4$ Pa and T=550°C, (b) the corresponding Tafel plots.

Figure 5-8 shows the variation of the relaxation frequency with pH_2O at OCV. The relaxation frequency increases with increasing pH_2O at 550°C indicating the electrode process becomes faster with increasing pH_2O. Water related processes may contribute to it.

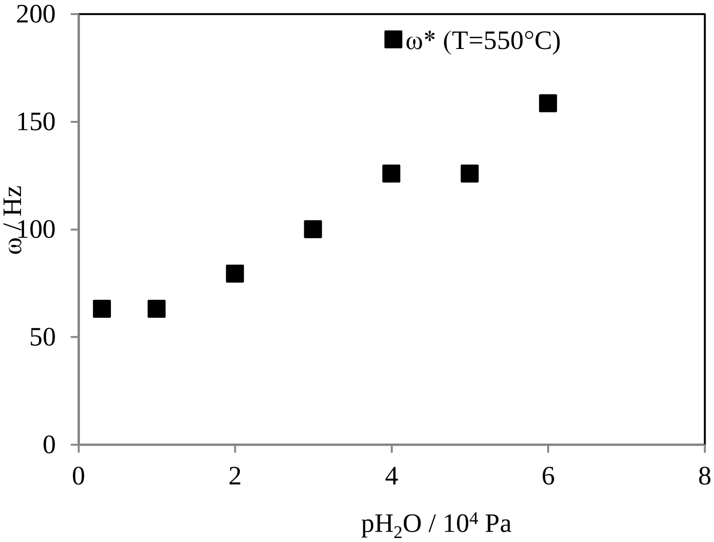

Figure 5-8 Relaxation frequency as a function of pH_2O at 550°C and 700°C, $pH_2=2\times10^4$ Pa (20%).

5.3.5 Effect of Triple Phase Boundary Length

For samples with different TPB lengths, the polarization resistance was recorded when the cell performance was stable under 50%/3% H_2/H_2O (balance N_2) conditions. This low level of water does not affect the TPB length. The dependence of polarization resistance on TPB length at 700°C and 750°C is presented in Figure 5-9. On a log-log scale, polarization resistance decreases linearly with increasing TPB length with slopes of -0.70 and -0.72 at 700°C and 750°C, respectively. Bieberle (2000) reported the slope to be -0.70 when the TPB length was between 0.04 m/cm^2 and 4 m/cm^2, and a higher value of -1.2 in the L_{TPB} range of 4 m/cm^2 - 13 m/cm^2. Since, the range of TPB length is between 1.16 m/cm^2 and 5.19 m/cm^2 in our study, the results are very similar to that of Bieberle for the same range of TPB length.

Utz (2011) reported a slope of -1.19 for their experiments when the polarization resistance was plotted versus TPB length in double logarithmic scale. The TPB length used in their study was between 1 m/cm^2 and 8 m/cm^2. Utz (2011) also calculated the slope from the data of Mizusaki et al. (1994a) and de Boer (1998) to be-0.5 and -0.68, respectively. Ehn et al. (2010) reported a weak dependence of R_p on TPB length, although the slope was not disclosed. According to Equation 5-1, the slope is expected to be -1. However, from most of the studies, the slope including ours is smaller and only Utz (2011) obtained a larger value than expected. Bieberle (2000) attributed the smaller slope value to underestimation of the TPB length. Utz (2011) explained that deviations in the slopes obtained from the literature are due to different measurement conditions, such as pH_2, pH_2O and temperature, which affect R_p. Based on our results, our interpretation of a negative slope value lower than -1 is that the overall electrode process is comprised of not only charge transfer processes but also other diffusion process (e.g. H_2O diffusion in the gas channel).

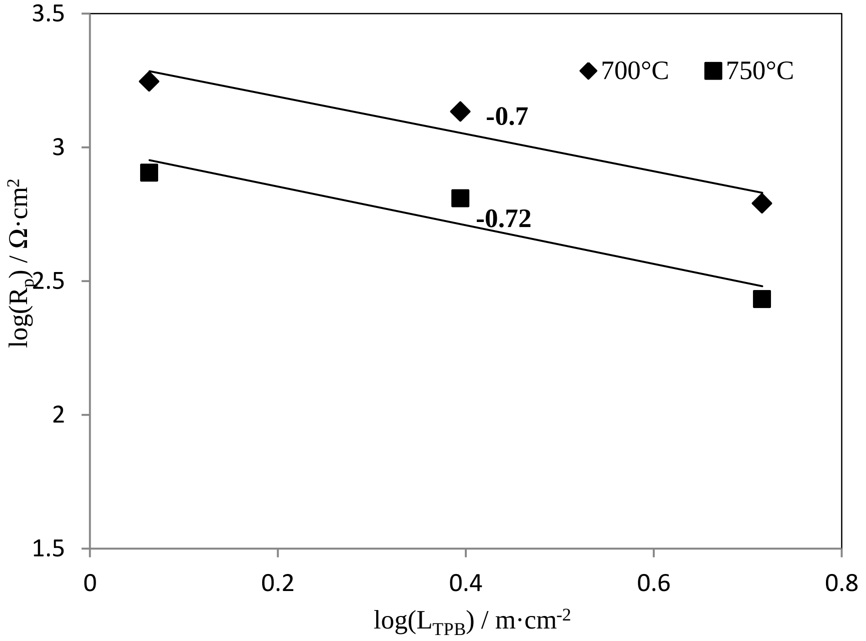

Figure 5-9 Plots of R_p versus TPB length in double logarithmic scale, $pH_2=5\times10^4$ Pa (50%), $pH_2O=3\times10^3$ Pa (3%).

As a summary, comparison between our results and literature results regarding activation energy, reaction orders of H_2 and H_2O, and dependence of R_p on L_{TPB} (slope) is given in Table 5-2.

Table 5-2 Comparison between our results and literature results regarding activation energy, reaction orders of H_2 and H_2O, and the dependence of R_p on L_{TPB}. By plotting $log(R_p)$ versus $log(L_{TPB})$, the slope of this plot is used to describe the dependence of R_p on L_{TPB}.

Research groups	Activation energy for the overall electrode process (eV)	H_2 reaction order (a)	H_2O reaction order (b)	Dependence of R_p on L_{TPB} (slope)	References
Utz et al.	1.37 (450°C–650°C) 1.01 (700°C–800°C)	–0.15 to 0.14 (800°C)	0.68 (800°C)	–1.19 (800°C)	(Utz et al., 2010; Utz, 2011)
Bieberle et al.	0.88 (400°C–700°C)	0.11 (700°C)	0.67 (700°C)	–0.7 (700°C)	(Bieberle, 2000; Bieberle et al., 2001; Utz et al., 2010)
de Boer	1.61 (600°C–850°C)	–0.26 (850°C)	0.37 (850°C)	–0.68 (800°C)	(Boer de, 1998; Utz et al., 2010)
Mizusaki et al.	0.75 (700°C–850°C)	0.09 to 0.15 (700°C)	0.32 to 0.88 (700°C)	–0.5 (800°C)	(Utz et al., 2010)
This study	0.73±0.05 (500°C–650°C) 1.17±0.01 (650°C–800°C)	0.092 to 0.145 (700°C)	0.3 (700°C)	–0.7 (700°C)	

5.4 Conclusions

In this study, electrochemical oxidation of H_2 was investigated using Ni/YSZ pattern anodes. The pattern anode performance as a function of temperature, overpotential, pH_2 and pH_2O under a wide range of conditions was evaluated. The main results are summarized as:

- Two different activation energies for the temperature dependence of R_p were observed in the temperature range of 500-800°C. This may indicate changes in the dominating process(es) depending on the temperature range.
- The dependence of polarization resistance and relaxation frequency on overpotential follows an exponential function, indicating that charge transfer reactions may contribute to the rate-limiting steps.
- Polarization resistance increases with decreasing pH_2, and the hydrogen reaction order varies between 0.092 and 0.145. The difference of hydrogen reaction order at different temperatures is very small.
- The polarization resistance increases when increasing H_2O content from 3% to 30-40%. Further increase of H_2O content does not significantly affect the polarization resistance. The H_2O reaction order is 0.3 when pH_2O is between 3×10^3 Pa and 7×10^4 Pa. In this range, H_2O related processes coupled with charge transfer reaction may contribute to the rate-limiting processes of H_2 electrochemical oxidation.
- When plotting polarization resistance versus TPB length in logarithmic scale, slopes of the plots are -0.70 and -0.72 at 700°C and 750°C, respectively. Those values for the slope are lower than the expected slope of -1 if only charge transfer reactions control the overall reaction, further indicating that other processes are contributing to the overall process (e.g. diffusion on the gas channel).

Chapter 6

Electrochemical performance of Ni/YSZ pattern anodes in CO-CO_2 environments

In this chapter, experiments on the electrochemical performance of Ni/YSZ pattern anodes in CO-CO_2 atmosphere are presented. The dependence of polarization resistance on partial pressure of CO and CO_2, temperature and overpotential was evaluated. The activation energy and reaction orders of CO and CO_2 were determined. In addition, the electrochemical performance of Ni/YSZ pattern anodes in CO-CO_2 system and H_2-H_2O atmosphere were compared.

6.1 Introduction

SOFCs can operate directly with hydrocarbons, which could lower equipment cost and further increase the energy efficiency. However, the state-of-art Ni/YSZ cermet anodes are susceptible to carbon deposition with hydrocarbons as fuels. Carbon deposition can be caused by cracking, Boudouard and carbon monoxide (CO) hydrogenation reactions.

Since carbon formation degrades the Ni catalyst (Lauvstad et al., 2002b), it is desirable to internally or externally reform those hydrocarbons before they reach the SOFC anode. In both cases, the main products reaching the SOFC active sites are H_2 and CO (Habibzadeh, 2007; Yurkiv et al., 2011). Good understanding of the elementary reaction pathways of the reformate gases (H_2 and CO) should provide insight into addressing the problem of carbon deposition on SOFC anodes, and improve the overall cell performance.

Far fewer studies on CO oxidation have been reported than those dealing with H_2 oxidation. Moreover, most of the previous on CO electrochemical oxidation made use of Ni/YSZ cermet or Pt/Ni point electrodes (Mizusaki et al., 1992; Holtappels et al., 1999c; Lauvstad et al., 2002b; Weber et al., 2002). So far, only three groups have studied CO oxidation using Ni/YSZ pattern anodes (Sukeshini et al., 2006; Habibzadeh, 2007; Ehn et al., 2010; Utz et al., 2011). Furthermore, no agreement has been reached on the reaction orders of CO and CO_2 as well as on activation energy of the electrode process.

Some researchers reported that CO oxidation is much slower than H_2 oxidation (Holtappels et al., 1999c; Sukeshini et al., 2006; Habibzadeh, 2007). However, others reported that the reaction rate in CO-CO_2 environments was only slightly lower than that in H_2-H_2O environments (Ehn et al., 2010; Utz et al., 2011).

Mizusaki et al. (1992) claimed that the rate-controlling process for CO oxidation was the chemical reaction across the TPB line between CO and oxygen ions. Lauvstad et al. (2002a) proposed that the possible rate-limiting reaction might be CO adsorption or CO_2 desorption reaction. Habibzadeh (2007) claimed that the rate-determining process was related to the overpotential and temperature. At high overpotential and temperature, charge-transfer was rate-limiting. At low overpotential and temperature, adsorption or surface diffusion combined with charge transfer were the rate-limiting processes. In the most recent study, Yurkiv et al. (2011) proposed that a two-step oxygen spillover reaction mechanism could interpret the experimental data reported by Lauvstad et al. (2002b). In another study, Yurkiv et al. (2012) proposed that the charge transfer reaction of CO oxidation proceeds via either a two-step oxygen spillover mechanism with CO oxidized on the Ni surface or a mechanism with CO oxidized on the YSZ surface. Shi et al. (2012) suggested surface diffusion as possibly one of the rate-determining steps under low temperature and higher polarization voltage conditions.

In this study, CO electrochemical oxidation was studied using Ni/YSZ pattern anodes. The cell was pre-treated in H_2/H_2O environments to achieve stable performance. Then, the dependence of polarization resistance on the partial pressure of CO and CO_2, temperature and overpotential was investigated.

6.2 Experimental

During the electrochemical tests of Ni/YSZ pattern anodes with CO/CO_2, carbon formation caused by Boudouard reaction could block the gas delivery tube. Although the actual temperature on the cell surface is the same as the set value, the temperature along the whole gas delivery tube is not consistent. Carbon deposition is favoured at lower temperature from a thermodynamic point of view. However, if the temperature is too low, the kinetics of carbon deposition will be slow enough that it will not cause a problem. Thus, a temperature window may exist where the temperature is low enough to favour carbon deposition, but high enough for the kinetics to be sufficiently fast to allow carbon deposition in the gas delivery tube. It would be therefore desirable to limit this temperature window by trying to heat up the feed gas as rapidly as possible.

In order to avoid carbon formation on the gas delivery tube, a test was necessary to measure the temperature distribution along the gas delivery tube and determine the temperature which favored carbon formation. Thus, tests close to this temperature should be avoided to prevent carbon formation on the gas delivery tube.

The Ni/YSZ pattern anode was first treated with humidified H_2 (50% H_2 / 3% H_2O) at 750°C until the polarization resistance reached a constant value. Then, the feed gas was switched to a CO/CO_2 mixture. The electrochemical test conditions are given in Table 6-1. The ranges of parameters were: 1×10^4 Pa (10%) $\leq$ pCO $\leq$ 3×10^4 Pa (30%) and 1×10^4 Pa (10%) $\leq$ pCO_2 $\leq$ 3×10^4 Pa (30%). This range was chosen to avoid Ni oxidation and Boudouard based on the work of Utz et al. (2011b). Detailed thermodynamic calculation determining the theoretical ranges of pCO and pCO_2 can be found in Appendix B.

In order to determine the effects of the different variables on polarization resistance, a series of experiments was performed by changing one parameter at a time while keeping others constant. Effects of temperature, overpotential, pCO and pCO_2 were evaluated. N_2 was used as the balance gas for the individual variation of pCO and pCO_2. EIS under these various conditions were measured.

Table 6-1 Electrochemical test conditions with CO/CO_2

Parameters	Value (unit)
Temperature	700 ºC - 800 ºC
Total gas flow rate	100 ml/min
Partial pressure of CO	1×10^4 Pa - 3×10^4 Pa
Partial pressure of CO_2	1×10^4 Pa - 3×10^4 Pa
Overpotential	0 - 0.3 V
Frequency	0.1 Hz – 1×10^5 Hz
Excitation voltage	10 mV

6.3 Results and Discussion

6.3.1 Measurements of the Temperature Distribution along the Gas Delivery Tube

A schematic of the gas delivery tube is shown in Figure 6-1. After the electrochemical tests, the position where most carbon formed was found to be ~16 cm away from the bottom of the tube. This is also the position on the tube just outside the furnace.

In order to determine the temperature that favors the formation of carbon, a test measuring the temperature distribution along the gas delivery tube was conducted. The setup temperature of the furnace was varied from 600°C to 800°C in steps of 50°C. The temperatures were measured at different positions along the gas delivery tube. The results are shown in Figure 6-2. At a distance of ~ 22 cm, the temperature in the tube is very close to the furnace set temperature. Below 22 cm, the temperature in the tube is lower than the furnace set temperature. When the furnace set temperature is 750°C, the actual temperature of the tube is 626°C at a distance of ~16 cm, which is very close to the location where most carbon formed. This suggests that a temperature of ~ 626°C favors the formation of carbon, and tests around or below this temperature should be avoided.

In order to avoid carbon formation in the gas delivery tube, a heating tape was added to ensure rapid heating of the feed gas. After the electrochemical test, it was also confirmed that under the feed conditions chosen, carbon was not observed on the pattern anode surface.

Under the above test conditions, holes formed on the Ni surface. Thus, the TPB length could not be precisely determined. However, it was possible to reach stable performance of the cell in CO/CO_2 environments, albeit without knowledge of the corresponding TBP length. Subsequent experiments were carried out to determine the effects of different conditions on the pattern anode performance.

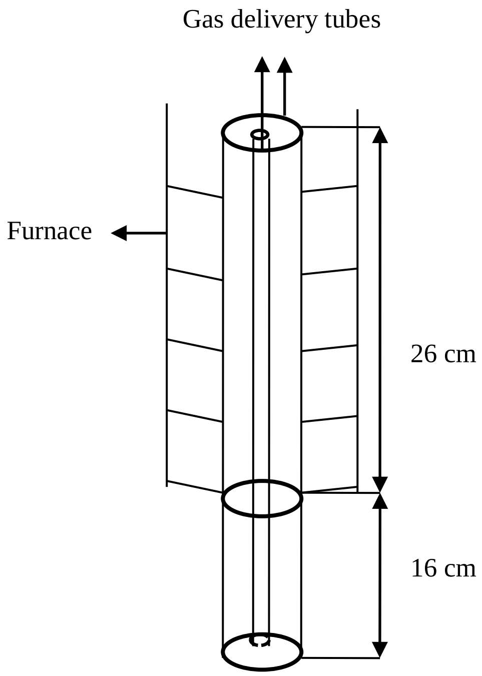

Figure 6-1 Scheme of the gas delivery tubes

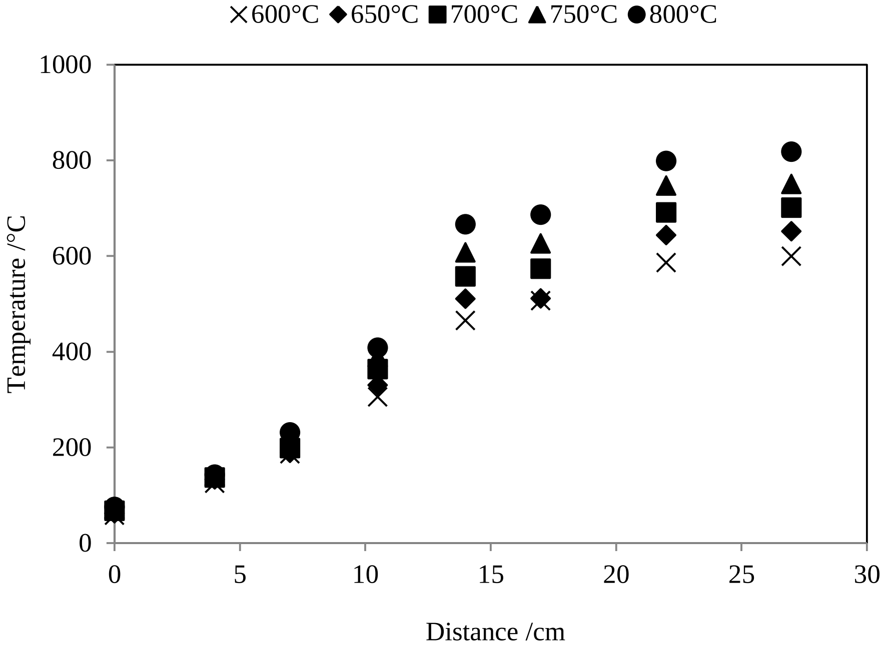

Figure 6-2 Temperature distribution along the gas delivery tube

6.3.2 Electrochemical Characterization of Ni/YSZ Pattern Anodes with CO/CO_2

A Ni/YSZ pattern anode with Ni thickness of 1.0 μm and Ni pattern width of 100 μm was first electrochemically tested in a H_2-H_2O environments at 750°C and it require about 22 hrs for its polarization resistance to stabilize. Then, the H_2/H_2O mixtures were switched to CO/CO_2 mixtures. The test was continued under constant conditions for about two hours until stable performance was reached, before the effect of overpotential on performance was evaluated. Impedance spectra of different overpotentials are shown in Figure 6-3. Figure 6-4(a) presents the dependence of polarization resistance on overpotential. Partial pressures of CO and CO_2 were kept constant at 1×10^4 Pa and 2×10^4 Pa, respectively. The logarithm of polarization resistance decreases linearly with increasing the overpotential from 0 to 0.1 V. With a further increase the overpotential, the polarization resistance starts to increase. The shape of the impedance is also dramatically changed when a high overpotential is imposed. Lauvstad et al. (2002b) studied the effect of overpotential on polarization resistance using both Pt and Ni point anodes. The impedance spectra were recorded under OCV, cathodic and anodic overpotential conditions. They found that the polarization resistance decreased when the overpotential was changed from cathodic overpotential to OCV, and then to anodic overpotential. Because only one anodic overpotential condition was applied in their study, it is hard to compare with the results obtained in our study. However in their study, the shape of the impedance spectra at high anodic overpotential (0.49 V) did not show too much difference compared to the impedance at OCV when using a porous Pt anode. The increased polarization resistance caused by high anodic overpotential in our study may be due to oxidation of Ni patterns or the diffusion of gas species.

In Figure 6-4(b), the relaxation frequency increases exponentially with rise in the overpotential from 0 to 0.2 V. Combined with the fact that the polarization resistance decreases exponentially when the overpotential is from 0 to 0.1, we conclude that the rate-limiting step involving charge transfer reactions. In their modeling study, Yurkiv et al. (2011) claimed that charge transfer reaction through oxygen spillover is the rate-limiting step. They also mentioned that surface reactions of gas components on both Ni and YSZ surface are fast and not rate-limiting steps.

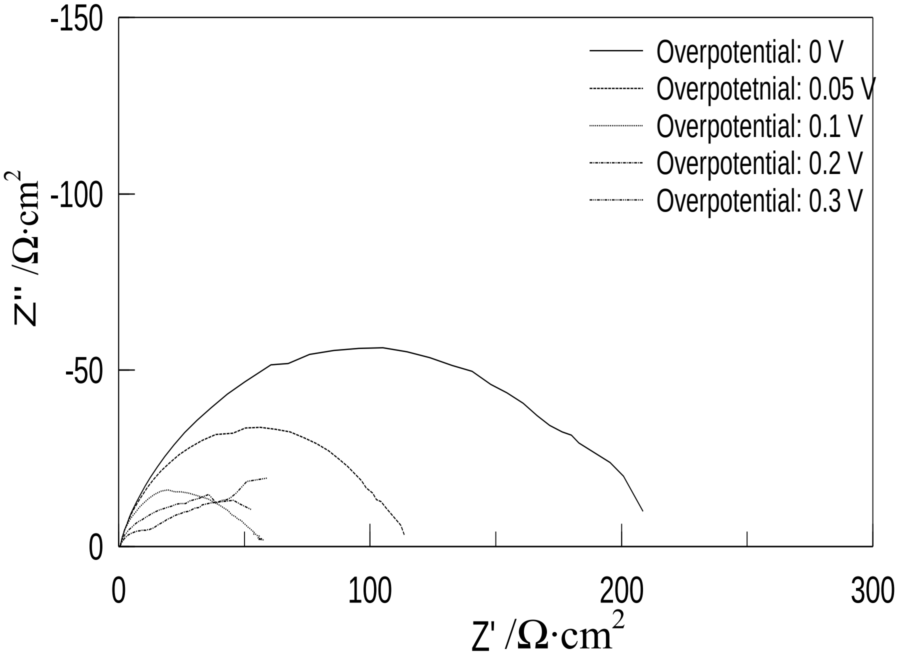

Figure 6-3 Effect of overpotential on the impedance spectra, pCO= 1×10^4 Pa, pCO_2=2×10^4 Pa, T=800°C.

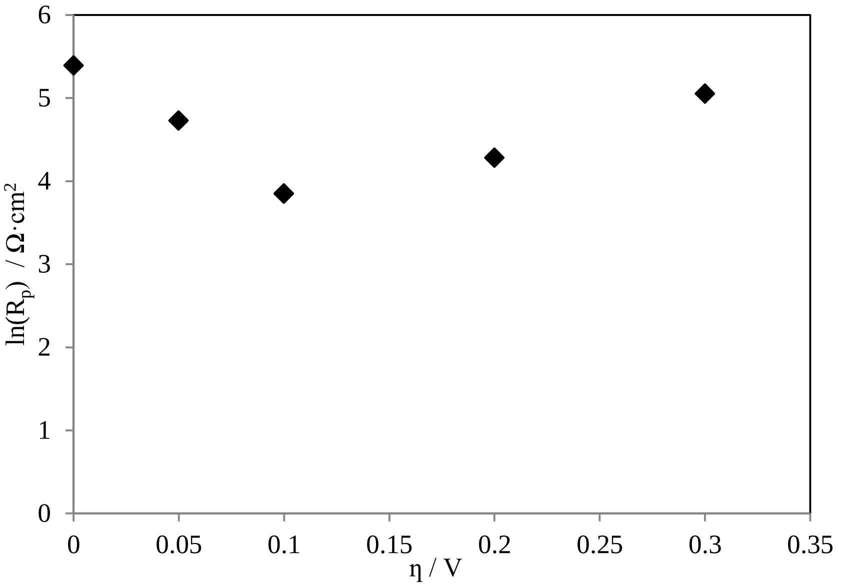

(a)

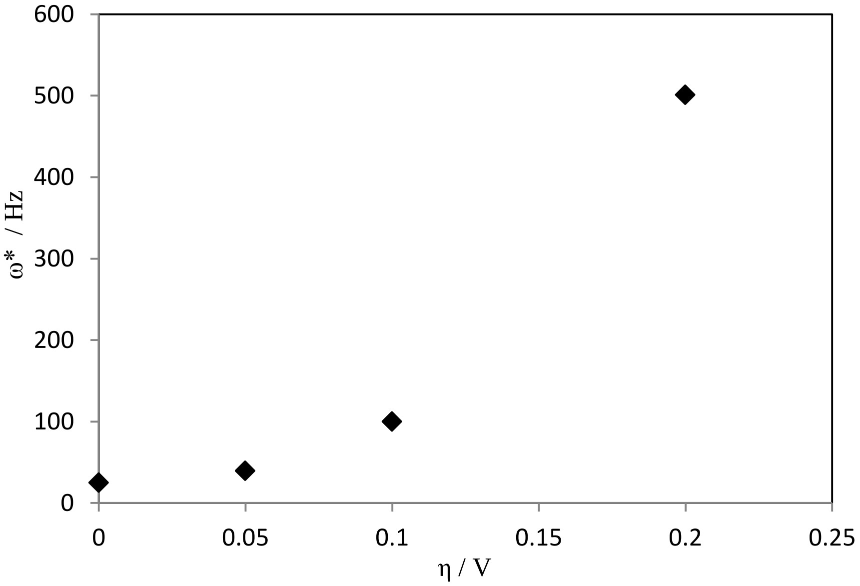

(b)

Figure 6-4 (a) Variations of R_p with overpotential, pCO= 1×10^4 Pa, pCO_2=2 ×10^4 Pa, T=800°C, (b) variation of relaxation frequency with overpotential.

The effect of temperature on the polarization resistance is shown in Figure 6-5. The test was performed under the following conditions: pCO= 1×10^4 Pa (10%), pCO_2=2 ×10^4 Pa (20%), T: 700-800°C, EIS around OCV.

At the OCV, the activation energy was found to be 1.04 eV. Utz et al. s (2011b) reported an activation energy of 1.42 eV. Ehn et al. (2010) claimed the activation energy of CO oxidation to be the same as that of H_2 oxidation, which is 1.0 eV. Lauvstad et al. (2002b) observed a monotonous increase in polarization resistance for a porous Pt anode when decreasing the temperature at constant pCO/pCO_2, and the activation energy was about 290.5kJ/mol (~0.29 eV). For Ni electrodes, they found that polarization resistance first decreased when increasing temperature (775-825°C) and then increased with further rise in temperature (825 to 924°C). A minimum value in polarization resistance was observed in the temperature range studied.

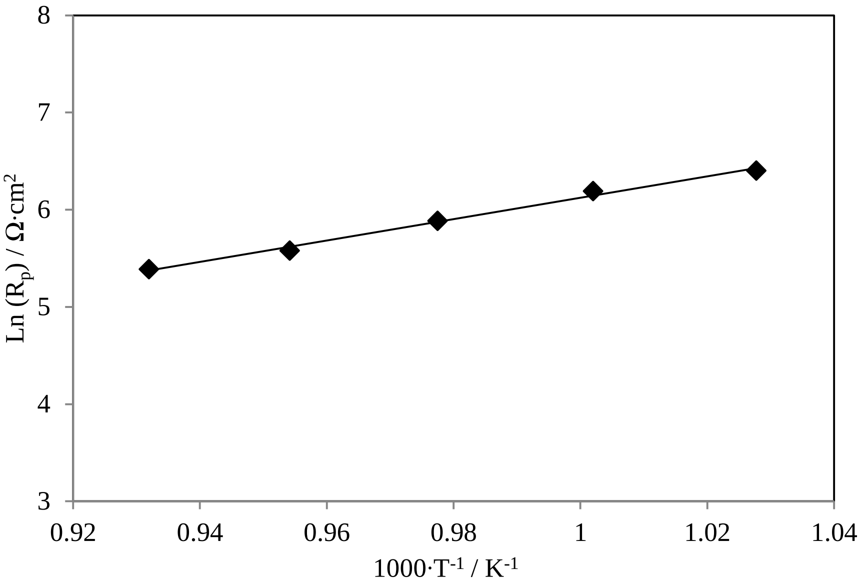

Figure 6-5 Dependence of R_p on temperature, pCO =1.0×10^4 Pa, pCO$_2$=2×10^4 Pa

The dependence of polarization resistance on pCO is shown in Figure 6-6(a). The partial pressure of CO$_2$ was kept constant at 2.0×10^4 Pa, and pCO varied in the range of 1×10^4 Pa - 3×10^4 Pa at 800°C. Under these conditions, the polarization resistance increases when increasing the partial pressure of CO, and the reaction order is -0.5. Utz et al. (2011b) reported a value of -0.34 at the same conditions. Boulenouar et al. (2001) reported the value to be -0.5 for CO. Ehn et al. (2010) observed different trends in the dependence on pCO when using thin (0.5 μm) and thicker (1.0 μm) Ni pattern anodes. For thin Ni pattern anodes, the polarization resistance decreased as pCO increased. The opposite trend was observed when thicker Ni pattern anodes were used. The reaction order of CO was not reported in their study. Mizusaki et al. (1992) studied the effect of pCO on current density using porous Pt-stabilized zirconia. They observed that the anodic current dependent on pCO, whereas the cathodic current was independent of pCO. The reaction order of CO was 0.5. This means that the polarization resistance decreases when increasing pCO, which is the opposite of what we and other researchers reported. Lauvstad et al. (2002b) reported that the polarization resistance decreased sharply when reducing pCO from 0.333 atm to 0.067 atm on porous Ni anodes. However, a different behavior was observed when Pt was used as the anode material. Figure 6-6(b) shows the effect of pCO on the relaxation frequency (ω*) in our study. The relaxation frequency varies from 19.95 Hz to 25.12 Hz when pCO is in the range of 1.0×10^4 Pa - 3.0×10^4 Pa. The small change of relaxation frequency may indicate that the rate-limiting step for CO electrochemical oxidation is not caused by surface reactions of CO on either Ni or YSZ surface.

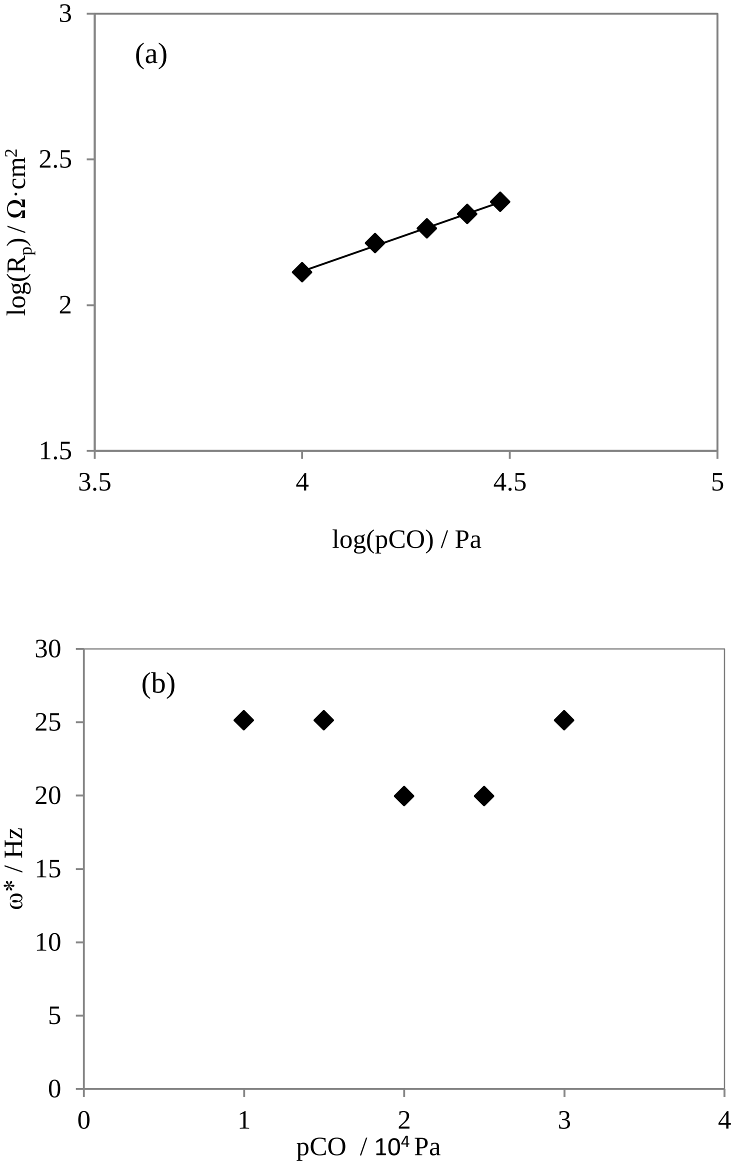

Figure 6-6 Dependence of R_p on partial pressure of CO, (b) relaxation frequency as a function of pCO, $pCO_2 = 2.0\times10^4$ Pa, pCO: $1\times10^4 - 3\times10^4$ Pa, T=800°C.

Figure 6-7(a) presents the dependence of polarization resistance on pCO_2. pCO was kept constant at 1.0×10^4 Pa, and pCO_2 varied in the range of 1×10^4 Pa - 3×10^4 Pa at 800°C. The polarization resistance shows a negative trend when increasing partial pressure of CO_2, and the reaction order of CO_2 was found to be 0.3. Utz et al. (2011b) reported CO_2 reaction order of 0.41 under the similar conditions as in this study. Lauvstad et al. (2002b) also observed the negative trend in the polarization resistance dependence on pCO_2, but no reaction order was reported. At constant pCO condition, the relaxation frequency remains close to25 Hz when changing pCO_2, and shows small dependence on pCO_2 (see Figure 6-7(b)).

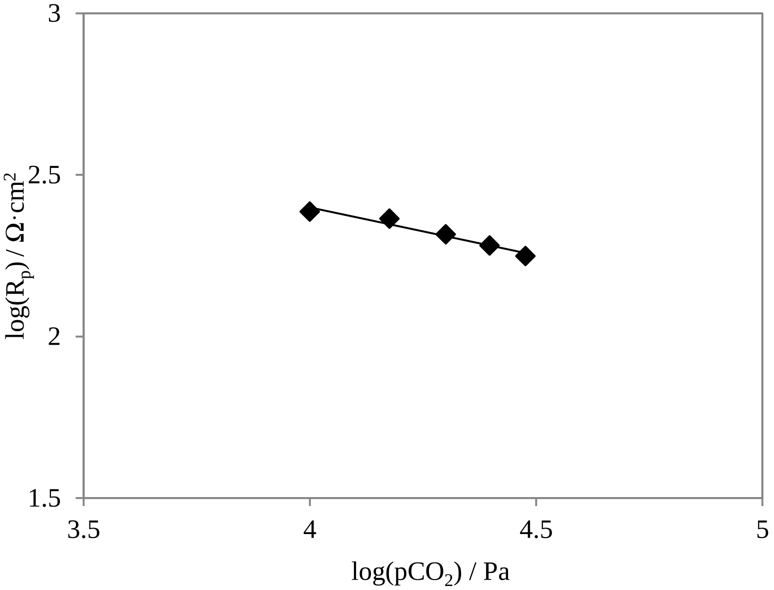

(a)

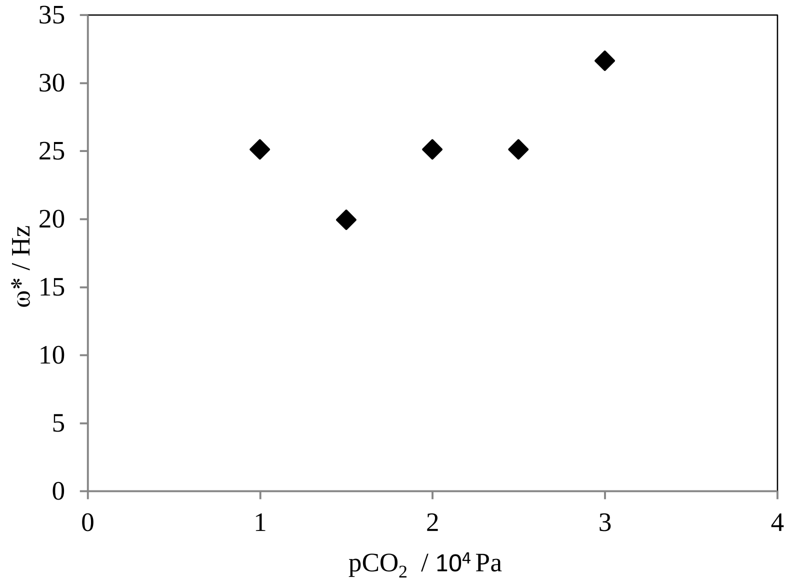

(b)

Figure 6-7 (a) Dependence of R_p and, (b) relaxation frequency on pCO_2, pCO =1.0×10^4 Pa, pCO_2: 1×10^4 - 3×10^4 Pa, T=800°C.

6.3.3 Comparison of Electrochemical Behavior between CO-CO_2 and H_2-H_2O Systems

In this section, the electrochemical performance of Ni/YSZ pattern anodes in CO-CO_2 atmosphere is compared to that in H_2-H_2O atmosphere. Figure 6-8 describes the impedance spectra when the Ni/YSZ pattern anodes were tested with H_2-H_2O and CO-CO_2 mixtures. The test conditions were: $pH_2=2\times10^4$ Pa (20%), $pH_2O=1\times10^4$ Pa (10%) or $pH_2O=3\times10^4$ Pa (30%) for the H_2-H_2O system, and $pCO=2\times10^4$ Pa (20%), $pCO_2=2\times10^4$ Pa (20%) for the CO-CO_2 system. The test temperature was 800°C for both gas mixtures. For the Nyquist plots, the impedance arc of the H_2-H_2O system is about 7.4 times smaller than that of the CO-CO_2 system at OCV. The bode plots (phase angle versus frequency) of the two different gas systems are very different (see Figure 6-8 (b)), and show that more electrode processes contribute to the rate-limiting steps in CO-CO_2 than in H_2-H_2O. This is different from the conclusion that H_2 and CO electro-oxidation proceeds in a similar way as claimed by Utz et al. (2011b).

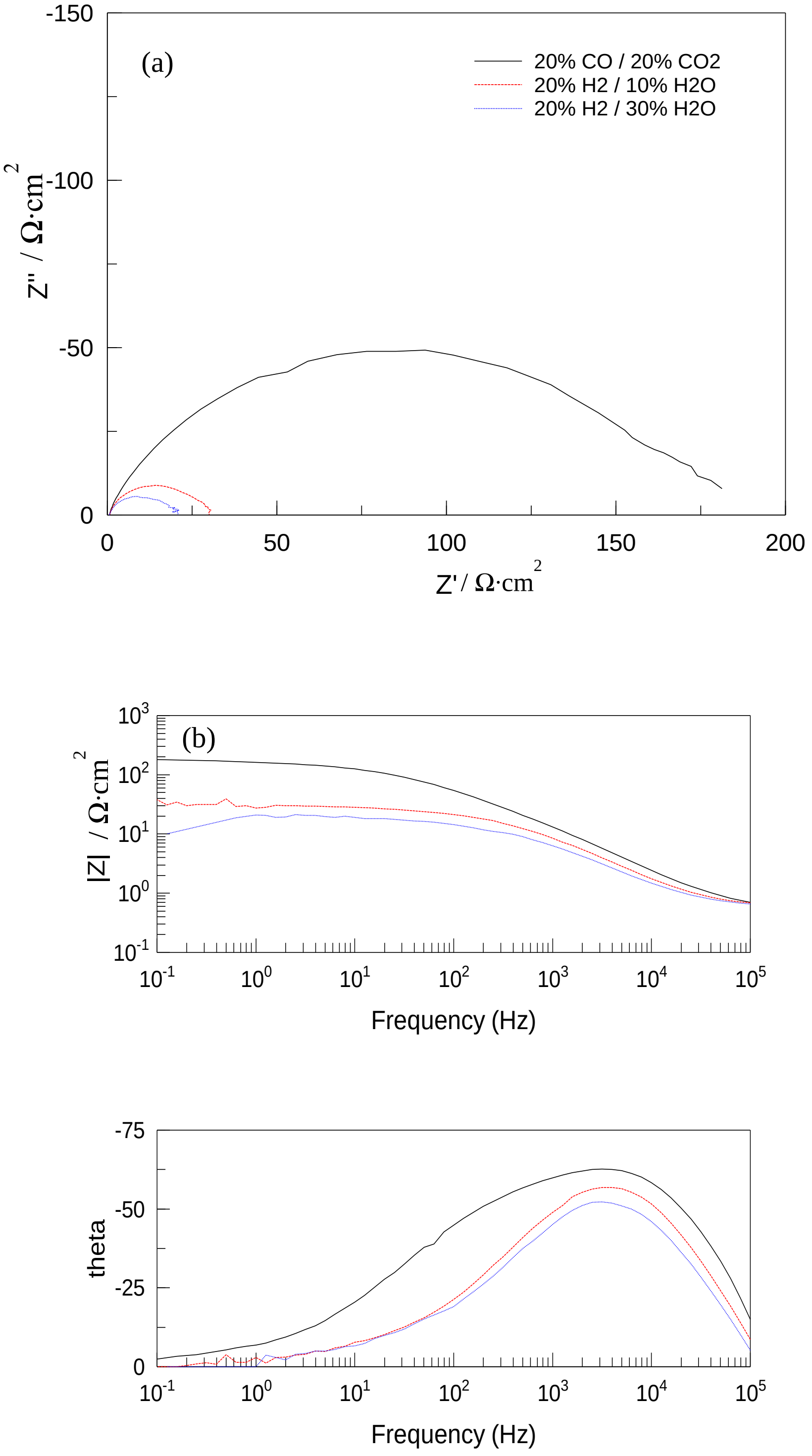

Figure 6-8 Comparison of electrochemical behavior of Ni/YSZ pattern anode between H_2-H_2O and CO-CO_2 systems, (a) Nyquist plots, (b) Bode plots.

For the H_2-H_2O system, the polarization resistance decreased with increasing the amount of fuel (pH_2: 5×10^3 Pa - 3×10^4 Pa). However, an increase of the fuel amount (pCO: 1×10^4 Pa - 3×10^4 Pa) resulted in an increase of polarization resistance for the CO-CO_2 system. In these two atmospheres, an increase in both pH_2O (3×10^3 Pa - 3×10^4 Pa) and pCO_2 (1×10^4 Pa - 3×10^4 Pa) led to a decrease of polarization resistance. Variations of gas compositions for both H_2-H_2O and CO-CO_2 caused a decrease of the polarization resistance and took about 30 min for the polarization resistance to stabilize.

Activation energy for H_2-H_2O of 1.17 eV is obtained for the temperature range of 650-800°C ($pH_2=5\times10^3$ Pa, $pH_2O=3\times10^3$ Pa). For CO-CO_2, the activation energy is 1.04 eV in the temperature range of 700-800°C ($pCO=1\times10^4$ Pa, $pCO_2=2\times10^4$ Pa). For both H_2-H_2O and CO-CO_2 systems, charge transfer reactions are possible rate-limiting steps.

6.4 Conclusions

Electrochemical characterization of Ni/YSZ pattern anode with CO-CO_2 was restricted by the range of gas compositions due to the oxidation of Ni and Boudouard reaction. Gas delivery tube was very susceptible to carbon deposition because of the uneven temperature distribution in the tube. An extra heating tube added to the tube outside the furnace increased the temperature of the tube and greatly alleviate carbon formation in the gas delivery tube.

Electrochemical tests revealed that the polarization resistance depends on the partial pressure of CO and CO_2, temperature and overpotential. The polarization resistance increases when increasing the partial pressure of CO, and the reaction order is -0.5. The partial pressure of CO_2 has a negative effect on the polarization resistance, and the reaction order is 0.3.

The activation energy is 1.04 eV for CO electrochemical oxidation, which is lower than that for H_2 oxidation. For CO-CO_2 system, the polarization resistance experiences a minimum when increasing the overpotential. A minimum polarization resistance appears when the overpotential is 0.1 V. For H_2-H_2O system, the polarization resistance increases exponentially with increasing overpotential in the overpotential range of 0 - 0.3 V.

For both H_2-H_2O and CO-CO_2 systems, charge transfer reactions are possible contributions for the rate-limiting steps.

Chapter 7

Kinetic Modeling studies of Hydrogen Electrochemical Oxidation on Ni/YSZ pattern Anodes

In this study, a kinetic model describing the electrochemical behavior of the H_2/H_2O system on a SOFC pattern anode is presented. The model includes chemical reactions (adsorption/desorption of gas species and surface reactions), electrochemical reactions (charge transfer reactions), and surface diffusion. A simpler H_2 reaction mechanism considering six elementary reactions on Ni surface (Reaction mechanism I) was first studied in this work. One purpose of considering this simpler reaction mechanism was to validate our simulations, by comparison with those of the literature. Simulations of reaction mechanism I were also compared with our experimental data. A more comprehensive reaction mechanism (reaction mechanism II) considering elementary reactions on both Ni and YSZ surfaces was also evaluated in this work. The charge transfer reactions in reaction mechanism II were proposed by Shishkin and Ziegler (2010) based on a DFT study. The two charge transfer reactions involve a hydrogen atom reacting with the oxygen bound to both Ni and YSZ surface producing hydroxyl, which reacts with another hydrogen atom to form water at the interface. The capability of the reaction mechanism II to predict our experimental results was evaluated. All the simulation work was performed using the commercial software gPROMS for solving differential algebraic equations. Gas species were considered as ideal gases.

7.1 Introduction

Extensive studies have been performed in order to elucidate the electrochemical oxidation of H_2 on Ni/YSZ anodes. Researchers usually agree about the overall hydrogen oxidation reaction, which is expressed as (Goodwin et al., 2009; Vogler, 2009):

$$\mathrm{H_2(g) + O_O^X \rightleftharpoons H_2O(g) + V_{\ddot{O}} + 2e^-(Ni)} \qquad 7.1$$

However, controversies still exist regarding the detailed elementary reaction steps.

Several reaction mechanisms of hydrogen oxidation have been proposed through kinetic modeling studies. Bieberle and Gaukler (2002) assumed that the charge transfer reaction is oxygen spillover from YSZ surface to Ni surface. In their work, a kinetic model describing six elementary reaction steps was developed and validated using experimental results from Bieberle et al. (2001). However, effects of water on the anode performance were evaluated only over a small range of operating conditions for both modeling and experimental studies (H_2O: 0.04-2% at 700°C). Also, no studies were performed under cathodic conditions. Moreover, their experimental results varied considerably from sample to sample (Vogler et al., 2009).

Vogler et al. (2009) investigated different charge transfer reactions by comparing simulation results with the experimental data reported by Bieberle et al. (2001). They concluded that hydrogen spillover with water formation on YSZ surface correctly predicts the observed relationship between polarization resistance and H_2 and H_2O partial pressures. Due to lack of experimental data, the model was validated only over a limited range of conditions (H_2O: 0.04-2%).

Goodwin et al. (2009) assumed that hydrogen spills over to the YSZ surface to form hydroxyls, which subsequently spill over back to the Ni surface to form water on the Ni surface. They claimed that this mechanism provides a good fit to the experimentally observed Tafel plots reported by Mizusaki et al. (1994b). Again, both experiments and simulations were conducted in a small range of gas compositions (H_2: 1-10%, H_2O: 0.4-1.7% at 700°C).

Based on density functional theory, Shishkin and Ziegler (2010) proposed that H_2 oxidation occurs primarily on the oxygen ions at the interface between Ni and ZrO_2 (or Y_2O_3). Their DFT study revealed that oxygen vacancy formation at the Ni/YSZ interface was more favorable than at the Ni or YSZ surface. The easier vacancy formation directly leads to more negative charges transferring from the YSZ to the Ni surface. Moreover, it was found that the energy barrier of water formation at the interface is lower than that on Ni or YSZ surface. Thus, the pathway of charge transfer reactions occurring at the interface is more feasible than oxygen and hydrogen spillover pathways.

The main goal of this study is to perform a kinetic study based on the charge transfer reactions proposed by Shishkin and Ziegler (2010) and surface chemical reactions used in Vogler et al. (2009) and evaluate the capability of this model to represent the experimentally observed behavior of H_2 oxidation on Ni/YSZ pattern anodes.

A kinetic model including surface chemical reactions, electrochemical reactions, and surface diffusion of H_2/H_2O system on a SOFC pattern anode was developed and built in gPROMS. In order to check the kinetic model built in gPROMS, a simpler H_2 reaction mechanism considering six elementary steps on the Ni surface was first implemented into the kinetic model, therein referred to as reaction mechanism I. The simulation results from this work were compared with the results reported by Bessler (2005) and Vijay et al. (2010), who investigated the same reaction mechanism. Since our simulation results proved to match with the results in literature, the next step was to investigate the reaction mechanism (reaction mechanism II) with charge transfer reactions proposed by Shishkin and Ziegler (2010) through kinetic studies.

Similar to the experimental procedure, Tafel plots were simulated over a wide range of pH_2 (1×10^4 Pa - 9×10^4 Pa) and pH_2O (3×10^3 Pa - 5×10^4 Pa) conditions. The simulated Tafel plots at different pH_2 were compared with the experimentally determined Tafel plots at 700°C. This temperature was chosen because previous modeling results were also reported at 700°C. In addition, simulated Tafel plots at different pH_2O were compared with experimental Tafel plots at 550°C. As presented in Chapter 4, a stable structure and precise TPB length could be measured when the pattern anode was tested in the percentage of high H_2O (>10%) content at 550°C, but not at 700°C.

Thermodynamic and kinetic parameters for surface chemical reactions at 700 °C were taken from Vogler et al. (2009). Activation energy and changes in Gibbs free energy for charge transfer reactions were taken from Shishkin and Ziegler (2010). Pre-exponential factors for the charge transfer reactions were treated as fitting parameters. At 550°C, more parameters were treated as fitting parameters (to be discussed later) due to a lack of data in the literature at this temperature.

7.2 Modeling Approach

In traditional fuel cell models, electrochemistry is described by overall reactions and the current density is calculated based on the Butler-Volmer equation. This simplified approach cannot fully represent the complex processes occurring at the triple phase boundary (Bessler et al. 2007). In this work, detailed 1-D models representing the coupled behavior of surface chemistry, electrochemistry and surface diffusion were developed. Similar models were also used in previous studies (Bieberle & Gauckler, 2002; Goodwin et al., 2009; Vogler et al., 2009). The model describes not only the electrochemical reactions, but also the non-faradaic chemical reactions and surface-diffusive transport on Ni and YSZ surfaces. The reaction rates of these chemical and electrochemical reactions were obtained through mass-action kinetics. The current density was calculated directly via electrochemical reactions (charge transfer reactions). Both steady-state and dynamic electrode behavior can be simulated with these models.

Simulations Tafel plots were conducted by calculating current density for a series of overpotentials. The current density was obtained by solving the system of equations at each overpotential. Impedance simulations were performed based on the physicochemical processes described above using a transient numerical technique used by Bessler (2005). When a sinusoidal overpotential is imposed, the elementary reaction system exhibits periodic transient behavior. Hence, the resulting current density also exhibits this periodic transient behavior. The impedance can be calculated in the time-domain through numerical integration of the ordinary differential equations (Bessler, 2005; Bessler, 2007). Compared to the widely used equivalent circuit fitting method, this method has the advantage of directly interpreting physicochemical processes occurring on the electrode (Bessler, 2007).

A Ni/YSZ pattern anode half-cell set-up, used by both Goodwin et al. (2009) and Vogler et al. (2009), was chosen for this study. Under the experimental conditions, the cell consists of a dense YSZ disk as the supporting electrolyte, an array of thin, straight Ni strips on one side of the electrolyte. Because of the symmetry of the pattern anode, the domain for the simulations extends from the centre line of the Ni strip to the centre line of the adjacent YSZ strip. As shown in Figure 7-1, d_{Ni} and d_{YSZ} are the widths of Ni and YSZ strips, respectively, while h_{Ni} is the thickness of the Ni layer. The red line in Figure 7-1 (b) is the TPB line.

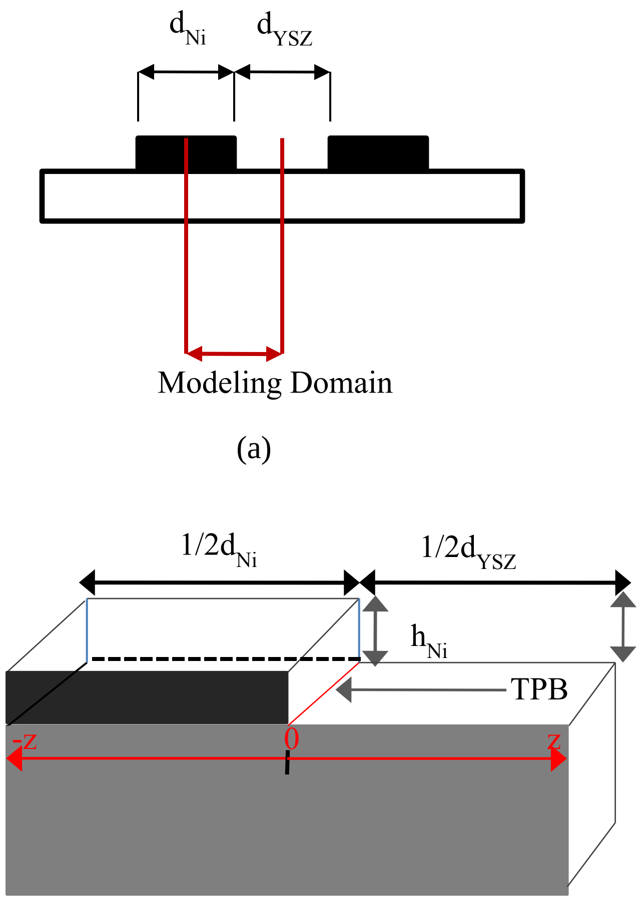

(a)

(b)

Figure 7-1 (a) Side view of the pattern anode, (b) the half-cell model (Vogler et al., 2009)

7.3 Model Formulation

7.3.1 Elementary Chemical Reaction Steps

Both Ni and YSZ surface chemical reactions in this study are written as reversible elementary reaction steps. The general form of the chemical reaction is expressed as:

$$A_i + B_i \underset{k_{r,m}}{\overset{k_{f,m}}{\rightleftharpoons}} C_i + D_i \tag{7.2}$$

where m corresponds to surface reactions that include adsorption/desorption of gas species and surface reactions, A_i, B_i, C_i *and* D_i are species involved in these reactions, $k_{f,m}$, and $k_{r,m}$ are the forward and reverse reaction-rate constants.

The reaction rate for forward and reverse reactions can be represented using Equations 7.3-7.10. The forward reaction rate constants are calculated using Arrhenius expressions, and the reverse reaction rate constants are obtained in a thermodynamically consistent way (Fogler, 1999; Hecht et al., 2005, Li, 2005).

$$r_{f,m} = k_{f,m} \prod_{i \in R_{f,m}} c_i^{v_i'} \tag{7.3}$$

$$k_{f,m} = k_{f,m}^{0} T^{\beta_m} \exp(-E_{f,m}^{act} / RT) \tag{7.4}$$

$$r_{r,m} = k_{r,m} \prod_{i \in R_{r,m}} c_i^{v_i''} \tag{7.5}$$

$$k_{r,m} = k_{f,m} exp\ (\Delta G_m\ /\ RT) \tag{7.6}$$

$$\Delta G_m = \sum_{i \in R_{f,m}} v_{i,m}'(h_i - Ts_i) - \sum_{i \in R_{r,m}} v_{i,m}''(h_i - Ts_i) \tag{7.7}$$

$$h_i = h_{0,i} + C_p(T - T_{ref}) \tag{7.8}$$

$$C_p = a' + \frac{1}{2} b'(T + T_{ref}) \tag{7.9}$$

$$s_i = s_{0,i} + a'(ln\, T - ln\, T_{ref}) + b'(T - T_{ref}) \tag{7.10}$$

Here, $r_{f,m}$ and $r_{r,m}$ represent forward and reverse reaction rates (mol/(s cm^2)), c_i is the area-specific concentration of species *i* (mol/cm^2), v_i', v_i'' are stoichiometric coefficients of species *i* in the forward and reverse reactions, $k_{f,m}^{0}$ is the pre-exponential factor of the forward reaction, $E_{f,m}^{act}$ is the activation energy for the forward reaction (kJ/mol), β_m is the temperature coefficient. ΔG_m is the Gibbs free energy change of the reaction (kJ/mol), h_i (kJ/mol) and s_i (J/(K mol)) are molar enthalpy and molar entropy of species *i* at temperature T (K). h_0 and s_0 are molar enthalpy and molar entropy of species *i* at reference temperature T_{ref}: 25°C, C_p is the average specific heat over the temperature range involved. a' and b' are constants used to calculate the average specific heat.

The concentration change of surface species *i* due to chemical reactions is given by Equation 7.11 (Fogler, 1999; Bieberle & Gauckler, 2002)

$$\frac{dc_i}{dt} = \sum_{\mathrm{i}}^{\mathrm{m}} (v_i' * r_{f,m} - v_i'' * r_{r,m}) \tag{7.11}$$

For surface chemistry, the reaction rate is usually expressed in the form of surface coverage (θ_i), which is defined as (Bieberle & Gauckler, 2002; Li, 2005)

$$\theta_i = c_i / N_k \qquad 7.12$$

$$\sum \theta_i = 1$$

where N_k is the area-specific density of Ni or YSZ (mol/cm^2). The surface coverage of species *i* is between 0 and 1 and the total surface coverage of all the species is 1. Usually, the unfilled surface sites are also considered as an individual species (Goodwin et al., 2009).

7.3.2 Charge Transfer (CT) Reactions

Charge transfer reaction rates directly determine the faradaic current produced. They are expressed in the same way as those for the chemical reactions (Bieberle & Gauckler, 2002; Li, 2005; Vogler et al., 2009).

$$r_{CT,k} = k_{CT,f} \prod_{i \in R_{f,k}} c_i^{v_i'} - k_{CT,r} \prod_{i \in R_{r,k}} c_i^{v_i''} \qquad 7.13$$

$$k_{CT,f} = k_{CT,f}^0 \exp(-E_{CT,f} / RT) \, exp(\alpha n F \eta / RT) \qquad 7.14$$

$$k_{CT,r} = k_{CT,f}^0 \exp(-E_{CT,f} / RT) \, exp\,(\Delta G_{CT} \,/\, RT) \, exp\,(-(1-\alpha) n F \eta / RT) \quad 7.15$$

where $r_{CT,k}$ is the net reaction rate of the charge transfer reaction *k* (mol/(s cm), $k_{CT,f}$, $k_{CT,r}$ are forward and reverse reaction rate constants (cm^3/(mol s)), $k_{CT,f}^0$ (cm^3/(mol s)) and $E_{CT,f}$ (kJ/mol) are pre-exponential coefficient and activation energy of the forward reaction respectively, ΔG_{CT} (kJ/mol) is the Gibbs free energy change of the charge transfer reaction, *n* is the number of electron transferred in the electrochemical reaction, α is the transfer coefficient, η is the overpotential, and *F* is the Faraday constant (96,487 C/mol).

The faradaic current density produced due to a charge transfer reaction is described as (Bessler, 2005; Vogler et al., 2009):

$$j_F = nFL_{TPB} r_{CT,k} \,,\ j_{F,T} = \sum_{all\ CTRs} j_F \qquad 7.16$$

where j_F is the current density (A/cm^2), L_{TPB} is the TPB length (cm/cm^2). The total current density $j_{F,T}$ is the sum of current density produced by all the charge transfer reactions.

7.3.3 Surface Diffusion

Surface diffusion is described by Fick's law, as shown in Equation 7.17 (Fogler, 1999; O'Hayre, et al., 2006).

$$J_i = -D_i \frac{dc_i}{dz} \quad 7.17$$

$$D_i = D_i^0 \exp(-\frac{E_i^{act}}{RT}) \quad 7.18$$

where J_i is the surface flux of adsorbate i (mol/cm s), c_i is the concentration of species i (mol/cm^2), D_i is the surface diffusion coefficient of species i (cm^2/s), z is the distance along the surface perpendicular to the TPB line (cm), D_i^0 is the pre-exponential constant (cm^2/s), and E_i^{act} is the activation energy (kJ/mol) for the surface diffusion.

The change in surface concentration of adsorbed species i, which is described in Equation 7.19, is determined by both chemical reaction and surface diffusion (Vogler et al., 2009).

$$\frac{dc_i}{dt} = \sum_{\mathrm{i}}^{\mathrm{m}} (v_i' * r_{f,m} - v_i'' * r_{r,m}) - \frac{dJ_i}{dz} \quad 7.19$$

Due to the symmetry of the model, the boundary conditions are (Goodwin et al., 2009):

At $z = -\frac{1}{2} d_{Ni}$ and $z = \frac{1}{2} d_{YSZ}$,

$$J_i = 0 \quad 7.20$$

At the interface of Ni and YSZ (z=0), for reactant species directly involved in the charge transfer reactions,

$$J_i = -j_F/nF \quad 7.21$$

For product species directly involved in the charge transfer reactions,

$$J_i = j_F/nF \quad 7.22$$

For those surface species that are not involved in charge transfer reactions,

$$J_i = 0 \quad 7.23$$

7.3.4 EIS Simulations

For the EIS simulations, a transient numerical technique based on the method reported by Bessler (2005) and Shi et al. (2008) was used. The imposed voltage which serves as the input signal, contains a stationary part E_{st} *(V)* and a transient part $E_v \sin(\omega t)$, as shown in Equation 7.24. The stationary part represents the bias voltage used in the EIS measurements and the transient part is the sinusoidal perturbation in voltage (Bessler, 2005; Shi et al., 2008).

$$E(t) = E_{st} + E_v sin(\omega t) \qquad 7.24$$

$$\omega = \frac{2\pi}{\tau} = 2\pi f$$

where E_v is the perturbation amplitude of the voltage (V), ω is the angular frequency (measured in radians per second), f is the frequency (Hz) and τ is the period of the sinusoidal signal.

In this study, a small perturbation amplitude of E_v (10 mV) was applied to obtain a pseudo-linear current response. The corresponding current response with time is described as (Bessler, 2005; Shi et al., 2008):

$$i(t) = i_{st} + i_v sin(\omega t - \varphi) \qquad 7.25$$

where i_{st} is the stationary part of the current (A), i_v is the amplitude of the harmonic current, and φ is the phase angle change from the imposed voltage to the current.

The following two time integrals were used to calculate i_v and φ, which were used in real and imaginary parts of the impedance calculation (Bessler, 2005; Shi et al., 2008).

$$i_v cos\varphi = \frac{2}{\tau}\int_0^{\tau} i\,(t) sin(\omega t)\, dt \qquad 7.26$$

$$i_v sin\varphi = \frac{2}{\tau}\int_0^{\tau} i\,(t) cos(\omega t)\, dt \qquad 7.27$$

The impedance response can be calculated as (Shi et al., 2008):

$$Z = \frac{E}{i} = \frac{E_v exp(j'\omega t)}{i_v exp(j'\omega t - j'\varphi)} = Z' + Z'' = \frac{E_v}{i_v} cos\varphi + j' \frac{E_v}{i_v} sin\varphi \qquad 7.28$$

In order to solve the system of equations in gPROMS, two variables (X1 and X2), representing the left-hand side of Equations 7.26 and 7.27, were introduced (see Equations 7.29 and 7.31). Equations 7.26 and 7.27 were then written in the form of time derivatives

(Equations 7.30 and 7.32), and where integrated over one full period (τ). Simulated periodic steady-state was achieved usually within 10 periods, depending on the initial guesses. The impedance was then simulated for a given frequency. i_v and φ were calculated based on equation 7.29 and 7.31, and then Z' and Z'' were calculated separately (Hofmann & Panopoulos, 2010).

$$X1 = i_v cos\varphi \qquad 7.29$$

$$\frac{\partial X1}{\partial t} = 2f \cdot i\,(t) sin(2\pi f \cdot t) \qquad 7.30$$

$$X2 = i_v sin\varphi \qquad 7.31$$

$$\frac{\partial X2}{\partial t} = 2f \cdot i\,(t) cos(2\pi f \cdot t) \qquad 7.32$$

7.4 Investigation of Hydrogen Oxidation at Ni/YSZ Interface

In order to check the developed kinetic model, the model was first implemented for a simpler H_2 reaction mechanism proposed by Bieberle & Gauckler (2002), referred therein as reaction mechanism I. The simulation results based on reaction mechanism I were compared to the results presented in previous studies (Bessler, 2005; Vijay et al., 2010) and our experimental results. In the next step, a more comprehensive model was used to investigate the charge transfer reaction mechanism proposed by Shishkin and Ziegler (2010) (referred to as reaction mechanism II). Simulated results for reaction mechanism II were compared to the experimental results presented in chapter 5, while best fits were achieved by adjusting some parameters (mostly charge transfer rate constants). Non-fitted parameters were taken from different literature sources.

7.4.1 Reaction Mechanism I

The mechanism proposed by Bieberle & Gauckler (2002), which was also used by Bessler (2005) and Vijay et al. (2010) includes six elementary reaction steps on Ni surface. Adsorption and dissociation of H_2 and H_2O are assumed to occur only on the Ni surface. The charge transfer reaction is assumed to be oxygen spillover from the YSZ surface to the Ni surface. The detailed elementary reaction steps and the corresponding kinetic parameters are given in Table 7-1.

Table 7-1 Six-step elementary reactions and kinetic parameters (Bessler, 2005)

	Reversible reactions	Forward reaction rate constants (1/s) at 700°C	Reverse reaction rate constants (1/s) at 700°C
1	$O_O^X + (Ni) \underset{k_{r,1}}{\overset{k_{f,1}}{\rightleftharpoons}} O_{Ni} + V_{\ddot{O}} + 2e^-(Ni)$	2×10^{2} (η=0)	5.6×10^{10} (η=0)
2	$H_{Ni} + O_{Ni} \underset{k_{r,2}}{\overset{k_{f,2}}{\rightleftharpoons}} OH_{Ni} + (Ni)$	2×10^{11}	1.3×10^{4}
3	$H_2O_{Ni} + O_{Ni} \underset{k_{r,3}}{\overset{k_{f,3}}{\rightleftharpoons}} 2OH_{Ni}$	1×10^{12}	5.8×10^{2}
4	$OH_{Ni} + H_{Ni} \underset{k_{r,4}}{\overset{k_{f,4}}{\rightleftharpoons}} H_2O_{Ni} + (Ni)$	1.5	6×10^{5}
5	$H_2O + (Ni) \underset{k_{r,5}}{\overset{k_{f,5}}{\rightleftharpoons}} H_2O_{Ni}$	8×10^{4}	1×10^{11}
6	$H_2 + 2(Ni) \underset{k_{r,6}}{\overset{k_{f,6}}{\rightleftharpoons}} 2H_{Ni}$	6×10^{7}	2.4×10^{8}

In this system, only the Ni surface was assumed to be active for all the elementary reactions. There are in total nine species, including two gas phase species (H_2, H_2O), four surface species (H_{Ni}, O_{Ni}, OH_{Ni}, H_2O_{Ni}), and two bulk species (lattice oxygen (O_O^X) and oxygen vacancy ($V_{\ddot{O}}$)). The free surface of Ni is also considered as a single species. The fractional surface coverages are related as follows:

$$\theta(Ni) = 1 - (\theta(H_{Ni}) + \theta(O_{Ni}) + \theta(H_2O_{Ni}) + \theta(OH_{Ni})) \tag{7.33}$$

The rate equations for all surface species are described as follows (Bessler, 2005; Bieberle & Gauckler, 2002; Vijay et al., 2010):

$$\frac{d\theta(O_{Ni})}{dt} = k_{f,1}\theta(Ni) - k_{r,1}\theta(O_{Ni}) - k_{f,2}\theta(O_{Ni})\theta(H_{Ni}) + k_{r,2}\theta(OH_{Ni})\theta(Ni) - k_{f,3}\theta(O_{Ni})\theta\left(H_2O_{Ni}\right) + k_{r,3}\theta(OH_{Ni})^2 \tag{7.34}$$

$$\frac{d\theta(H_{Ni})}{dx} = -k_{f,2}\theta(O_{Ni})\theta(H_{Ni}) + k_{r,2}\theta(OH_{Ni})\theta(Ni) - k_{f,4}\theta(H_{Ni})\theta(OH_{Ni}) + k_{r,4}\theta\left(H_2O_{Ni}\right)\theta(Ni) + 2k_{f,6}\theta(Ni)^2 - 2k_{r,6}\theta(H_{Ni})^2 \tag{7.35}$$

$$\frac{d\theta(OH_{Ni})}{dx} = k_{f,2}\theta(O_{Ni})\theta(H_{Ni}) - k_{r,2}\theta(OH_{Ni})\theta(Ni) + 2k_{f,3}\theta(O_{Ni})\theta\left(H_2O_{Ni}\right) - 2k_{r,3}\theta(OH_{Ni})^2 - k_{f,4}\theta(H_{Ni})\theta(OH_{Ni}) + k_{r,4}\theta\left(H_2O_{Ni}\right)\theta(Ni) \tag{7.36}$$

$$\frac{d\theta(H_2O_{Ni})}{dx} = -k_{f,3}\theta(O_{Ni})\theta\left(H_2O_{Ni}\right) + k_{r,3}\theta(OH_{Ni})^2 + k_{f,4}\theta(H_{Ni})\theta(OH_{Ni}) - k_{r,4}\theta\left(H_2O_{Ni}\right)\theta(Ni) + k_{f,5}\theta(Ni) - k_{r,5}\theta\left(H_2O_{Ni}\right) \tag{7.37}$$

The simulation for mechanism I was performed at 700°C. Rate constants for the charge transfer reaction depend on the overpotential. When a time dependent overpotential is imposed, the rate constants for the charge transfer reactions will also be time dependent. Charge transfer reaction rate constants are expressed as (Bessler, 2005; Bieberle & Gauckler, 2002; Vijay et al., 2010):

$$k_{f,1} = k_{f,1}^0 exp\left(\frac{\alpha nF\eta}{RT}\right) \tag{7.38}$$

$$k_{r,1} = k_{r,1}^0 exp\left(\frac{-(1-\alpha)nF\eta}{RT}\right) \tag{7.39}$$

here, $k_{f,1}^0$ and $k_{r,1}^0$ are the reaction rate constants (*1/s*) when the overpotential is 0. $\mathrm{O}_{\mathrm{O}}^{\mathrm{X}}$ and $\mathrm{V}_{\ddot{\mathrm{O}}}$ are also assumed to be constant and are incorporated into $k_{f,1}^0$ and $k_{r,1}^0$. The values of $k_{f,1}^0$ and $k_{r,1}^0$ at 700°C are given in Table 7-1.

7.4.2 Reaction Mechanism II

In the reaction mechanism II, Ni and YSZ surface reactions are the same as those used in Vogler et al. (2009). The difference with the Vogler et al. reaction mechanism resides in different charge transfer reactions that are taken from the work of Shishkin and Ziegler (2010). Unlike in reaction mechanism I, multiple elementary reactions of H_2/H_2O system were considered to happen on both Ni and YSZ surfaces in reaction mechanism II. Adsorption and dissociation of H_2 are still assumed to take place on the Ni surface only, whereas adsorption and dissociation of H_2O is allowed to occur on both Ni and YSZ surfaces.

Table 7-2 summarizes the elementary reaction steps on Ni and YSZ surfaces, as well as the corresponding kinetic parameters (pre-exponential factors and activation energy for forward reactions at 700°C) used in reaction mechanism II. On the Ni surface, pre-exponential factors of the reactions 4 and 5 in Table 7-2 from different literature sources vary significantly (several orders of magnitude). Pre-exponential factors for YSZ surface reactions are much less studied, and not fully validated (Vogler et al. 20009). We took most of these kinetic parameters from Vogler et al. (2009). But the pre-exponential factors for reaction 1, 4 and 5 are slightly different from that in Vogler et al. (2009). In our work, the concentrations of H_2 or H_2O are incorporated into these the values of theses pre-exponential factors. Therefore, their units are 1/s. The reverse reaction rate constants are calculated based on equilibrium constants. Ni and YSZ surface densities are taken as 1.3 mol/cm^2 and 6.1 mol/cm^2, respectively (Vogler et al., 2009).

Regarding the charge transfer reactions, Shishkin and Ziegler (2010) claimed that oxygen vacancy formation at the interface of Ni/YSZ is more favorable than at the YSZ surface, which results in more negative charges being transferred from YSZ to Ni surface. Moreover, it was found that the energy barrier of water formation at the interface was lower than that on Ni or YSZ surface. These indicate that charge transfer reactions occurring at the interface are more likely than oxygen and hydrogen spillover. In addition, water produced at the interface is assumed to be in gas phase, since the energy barrier for water desorption from the interface is very small based on DFT calculations (Shishkin & Ziegler, 2010). The charge transfer reactions are listed in Reactions 7.40 and 7.41, and schematically demonstrated in Figure 7-2. H_2 oxidation at the Ni/YSZ interface involves a hydrogen atom reacting with the oxygen bound to both Ni and YSZ surfaces to produce hydroxyl, which reacts with the other hydrogen atom to form water. The oxygen ions at the interface are assumed to be from reaction 2 in Table 7-2. Hydroxyl ions at the interface are contributed by both reaction 7.40 and reaction 2 in Table 7-2.

$$\mathrm{H_{Ni} + O^{2-}_{inter} \rightleftharpoons OH^{-}_{inter} + (Ni) + e^{-}_{Ni}} \qquad 7.40$$

$$\mathrm{H_{Ni} + OH^{-}_{inter} \rightleftharpoons H_2O_{gas} + (inter) + (Ni) + e^{-}_{Ni}} \qquad 7.41$$

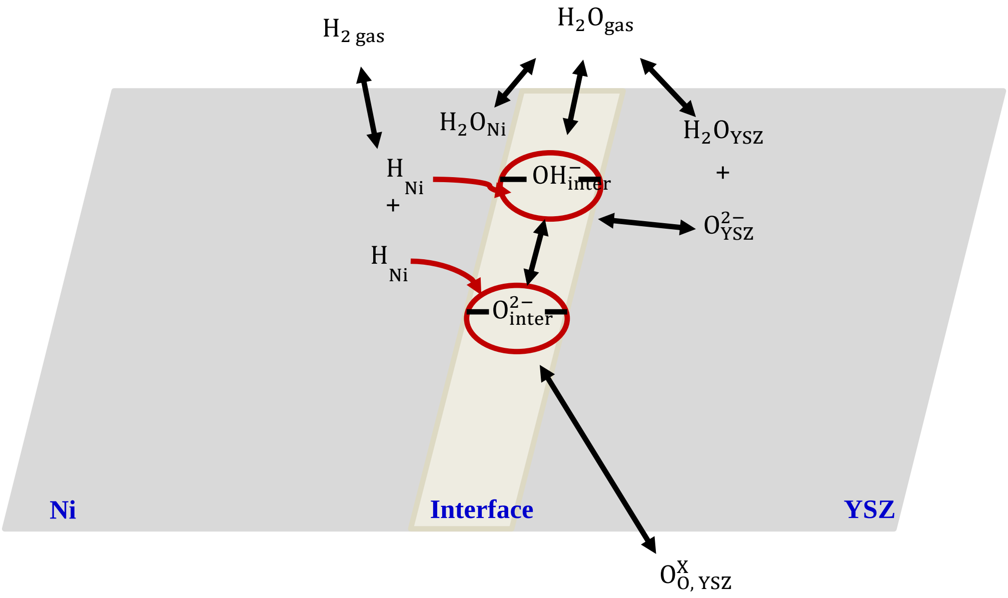

Figure 7-2 Schematic illustration of hydrogen oxidation at the interface of Ni/YSZ

Reaction mechanism II involves two gas phase species (H_2, H_2O), four Ni surface species (H_{Ni}, O_{Ni}, OH_{Ni}, H_2O_{Ni}), three YSZ surface species (H_2O_{YSZ}, O^{2-}_{YSZ}, OH^{-}_{YSZ}), two bulk species (lattice oxygen(O^{X}_{O}) and oxygen vacancy($V_{\ddot{O}}$)), and three species at the interface (O^{2-}_{inter} , OH^{-}_{inter} , and free surface (inter)). The Ni free surface (Ni) and YSZ free surface (YSZ) are also considered as two single species. At 700°C, Shishkin and Ziegler (2010) calculated the activation energy for the forward reactions of the charge transfer reactions and obtained 13 kJ/mol and 154.9 kJ/mol for charge reactions 7.40 and 7.41, respectively. Changes in Gibbs free energy of the charge transfer reactions obtained through the DFT calculations are 113 kJ/mol and -75.4 kJ/mol, respectively.

In order to evaluate the effects of surface diffusion on the pattern anode performance, models without and with surface diffusion were developed in gPROMS when evaluating reaction mechanism II. Equations describing the reaction rates of chemical reactions on Ni and YSZ surfaces are given in Table 7-3. Reaction rate equations used in the model without surface diffusion (model II-1) are given in Table 7-4. Equations used in the model with surface diffusion (model II-2) are presented in Table 7-5. Surface diffusion parameters are taken from Vogler et al. (2009) and listed in Table 7-6.

Table 7-2 Elementary reaction steps and kinetic parameters used in Vogler et al. (2009)

	Reversible reactions	Pre-exponential factor (k_m^0)	Activation energy (E_m^{act}) (kJ/mol)	β_m
1	$H_2O_{gas} + (YSZ) \underset{k_{-1}}{\overset{k_1}{\rightleftharpoons}} H_2O_{YSZ}$	6.6×10^{11} 1/s	0	0.5
2	$O^{2-}_{YSZ} + H_2O_{YSZ} \underset{k_{-2}}{\overset{k_2}{\rightleftharpoons}} 2\ OH^{-}_{YSZ}$	1.6×10^{22} $cm^2/(mol\ s)$	9.6	0
3	$V_{\ddot{O}}(YSZ) + O^{2-}_{YSZ} \underset{k_{-3}}{\overset{k_3}{\rightleftharpoons}} O^{X}_{O}(YSZ) + (YSZ)$	1.6×10^{22} $cm^2/(mol\ s)$	90.9	0
4	$H_2O_{gas} + (Ni) \underset{k_{-4}}{\overset{k_4}{\rightleftharpoons}} H_2O_{Ni}$	1.4×10^{10} 1/s	0	0.5
5	$H_{2\ gas} + 2(Ni) \underset{k_{-5}}{\overset{k_5}{\rightleftharpoons}} 2H_{Ni}$	9.8×10^{17} 1/s	0	0.5
6	$H_{Ni} + O_{Ni} \underset{k_{-6}}{\overset{k_6}{\rightleftharpoons}} OH_{Ni} + (Ni)$	5.0×10^{22} $cm^2/(mol\ s)$	97.0	0
7	$H_2O_{Ni} + O_{Ni} \underset{k_{-7}}{\overset{k_7}{\rightleftharpoons}} 2OH_{Ni}$	5.4×10^{23} $cm^2/(mol\ s)$	20.9	0
8	$OH_{Ni} + H_{Ni} \underset{k_{-8}}{\overset{k_8}{\rightleftharpoons}} H_2O_{Ni} + (Ni)$	3.0×10^{20} $cm^2/(mol\ s)$	43.0	0

Table 7-3 Equations describing reaction rates of chemical reactions on Ni and YSZ surfaces

$k_1 = k_1^0 T^{\beta_1} exp\left(\frac{-\Delta E_1}{RT}\right)$	$k_{-1} = k_1 exp\left(\frac{\Delta G_1}{RT}\right)$
$k_2 = k_2^0 T^{\beta_2} exp\left(\frac{-\Delta E_2}{RT}\right)$	$k_{-2} = k_2 exp\left(\frac{\Delta G_2}{RT}\right)$
$k_3 = k_3^0 T^{\beta_3} exp\left(\frac{-\Delta E_3}{RT}\right)$	$k_{-3} = k_3 exp\left(\frac{\Delta G_3}{RT}\right)$
$k_4 = k_4^0 T^{\beta_4} exp\left(\frac{-\Delta E_4}{RT}\right)$	$k_{-4} = k_4 exp\left(\frac{\Delta G_4}{RT}\right)$
$k_5 = k_5^0 T^{\beta_5} exp\left(\frac{-\Delta E_5}{RT}\right)$	$k_{-5} = k_5 exp\left(\frac{\Delta G_5}{RT}\right)$
$k_6 = k_6^0 T^{\beta_6} exp\left(\frac{-\Delta E_6}{RT}\right)$	$k_{-6} = k_6 exp\left(\frac{\Delta G_6}{RT}\right)$
$k_7 = k_7^0 T^{\beta_7} exp\left(\frac{-\Delta E_7}{RT}\right)$	$k_{-7} = k_7 exp\left(\frac{\Delta G_7}{RT}\right)$
$k_8 = k_8^0 T^{\beta_8} exp\left(\frac{-\Delta E_8}{RT}\right)$	$k_{-8} = k_8 exp\left(\frac{\Delta G_8}{RT}\right)$
$k_{f,CT1} = k_{CT1}^0\ exp\left(-\frac{\Delta E_{CT1}}{RT}\right) exp\left(\frac{\alpha zF\eta}{RT}\right)$	$k_{r,CT1} = k_{CT1}^0\ exp\left(-\frac{\Delta E_{CT1}}{RT}\right) exp\left(\frac{\Delta G_{CT1}}{RT}\right) exp\left(\frac{-(1-\alpha)zF\eta}{RT}\right)$
$k_{f,CT2} = k_{CT2}^0\ exp\left(-\frac{\Delta E_{CT2}}{RT}\right) exp\left(\frac{\alpha zF\eta}{RT}\right)$	$k_{r,CT2} = k_{CT2}^0\ exp\left(-\frac{\Delta E_{CT2}}{RT}\right) exp\left(\frac{\Delta G_{CT2}}{RT}\right) exp\left(\frac{-(1-\alpha)zF\eta}{RT}\right)$
$\Delta G_1 = (h_{H_2O,YSZ} - h_{H_2O,gas}) - T(s_{H_2O,YSZ} - s_{H_2O,gas})$	$\Delta G_2 = (2h_{OH^-_{YSZ}} - h_{H_2O,YSZ} - h_{O^{2-}_{YSZ}}) - T(2s_{OH^-_{YSZ}} - s_{H_2O,YSZ} - s_{O^{2-}_{YSZ}}))$
$\Delta G_3 = (h_{O^X_{O,YSZ}} - h_{O^{2-}_{YSZ}} - h_{V_{\ddot{O},YSZ}}) - T(s_{O^X_{O,YSZ}} - s_{O^{2-}_{YSZ}} - s_{V_{\ddot{O},YSZ}})$	$\Delta G_4 = (h_{H_2O,Ni} - h_{H_2O,gas}) - T(s_{H_2O,Ni} - s_{H_2O,gas})$
$\Delta G_5 = (2h_{H,Ni} - h_{H_2,gas}) - T(2s_{H,Ni} - s_{H_2,gas})$	$\Delta G_6 = (h_{OH,Ni} - h_{H,Ni} - h_{O,Ni}) - T(s_{OH,Ni} - s_{H,Ni} - s_{O,Ni})$
$\Delta G_7 = (2h_{OH,Ni} - h_{H_2O,Ni} - h_{O,Ni}) - T(2s_{OH,Ni} - s_{H_2O,Ni} - s_{O,Ni})$	$\Delta G_8 = \left(h_{H_2O,Ni} - h_{H,Ni} - h_{OH,Ni}\right) - T(s_{H_2O,Ni} - s_{H,Ni} - s_{OH,Ni})$
$r_1 = N_{YSZ}(k_1 \frac{P(H_2O)}{RT} * \theta_{YSZ} - k_{-1}\theta_{H_2O,YSZ})$	$r_2 = k_2 * N_{YSZ} * N_{YSZ}\ \theta_{H_2O,YSZ}\theta_{O^{2-}_{YSZ}} - k_{-2}N_{YSZ} * N_{YSZ}\theta^2_{OH^-_{YSZ}}$
$r_3 = k_3 * \left[V^{\cdot\cdot}_{O,YSZ}\right] * N_{YSZ}\ \theta_{O^{2-}_{YSZ}} - k_{-3} * \left[O^X_{O,YSZ}\right] * N_{YSZ}\ \theta_{YSZ}$	$r_4 = k_4 * \frac{P(H_2O)}{RT} * N_{Ni} * \theta_{Ni} - k_{-4} * N_{Ni}\ \theta_{H_2O,Ni}$
$r_5 = k_5 * \frac{P(H_2)}{RT} * N_{Ni} * N_{Ni} * \theta^2_{Ni} - k_{-5} * N_{Ni} * N_{Ni} * \theta^2_{H,Ni}$	$r_6 = k_6 * N_{Ni} * N_{Ni} * \theta_{H,Ni}\ \theta_{O,Ni} - k_{-6} * N_{Ni} * N_{Ni} * \theta_{OH,Ni}\ \theta_{Ni}$
$r_7 = k_7 * N_{Ni} * N_{Ni} * \theta_{H_2O,Ni}\ \theta_{O,Ni} - k_{-7} * N_{Ni} * N_{Ni} * \theta^2_{OH,Ni}$	$r_8 = k_8 * N_{Ni} * N_{Ni} * \theta_{H,Ni}\ \theta_{OH,Ni} - k_{-8} * N_{Ni} * N_{Ni} * \theta_{H_2O,Ni}\ \theta_{Ni}$

Table 7-4 Reaction rate equations used in model II-1 (reaction mechanism II without surface diffusion)

Reaction rates for charge transfer reactions	$r_9 = N_{Ni} N_{YSZ} (k_9 \theta_{H,Ni} \theta_{O^{2-}_{inter}} - k_{-9} \theta_{OH^-_{inter}} \theta_{Ni})$
	$r_{10} = N_{Ni} N_{YSZ} (k_{10} \theta_{H,Ni} \theta_{OH^-_{inter}} - k_{-10} \theta_{inter} \theta_{Ni} (\frac{P(H_2O)}{RT}))$
Surface coverages of YSZ surface species	$\frac{\partial\, \theta_{H_2O,YSZ}}{\partial t} = \frac{r_1}{N_{YSZ}} - \frac{r_2}{N_{YSZ}}$
	$\frac{\partial\, \theta_{O^{2-}_{YSZ}}}{\partial t} = -\frac{r_2}{N_{YSZ}} - \frac{r_3}{N_{YSZ}} - \frac{r_9}{N_{YSZ}}$
	$\frac{\partial\, \theta_{OH^-_{YSZ}}}{\partial t} = \frac{2r_2}{N_{YSZ}} + \frac{r_9}{N_{YSZ}} - \frac{r_{10}}{N_{YSZ}}$
	$\theta_{YSZ} = 1 - \theta_{H_2O,YSZ} - \theta_{O^{2-}_{YSZ}} - \theta_{OH^-_{YSZ}}$
Surface coverages of Ni surface species	$\frac{\partial \theta_{H,Ni}}{\partial t} = \frac{2r_5}{N_{Ni}} - \frac{r_6}{N_{Ni}} - \frac{r_8}{N_{Ni}} - \frac{r_9}{N_{Ni}} - \frac{r_{10}}{N_{Ni}}$
	$\frac{\partial \theta_{OH,Ni}}{\partial t} = \frac{r_6}{N_{Ni}} + \frac{2r_7}{N_{Ni}} - \frac{r_8}{N_{Ni}}$
	$\frac{\partial\, \theta_{H_2O,Ni}}{\partial t} = \frac{r_4}{N_{Ni}} - \frac{r_7}{N_{Ni}} + \frac{r_8}{N_{Ni}}$
	$\frac{\partial \theta_{O,Ni}}{\partial t} = -\frac{r_6}{N_{Ni}} - \frac{r_7}{N_{Ni}}$
	$\theta_{Ni} = 1 - \theta_{H,Ni} - \theta_{OH,Ni} - \theta_{O,Ni} - \theta_{H_2O,Ni}$
Surface coverages of Ni/YSZ interface species	$\theta_{O^{2-}_{inter}} = \theta_{O^{2-}_{YSZ}};\ \theta_{OH^-_{inter}} = \theta_{OH^-_{YSZ}};\ \theta_{inter} = 1 - \theta_{O^{2-}_{inter}} - \theta_{OH^-_{inter}}$
Current density	$j_F = nFL_{TPB}(r_9 + r_{10})$

Table 7-5 Reaction rate equations used in in model II-2 (with surface diffusion)

Surface coverages of YSZ surface species	On the YSZ surface	$\frac{\partial\theta_{H_2O,YSZ}}{\partial t}=\frac{r_1}{N_{YSZ}}-\frac{r_2}{N_{YSZ}}-\frac{\partial J_{H_2O,YSZ}}{\partial z}\frac{1}{N_{YSZ}}$	$\frac{\partial\theta_{O^{2-}_{YSZ}}}{\partial t}=-\frac{r_2}{N_{YSZ}}-\frac{r_3}{N_{YSZ}}-\frac{\partial J_{O^{2-}_{YSZ}}}{\partial z}\frac{1}{N_{YSZ}}$
		$\frac{\partial\theta_{OH^-_{YSZ}}}{\partial t}=\frac{2r_2}{N_{YSZ}}-\frac{\partial J_{OH^-_{YSZ}}}{\partial z}\frac{1}{N_{YSZ}}$	$\theta_{YSZ}=1-\theta_{H_2O,YSZ}-\theta_{O^{2-}_{YSZ}}-\theta_{OH^-_{YSZ}}$
	At Ni/YSZ interface (z=0)	$\frac{\partial\ \theta_{H_2O,YSZ}}{\partial t}=\frac{r_1}{N_{YSZ}}-\frac{r_2}{N_{YSZ}}$	$\frac{\partial\theta_{O^{2-}_{YSZ}}}{\partial t}=-\frac{r_2}{N_{YSZ}}-\frac{r_3}{N_{YSZ}}-\frac{r_9}{N_{YSZ}}$
		$\frac{\partial\ \theta_{OH^-_{YSZ}}}{\partial t}=\frac{2r_2}{N_{YSZ}}+\frac{r_9}{N_{YSZ}}-\frac{r_{10}}{N_{YSZ}}$	
Surface coverages of Ni surface species	On the Ni surface	$\frac{\partial\theta_{H,Ni}}{\partial t}=\frac{2r_5}{N_{Ni}}-\frac{r_6}{N_{Ni}}-\frac{r_8}{N_{Ni}}-\frac{\partial J_{H,Ni}}{\partial z}\frac{1}{N_{Ni}}$	$\frac{\partial\theta_{OH,Ni}}{\partial t}=\frac{r_6}{N_{Ni}}+\frac{2r_7}{N_{Ni}}-\frac{r_8}{N_{Ni}}-\frac{\partial J_{OH,Ni}}{\partial z}\frac{1}{N_{Ni}}$
		$\frac{\partial\theta_{H_2O,Ni}}{\partial t}=\frac{r_4}{N_{Ni}}-\frac{r_7}{N_{Ni}}+\frac{r_8}{N_{Ni}}-\frac{\partial J_{H_2O,Ni}}{\partial z}\frac{1}{N_{Ni}}$	$\frac{\partial\theta_{O,Ni}}{\partial t}=-\frac{r_6}{N_{Ni}}-\frac{r_7}{N_{Ni}}-\frac{\partial J_{O,Ni}}{\partial z}\frac{1}{N_{Ni}}$
	At Ni/YSZ interface (z=0)	$\frac{\partial\theta_{H,Ni}}{\partial t}=\frac{2r_5}{N_{Ni}}-\frac{r_6}{N_{Ni}}-\frac{r_8}{N_{Ni}}-\frac{r_9}{N_{Ni}}-\frac{r_{10}}{N_{Ni}}$	$\frac{\partial\theta_{OH,Ni}}{\partial t}=\frac{r_6}{N_{Ni}}+\frac{2r_7}{N_{Ni}}-\frac{r_8}{N_{Ni}}$
		$\frac{\partial\ \theta_{H_2O,Ni}}{\partial t}=\frac{r_4}{N_{Ni}}-\frac{r_7}{N_{Ni}}+\frac{r_8}{N_{Ni}}$	$\frac{\partial\theta_{O,Ni}}{\partial t}=-\frac{r_6}{N_{Ni}}-\frac{r_7}{N_{Ni}}$
	$\theta_{Ni}=1-\theta_{H,Ni}-\theta_{OH,Ni}-\theta_{O,Ni}-\theta_{H_2O,Ni}$		
Surface coverages of Ni/YSZ interface species	$\theta_{O^{2-}_{inter}}=\theta_{O^{2-}_{YSZ}};\theta_{OH^-_{inter}}=\theta_{OH^-_{YSZ}};\ \theta_{inter}=1-\theta_{O^{2-}_{inter}}-\theta_{OH^-_{inter}}$		
Surface species diffusion	$J_{H_2O,YSZ}=-D^{surf}_{H_2O,YSZ}N_{YSZ}\frac{\partial\theta_{H_2O,YSZ}}{\partial z}$		$J_{H,Ni}=-D^{surf}_{H,Ni}N_{Ni}\frac{\partial\theta_{H,Ni}}{\partial z}$
	$J_{O^{2-}_{YSZ}}=-D^{surf}_{O^{2-}_{YSZ}}N_{YSZ}\frac{\partial\theta_{O^{2-}_{YSZ}}}{\partial z}$		$J_{H_2O,Ni}=-D^{surf}_{H_2O,Ni}N_{Ni}\frac{\partial\theta_{H_2O,Ni}}{\partial z}$
	$J_{OH^-_{YSZ}}=-D^{surf}_{OH^-_{YSZ}}N_{YSZ}\frac{\partial\theta_{OH^-_{YSZ}}}{\partial z}$		$J_{OH,Ni}=-D^{surf}_{OH,Ni}N_{Ni}\frac{\partial\theta_{OH,Ni}}{\partial z}$
	$J_{YSZ}=-D^{surf}_{YSZ}N_{YSZ}\frac{\partial\theta_{YSZ}}{\partial z}$		$J_O=-D^{surf}_{O}N_{Ni}\frac{\partial\theta_O}{\partial z}$
			$J_{Ni}=-D^{surf}_{Ni}N_{Ni}\frac{\partial\theta_{Ni}}{\partial z}$
Boundary conditions			
At the symmetry plane of Ni and YSZ surface	YSZ surface (z=1/2 d_{YSZ}): $J_{H_2O,YSZ}=0, J_{O^{2-}_{YSZ}}=0$, $J_{OH^-_{YSZ}}=0, J_{YSZ}=0$		Ni surface (z=-1/2 d_{Ni}): $J_{H,Ni}=0, J_{OH,Ni}=0,$ $J_{H_2O,Ni}=0, J_O=0, J_{Ni}=0$
At TPB line for Ni and YSZ surface species (z=0)	YSZ surface: $J_{H_2O,YSZ}=0,$ $J_{O^{2-}_{YSZ}}=r_{9,}\ J_{OH^-_{YSZ}}=r_9+r_{10,}$ $J_{YSZ}=0$		Ni surface: $J_{H,Ni}=-r_9-r_{10},$ $J_{Ni}=-r_9-r_{10},\ J_{OH,Ni}=0,$ $J_{H_2O,Ni}=0,\ J_O=0$

Table 7-6 Surface diffusion parameters (Vogler et al., 2009)

Species	D_i^0 (cm^2/s)	E_i^{act} (kJ/mol)
H_{Ni}	4.6×10^{-3}	14.4
O_{Ni}	6.3×10^{-3}	61.3
OH_{Ni}	6×10^{-3}	30.5
H_2O_{Ni}	6×10^{-3}	28.0
O_{YSZ}^{2-}	5.5×10^{-7}	90.0
H_2O_{YSZ}	1.3×10^{-2}	55.0
OH_{YSZ}^{-}	1.3×10^{-2}	55.0

7.5 Results and Discussion

7.5.1 Reaction Mechanism I

7.5.1.1 Comparison between simulated results and results from the literature

The conditions used in the simulation are the same as those in Bieberle & Gauckler (2002), Bessler (2005) and Vijay et al. (2010), which are given in Table 7-7.

Table 7-7 Conditions for reaction mechanism I simulation

Parameters	Value (unit)
T	973 K
N_{Ni}	1.67×10^{-9} mol/cm^2
pH_2	2.5×10^{4} Pa
pH_2O	40 Pa
d_{Ni}	20 μm
h_{Ni}	1 μm

At OCV, the surface coverages of the different Ni surface species were calculated using two sets of rate constants: one set is the same as that used in Bessler (2005), while the other set is taken from Vijay et al. (2010), who claimed better prediction of the experimental data with this set of parameters. Most of the rate constants used in Vijay et al. (2010) are the same as that used in Bessler (2005) (see Table 7-1) except for $k_{f,3}$, $k_{r,3}$, $k_{f,4}$, and $k_{r,4}$, which are 1.5068×10^{14} s^{-1}, 5.7041×10^{2} s^{-1}, 22.4927, and 3.8620×10^{5} s^{-1}. Because no surface coverage values were reported by Bessler, results obtained from our work were compared with the results reported by Vijay et al (2010). Table 7-8 and Table 7-9 show the results when the two sets of kinetic parameters were used. Surface coverages obtained from this study are exactly the same as those reported by Vijay et al. (2010) and there are relatively minor differences between surface coverages when using these two sets of parameters. This means that the kinetic model built in our work is correct and reliable.

Table 7-8 Surface coverages of different Ni surface species at OCV condition with reaction rate constants from Bessler (2005)

	$\theta(O_{Ni})$	$\theta(H_{Ni})$	$\theta(OH_{Ni})$	$\theta(H_2O_{Ni})$	$\theta(Ni)$
Our results	2.3384×10^{-9}	0.3273	1.7967×10^{-2}	5.2375×10^{-7}	0.6547
Vijay et al's results	2.3384×10^{-9}	0.3273	1.7967×10^{-2}	5.2375×10^{-7}	0.6547

Table 7-9 Surface coverages of different Ni surface species at OCV condition with reaction rate constants from Vijay et al. (2010)

	$\theta(O_{Ni})$	$\theta(H_{Ni})$	$\theta(OH_{Ni})$	$\theta(H_2O_{N})$	$\theta(Ni)$
Our results	2.3381×10^{-9}	0.3273	1.7986×10^{-2}	5.2374×10^{-7}	0.6547
Vijay et al's results	2.3381×10^{-9}	0.3273	1.7985×10^{-2}	5.2374×10^{-7}	0.6547

Using the same set of parameters as Bessler (2005), the current and surface coverages of adsorbed species as a function of polarization (η) were simulated. The results are shown in Figure 7-3. In the current/overpotential curve (Figure 7-3(a)), the reaction system reaches saturation at overpotential around 500 mV, which is similar to the results obtained by Bieberle & Gauckler (2002) and Bessler (2005). Bessler explained that the saturation is due to a blocking of the surface with OH_{Ni}. The high overpotential causes a high concentration of O_{Ni} through the charge transfer reaction (Figure 7-3(c)), which results in rapid formation of OH_{Ni}, as shown in Figure 7-3(b). Species OH_{Ni} cannot be consumed at the same rate as they are formed, which leads to the accumulation of OH_{Ni}. The surface coverage of OH_{Ni} is 0.996, and the Ni surface is covered mostly by OH_{Ni}. Thus, the free surface coverage of Ni decreases, and the adsorption of H_2 also slows down. Consequently, the amount of H_2O produced as well as the overall reaction rate decreases.

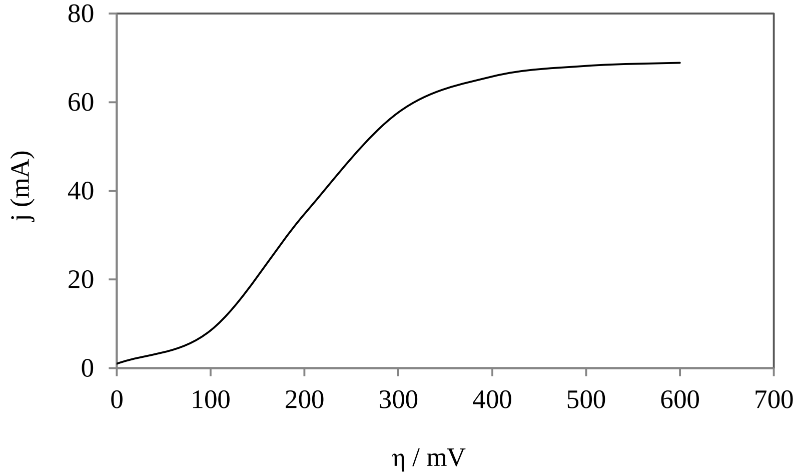

(a)

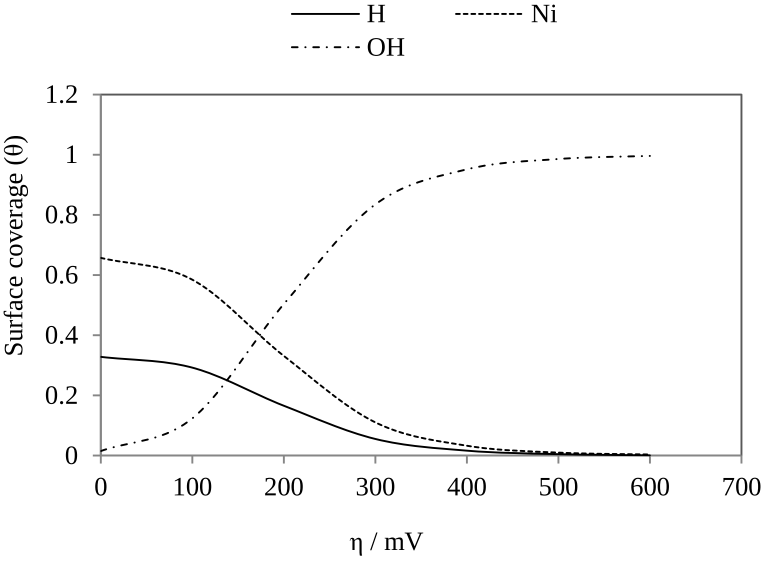

(b)

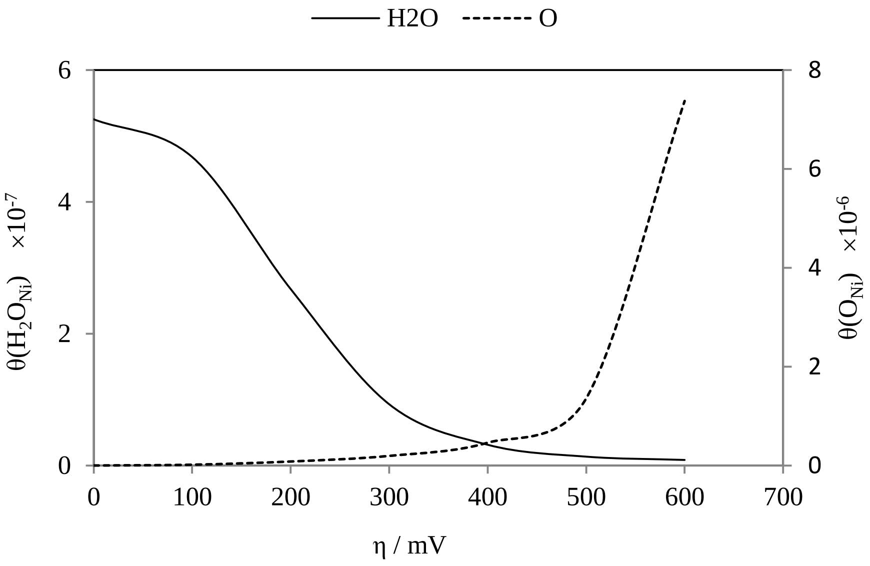

(c)

Figure 7-3 Variations of (a) current, (b) $\theta(H_{Ni})$, $\theta(OH_{Ni})$, $\theta(Ni)$, (c) $\theta(O_{Ni})$ and $\theta(H_2O_{Ni})$ with overpotential as simulated with parameters of Bessler (2005).

For dynamic simulations, when an imposed oscillating overpotential is imposed, the electrode response of current and surface coverages of the different species also exhibit oscillating dynamic behavior. The dynamic responses of current and surface coverages of these surface species presented in Figure 7-4 are also consistent with the results obtained by Vijay et al. (2010) and Bessler (2005). At a frequency of 1 Hz, surface coverages of O_{Ni} and OH_{Ni} change with amplitudes of about 25% around their steady-state values; in contrast, H_{Ni} and H_2O_{Ni} surface coverages vary only by about 0.5% from their steady state value. Compared to the variation of $\theta(O_{Ni})$ and $\theta(OH_{Ni})$ around the steady state, the variation of $\theta(H_{Ni})$ and $\theta(H_2O_{Ni})$ is much smaller. This behavior also observed by Vijay et al. and Bessler was attributed to the more direct coupling of $\theta(O_{Ni})$ and $\theta(OH_{Ni})$ with the charge transfer reaction than $\theta(H_{Ni})$ and $\theta(H_2O_{Ni})$ (Bessler, 2005). By increasing the frequency, this trend is maintained. However, the variation of all the surface species about their steady state becomes smaller.

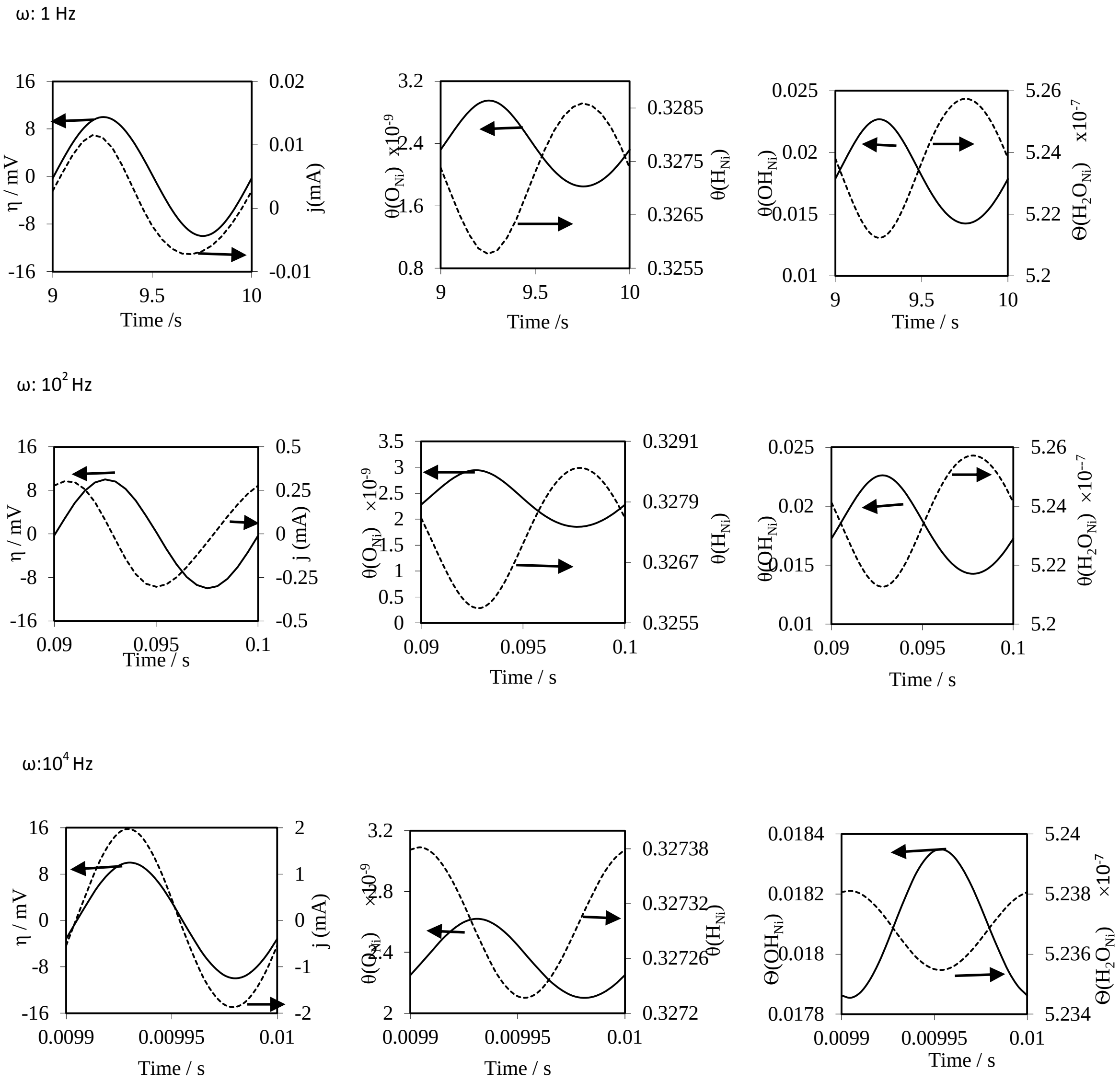

Figure 7-4 Response of the SOFC pattern anode electrochemical system (current, surface coverages of different species) to the imposed oscillating overpotential at three different frequencies. In the left column, the solid lines represent overpotential and the dashed lines represent the current. In the middle column, dash lines represent $\theta(H_{Ni})$, whereas solid lines represent $\theta(O_{Ni})$. In the right column, dash lines represent $\theta(H_2O_{Ni})$, and solid lines represent $\theta(OH_{Ni})$.

7.5.1.2 Comparison between simulation results and our experimental results

In order to evaluate the capability of mechanism I to reproduce our experimental results under a wide range of overpotential conditions, Tafel plots were simulated and compared with our experimental data. The kinetic parameters used for the simulation are still taken from Bessler (2005). Simulation conditions are as follows: pH_2: 3×10^4 - 9×10^4 Pa, pH_2O: 3×10^3 Pa, L_{tpb}: 117.1 cm/cm^2, T: 700°C. Figure 7-5 shows the simulation and experimental results. The current density along the anodic branch increases with increasing anodic potential and the simulation results are in reasonable agreement with the experimental data. Thus, the elementary chemical reactions on the Ni surface included in reaction mechanism I represent well the electrochemical behavior of the pattern anode in H_2/H_2O environments. However, the simulated current density does not show any change when increasing cathodic potential. Moreover, the simulated current density is much smaller than the experimental current density under the same conditions. The experimental results presented in chapter 5 show that the cathodic current density strongly depends on pH_2O. In reaction mechanism I, H_2O related processes on the YSZ surface are not considered. This neglect may explain the deviation between the simulated and experimental data along the cathodic branch.

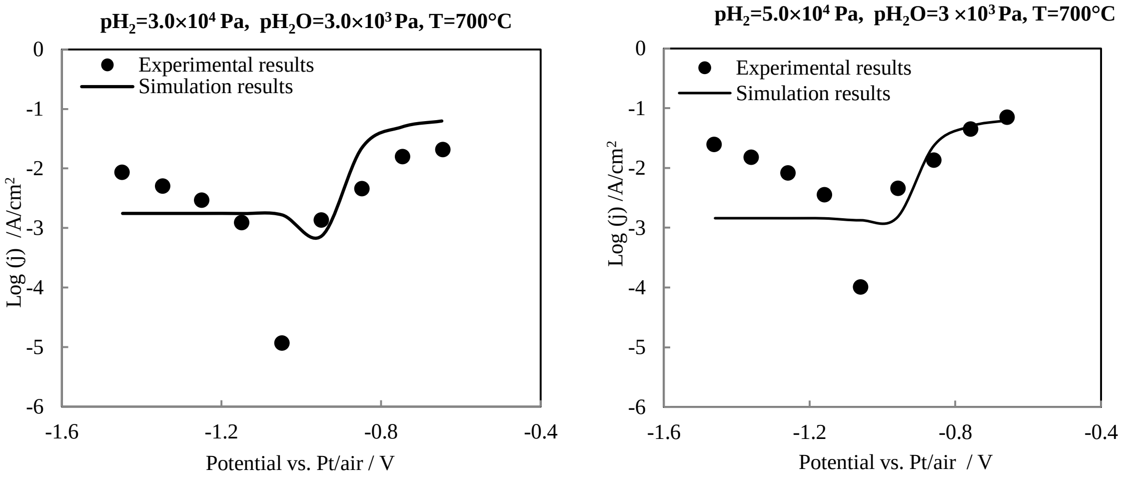

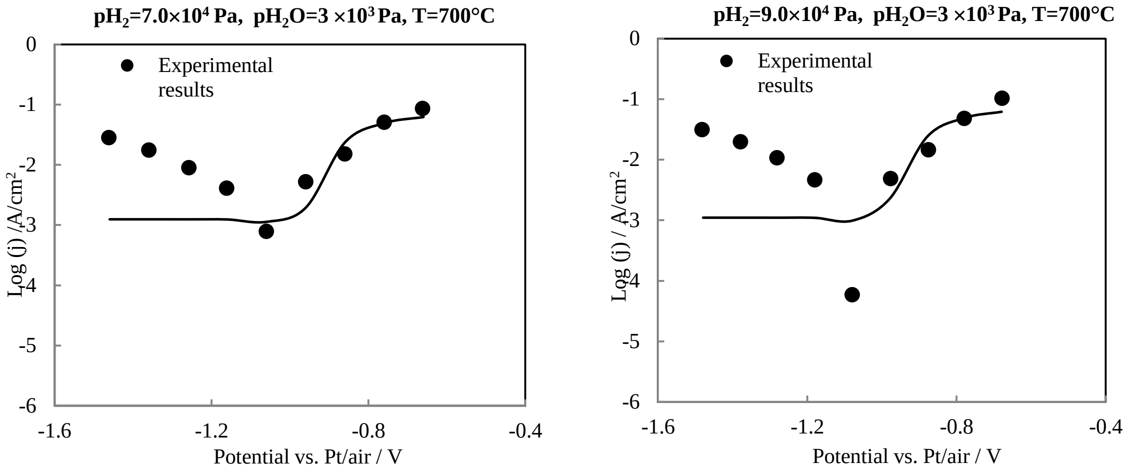

Figure 7-5 Simulation and experimental Tafel plots under various gas composition conditions at 700°C.

The impedance spectra were also simulated under various pH_2 conditions. Comparison between the simulation and experimental Nyquist plots are illustrated in Figure 7-6 for the following conditions: $pH_2 = 3\times10^4$ Pa and 5×10^4 Pa, $pH_2O=3\times10^3$ Pa, $L_{tpb}=285$ cm/cm^2, T=700°C. The impedance plots obtained via simulation is close to a perfect semi-circle, whereas the experimental impedance is composed of two semi-circles. The total polarization resistance (R_p: 278 Ω cm^2) obtained from the simulated and experimental data are close when the partial pressure of H_2 is 3×10^4 Pa. However, when pH_2 increases to 5×10^4 Pa, R_p from the simulation is larger than the R_p from the experiment. Figure 7-7 shows the dependence of polarization resistance on pH_2 a log-log scale for both simulation and experiment. For the simulation, the polarization resistance slightly decreases when increasing pH_2, and a reaction order of -0.057 is obtained, which is lower than the value -0.135 obtained experimentally. Both experimental and simulation results revealed a relatively weak dependence of anode performance on pH_2.

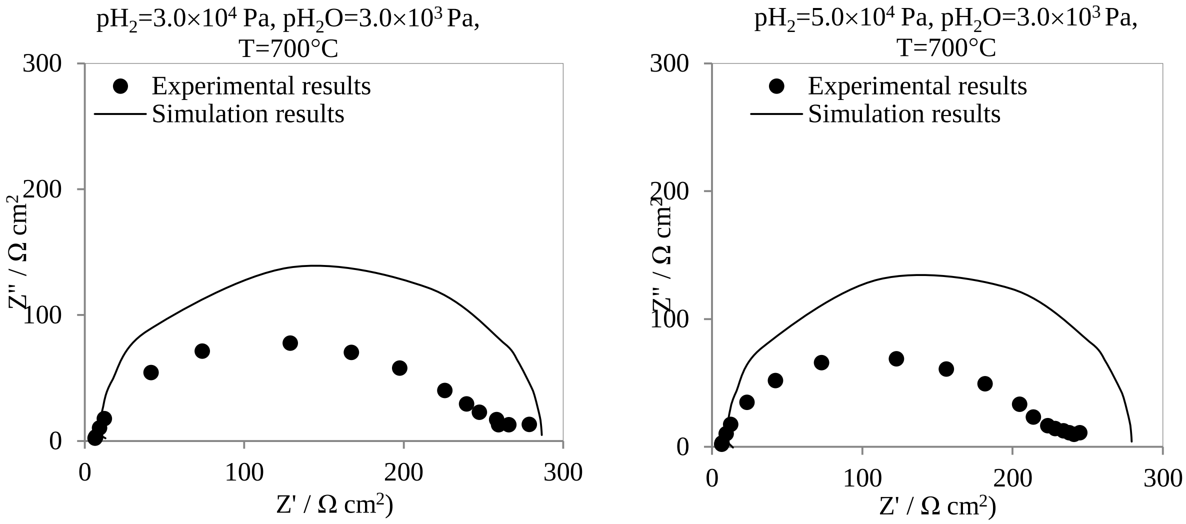

Figure 7-6 Comparison between the simulated and experimental Nyquist plots

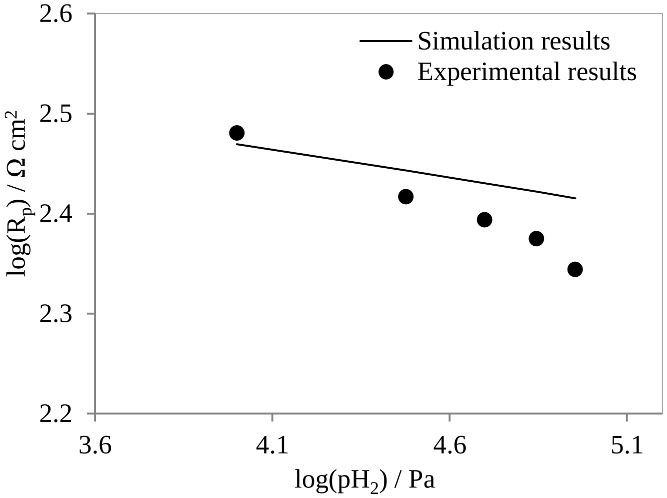

Figure 7-7 Dependence of polarization resistance on partial pH$_2$ for both simulation and experiment, pH$_2$O=3×10^3 Pa, T=700°C.

7.5.2 Reaction Mechanism II

Thermodynamic parameters for surface species at 25°C and 700°C used in the model describing reaction mechanism II are shown in Table 7-10. Kinetic and thermodynamic parameters for charge transfer reactions were either taken from Shishkin and Ziegler or determined through fitting of the experimental results. Those parameters are given in Table 7-11.

Table 7-10 Thermodynamic parameters for surface species at 700°C and 25°C (O'Hayre et al., 2006; Habibzadeh, 2007; Vogler et al., 2009)

Species	h_{0i} (kJ/mol) at 25°C	s_{0i} (J/mol K) at 25°C	h_i (kJ/mol) at 700°C	s_i (J/mol K) at 700°C
H_2O_{gas}	-241.8	188.8	-217.0[b]	232.0[b]
$H_{2\ gas}$	0	130.7	20.0[b]	165.0[b]
H_2O_{YSZ}	-291.9	49.3	-273.0	98.0
O^{2-}_{YSZ}	-183.5	0[a]	-236.0	0
OH^{-}_{YSZ}	-270.3[a]	62.5[a]	-283.0	67.0
YSZ	0	0	0	0
H_2O_{Ni}	-302.6	87.6	-273.0	130.0
H_{Ni}	-48.3[a]	28.3	-32.0	41.0
O_{Ni}	-237.5	19.4	-222.0	39.0
OH_{Ni}	-214.6	75.8	-193.0	106.0
Ni	0	0	0	0
$V_{\ddot{O}}(YSZ)$	0	0	0	0
$O^{X}_{O}(YSZ)$	-192.0 [a]	0	-236.0	0

a: free fit parameters. b: taken from O’Hayre et al. (2006). The other parameters at 25°C and 700°C are taken from Habibzadeh (2007) and Vogler et al (2009), respectively.

Table 7-11 Kinetic and thermodynamic parameters used for charge transfer reactions in reaction mechanism II

	700°C	550°C
k_{CT1}^{0} (cm^3/mol s)	3.5×10^{10}	3.5×10^{10}
k_{CT2}^{0} (cm^3/mol s)	2.0×10^{25}	2.0×10^{25}
ΔG_{CT1} (kJ/mol)	6.31	4.30
ΔG_{CT2} (kJ/mol)	-75.4[a]	-75.4[a]
E_{CT1} (kJ/mol)	13.0[a]	45.0
E_{CT2} (kJ/mol)	154.9[a]	154.9[a]

a: taken from Shishkin and Ziegler (2010), the others are all fitted parameters.

At 700°C, activation energies of the both charge transfer reactions were taken from Shishkin and Ziegler (2010). It was realized that the location for the minimum of the logarithm of current density on the Tafel plots depends on the Gibbs free energy change of both charge transfer reactions. This Gibbs free energy changes were then adjusted for best fit, resulting in a value of 6.3 kJ mol^{-1} for reaction 7.40 and a value of -88.8 kJ mol^{-1} for reaction 7.41. It is also important to notice that one would expect a current density close to zero at OCV, but the experimental and simulation results give a baseline current. For the experimental data, the reason for a baseline current is due to the chemical potential difference between the cathode and anode, which leads to a small exchange current density at equilibrium conditions. Gas leaks as well as electronic leaks may also cause a small exchange current density. For the simulation, the value of the minimum current density is extremely sensitive to very small changes in the value of the Gibbs free energy. For example, in Figure 3b, the set of Gibbs free energies yields a very small current density (log(i) = -10.76 A cm^{-2}). Would we change the value of those free energies by less than 0.5%, the logarithm of the minimum current density would increase to -6.0 A cm^{-2}. Note that the changes in Gibbs free energy of this magnitude, although they did affect significantly the minimum value of the current density, they did not have any effect on the values of the cathodic and anodic current densities. Note that the value of 6.31 kJ mol^{-1} for reaction 7.40 is significantly smaller than the calculated value through DFT (113 kJ mol^{-1}) by Shishkin and Ziegler. The Gibbs free energy change of the overall H_2 oxidation reaction is the sum of the Gibb free energy change of all the elementary reactions. With the fitting value (6.3 kJ mol^{-1}), the sum of the Gibbs free energy change of all the elementary reactions is much closer to the Gibbs free energy change of the overall H_2 reaction than when using the DFT calculated value.

At 550°C, charges in Gibbs free energy as well as the activation energy for reaction 7.40 were treated as free fit parameter to obtain good fitting between simulation and experimental results. The activation energy for reaction 7.41 had insignificant effect on the simulation results, and was taken from the DFT calculation.

In Figure 7-8, both simulation and experimental results regarding the effect of H_2 partial pressure on current density are presented. The simulation and experimental conditions are: 3×10^4 Pa $\leq pH_2 \leq 9\times10^4$ Pa, $pH_2O=3\times10^3$ Pa, T=700°C.

Simulation results from models with and without surface diffusion are the same, indicating that surface diffusion is fast under the above simulation conditions. On both Ni and YSZ surfaces, surface coverage profiles are uniform. The experimental results can be well reproduced by simulation under each pH_2 condition. Figure 7-9 shows that pH_2 has positive effects on the current density under anodic polarization, where the effect on the cathodic current density is less pronounced, which agrees well with the experimental data. As seen in Figure 7-9, the experimentally observed anodic current density rises with increasing pH_2, while the experimental cathodic current density is almost independent of pH_2.

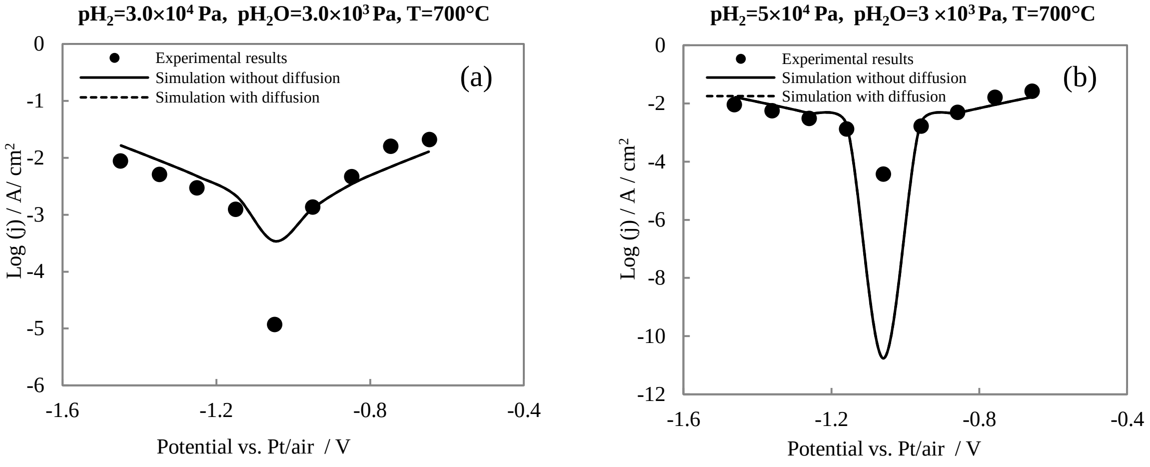

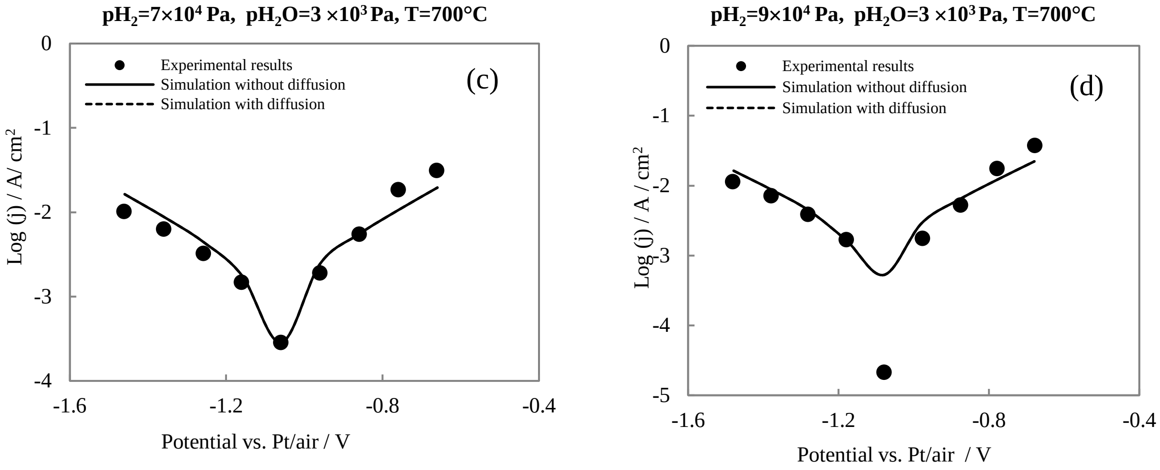

Figure 7-8 Comparison between experimental and simulation Tafel plots upon variation of pH_2 at 700°C when reaction mechanism II is implemented in the kinetic model.

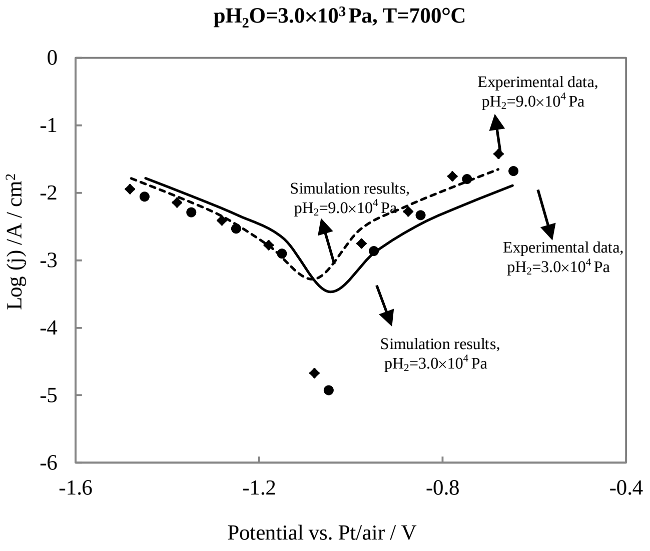

Figure 7-9 Effect of pH_2 on the current density at 700°C

Figure 7-10 evaluates the influence of pH_2O on current density as determined from both experiments and simulations. The simulation and experimental conditions are: 3×10^3 Pa $\leq$ $pH_2O \leq 5\times10^4$ Pa, $pH_2=2\times10^4$ Pa, T=550°C. The effect of surface diffusion on both anodic and cathodic current density is negligible. Under high cathodic potential, the simulated current density is systematically larger than the experimental current density, but the simulation results still predict the experimental data reasonably well. As shown in Figure 7-11, the experimentally observed decrease in cathodic current density with increasing pH_2O can be reproduced by the simulation. For both simulation and experimental results, the effect of pH_2O on the anodic current density is small.

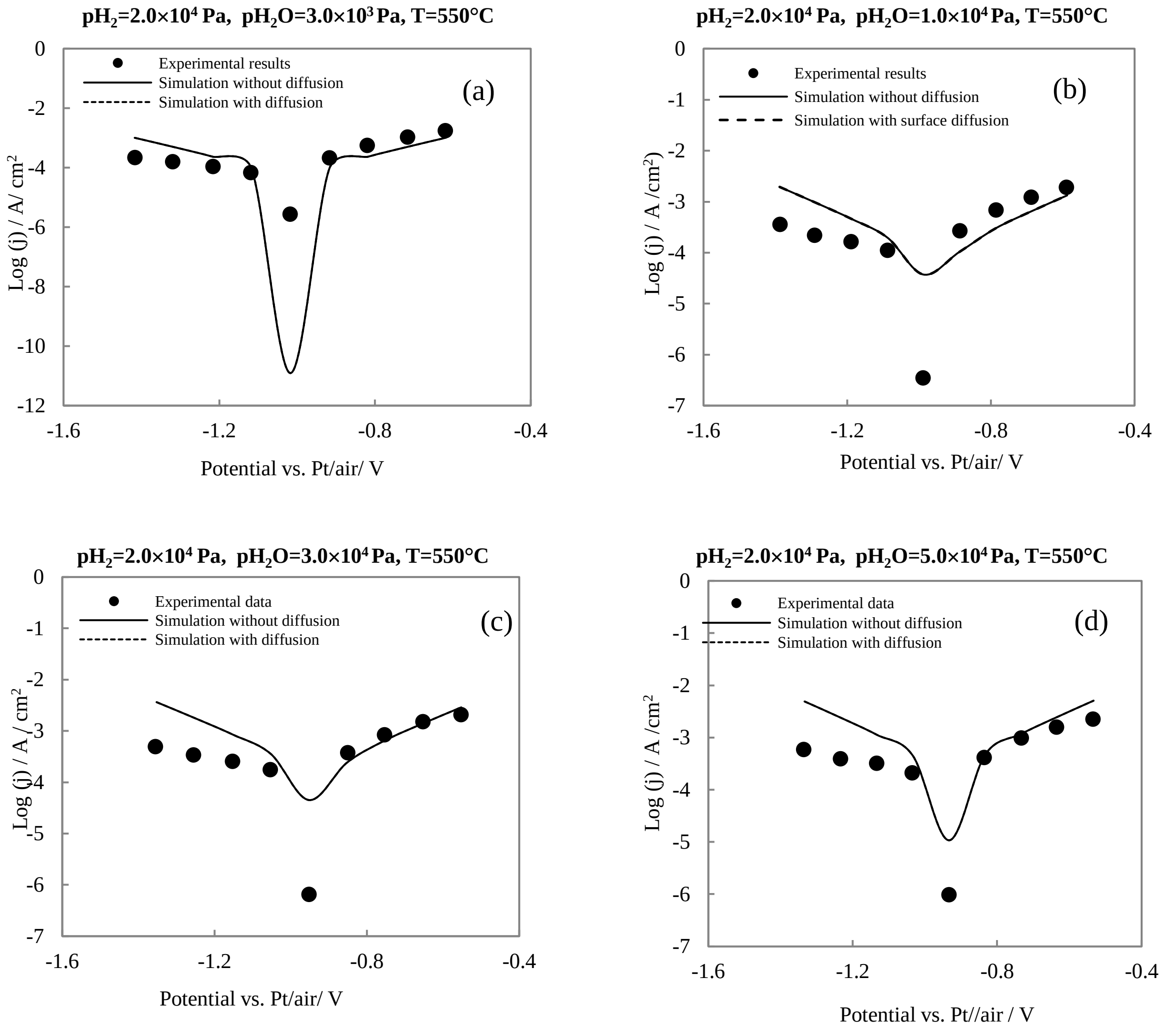

Figure 7-10 Comparison between experimental and simulation Tafel plots upon variation of pH_2O at 550°C when reaction mechanism II is implemented in the kinetic model.

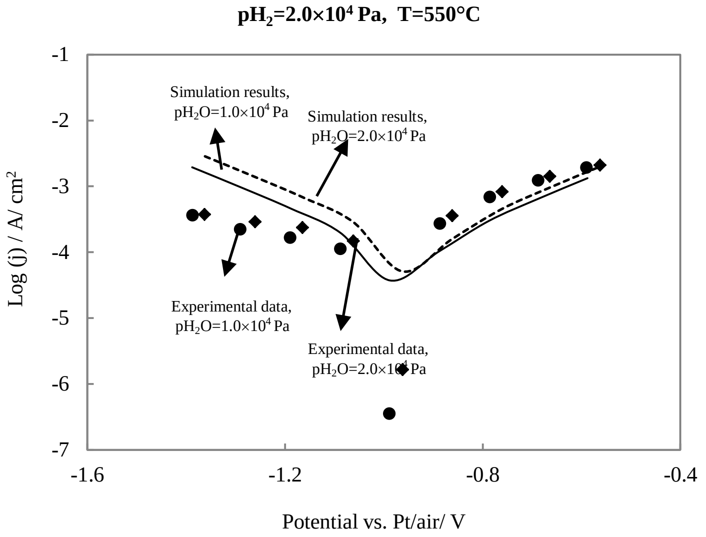

Figure 7-11 Effect of pH_2O on the current density at 550°C

In order to compare the simulation results with the experimental results, the effect of pH_2 on current densities was simulated at 700°C and the effect of pH_2O on current densities was simulated at 550°C, as presented in Figure 7-8 and Figure 7-10, respectively. As mentioned earlier, it was not possible to conduct a complete experimental kinetic study at 700°C because the Ni/YSZ pattern anodes experienced significant structure changes at this temperature for H_2O content greater than 10%. Nonetheless, the effect of H_2O at 700°C can be studied from simulation. Figure 7-12 shows the dependence of the simulated current density on pH_2O at 700°C. Figure 7-12 also shows the effect of pH_2 on current density at 550°C. At both 550°C and 700°C, surface diffusion does not show any effects on the current density at different pH_2 and pH_2O. At 550°C, pH_2 has a positive effect on the anodic current density and a very weak effect on cathodic current density similar to results obtained at 700°C. At 700°C, the cathodic current density increases when increasing pH_2O, whereas the dependence of anodic current density on pH_2O is much weaker. This is also consistent with the simulation results obtained at 550°C.

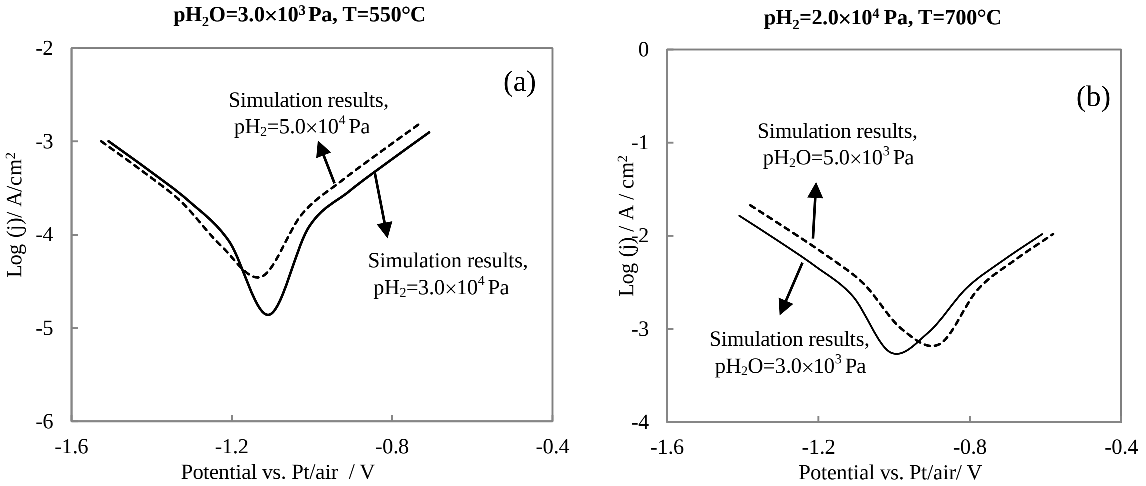

Figure 7-12 Effect of pH_2 and pH_2O on the current density at 550°C and 700°C, respectively.

Table 7-12 presents the surface coverages of Ni and YSZ surface species for various pH_2 and pH_2O conditions when an overpotential of 0.3 V is imposed. When increasing both pH_2 and pH_2O, Ni free sites slightly decrease. With an increase in pH_2, $\theta(H_{Ni})$ increases, but $\theta(O_{Ni})$ and $\theta(OH_{Ni})$ decrease. Surface coverages of H_2O_{Ni} and YSZ surface species are slightly affected by pH_2. $\theta(O^{2-}_{YSZ})$ slightly decreases, and $\theta(OH^{-}_{YSZ})$ increases. When increasing pH_2O, surface coverage of O^{2-}_{YSZ} decreases and more H_2O_{YSZ} and OH^{-}_{YSZ} are generated. In addition, the amount of H_2O_{Ni}, O_{Ni} and OH_{Ni} increase, and H_{Ni} remains almost constant with increasing pH_2O. At the Ni/YSZ interface, surface coverage of OH^{-}_{inter} slightly increases and $\theta(O^{2-}_{inter})$ shows small decrease with increases in both pH_2 and pH_2O.

As discussed before, anodic current density increases with an increase in pH_2. Therefore, current density change is related to the change in $\theta(H_{Ni})$ and $\theta(OH^{-}_{inter})$ upon variation of pH_2 at constant pH_2O and temperature. When increasing pH_2, $\theta(H_{Ni})$ and $\theta(OH^{-}_{inter})$ increase and lead to a rise in anodic current density. Under cathodic polarization, the extent of $\theta(H_{Ni})$ change is the same as under anodic polarization when increasing the same amount of H_2. But, the extent of $\theta(OH^{-}_{inter})$ change under cathodic polarization is smaller than under anodic polarization. This explains the strong dependence of anodic current density and the weak dependence of cathodic current density on pH_2. When pH_2 and temperature are kept constant, the current density increases with increasing pH_2O, and the trend of current density changes is mainly related to $\theta(OH^{-}_{inter})$ changes. According to the charge transfer reaction 7.40 and

7.41, electrons produced are directly related to θ(H_{Ni}), θ(OH^-_{inter}) and θ(O^{2-}_{inter}). At constant pH_2 and temperature conditions, θ(H_{Ni}) is almost constant, while θ(O^{2-}_{inter}) decreases with an increase in pH_2O leading to the production of more θ(OH^-_{inter}), which explains the rise of current density. In addition, the extent of θ (OH^-_{inter}) change is faster under cathodic polarization than under anodic polarization when increasing the same amount of H_2O. This is the reason that cathodic current density depends strongly on pH_2O than anodic current density.

Under constant pH_2 and pH_2O conditions, θ(H_2O_{Ni}) and θ(H_{Ni}) increase with decreasing temperature, while surface coverages of other Ni surface species decrease. On the YSZ surface, θ(H_2O_{YSZ}) and θ(OH^-_{YSZ}) increases when decreasing the temperature. Surface coverages of other YSZ surface species remain constant with a decrease in temperature. At the interface, θ(OH^-_{inter}) increases when decreasing temperature.

Table 7-12 Surface coverages of Ni and YSZ surface species changes with pH_2 and pH_2O when the overpotential is 0.3 V

		$\theta(H_2O_{Ni})$	$\theta(H_{Ni})$	$\theta(O_{Ni})$	$\theta(OH_{Ni})$	$\theta(Ni)$	$\theta(H_2O_{YSZ})$	$\theta(O^{2-}_{YSZ})$	$\theta(OH^-_{YSZ})$	$\theta(YSZ)$	$\theta(OH^-_{inter})$	$\theta(inter)$
pH_2 (Pa) Constant pH_2O: 3.0×10^3 Pa 700°C	1.0×10^4	1.76×10^{-9}	1.35×10^{-3}	1.62×10^{-3}	2.66×10^{-8}	0.997	7.48×10^{-12}	0.800	1.11×10^{-3}	0.199	1.12×10^{-3}	0.199
	2.0×10^4	1.76×10^{-9}	1.92×10^{-3}	8.09×10^{-4}	1.88×10^{-8}	0.997	7.48×10^{-12}	0.800	1.12×10^{-3}	0.199	1.12×10^{-3}	0.199
	3.0×10^4	1.76×10^{-9}	2.35×10^{-3}	5.39×10^{-4}	1.54×10^{-8}	0.997	7.48×10^{-12}	0.800	1.12×10^{-3}	0.199	1.12×10^{-3}	0.199
	5.0×10^4	1.76×10^{-9}	3.03×10^{-3}	3.23×10^{-4}	1.19×10^{-8}	0.997	7.48×10^{-12}	0.800	1.12×10^{-3}	0.199	1.12×10^{-3}	0.199
	7.0×10^4	1.76×10^{-9}	3.58×10^{-3}	2.31×10^{-4}	1.00×10^{-8}	0.996	7.48×10^{-12}	0.800	1.12×10^{-3}	0.199	1.12×10^{-3}	0.199
	9.0×10^4	1.76×10^{-9}	4.06×10^{-3}	1.79×10^{-4}	8.86×10^{-9}	0.996	7.48×10^{-12}	0.800	1.12×10^{-3}	0.199	1.12×10^{-3}	0.199
pH_2O (Pa) Constant pH_2: 2.0×10^4 Pa 550°C	3.0×10^3	3.99×10^{-9}	4.49×10^{-3}	6.06×10^{-5}	2.40×10^{-9}	0.996	9.09×10^{-11}	0.800	1.93×10^{-3}	0.199	1.93×10^{-3}	0.199
	1.0×10^4	1.33×10^{-8}	4.49×10^{-3}	2.02×10^{-4}	7.99×10^{-9}	0.995	3.02×10^{-10}	0.798	3.50×10^{-3}	0.198	3.50×10^{-3}	0.198
	3.0×10^4	3.99×10^{-8}	4.49×10^{-3}	6.06×10^{-4}	2.40×10^{-8}	0.995	9.05×10^{-10}	0.796	6.05×10^{-3}	0.198	6.05×10^{-3}	0.198
	5.0×10^4	6.64×10^{-8}	4.49×10^{-3}	1.01×10^{-3}	3.99×10^{-8}	0.995	1.51×10^{-9}	0.795	7.80×10^{-3}	0.197	7.80×10^{-3}	0.197

On Ni surface, surface coverages of different species are not influenced by variations of the electrode potential. However, surface coverages of species on YSZ surface depends slightly on the electrode potential. As shown in Figure 7-13(a)-(c), from cathodic polarization to anodic polarization, surface coverage of $\mathrm{OH}_{\mathrm{YSZ}}^{-}$ increases by only 1.78%, and surface coverages of other YSZ surface species slightly decrease. $\theta(\mathrm{O}_{\mathrm{YSZ}}^{2-})$ decreases by about 0.0013%, and surface coverage of free YSZ surface decreases by about 0.005%. Figure 7-13(d) describes the effect of electrode potential on total current density (j) as well as on current densities contributed by charge transfer reaction 7.40 (j_1) and 7.41(j_2). The total current density is the sum of j_1 *and* j_2. Figure 7-13(d) shows that the total current density is mainly due to j_1 under the operating conditions for this figure. The contribution of current density from reaction 7.41 is very small. Therefore, charge transfer reaction 7.40 dominates the overall charge transfer reaction of H_2 oxidation.

Under anodic polarization, the trend of $\theta(\mathrm{OH}_{\mathrm{YSZ}}^{-})$ changes with electrode potential is consistent with the trend of current density changes when pH_2 and pH_2O are kept constant. The overall H_2 oxidation becomes faster when increasing $\theta(\mathrm{OH}_{\mathrm{YSZ}}^{-})$.

Under cathodic polarization, the trend of current density changes with electrode potential is similar to changes in $\theta(\mathrm{O}_{\mathrm{YSZ}}^{2-})$ and free YSZ surface. Similar behavior was observed when changing pH_2, while keeping pH_2O (3.0×10^{3} Pa) and temperature (700°C) constant.

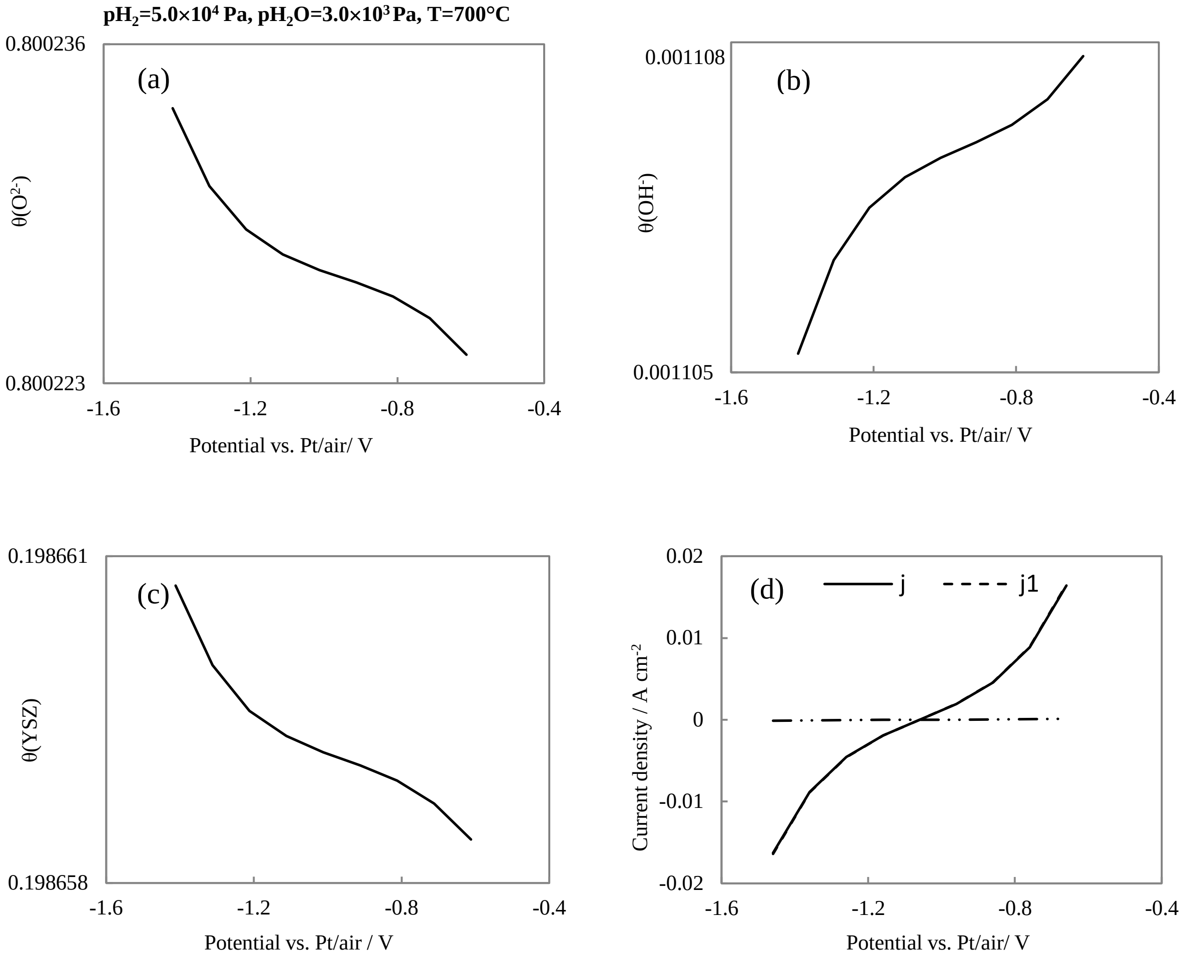

Figure 7-13 Dependence of surface coverages of YSZ surface species and current densities on electrode potential: $pH_2=5.0\times10^4$ Pa, $pH_2O=3.0\times10^3$ Pa, T=700°C.

Figure 7-14 shows the changes at 550°C of various surface species and current density when varying the electrode potential. At 550°C, the effect of electrode potential on surface coverages of YSZ surface species and current density was evaluated at different pH_2O conditions. When pH_2O is 3.0×10^3 Pa, the dependence of surface coverage and current density on electrode potential is very similar to observed at 700°C under the same pH_2O condition (not shown here). With further increase in pH_2O to 2.0×10^4 Pa, surface coverage of OH^-_{YSZ} increases and surface coverages of O^{2-}_{YSZ}, H_2O_{YSZ} and free YSZ surface decrease with a decrease in cathodic potential. Surface coverages of all the species remain constant under anodic polarization (see Figure 7-14(a)-(c)). In Figure 7-14(d), the total cathodic current density is mainly due to j_1, while j_2 has a minor effect on the total cathodic current density. Under anodic polarization, j_1 is similar to j_2 and the current density from both charge transfer reactions equally affects the total current density. Therefore, charge transfer reaction 7.40 dominates the whole charge transfer reaction under cathodic polarization, and both reactions (7.40 and 7.41) equally affect the overall charge transfer reactions under anodic polarization.

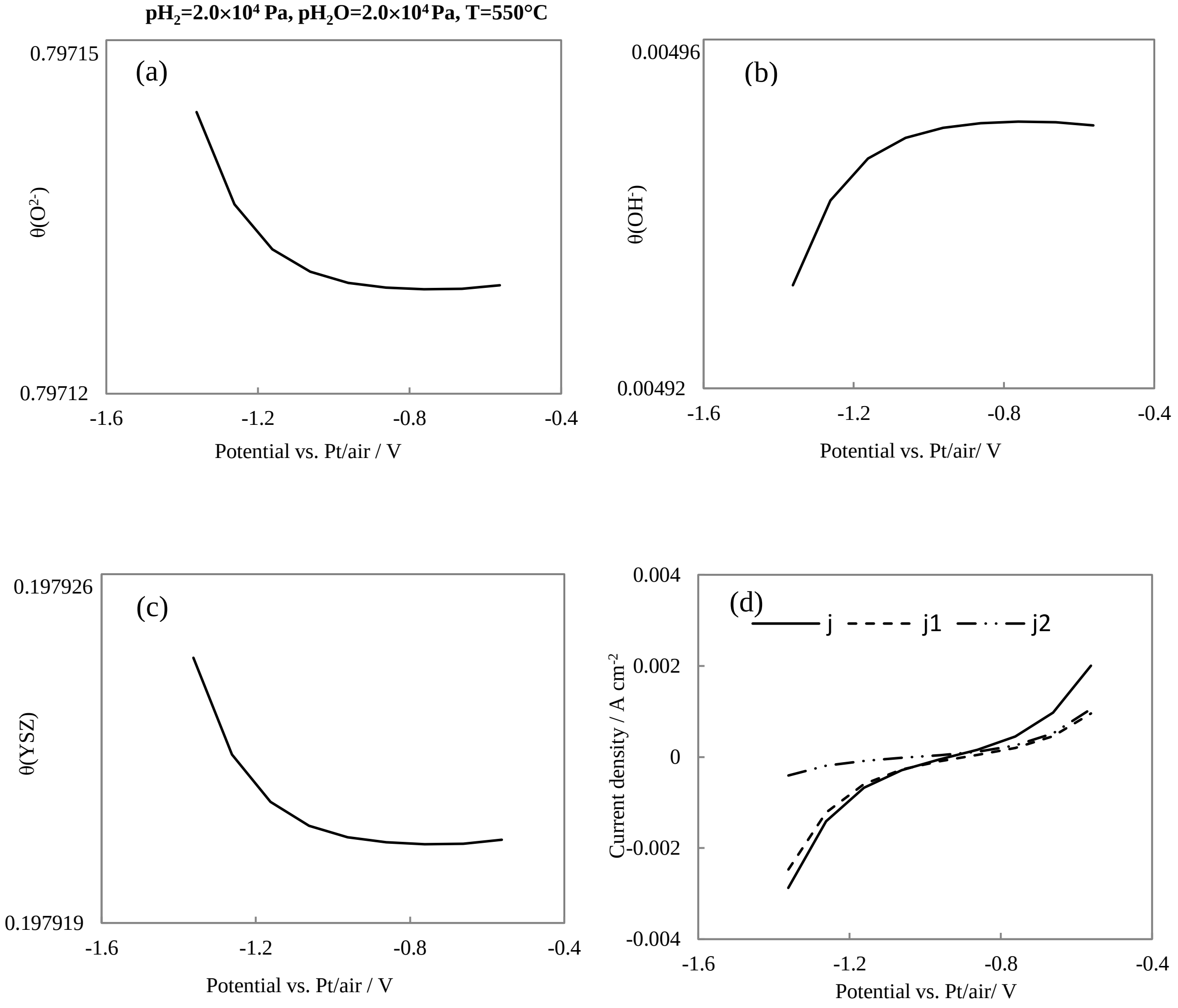

Figure 7-14 Dependence of surface coverages of YSZ surface species and current densities on electrode potential: $pH_2=2.0\times10^4$ Pa, $pH_2O=2.0\times10^4$ Pa, T=550°C.

In Figure 7-15, changes in surface coverage as well as current density upon variation of electrode potential are presented when partial pressure of H_2O is 5.0×10^4 Pa, still at 550°C. Under cathodic conditions, surface coverage of $\mathrm{OH}^{-}_{\mathrm{YSZ}}$ increases and surface coverages of $\mathrm{O}^{2-}_{\mathrm{YSZ}}$, H_2O_{YSZ} and free YSZ surface decrease with decreasing cathodic potential, which is similar to surface coverage changes at other pH_2O. The current density from charge transfer reaction 7.40 is still the main contributor to the total current density. Under anodic polarization, the surface coverage of $\mathrm{OH}^{-}_{\mathrm{YSZ}}$ decreases and surface coverages of $\mathrm{O}^{2-}_{\mathrm{YSZ}}$, H_2O_{YSZ} and free YSZ surface increase when decreasing anodic potential, which is opposite to surface coverage changes when pH_2O is 3.0×10^3 Pa. The total anodic current density is mainly from charge transfer reaction 7.41, and the charge transfer reaction 7.40 has a minor influence on the total anodic current density. Charge transfer reaction 7.41 dominates the overall charge transfer reaction.

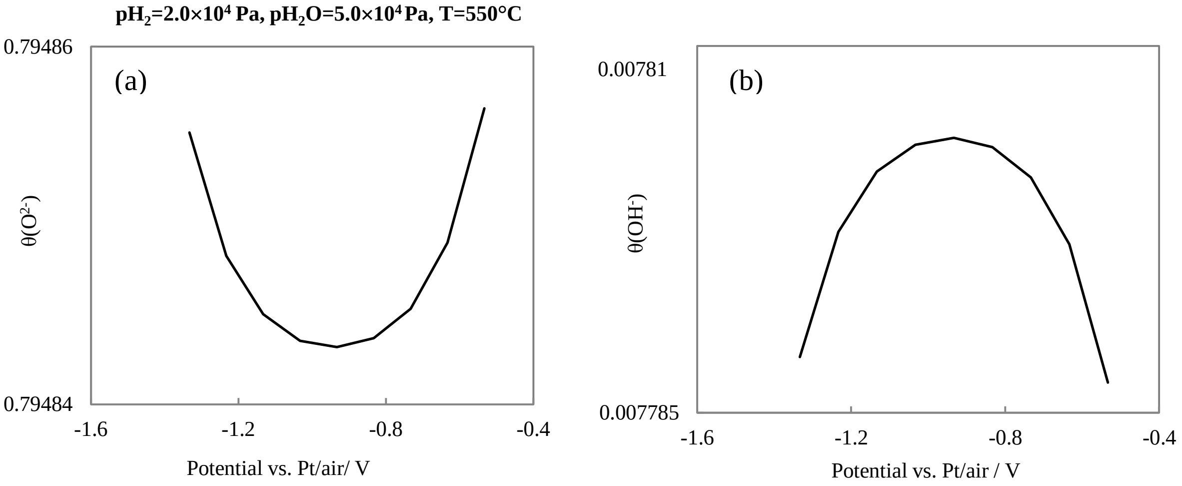

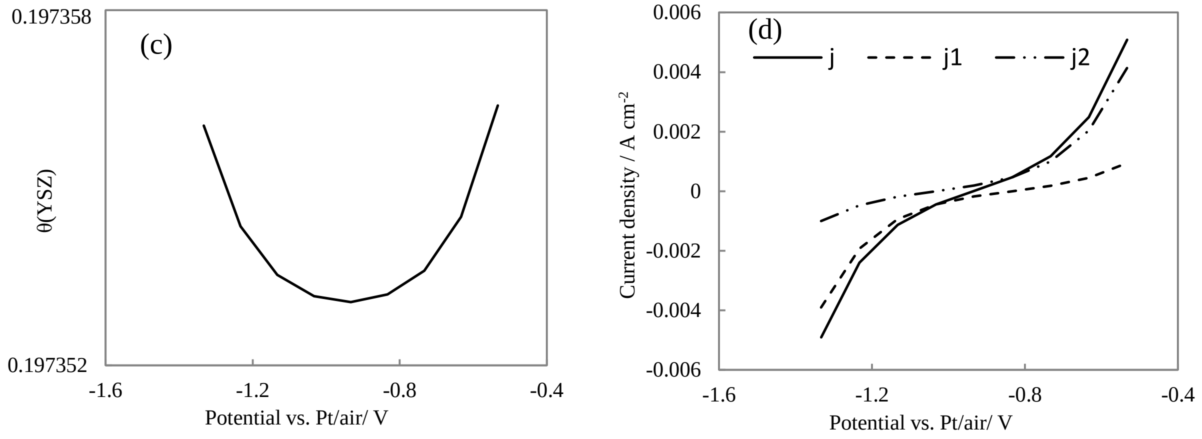

Figure 7-15 Dependence of surface coverages of YSZ surface species and current densities on electrode potential: pH_2=2.0×10^4 Pa, pH_2O=5.0×10^4 Pa, T=550°C.

Under cathodic polarization, the charge transfer reaction 7.40 generates H and O^{2-} species, which lead to an increase in $\theta(O^{2-})$ and a decrease in $\theta(OH^-)$ with increasing cathodic potential.

Under anodic polarization, the charge transfer reaction 7.40 produces hydroxyl ions and electrons, which result in an increase in $\theta(OH^-)$ and a decrease in $\theta(O^{2-})$ with increasing anodic potential when pH_2O is low (3.0×10^3 Pa). With increasing pH_2O, more hydroxyl ions are produced through reaction 2 in Table 7-2, which increases the reaction rate of charge transfer reaction 7.41. The increase of OH^- also leads to more O^{2-} production through reaction 7.40, which explains the increase of $\theta(O^{2-})$ under anodic polarization when pH_2O is high (5.0×10^4 Pa). At 700°C, simulated results similar to what was observed at 550°C were obtained when changing pH_2O. When increasing H_2O content from 3% to 50%, $\theta(O^{2-})$ decreases and $\theta(OH^-)$ increases (see the scale of y-axis in Figures 7-13, 7-14 and 7-15). This can explain the change of which charge transfer reaction dominates under anodic polarization.

The good agreement between the simulation and experimental data for a wide range of pH_2 and pH_2O conditions reveals that reaction mechanism II can reasonably predict the experimentally observed behavior of Ni/YSZ pattern anode in H_2/H_2O environments. Surface diffusion is fast and does not affect the pattern anode performance. Under cathodic polarization, the reaction 7.40 dominates the overall charge transfer reaction regardless of the partial pressure of H_2 and H_2O and temperature. Under anodic polarization, the dominating charge transfer reaction is still reaction 7.40), which does not change when changing pH_2 and temperature. However, it changes from charge transfer reaction 7.40 to charge transfer reaction 7.41 when increasing the partial pressure of H_2O from 3.0×10^3 Pa to 5.0×10^4 Pa.

7.5 Conclusions

This chapter presents a kinetic modeling study of H_2 electrochemical oxidation using Ni/YSZ pattern anodes as model anodes. The model represents elementary reactions of H_2 oxidation on Ni/YSZ pattern anodes. Surface reactions, electrochemical reactions and surface diffusions are described in the model. Two reaction mechanisms were considered. Reaction mechanism I is a simpler reaction mechanism that does not take into account reaction on YSZ surface. Reaction mechanism II is a more comprehensive reaction mechanism, based on the work of Vogler et al. (2009). However, important differences in mechanism II with that of Vogler et al, are the charge transfer reactions. In this work, the charge transfer reactions proposed by Shishkin and Ziegler (2010) were implemented into the kinetic model and applied to interpret our experimental results. Those charge transfer reactions are:

Charge transfer reaction 1: $\mathrm{H_{Ni}} + \mathrm{O^{2-}_{inter}} \rightleftharpoons \mathrm{OH^{-}_{inter}} + (\mathrm{Ni}) + \mathrm{e^{-}_{Ni}}$

Charge transfer reaction 2: $\mathrm{H_{Ni}} + \mathrm{OH^{-}_{inter}} \rightleftharpoons \mathrm{H_2O_{gas}} + (\mathrm{inter}) + (\mathrm{Ni}) + \mathrm{e^{-}_{Ni}}$

The main results are summarized as follows.

- Reaction mechanism I

  - The simulated anodic branch in the Tafel plot can predict the experimental results. However, the simulated cathodic branch deviates significantly from the experimental data, which may be due to lack of surface reactions on YSZ, especially H_2O related processes.
  - The simulated impedance is composed of one arc, whereas the experimental impedance contains two arcs. It was possible to reasonably predict the total polarization resistance when pH_2 is 3.0×10^4 Pa. However, as pH_2 increases, deviation between simulated and experimental polarization resistance increases.
- Reaction mechanism II
  - Experimental data (both anodic and cathodic currents in the Tafel plots) can be well reproduced by simulation under a wide range of pH_2 and pH_2O conditions at both 700 and 550°C.
  - It was found that the effect of surface diffusion on the pattern anode performance is negligible under all conditions in this work.
  - Under cathodic polarization, charge transfer reaction 1 is always the dominating reaction, irrespective of pH_2, pH_2O and temperature.
  - Under anodic polarization, the dominating reaction switches from charge transfer reaction 1 to charge transfer reaction 2 when increasing the partial pressure of H_2O from 3.0×10^3 Pa to 5.0×10^4 Pa.

Chapter 8

Conclusions and Recommendations

8.1 Conclusions

The focus of this study was to obtain valuable insight into the electrochemical reaction mechanisms of H_2 and CO on SOFC anodes. As ideal SOFC anodes for kinetic studies, Ni/YSZ pattern anodes were fabricated using a bi-layer lift-off method. Microstructure and electrochemical behavior changes of the pattern anodes in H_2-H_2O atmosphere were characterized. The stabilization of the pattern anodes was investigated and a comprehensive data set of the electrochemical oxidation reactions of H_2 and CO on Ni/YSZ pattern anodes were obtained under stable conditions.

A kinetic model predicting the electrochemical performance of Ni/YSZ pattern anodes in H_2-H_2O environments was developed. The model describes elementary chemical reactions, electrochemical reactions and surface diffusion on Ni/YSZ pattern anodes. A new charge transfer reactions mechanism proposed by Shishkin and Ziegler (2010) based on Density Functional Theory (DFT) study was investigated through kinetic modeling and pattern anode experimental validation. The predictive capability of this reaction mechanism to represent our experimental results was evaluated by comparing the simulated Tafel plots with our experimental data under a wide range of H_2 and H_2O partial pressures. Good agreements between simulation and experimental results were obtained.

The important conclusions obtained through this work are summarized in the following subsections.

8.1.1 Fabrication of Ni/YSZ Pattern Anodes

In this work, an effective method for fabricating Ni/YSZ pattern anodes was developed and presented in great details. This method includes a photolithographic process using a bi-layer resist system and Ni deposition by DC magnetron sputtering. Imaging resist nLOF2035 and sacrificial resist PGMI SF11 were chosen for the photolithographic process. It was found that a suitable size of the undercut is a key factor for the successful fabrication of pattern anodes. A simple way, involving taking microscopic photographs of photoresist pattern, to check if the undercut size is large enough for the lift-off was proposed; semi-circle wrinkles shown in the photograph indicates that the undercut is large enough for successful pattern anode fabrication. The final product prepared in this way showed straight and clear Ni patterns.

8.1.2 Stability Analysis of Ni/YSZ Pattern Anodes in H_2-H_2O Environments

In order to obtain a comprehensive and consistent data set for H_2 and CO electrochemical reactions, conducting electrochemical characterization of Ni/YSZ pattern anodes in H_2-H_2O and CO-CO_2 environments under stable conditions is necessary.

An extensive study was carried out to evaluate the effects of Ni thickness (0.5-1μm), temperature (500-800°C), and H_2O concentrations (3-70%) on Ni/YSZ pattern anode microstructure and electrochemical behavior changes in H_2-H_2O atmospheres. The important findings are summarized as:

- Ni/YSZ pattern anodes with 0.5 µm Ni thickness remained dense and stable patterns in dry H_2 at 550°C. However, significant changes in the TPB length with both dry and wet H_2 above 550°C were observed. Holes even formed in humidified H_2 with 3% H_2O at 550°C.

- Ni/YSZ pattern anodes with Ni thickness of 0.8 µm did not show significant changes in TPB line for all dry H_2 and humidified H_2 (3-70% H_2O) tests at 550°C. At 700°C, the TPB line did not change for tests carried out with dry and humidified (3%) H_2. However, holes formed when the H_2O content was 10% or above. At 800°C, the TPB line experienced coarsening and holes appeared in the Ni pattern when the cell was exposed to 3% H_2O.

- Ni/YSZ pattern anodes with Ni thickness of 1.0 µm maintained its dense structure when the cell was tested in H_2 with 3% H_2O in the temperature range of 500-800°C, although the TPB line was slightly modified. When the cell was tested in H_2 with 3-70% H_2O at 700°C, Ni patterns experienced holes formation. However, the new TPB length can be estimated through imaging techniques or modeling (treated as a free fit parameter).

- The time for pattern anode to reach stable performance is correlated to the temperature: the 1.0 μm thick Ni pattern microstructure stabilized faster when the temperature was increased to 750°C or 800°C (where it took ~22 hrs) compared to 700°C (where it took more than 50 hrs). A similar stabilization time was observed when the cells were made with different Ni pattern widths (20 μm and 50 μm), but with the same Ni thickness. The stabilization time was also not affected by pH_2. For a thinner Ni layer (0.8 μm), the pre-treatment time was shorter (~17 hrs at 700°C).

8.1.3 Experimental Characterization of H_2 Electrochemical Oxidation

In this section, effects of temperature, overptotential, triple phase boundary length, and a wide range of gas compositions on the pattern anode performance were evaluated under stable test conditions.

- Two different activation energies for the temperature dependence of R_p were observed in the temperature range of 500-800°C: an activation energy of 0.73±0.05 eV when the temperature varies between 500°C and 650°C and an higher activation energy of 1.17±0.01eV in the temperature range of 650-800°C. This may indicate changes in the dominating process(es) around 650°C.
- The dependence of polarization resistance on overpotential follows an exponential function, indicating that charge-transfer reactions may contribute to the rate-limiting steps.
- The polarization resistance increases with decreasing pH_2, and the hydrogen reaction order varies between 0.092 and 0.145. The difference of hydrogen reaction order at different temperatures is very small.

- The polarization resistance increases when increasing H_2O content from 3% to 30-40%. Further increase of H_2O content does not significantly affect the polarization resistance. The H_2O reaction order is 0.3, and H_2O related processes may also contribute to the rate-limiting processes of H_2 electrochemical oxidation.
- When plotting polarization resistance versus TPB length in logarithmic scale, slopes of the plots are -0.70 and -0.72 at 700°C and 750°C, respectively. Those values for the slope are lower than the expected slope of -1 if only charge transfer reactions control the overall reaction, further indicating that other processes are contributing to the overall process (e.g. H_2O diffusion in the gas channel).

8.1.4 Experimental Characterization of CO Electrochemical Oxidation

Electrochemical tests revealed that the polarization resistance depends on partial pressure of CO and CO_2, temperature and overpotential.

- The polarization resistance increases when increasing the partial pressure of CO, and the reaction order is -0.5. The partial pressure of CO_2 has a negative effect on the polarization resistance, and the reaction order is 0.3.
- The activation energy is 1.04 eV for CO electrochemical oxidation, which is lower than that for H_2 oxidation. For the CO-CO_2 system, the polarization resistance experiences a minimum when increasing the overpotential. A minimum polarization resistance appears when the overpotential is 0.1 V. For the H_2-H_2O system, the polarization resistance increases exponentially with increasing overpotential in the overpotential range of 0-0.3 V.
- For both H_2-H_2O and CO-CO_2 systems, charge transfer reactions are possible rate-limiting steps.

8.1.5 Kinetic Modeling Studies of H_2 Reaction Mechanism on SOFC Anodes

A kinetic model describing elementary reactions of H_2 electrochemical oxidation was developed. Surface reactions, electrochemical reactions and surface diffusions are described in the model. Two reaction mechanisms were considered. Reaction mechanism I is a simpler reaction mechanism that does not take into account reactions on YSZ surface. Reaction mechanism II is a new charge transfer reactions mechanism proposed by Shishkin and Ziegler (2010) based on Density Functional Theory (DFT) study. The new charge transfer reactions mechanism considers hydrogen oxidation at the interface of Ni and YSZ. It involves a hydrogen atom reacting with the oxygen ions bound to both Ni and YSZ to produce hydroxyl (Charge transfer reaction 1), the latter reacting with the other hydrogen atom to form water (Charge transfer reaction 2). The predictive capability of this reaction mechanism to represent our experimental results was evaluated. The simulated Tafel plots were compared with our experimental data for a wide range of H_2 and H_2O partial pressures and at different temperatures.

- For the reaction mechanism I, the simulated anodic branch in the Tafel plot can predict the experimental results. However, the simulated cathodic branch deviates significantly from the experimental data, which may be due to lack of surface reactions on YSZ, especially H_2O related processes. In addition, the simulated impedance is composed of one arc, whereas the experimental impedance contains two arcs. It was possible to reasonably predict the total polarization resistance when pH_2 is 3.0×10^4 Pa. However, as pH_2 increases, deviation between simulated and experimental polarization resistance increases.
- Regarding the reaction mechanism II, experimental data (both anodic and cathodic currents in the Tafel plots) can be well reproduced by simulation under a wide range of pH_2 and pH_2O conditions at both 700 and 550°C. It was found that the effect of surface diffusion on the pattern anode performance is negligible under all conditions in this work. Under cathodic polarization, charge transfer reaction 1 is always the dominating reaction

for charge transfer, irrespective of pH_2, pH_2O and temperature. Under anodic polarization, the dominating reaction switches from charge transfer reaction 1 to charge transfer reaction 2 when increasing the partial pressure of H_2O from 3.0×10^3 Pa to 5.0×10^4 Pa.

8.2 Recommendations for Future Work

In this work, extensive studies were performed regarding the electrochemical oxidation of H_2 and CO on Ni/YSZ pattern anodes. Although pattern anodes are a very useful tool to study the kinetics of electrochemical reactions for SOFC, there are some stability issues with such pattern anodes under certain operating conditions, especially in CO/CO_2 environments and H_2 environment with high amount of H_2O content (>10%) at elevated temperature (>600°C). Furthermore, the fabrication of the pattern anodes is a very sensitive and difficult technique. It is also time consuming and requires special facilities (clean room). Alternative simpler methods to study electrochemical kinetics are highly desirable. Below are suggested recommendations for future work.

- An alternative technique, which was reported by Kim et al. (2010), can be employed to make Ni/YSZ pattern anodes. With this new technique, the Ni patterns are fabricated as nanopores (circular openings array), and TPB length can be varied with changing the size of the nanopores. Ni patterns can be fabricated in the following way. First, a mask solution with desired size of monosized silica particles is created. Secondly, the monosized spherical silica particles are transferred onto YSZ surface with a Langmuir–Blodgett trough technique to form a close-packed monolayer of spherical particles on YSZ surface. Ni with desired thickness is then deposited using PVD techniques on the YSZ surface through the interspacing between the particles. Last, the silica particles are stripped off the YSZ substrate using ultrasonication.

  The Ni/YSZ pattern anodes fabricated with this new method can be used for evaluating the electrochemical behavior of H_2/CO mixtures in order to have a clear picture of the carbon formation when using hydrocarbon fuels. Suitable test conditions (temperature and H_2/CO ratio) need to be carefully chosen to prevent carbon formation during the tests. Moreover, kinetic models considering elementary H_2 and CO reaction steps needs to be developed and validated by the pattern anode experimental results. The elementary reaction steps of H_2 electro-oxidation can be taken from this study, whereas CO elementary reactions can be referred to the work performed by Shi et al. (2012) and Yurkiv et al. (2012).

- Ceria based SOFCs are promising materials for low and intermediate SOFC operating temperature because of their high ionic conductivity at lower temperature. However, details of the fuel electro-oxidation on such materials are still not clear. In the literature, only Haile's group (Chueh et al. 2011) experimentally studied the electrochemical oxidation of H_2 using ceria-metal patterned anodes. Therefore, there is still a lot of work to be done regarding H_2 and CO reaction mechanism on ceria based anodes.

  Currently, Ceria single crystal (CeO_2) with 40 nm thickness on YSZ surface (0.5 mm) is available in the market, and can be directly used for the Ni pattern anodes fabrication. Other ceria based single crystal (SDC/GDC) could be prepared by pulsed laser deposition (PLD). Either the bi-layer lift-off technique or the alternative technique mentioned above could be employed for the fabrication of Ni ceria based patterned anodes.

8.3 Contributions

In this work, four main contributions were made, which are described as:

- For the first time in the literature, a robust bi-layer lift-off method for Ni/YSZ pattern anodes fabrication was reported in great details. A simple and fast way to check the suitable size of undercuts was proposed. This can be widely used in thin film micro-fabrication process.
- A systematic stability analysis was conducted to evaluate the microstructure and electrochemical behavior changes of the pattern anode in H_2/H_2O environments. Factors that affect the stabilization of pattern anode performance were determined, which was not reported in the previous study.
- For both H_2 and CO electrochemical oxidation, comprehensive experimental data sets were obtained under stable conditions. These results contribute to new insights of H_2 and CO oxidation. In addition, these experimental data can be used for validating possible reaction mechanisms of both H_2 and CO.
- A new H_2 charge transfer reactions mechanism based on DFT study was validated through kinetic modeling and our pattern anode experimental data. Both simulation and experiment were performed in a wide range of pH_2O conditions. Furthermore, both anodic and cathodic current density was evaluated upon variations of pH_2 and pH_2O.

References

Aaberg, R.J, Tunold, R., Mogensen, M., Berg, R.W., Odegard, R. (1998). Morphological changes at the interface of the nickel-yttria stabilized zirconia point electrode. *147*(7), 2244.

Adams, T.M., Layton, R.A. Siahmakoun, A. (2010). Introductory MEMS fabrication and applications. New York., USA,: Springer.

Atkinson, A., Barnett, S., Gorte, R. J., Irvine, J. T. S., Mcevoy, A. J., Mogensen, M. (2004). Advanced anodes for high-temperature fuel cells. *Nature Materials, 3*(1), 17-27.

Beckel, D., Bieberle-Hütter, A., Harvey, A., Infortuna, A., Muecke, U., Prestat, M. (2007). Thin films for micro solid oxide fuel cells. *Journal of Power Sources, 173*(1), 325-345.

Bessler, W. G. (2005). A new computational approach for SOFC impedance from detailed electrochemical reaction-diffusion models. *Solid State Ionics, 176*(11-12), 997-1011.

Bessler, W. G. (2007). Rapid impedance modeling via potential step and current relaxation simulations. *Journal of the Electrochemical Society, 154*(11), B1186-B1191.

Bessler, W. G., Gewies, S., & Vogler, M. (2007). A new framework for physically based modeling of solid oxide fuel cells. *Electrochimica Acta, 53*(4), 1782-1800.

Bieberle, A. (2000). The electrochemistry of solid oxide fuel cell anodes: experiments, modeling, and simulations. Ph.D thesis, Swiss federal institute of technology, Switzerland.

Bieberle, A., & Gauckler, L. J. (1999). Modeling, simulations and experiments in the Ni, H_2-H_2O/YSZ system. *The Electrochemical Society Proceedings, Vol.99-19,* 549-559.

Bieberle, A., & Gauckler, L. J. (2000). Reaction mechanism of Ni pattern anodes for solid oxide fuel cells. *Solid State Ionics, 135*(1-4), 337-345.

Bieberle, A., & Gauckler, L. J. (2001). Ni-based SOFC anodes: Microstructure and Electrochemistry. *Z. Metallkd, 92*(7), 796-802.

Bieberle, A., & Gauckler, L. J. (2002). State-space modeling of the anodic SOFC system Ni, H_2-H_2O|YSZ. *Solid State Ionics, 146*(1-2), 23-41.

Bieberle, A., Meier, L. P., & Gauckler, L. J. (2001). The electrochemistry of Ni pattern anodes used as solid oxide fuel cell model electrodes. *Journal of the Electrochemical Society, 148*(6), A646-A656.

Boulenouar, F.Z., K. Yashiro, M. Oishi, A. Kaimai, Y. Nigara, T. Kawada, J. Mizusaki. (2001). Electrochemical oxidation of CO in a CO-CO_2 system at the interface of ni grid electrode/ YSZ electrolyte. *The Electrochemical Society Proceeding,* (16), 759.

Cherry, Owen. (2007). Fabrication of an atom chip for rydberg atom-metal surface interaction studies. Master Thesis, University of Waterloo, Waterloo, Canada

Costa-Nunes, O., Gorte, R. J., & Vohs, J. M. (2005). Comparison of the performance of Cu-CeO_2-YSZ and Ni-YSZ composite SOFC anodes with H_2, CO, and syngas. *Journal of Power Sources*, *141*(2), 241-249.

Chueh, W.C., Hao, Y., Jung, W., Haile, M. (2011). High electrochemical activity of the oxide phase in model ceria–Pt and ceria–Ni composite anodes. *Nature materials, 11*(2), 155-161.

de Boer, B. (1998). SOFC anode: Hydrogen oxidation at porous nickel and nickel/zirconia electrodes. PhD Thesis, University of Twente, Twente.

EG&G Technical Services, I. (Ed.). (2004). *Fuel cell handbook*

Ehn, A., Høgh, J., Graczyk, M., Norrman, K., Montelius, L., Linne, M., et al. (2010). Electrochemical investigation of nickel pattern electrodes in H_2/H_2O and CO/CO_2 atmospheres. *Journal of the Electrochemical Society, 157*, B1588.

Etsell, T. H., & Flengas, S. N. (1971). Overpotential behavior of stabilized zirconia solid electrolyte fuel cells. *Journal of the Electrochemical Society, 118*, 1890.

Evgenij Barsoukov, J. Ross Macdonald. (2005). *Impedance spectroscopy: Theory, experiment, and applications* (2nd ed.). Hoboken, N.J.: Wiley-Inter science.

Fogler, H. S. (Ed.). (1999). *Elements of chemical reaction engineering* (3rd ed.) Upper Saddle River, N.J. : Prentice Hall PTR.

Fuel cell today. (2012). *The fuel cell industry review,* Johnson Mattey PLC.

Geng, H. (2005). *Semiconductor manufacturing handbook*. New York: The McGraw-Hill Inc.

Gewies, S., & Bessler, W. G. (2008). Physically based impedance modeling of Ni/YSZ cermet anodes. *Journal of the Electrochemical Society, 155*(9), B937-B952.

Gewies, S., Bessler, W. G., Sonn, V., & Ivers-Tiffée, E. (2007). Experimental and modeling study of the impedance of Ni/YSZ cermet anodes. *ECS Transactions, 7*(1), 1573-1582.

Goodwin, D. G., Zhu, H., Colclasure, A. M., & Kee, R. J. (2009). Modeling electrochemical oxidation of hydrogen on Ni-YSZ pattern anodes. *Journal of the Electrochemical Society, 156*(9), B1004-B1021.

Habibzadeh, B. (2007). Understanding CO oxidation in SOFC'S using nickel patterned anode. PhD Thesis, University of Maryland, USA.

Hecht, E. S., Gupta, G. K., Zhu, H., Dean, A. M., Kee, R. J., Maier, L. (2005). Methane reforming kinetics within a Ni–YSZ SOFC anode support. *Applied Catalysis A: General, 295*(1), 40-51.

Hofmann, P., & Panopoulos, K. (2010). Detailed dynamic solid oxide fuel cell modeling for electrochemical impedance spectra simulation. *Journal of Power Sources, 195*(16), 5320-5339.

Holtappels, P., De Haart, L., & Stimming, U. (1999a). Reaction of Hydrogen/Water mixtures on nickel-zirconia cermet electrodes: I. DC polarization characteristics. *Journal of the Electrochemical Society, 146*, 1620.

Holtappels, P., Vinke, I., de Haart, L., & Stimming, U. (1999b). Reaction of hydrogen/water mixtures on nickel-zirconia cermet electrodes - II. AC polarization characteristics. *Journal of the Electrochemical Society, 146*(8), 2976-2982.

Holtappels, P., Haart, L. G. J. D., Stimming, U., Vinke, I. C., & Mogensen, M. (1999c). Reaction of CO/CO_2 gas mixtures on Ni–YSZ cermet electrodes. *Journal of Applied Electrochemistry, 29*(5), 561-568.

Janardhanan, V. M., & Deutschmann, O. (2006). CFD analysis of a solid oxide fuel cell with internal reforming: Coupled interactions of transport, heterogeneous catalysis and electrochemical processes. *Journal of Power Sources, 162*(2), 1192-1202.

Jiang, S. P., & Badwal, S. P. S. (1999). An electrode kinetics study of H_2 oxidation on Ni/Y_2O_3-ZrO_2 cermet electrode of the solid oxide fuel cell. *Solid State Ionics, 123*(1-4), 209-224.

Kendall, K. (2005). Progress in solid oxide fuel cell materials. *International Materials Reviews, 50*(5), 257-264.

Kim, Y. B., Hsu, C., Connor, S. T., Gür, T. M., Cui, Y., & Prinz, F. B. (2010). Nanopore patterned pt array electrodes for triple phase boundary study in low temperature SOFC. *Journal of the Electrochemical Society, 157*(9), B1269-B1274.

Koep, Erik. (2006). A quantitative determination of electrode kinetics using micropatterned electrodes. PhD thesis, Georgia Institute of Technology, Atlanta.

Lauvstad, G. O., Tunold, R., & Sunde, S. (2002a). Electrochemical oxidation of CO on Pt and Ni point electrodes in contact with an yttria-stabilized zirconia electrolyte I. Modeling of Steady-State and Impedance Behavior. *Journal of the Electrochemical Society, 149*(12), E497-E505.

Lauvstad, G.O., Tunold, R., & Sundeb, S. (2002b). Electrochemical oxidation of CO on Pt and Ni point electrodes in contact with an yttria-stabilized zirconia electrolyte II. steady-state and impedance measurements. *Journal of the Electrochemical Society, 149*(12), E506-E514

Li, X. (2005). *Principles of fuel cells* (1st ed.) Taylor & Francis, New York.

Mark E. Orazem, Bernard Tribollet. (2008). *Electrochemical impedance spectroscopy*. Hoboken, New Jersey: John Wiley & Sons, Inc.

Matsuzaki, Y., Hishinuma, M., & Yasuda, I. (1999). Electrochemical characteristics of a Ni-YSZ cermet electrode on YSZ in a H_2-H_2O-CO-CO_2 system. in Proceedings of Solid Oxide Fuel Cell VI, S. C. Singhal and M. Dokiya, Editors, PV 99-19, p. 560-570, The Electrochemical Society Proceedings Series, Pennington, NJ.

Mattox, D. M. (2010). *Handbook of physical vapour deposition (PVD) processing* (2nd ed.). Oxford., UK: William Andrew Applied Science.

Minh, N. Q. (2004). Solid oxide fuel cell technology—features and applications. *Solid State Ionics, 174*(1), 271-277.

Minh, N. Q., & Takahashi, T. (1995). *Science and technology of ceramic fuel cells* (1st ed.) Elsevier Science.

Mizusaki, J., Tagawa, H., Miyaki, Y., Yamauchi, S., Fueki, K., Koshiro, I., et al. (1992). Kinetics of the electrode reaction at the CO-CO_2, porous Pt/stabilized zirconia interface. *Solid State Ionics, 53-56*(Part 1), 126-134.

Mizusaki, J., Tagawa, H., & Saito, T. (1994a). Preparation of nickel pattern electrodes on YSZ and their electrochemical properties in H_2-H_2O atmospheres. *Journal of the Electrochemical Society, 141*, 2129-2134.

Mizusaki, J., Tagawa, H., Saito, T., Yamamura, T., Kamitani, K., Hirano, K., et al. (1994b). Kinetic studies of the reaction at the nickel pattern electrode on YSZ in H_2-H_2O atmospheres. *Solid State Ionics, 70-71*(pt 1), 52-58.

Mogensen, M., & Skaarup, S. (1996). Kinetic and geometric aspects of solid oxide fuel cell electrodes. *Solid State Ionics, 86*, 1151-1160.

Nishimura, T., Toi, H., Hoshino, Y., Toyoda, E., & Kido, Y. (2001). Surface structure of Y_2O_3(9.5 mol%)-stabilized ZrO_2(001) determined by high-resolution medium-energy ion scattering. *Physical Review B (Condensed Matter and Materials Physics), 64*(7), 073404/1-073404/4.

Offer, G. J., & Brandon, N. P. (2009). The effect of current density and temperature on the degradation of nickel cermet electrodes by carbon monoxide in solid oxide fuel cells. *Chemical Engineering Science, 64*(10), 2291-2300.

O'Hayre, R., Cha, S., Colella, W., & Prinz, F. B. (2006). *Fuel cell fundamentals*. Hoboken, N.J.: John Wiley & Sons.

Phongaksorn, M. (2010). The Development of $Ni_{1-x-y}Cu_xMg_yO$-SDC Anode for Intermediate Temperature Solid Oxide Fuel Cells (IT-SOFCs), Ph.D Thesis, University of Waterloo, Waterloo, Canada

Primdahl, S., & Mogensen, M. (1997). Oxidation of hydrogen on Ni/yttria-stabilized zirconia cermet anodes. *Journal of the Electrochemical Society, 144*, 3409-3419.

Primer on solid oxide fuel cells Retrieved 2/23/2010, 2010, from http://www.sofccanada.com/primer.html

Raz, S., Sasaki, K., Maier, J., & Riess, I. (2001). Characterization of adsorbed water layers on Y_2O_3-doped ZrO_2 . *Solid State Ionics, 143*(2), 181-204.

Shi, Y., Cai, N., Li, C., Bao, C., Croiset, E., Qian, J., et al. (2008). Simulation of electrochemical impedance spectra of solid oxide fuel cells using transient physical models. *Journal of the Electrochemical Society, 155*, B270.

Shi, Y., Li, C., & Cai, N. (2011). Experimental characterization and mechanistic modeling of carbon monoxide fueled solid oxide fuel cell. *Journal of Power Sources, 196*(13), 5526-5537.

Shi, Y., Cai, N., & Mao, Z. (2012). Simulation of EIS spectra and polarization curves based on Ni/YSZ patterned anode elementary reaction models. *International Journal of Hydrogen Energy, 37*(1), 1037-1043.

Shishkin, M and Ziegler, T (2008). The oxidation of H_2 and CH_4 on an oxygen-enriched yttria-stabilized zirconia surface: A theoretical study based on density functional theory. *Journal of Physical Chemistry* C 112(49):19662-9.

Shishkin, M and Ziegler, T (2009). Oxidation of H_2, CH_4, and CO molecules at the interface between nickel and yttria-stabilized zirconia: A theoretical study based on DFT. *Journal of Physical Chemistry* C 113(52):21667-78.

Shishkin, M and Ziegler, T (2010). Hydrogen oxidation at the Ni/Yttria-stabilized zirconia interface: A study based on density functional theory. *Journal of Physical Chemistry C*, 114 (2010) 11209-11214.

Singhal, S. C., & Kendall, K. (2004). *High-temperature solid oxide fuel cells: Fundamentals, design and application,* Elsevier Science Pub Co.

Snyder, G. J., & Haile, S. M. (2004). Fuel cell materials and components. *Advanced Materials for Energy Conversion II Proceedings, Start date 2004/03/14-End date 2004/03/18*, pp. 33-41.

Sukeshini, A. M., Habibzadeh, B., Becker, B. P., Stoltz, C. A., Eichhorn, B. W., & Jackson, G. S. (2006). Electrochemical oxidation of H_2, CO, and CO/H_2 mixtures on patterned Ni anodes on YSZ electrolytes. *Journal of the Electrochemical Society, 153*, A705.

Suwanwarangkul, R. (2005). Model Development and Validation of Solid Oxide Fuel Cells Using H_2-H_2O-CO-CO_2 Mixtures: From Button Cell Experiments to Tubular and Planar Cells. Ph.D thesis, University of Waterloo, Waterloo, Canada

Utz, A. (2011). The electrochemical oxidation of H_2 and CO at patterned ni anodes of SOFC. PhD Thesis, Karlsruhe Institute of Technology (KIT), Germany.

Utz, A., Störmer, H., Gerthsen, D., Weber, A., & Ivers-Tiffee, E. (2011a). Microstructure stability studies of Ni patterned anodes for SOFC. *Solid State Ionics, 192*(1), 565-570.

Utz, A., Leonide, A., Weber, A., & Ivers-Tiffée, E. (2011b). Studying the CO–CO_2 characteristics of SOFC anodes by means of patterned Ni anodes. *Journal of Power Sources, 196*(17), 7217-7224.

Utz, A., Störmer, H., Leonide, A., Weber, A., & Ivers-Tiffée, E. (2010). Degradation and relaxation effects of Ni patterned anodes in H_2–H_2O atmosphere. *Journal of the Electrochemical Society, 157*, B920.

Vijay, P., Samantaray, A., & Mukherjee, A. (2010). Development of a thermodynamically consistent kinetic model for reactions in the solid oxide fuel cell. *Computers & Chemical Engineering, 34*(6), 866-877.

Vogler, M., Bieberle-Hu¨tter, A., Gauckler, L., Warnatz, J., & Bessler, W. G. (2009). Modelling study of surface reactions, diffusion, and spillover at a Ni/YSZ patterned anode. *Journal of the Electrochemical Society, 156*(5), B663-B672.

Vogler, M. (2009). Elementary kinetic modelling applied to solid oxide fuel cell pattern anodes and a direct flame fuel cell system. Ph.D thesis, Combined Faculties for the Natural Sciences and for Mathematics of the Ruperto-Carola, University of Heidelberg, Germany.

Weber, A., Sauer, B., Müller, A. C., Herbstritt, D., & Ivers-Tiffée, E. (2002). Oxidation of H_2, CO and methane in SOFCs with Ni/YSZ cermet anodes. *Solid State Ionics, 152*, 543-550.

Yao, W., Croiset., E. (2013a). Ni/YSZ pattern anodes fabrication and their microstructure and electrochemical behaviour changes in H_2-H_2O environments. *J. Power Sources,* 226 162-172.

Yao, W., Croiset., E. (2013b). Investigation of H_2, CO and Syngas Electrochemical Performance using Ni/YSZ Pattern Anodes. This work was presented in 223rd ECS Meeting, and then submitted to *The Electrochemcial Society Transactions*.

Yao, W., Croiset., E. (2013c). Modeling and Ni/YSZ pattern anode experimental validation of a new charge transfer reactions mechanism for hydrogen electrochemical oxidation on SOFC anodes. Submitted to *J. Power Sources*. Feedback was received from reviewers and the paper is currently in the second revision stage.

Yao, W., Croiset., E. (2013d). Stability and electrochemical performance of Ni/YSZ pattern anodes in H_2/H_2O atmosphere. Submitted to *The Canadian Journal of Chemical Engineering*.

Yurkiv, V., Starukhin, D., Volpp, H. R., & Bessler, W. (2011). Elementary reaction kinetics of the CO⁄ CO_2⁄ Ni⁄ YSZ electrode. *Journal of the Electrochemical Society, 158*(1), B5-B10.

Yurkiv, V., Utz, A., Weber, A., Ivers-Tiffée, E., Volpp, H. R., & Bessler, W. G. (2012). Elementary kinetic modeling and experimental validation of electrochemical CO oxidation on Ni/YSZ pattern anodes. *Electrochimica Acta, 59*, 573-580.

Zhu, H., Kee, R. J., Janardhanan, V. M., Deutschmann, O., & Goodwin, D. G. (2005). Modeling elementary heterogeneous chemistry and electrochemistry in solid oxide fuel cells. *Journal of the Electrochemical Society.Vol.152, 152*(12), A2427-A2440.

Zhu, W. Z., & Deevi, S. C. (2003). A review on the status of anode materials for solid oxide fuel cells. *Materials Science and Engineering A, 362*(1-2), 228-239.

http://www.fuelcelltoday.com/using-fuel-cells/valorising-by-product-hydrogen

Appendix A

Chemical etching procedure

DC magnetron sputtering is employed for the Ni film deposition on the YSZ single crystal side. The size of Ni target used in this study is 6" dia. × 0.125", and its purity is 99.99%. After optimization of sputtering conditions, the parameters in Table A-1 were chosen for depositing 1 µm Ni film.

Table A-1 DC magnetron sputtering parameters for Ni film deposition

Parameters	Value (unit)
Sputtering gas flow rate	30 sccm
Basic pressure in the chamber	5.6×10^{-6} torr
Pressure during sputtering	3.8×10^{-3} torr
Power provided at the target	500 kw
Sputtering rate	16.67 nm/min

Positive photoresist AZ3312 (AZ Electronic Materials) is spin-coated on the Ni surface by using a spinner. By doing this, the photoresist is first dispensed on the Ni surface through a syringe and a 0.45 µm filter. This process is done with the help of a semi-automatic dispersing system.

The relationship between the spinning speed and the thickness of photoresist AZ3312 coated is showed in Figure A-1. Soft-bake is processed at 90°C for 30 s on a vacuum hotplate. After cooling down to room temperature, the substrate is placed in a mask aligner (Oriel Corp). The mask is centered on the mask holder with vacuum. Both positions of the mask and YSZ substrate are adjusted to make contact between them, so that the pattern on the mask can be transferred to the YSZ.

Ultraviolet Illumination System (Oriel Corp.) with wavelength from 350 to 450 nm is used for providing UV radiation. The photoresist shone through the mask is exposed 10 s under UV radiation. The photoresist pattern development is performed in an AZ300 MIF developer solution (AZ Electronic Materials) at room temperature. After development, the Ni pattern is etched in a ferric chloride solution for 20 s at 40°C. AZ Kwik Strip photoresist remover (AZ Electronic Materials) is used for the photoresist removal at 60°C for 5-10 min. The times periods for UV exposure, developing, and etching were optimized to avoid over-etching or under-etching for the desired pattern. The conditions of photolithography process using positive photoresist are summarized in Table A-2.

Table A-2 Parameters for Ni patterning by chemical etching

Parameters	Value (unit)
Spinning speed for photoresist coating	4000 rpm
Photoresist thichness	1 μm
Soft-bake temperature	90°C
Soft-bake time	60 s
UV exposure time	10 s
Post-bake temperature	110°C
Post-bake time	60 s
Developing time	120 s
Etching temperature	40°C
Etching time	20 s
Photoresist removal temperature	60°C
Photoresist removal time	10 min

Lift-off procudure

For lift-off process, negative photoresist AZ nLOF 2035 (AZ Electronic Material) is employed. The relationship between the spinning speed and the thickness of photoresist AZ nLOF 2035 coated is showed in Figure A-2. The photoresist spin speed curve of PGMI SF 11 is given in Figure A-3.

The Ni/YSZ pattern anode fabrication process is as follows:

1. Apply the negative photoresist on the YSZ surface
2. Spin at 3000 rpm for 30 s
3. Soft-bake at 110°C on a vacuum hotplate for 60 s
4. Centre mask on the mask holder and substrate on the substrate holder
5. Expose the photoresist with mask aligner for 12 s
6. Post-exposure bake at 110°C for 60 s
7. Develop in AZ MIF300 developer (AZ Electronic Material)
8. Deposit Ni layer by E-beam evaporation
9. Put the substrate in the acetone solution for 30 min and then rinse with IPA to remove the photoresist together with the unwanted Ni film

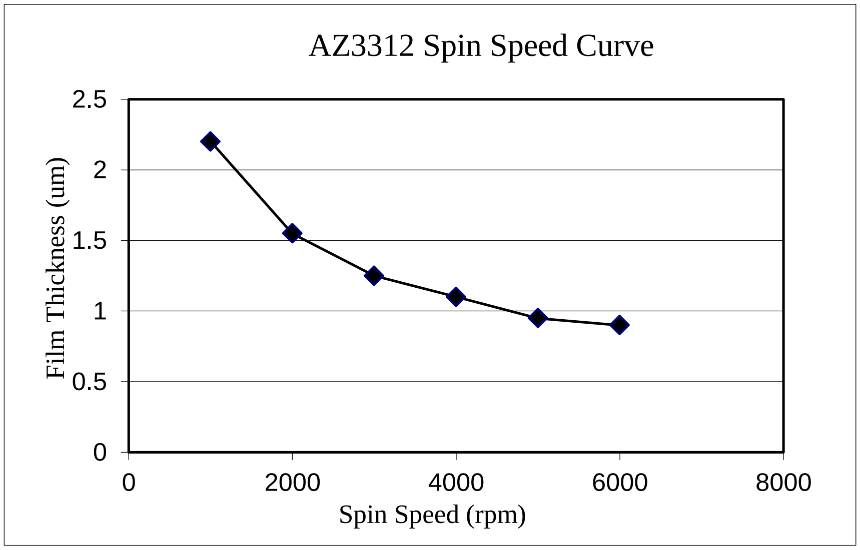

Figure A-1 Photoresist AZ3312 spin speed curve (prepared by AZ Electronic Material)

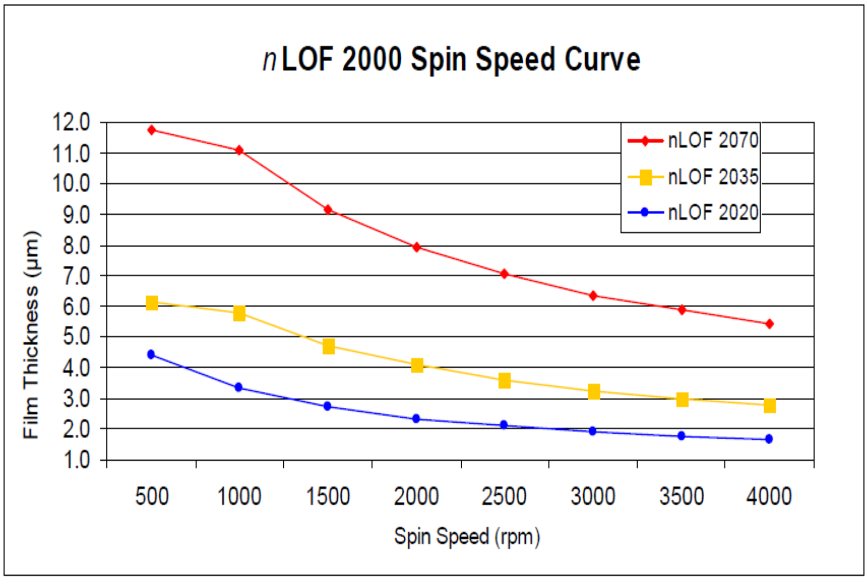

Figure A-2 Photoresist AZ nLOF 2000 spin speed curve (prepared by AZ Electronic Material)

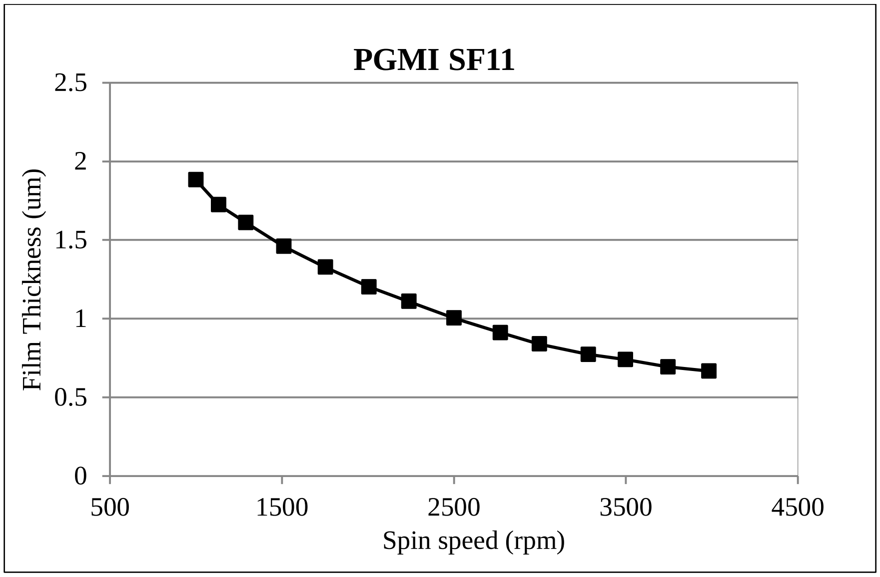

Figure A-3 Photoresist PGMI S11 spin speed curve (Prepared by MicroChem)

Appendix B

Thermodynamics calculation of the range of pCO and pCO$_2$ variation

The carbon formation in CO/CO$_2$ environments is caused by the Boudouard reaction, which is given as:

$$2\mathrm{CO} \rightleftarrows \mathrm{C} + \mathrm{CO_2} \qquad \text{B1}$$

The following condition must be satisfied in order to prevent carbon formation.

$$pCO_2 > K_{eq}(pCO)^2 \qquad \text{B2}$$

where K_{eq} is the equilibrium constant of reaction B1, and it can be obtained through calculating the Gibbs free energy change (ΔG).

$$\ln(K_{eq}) = \frac{-\Delta G}{RT} \qquad \text{B3}$$

The thermodynamic parameters in Table B1, G_{CO} and G_{CO2}, were taken from Li (2005). K_{eq} is calculated using Equation B3. Figure B-1 shows the plot of lnK_{eq} versus 1000/T. In our work, the electrochemical characterization of CO electrochemical oxidation was performed in the temperature range of 700-800°C. However, the thermodynamic parameters are not available in the literature at 700°C, 750°C and 800°C. Therefore, K_{eq} can not be calculated using Equation B3 at these temperatures. But, we can calculate K_{eq} based on the plot given in Figure B-1. K_{eq} is 1.06 at 700°C, 0.374 at 750°C and 0.145 at 800°C. Table B-2 presents the boundary values of pCO$_2$ under different pCO conditions at 700°C, 750°C and 800°C. These values are very similar to the values reported by Utz et al. (2011b), which is given in Figure B-2. The range of pCO and pCO$_2$ that avoids Ni oxidation in this study was referred from Utz et al. (2011b).

Table B-1 Thermodynamic parameters (Li, 2005)

T(°C)	T(K)	1000/T (1/K)	G_{CO} (kJ/kmol)	G_{CO2} (kJ/kmol)	ΔG (kJ/kmol)	lnK_{eq}	K_{eq}
25	298	3.36	-137163	-394428	-120102	48.47	1.13×10^{21}
27	300	3.33	-137328	-394433	-119777	48.02	7.16×10^{20}
127	400	2.5	-146332	-394718	-102054	30.69	2.12×10^{13}
227	500	2.0	-155403	-394983	-84177	20.25	6.22×10^{8}
327	600	1.67	-164470	-395226	-66286	13.29	589711.6
427	700	1.43	-173499	-395443	-48445	8.32	4120.66
527	800	1.25	-182473	-395635	-30689	4.61	100.87
627	900	1.11	-191386	-395799	-13027	1.74	5.70
727	1000	1.00	-200238	-395939	4537	-0.55	0.58
827	1100	0.91	-209030	-396056	22004	-2.41	0.090

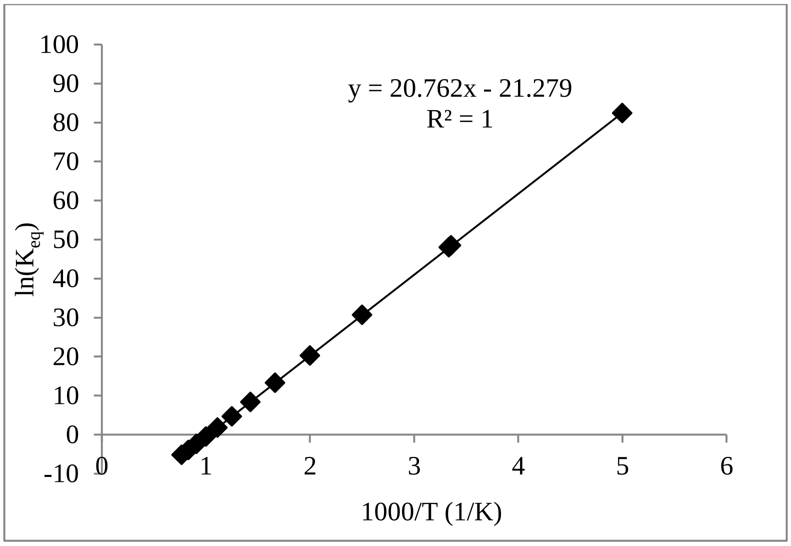

Figure B-1 Plot of ln(K_{eq}) versus 1000/T

Table B-2 Boundary values of pCO_2 under different pCO conditions at 700°C, 750°C and 800°C

700°C				750°C				800°C			
pCO (atm)	pCO (Pa)	pCO_2 (atm)	pCO_2 (Pa)	pCO (atm)	pCO (Pa)	pCO_2 (atm)	pCO_2 (Pa)	pCO (atm)	pCO (Pa)	pCO_2 (atm)	pCO_2 (Pa)
0.01	1000	0.000106	10.6	0.01	1000	0.0000374	3.74	0.01	1000	0.0000145	1.45
0.05	5000	0.002652	265.2	0.05	5000	0.000935	93.5	0.05	5000	0.0003625	36.25
0.1	10000	0.010609	1060.9	0.1	10000	0.00374	374	0.1	10000	0.00145	145
0.2	20000	0.042436	4243.6	0.2	20000	0.01496	1496	0.2	20000	0.0058	580
0.3	30000	0.095481	9548.1	0.3	30000	0.03366	3366	0.3	30000	0.01305	1305
0.4	40000	0.169744	16974.4	0.4	40000	0.05984	5984	0.4	40000	0.0232	2320
0.5	50000	0.265225	26522.5	0.5	50000	0.0935	9350	0.5	50000	0.03625	3625
0.6	60000	0.381924	38192.4	0.6	60000	0.13464	13464	0.6	60000	0.0522	5220
				0.7	70000	0.18326	18326	0.7	70000	0.07105	7105
								0.8	80000	0.0928	9280

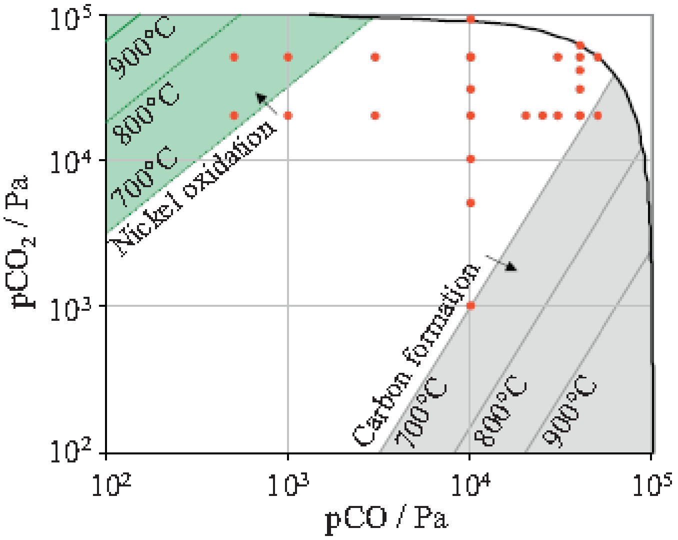

Figure B-2 Parameter variation range of pCO and pCO_2 used in Utz et al. (2011b) to avoid carbon deposition and Ni oxidation (taken from Utz et al., 2011b)

Appendix C

An Example of gPROMS simulation code

Surface coverages of different Ni surface species at OCV condition with reaction rate constants from Bessler (2005)

```
PARAMETER
 n as real default 2
 F as real default 96500
 L as real default 1.67E-9
 d as real default 0.37
 pi as real default 3.14
 Beta as real
 T as real default 973
 period as real default 1
 Eta_steady as real
 Eta_v as real
 R1 AS REAL default 8.314

VARIABLE
 Theta_O, Theta_H, Theta_OH,Theta_H2O,Theta_Ni as surface_coverage
 v1,v2,k1,k_1,k2,k_2,k3,k_3,k4,k_4,k5,k_5,k6,k_6 as reaction_rate_constant
 I_f as current_density
 Eta as voltage

 EQUATION
```

```
 $Theta_O=k1*theta_Ni-k_1*theta_O-k2*theta_O*theta_H+k_2*theta_OH*theta_Ni-
k3*theta_O*theta_H2O+k_3*theta_OH^2;
 $Theta_H=-k2*theta_O*theta_H+k_2*theta_OH*theta_Ni-
k4*theta_H*theta_OH+k_4*theta_H2O*theta_Ni+2*k6*theta_Ni^2-2*k_6*theta_H^2;
 $Theta_OH=k2*theta_O*theta_H-k_2*theta_OH*theta_Ni+2*k3*theta_O*theta_H2O-
2*k_3*theta_OH^2-k4*theta_H*theta_OH+k_4*theta_H2O*theta_Ni;
 $Theta_H2O=-k3*theta_O*theta_H2O+k_3*theta_OH^2+k4*theta_H*theta_OH-
k_4*theta_H2O*theta_Ni+k5*theta_Ni-k_5*theta_H2O;
 Theta_Ni=1-(theta_O+theta_H+theta_OH+theta_H2O) ;
 k1=2E2*exp(n*F*Beta*Eta/R1/T);
 k_1=5.6E10*exp(-(1-Beta)*n*F*Eta/R1/T);
 v1=k1*theta_Ni;
 v2=k_1*theta_O;
 I_f = n*F*L*d*(v1-v2);

UNIT
T101 as surfaceTPB_1

SET
Within T101 do
   Beta:=0.5;
   Eta_v :=0.0;
   Eta_steady:=0;
End

ASSIGN
Within T101 do
    T101.k2:=2E11;
```

```
    T101.k_2:=1.3E4;
    T101.k3:=1.0e12;
    T101.k_3:=5.8E2;
    T101.k4:=1.5;
    T101.k_4:=6.0E5;
    T101.k5:=8E4;
    T101.k_5:=1E11;
    T101.k6:=6E7;
    T101.k_6:=2.4e8;
    T101.Eta :=Eta_steady+Eta_v * sin(2*Pi*time/period) ;
END

INITIAL
Within T101 do
    Theta_H=0.32837284;
    Theta_H2O=5.254809E-7;
    Theta_OH=0.014880868;
    Theta_O=2.1946005E-9;
End

SOLUTIONPARAMETERS
   IndexReduction := ON ;

SCHEDULE
   Continue for 10
```